Dissertation

DENSITY FUNCTIONAL THEORY AND MODEL-BASED STUDIES OF CHARGE TRANSFER AND MOLECULAR SELF-ORGANIZATION ON SURFACES: IMPLICATIONS FOR MOLECULAR-BASED QUANTUM CELLULAR AUTOMATA

Alejandro Santana-Bonilla
Mat.-Nr.: 4033289

Density functional theory and model-based studies of charge transfer and molecular self-organization on surfaces: implications for molecular-based Quantum Cellular Automata

DISSERTATION

zur Erlangung des akademischen Grades

Doctor rerum naturalium

(Dr. rer. nat.)

vorgelegt

der Fakultät Mathematik und Naturwissenschaften

der Technischen Universität Dresden

von

MSc. Alejandro Santana-Bonilla

geboren am Bogotá, Kolumbien,

Tag der mündlichen Prüfung: 10.03.2017

Diese Arbeit entstand in der Arbeitsgruppe von Prof. Dr. Gianaurelio Cuniberti an der Technischen Universität Dresden.

CONFIRMATION

I confirm that I independently prepared the thesis and that I used only the references and auxiliary means indicated in the thesis.

Dresden, 24.10.2016

ABSTRACT

Molecular-based quantum cellular automata (m-QCA), as an extension of quantum-dot QCAs, offer a novel alternative in which binary information can be encoded in the molecular charge configuration of a cell and propagated via nearest-neighbor Coulombic cell-cell interactions. Appropriate functionality of m-QCAs involves a complex relationship between quantum mechanical effects, such as electron transfer processes within the molecular building blocks, and electrostatic interactions between cells. In the first part of this document, the influence of structural distortions in single m-QCA is addressed within a minimal model using an diabatic-to-adiabatic transformation. Thus, it is shown that even small changes of the classical square geometry between driver and target cells, such as those induced by distance variations or shape distortions, can make cells respond to interactions in a far less symmetric fashion, modifying and potentially impairing the expected computational behavior of the m-QCA. The model has been further extended to consider time-dependent external electric fields in which a special emphasis is given to the profiles in which this external parameter can interact with the associated molecular complex. The results of the model have been validated by a direct comparison with first-principle calculations allowing to conclude the plausibility to induce the intra-molecular charge transfer process in a controllable manner via the interaction with the external electric field. The influence played by the electric field profile in the response of the molecular complex is also investigated. The results suggests a major role played by this variable in terms of the time length in which the intra-molecular charge transfer can be observed. In the second part, first-principle theoretical calculations of the self-assembly properties and electronic structure of Ferrocene-functionalized complexes have been carried out. Hence, five different molecular complexes which offer a potential playground to realistic implement the m-QCA paradigm have been investigated. The main emphasis is given to study the interaction between localized charge-carrier molecular states and the delocalized surface states. The results of these calculations demonstrate the possibility to obtain real systems in which intra-molecular charge localization can be combined with self-assembly scaffolding and absorbed on either Highly oriented pyrolytic graphite (HOPG) or metallic-surfaces. Finally, the validation of these findings is carried out via comparison with accesible experimental results and opening the gate to plausible strategies where the paradigm can be implemented.

CONTENTS

1   INTRODUCTION

Since the statement "There is Plenty of Room at the Bottom" was coined by Richard Feynman [1], nanotechnology has become by itself a vivid branch of physics where its ultimate goal is not only merely restricted to functionalize effects known from quantum mechanical systems (such as quantum tunneling) but rather to question and expand the ideas of some established paradigms using those effects. In this matter, semiconductor technology has been the first playground in which physical systems have been used to represent information by employing the complementary metal-oxide semiconductor (CMOS) [2]. Despite all the advances carried out using this technology, the heat-dissipation problem produced by the continuous miniaturization of the device dimensions is imposing a physical limit to our cornerstone technology [3]. Therefore, many different alternatives have been suggested in the past years which includes but is not restricted to single-electron transistors, molecular electronics, spintronics among others [4]. As part of these new and revolutionary concepts Quantum Cellular Automata (QCA) and its ultimate implementation, the molecular Quantum Cellular Automata (m-QCA), has arisen as one alternative way both to store information and also to perform computation [5]. The paradigm has been already tested and implemented in various proof-of-principle devices using physical candidates like metallic, semiconductor quantum-dots and magnetic systems [6, 7, 8, 9, 10, 11]. However, in order to make this technology accessible to a room-temperature implementation still one crucial question must be answered concerning the suitable system that can host this paradigm. Hence, the molecular-QCA (m-QCA) implementation is one of the alternatives where the QCA concept can be implemented and further developed [12, 13, 14, 15, 16]. The results presented in this work have been carried out embedded into the European project MOLARNET in which six different experimental and theoretical partners have been involved in the achievement of the implementation of the m-QCA paradigm. The experimental partners from the University of Bologna were responsible for the synthesis and electrochemical characterization of the plausible candidates. Subsequently, at the Trinity College Dublin and the University of Strasbourg the deposition of such molecules over different surfaces were performed including STM images characterization. Finally, the groups based at CNR and STMicroelectronics (Italy) were responsible for the write-in device functionalization and further theoretical studies related with the circuitry of the paradigm, correspondingly. In this matter, the MOLARNET consortium attempts to combine two well-known controllable effects such as charge carrier localization within organometallic complexes and molecular self-assembly to offer the basic scaffold for subsequent circuitry construction [17].
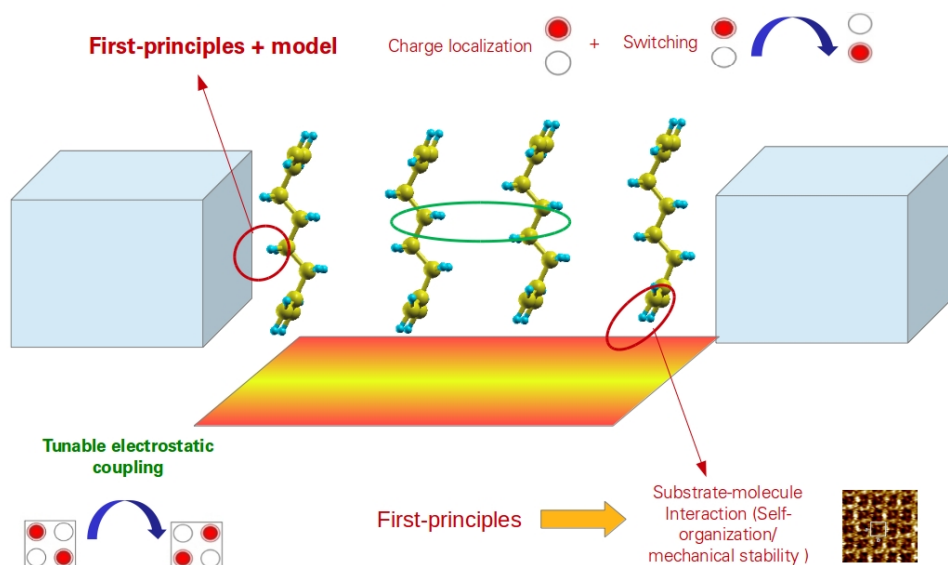
Figure 1.1: Schematic representation of the topics studied in this thesis. Firstly, a minimal modeling approach has been used in order to investigate the physical conditions needed to inscribe information in a molecular complex. Secondly, plausible candidates have been studied by employing first-principle calculations emphasizing the electronic structure properties of the possible candidates and the further influence in the electronic structure due to the surface-molecule interaction.

Thus, despite many attempts to implement the paradigm there are still many questions open concerning the applicability of the concept and the possibility to implement it in a real world device. Hence, as is shown in Fig 1.1, in order to carry out a systematic study to understand the fundamental requirements to implement m-QCA one has to investigate three main interactions. Firstly, the imprinting problem which implies to force a logical state in the molecule (read-in system) is one of the most important questions still to be solved in terms of viability and physical constraints. Secondly, the formation of molecular networks via H-bonding requires the support of a surface that is a physical system that interacts with the plausible molecular candidate. Hence, it is also important to study the influence of this interaction in the electronic structure of the molecule and its role played in the charge localization effect. Thirdly, the propagation of information via electrostatic coupling of the neighboring molecular complex is the last interaction important to fully understand the paradigm conditions. Hence, in this work I have developed a systematic study of the first two fundamental questions. The results of this thesis have been organized in the following way. Firstly, chapter 2 is reserved for the explanation of the paradigm cornerstone ideas and the employed theoretical tools used throughout this work and will serve as a reference point to understand the obtained results in this investigation. In chapter 3, I am investigating the nature of the switching behavior in a QCA cell under the influence of outer parameters such as geometrical distortions and external electric fields. To that end, I am presenting a combined theoretical methodologies, where minimal models are used to understand the nature of the effect and the obtained results are verified using ab-initio methods. In chapter 4 and 5, in a joint experimental and theoretical study, a family of Guanine- and Porphyrin- Ferrocene appended complexes are investigated in order

to explore the feasibility of the paradigm implementation where a detailed analysis of the electronic structure of the candidate molecules is carried out. Likewise, the functionalization of these complexes over surfaces, specifically over Highly ordered Pyrolytic Graphite (HOPG), is studied in order to understand the role played by the surface in the charge-carrier spatial localization properties of the molecular-complexes. In chapter 6, a third-generation of molecules is synthesized in which a doping with a metallic ion is investigated. Likewise, in order to try to implement a suitable clocking system for the m-QCA, the moieties are deposited onto a metallic surface in order to exploit the interface dipole effect as an effective clocking field. Interestingly, new theoretical methodologies are developed since the crux of the problem combines the description of a highly-localized molecular system such as the organometallic complexes with a highly delocalized system in which electrons are itinerants such as the Au(111) metallic surface. Moreover, three appendices are added in order to strengthen the results and interpretations carried out in the corresponding chapters. The final chapter is outlining the results of this work and the challenges ahead in order to implement this technology.

Part I

Theoretical Background

1.1 QUANTUM CELLULAR AUTOMATA: A BRIEF INTRODUCTION TO THE PARADIGM

In the first part of this chapter, the essential ideas of the QCA-model paradigm will be presented in order to give a brief introduction to this topic and serve as a reference of information to the reader. In the second part of the this chapter, the numerical methodologies used in this work will revised and presented in order to offer a broad vision of all the tools employed in the course of this thesis.

1.1.1 QCA-cell

In this paradigm, the first main important concept is to represent information via the distinguishable arrangement of charge configurations within metallic, semiconductor quantum dots [5, 6, 8, 10] or by employing molecular-complexes [12]. Thus, the corresponding states not only must have energetic barriers between them in order to make them differentiable but also to be controllable in order to perform a conditional change between states. This property is crucial since the classical binary "0" and "1" states must be mapped to some corresponding configuration of charge carriers that permits efficient encoding. Thus, the paradigm created by Lent and et.al uses basic units (QCA-cells) and those are composed either of quantum-dots (classical QCA) or redox-centers (molecular QCA) in which the charge can be spatially localized [5, 7]. In order to be implemented, the physical candidate system must fulfill three basic requirements that can be stated as:

1. Localization of charge within the cell
2. The bi-stability of the cell
3. Electrostatic interaction between neighboring cells

The classical QCA-cell is composed by four-dots with two-mobile electrons whose ground-state is an almost degenerated state where the electrons are located at the antipodal quantum-dots in order to minimize the repulsive Coulomb interaction and allowing to define the corresponding "1" and "0" logical binary states (see Fig 1.5) [5, 7]. The switching behavior (bi-stability condition) is achieved by driving the system towards an energetic instability region in which only the sudden change of the initial to the final configuration lowers the intra-cell Coulomb interaction between the corresponding charges ensuring to reach the ground-state configuration of the system [18].

1.1.2 Cell-cell response function

The most appealing feature about this paradigm is that information processing is made possible via Coulomb interaction between cells and therefore disregarding complicated wiring procedures and diminishing the energy dissipation of the computation. In this manner, the polarization of one cell induces a change in the polarization of the next one giving rise to a non-linear response which is the basic operational principle of the QCA paradigm as is presented in Fig 1.3. Consequently, a key-point aspect in this technology is to optimize this mechanism to make it as effective as possible in order to achieve high-density devices to operate at high-frequencies [11, 18, 19].

(a)   (b)
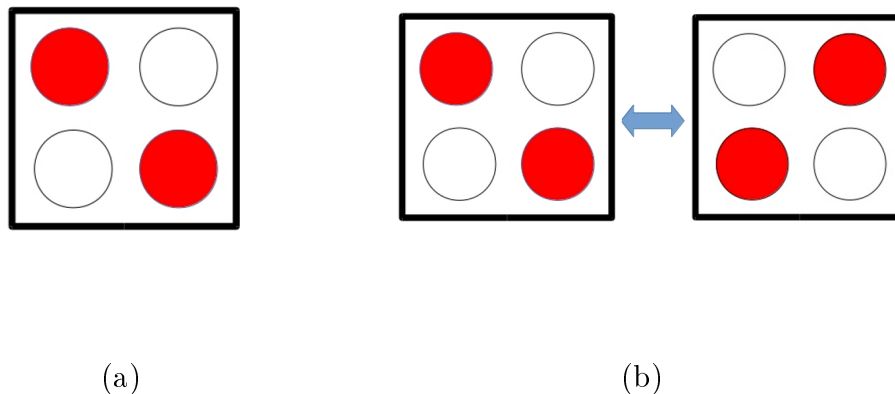
Figure 1.2: QCA basic requirements. (a) A simplified diagram of a four dot QCA-cell in which the electrons (red-dots) are confined within some spatial regions (white-dots). (b) Two-possible states of the classical QCA-cell representing the classical bits "0" and "1".

1.1.3   From cell to devices

For a device to function reliably, the interaction must exhibit a controllable nonlinear bi-stability that allows the switching mechanism to occur while driving it by an outer variable such as an external electric-field [5, 7, 20]. Once these conditions are fulfilled for the plausible candidate, one can create the layouts for some basic QCA devices [21, 22]. In this matter, many different architectures have been created ranging from a binary wire in which information is just transmitted (Fig 1.4(a)) to the majority gate in which truly computation can take place. Precisely, the majority gate is one of the simplest devices that can be built with this technology. In this layout, the QCA-cells are geometrical arranged to allow a three input structure while only one output is permitted [5]. The importance of this device is that can be further developed in order to construct the logical "AND" gate and "OR" gate basis of the digital computation [21, 23].

1.1.4   Clocked QCA cells

One of the key architectural-design features of the QCA paradigm is the clocking concept. A signal (clocking signal) offers an additional level of control that originally has been suggested to guide the way in which the cells can be used within circuits [5, 18, 24]. The working principle of the signal is to vary the relative energies between the two- or three- QCA-cell states in order to allow and control more easily the direction in which information is propagated. The signal has been already implemented in many of the proof of principle devices in a form of a time-varying voltage applied to a specific region of the metal-dot cell implementation [24]. In the case of a m-QCA, this implementation is not feasible since the regions in which the charge is localized are small (molecular-size) [18]. However, in the m-QCA
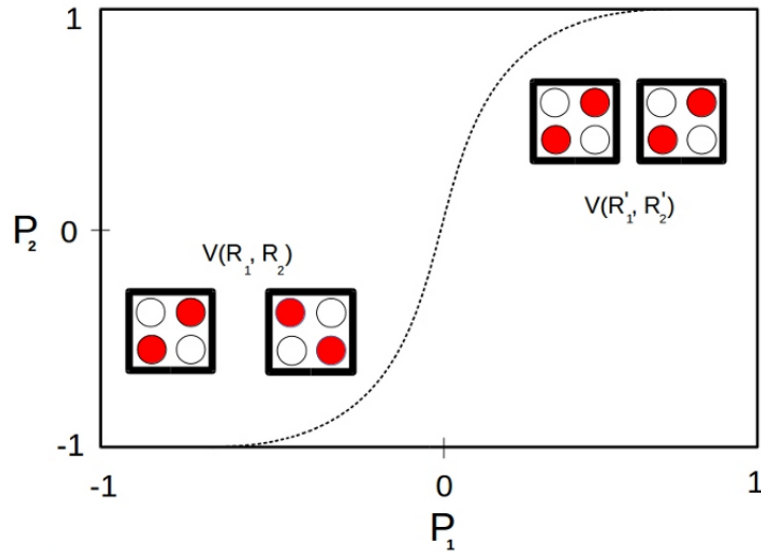
Figure 1.3: Switching behavior expected from two-interacting QCA-cells. The working-principle states that the polarization of one cell induces a change in the polarization of the next one causing the non-linear behavior. The functions $V(R_1,R_2)$ and $V(R_1',R_2')$ depict different cell-cell distances and how this response-function is a distance-dependent parameter.

implementation one can functionalize surfaces in order to create a nearly constant electric field that can produce the same effect in the electronic structure as the localized electric field in the metallic-QCA system [12].

1.1.5   m-QCA implementations

One of the most promising physical systems in which the QCA paradigm can be implemented are molecules. In recent years, the quest to find a plausible family of molecular-complexes in which the paradigm can be represented has awaken the interest of many scientists around the world [13, 14, 15, 25, 26]. These systems offer many advantages in comparison with other implementations such as identical copies of units, ultra high device density and room temperature operation. Additionally, molecules provide a wide range of options to control key-parameters such as electron localization, self-organization, among others by chemical tuning [14, 16]. The main characteristics seeked for a plausible candidate includes a moiety with two or three positions in which electrons can be spatially confined mimicking the charge-containers devices used in the metallic QCA implementation [5]. Encouraging molecular candidates have been suggested [5, 16, 27] and studied in detail and allowing to suggest the family of mixed valence (MV) moieties. These systems are highly flexible in terms of the electronic structure since they can be easily assembled to offer many different oxidation states and forming specific charge configurations [28]. In that respect, many different complexes have been synthesized and studied for further functionalized to be deposited over surfaces [12, 16, 28]. Despite many important efforts towards a successful realization of the paradigm, it is still an open question the plausible family of complexes in which the paradigm can be successfully implemented.
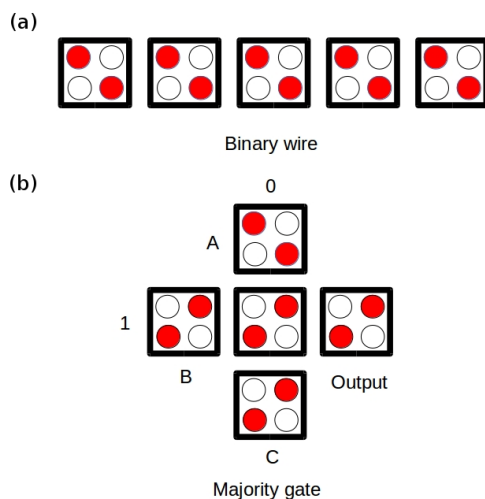
Figure 1.4: Designed devices for the QCA paradigm. (a) QCA-wire that propagates information trough the organized line of cells. (b) QCA Majority gate.

1.2 NUMERICAL METHODS

This chapter outlines the basic principles in order to solve the Many-body problem. Firstly, a review of wavefunction methods such as Hartree-Fock and Coupled Cluster is presented in order to establish the basic assumptions and capabilities of these methodologies. Secondly, density functional theory (DFT) is described with some special emphasis in extensions used in this thesis like time-dependent density-functional theory, external electric field and semi-empirical methods such as density functional tight-binding approach. In this manner, in the remaining chapters the focus is centered in the results and analysis of the calculations without going into full details of the theory. For more advanced details on DFT and its basic assumptions the reader can consult [29, 30, 31, 32].

1.2.1 The Initial Problem

For the investigations of real systems one has to solve a complicated N-body equation that includes a variety of interactions such as electron-electron, electron-nuclei, nuclei-nuclei, spin-spin, etc. In the simplest case, one can start considering a system of N interacting electrons which are interacting with an external potential created, for instance, by the positively charged nuclei present in a solid [29, 30, 33]. For this case, one can write a Hamiltonian of the electronic part in two parts:

$$\hat{H} = \sum_{i}^{N} h(i) + \frac{1}{2} \sum_{i \neq j} v(i,j), \tag{1.1}$$

where the first term represents the single-particle operator:

$$h(i) = -\frac{1}{2m}\nabla_i^2 + V(i), \qquad (1.2)$$

represents the sum of the kinetic energy and the energy of the external potential V(i) [29, 34]. In the aforehead case, the external potential can be specified as:

$$V(i) = -\sum_{\lambda,i} Z_\lambda \frac{e^2}{R_\lambda - r_i}, \qquad (1.3)$$

where R_λ is the position of one of the nuclei and r_i is the position of one of the electrons [29, 33]. The second part of the Hamiltonian involves an operator that describes the electron-electron repulsive interaction and can be written as:

$$v(i,j) = \frac{e^2}{r_{ij}}, \qquad (1.4)$$

where r_{ij} is the distance between the two electrons i and j [29]. At this point, one can write the Hamiltonian using the second quantization language, in which one can introduce the field operators $\boldsymbol{\psi}_\sigma(\vec{r})$ where $\vec{r}$ denotes the spatial part while $\boldsymbol{\sigma}$ states for the spin state of the electron. In terms of those operators, the Hamiltonian can be written as:

$$H = \sum_\sigma \int d^3\vec{r}\,\boldsymbol{\psi}_\sigma^\dagger(\vec{r})\hat{\mathbf{h}}(i)\,\boldsymbol{\psi}_\sigma(\vec{r}) + \sum_{\sigma\sigma'} \int d^3\vec{r}d^3\vec{r'}\,\boldsymbol{\psi}_\sigma^\dagger(\vec{r})\boldsymbol{\psi}_\sigma(\vec{r})\hat{\mathbf{v}}(i,j)\,\boldsymbol{\psi}_{\sigma'}^\dagger(\vec{r'})\,\boldsymbol{\psi}_{\sigma'}(\vec{r'}), \quad (1.5)$$

One of the main advantages of this transformation is the possibility to express the single-particle operator $\boldsymbol{\psi}_\sigma(\vec{r})$ in terms of basis functions as:

$$\boldsymbol{\psi}_\sigma(\vec{r}) = \sum_{i=1}^N a_{i\sigma}f_i(\vec{r}),$$

$$\boldsymbol{\psi}_\sigma(\vec{r}) = \sum_{i=1}^N a_{i\sigma}^\dagger f_i(\vec{r}).$$

where $a_{i\sigma}, a_{i\sigma}^\dagger$ are the associated creation and annihilation operators for the basis [33]. Thus, the initial Hamiltonian can be written using the second quantization language as:

$$H = \sum_{ij\sigma} t_{ij}a_{i\sigma}^\dagger a_{j\sigma} + \frac{1}{2}\sum_{\sigma\sigma'}\sum_{ijkl} V_{ijkl}a_{i\sigma}^\dagger a_{k\sigma'}^\dagger a_{l\sigma'}a_{j\sigma'}, \qquad (1.6)$$

where all the key interactions have been transformed into one- and two- body terms, which will be the subject of study in the following sections where different methodologies have been developed in order to solve this Hamiltonian [29, 33].

<center>(a)   (b)</center>
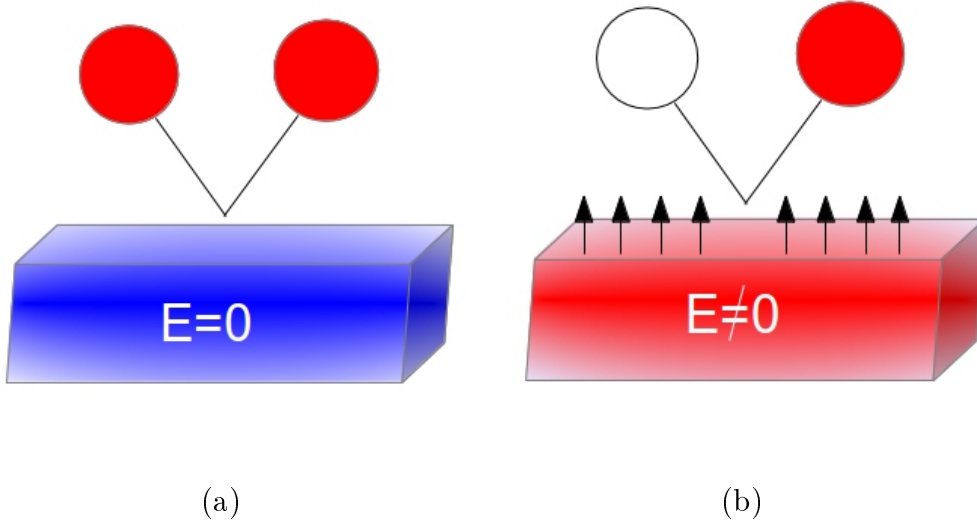
Figure 1.5: Schematic of a clocked QCA-cell. (a) A cell with two quantum dots (redox-positions) and the electrons delocalized over the whole complex (red-circles) deposited on an insulating surface that produces no image electric field. (b) A cell with two quantum dots (redox-positions) and two electrons (red-circles) deposited on a conducting surface that produces an image electric field. This electrostatic interaction influences the electronic structure of the moiety and enhance the localization of the charge-carrier at certain functional groups of the complex.

1.2.2   Electronic structure: The Hartree-Fock method

In order to find the electronic eigenfunctions and eigenvalues of the N-body Hamiltonian one has to resort in suitable approximations that still accurately describe the relevant physical situation [29]. Firstly, one can assume that the total wavefunction of the electron system can be written as an antisymmetrized of one-electron wavefunctions of the form:

$$\Phi(\vec{r}_1\sigma_1,....,\vec{r}_N\sigma_N) = \frac{A(N)}{\sqrt{N!}}(\phi(\vec{r}_1\sigma_1).....\phi(\vec{r}_N\sigma_N)), \tag{1.7}$$

where A(N) is the antisymmetrizing operator that can be formally recas as:

$$A(N) = \sum_{\eta}\alpha_\eta\beta_\eta, \tag{1.8}$$

where the sum is over all the possible permutations of the electrons (β_η) and (α_η) is the parity of the permutation that can take the values 1 for an even number of electrons and -1 for an odd number [32, 33]. Likewise, it is worth mentioning that the total wavefunction is already a product of the spatial orbital $(\psi_v(\vec{r}))$ and the spin part (the so-called spin-orbitals) adding an extra degree of freedom to the initial assumption. Furthermore, one can assume in principle that the studied system is in

a closed shell configuration enforcing a complete symmetry between the number of spin-up and spin-down electrons [29, 35]. Therefore, the total wavefunction can be written in terms of a single-dterminant as:

$$\Phi(\vec{r}_1\sigma_1,....,\vec{r}_N\sigma_N) = \begin{pmatrix} \phi_1(\vec{r}_1,\sigma_1) & \cdots & \phi_N(\vec{r}_1,\sigma_1) \\ \vdots & \ddots & \vdots \\ \phi_1(\vec{r}_N,\sigma_N) & \cdots & \phi_N(\vec{r}_N,\sigma_N) \end{pmatrix} \qquad (1.9)$$

where the functions fulfill the condition $\phi_\nu(\vec{r},\sigma)\phi_{\nu'}^*(\vec{r}',\sigma') = 0$. In order to ensure that the ansatz (Φ) provides the ground state eigenvalues and eigenvectors of the given Hamiltonian () one has to require that:

$$\delta\left(\frac{<\Phi|\hat{H}|\Phi>}{<\Phi|\Phi>}\right) = 0, \qquad (1.10)$$

Precisely, the condition 1.10 provides an efficent method in which one can iteratively search for an optimal total wavefunction in a self-consistent field (SCF) approach [29, 33]. Thus, one has to start with the expectation value for the ground state energy $E_0 = <\Phi|H|\Phi>$, and employing the obtained total wavefunction one can compute the ground state energy as:

$$E_0 = \sum_{\nu=1}^N <\phi_\nu|h|\phi_\nu> + \frac{1}{2}\sum_{\mu\nu}^N (<\phi_{\mu\nu}|v|\phi_{\mu\nu}> - <\phi_{\mu\nu}|v|\phi_{\nu\mu}>), \qquad (1.11)$$

where the one- and two- body expectation values are defined by:

$$<\phi_\nu|h|\phi_\nu> = \int d^3r \psi_\nu^*(\vec{r})h(\vec{r})\psi_\nu(\vec{r}),$$

$$<\phi_{\mu\nu}|h|\phi_{\mu\nu}> = \delta_{\sigma_\nu\sigma_\mu}\delta_{\sigma_\rho\sigma_\theta}\int d^3r d^3r' \psi_\nu^*(\vec{r})\psi_\mu(\vec{r})v(\vec{r},\vec{r}')\psi_\rho^*(\vec{r})\psi_\theta(\vec{r}).$$

the Kronoecker delta functions in the two-body operator ensures that the matrix is different from zero when all the associated wavefunctions have the same spins [33]. The energy E_0 must be minimized by variation of the wavefunctions $\psi_\nu(\vec{r})$ and $\psi_\nu^*(\vec{r})$ while the normalization condition $<psi_\nu|psi_\nu> = 1$ must be fulfilled. Thus, these equations lead to a situation of optimization procedure under restrictions that can be solved using the Lagrange formulation whose variational nature can be recast as:

$$\delta(E_0 - \sum_\nu \varepsilon_\nu <\phi_\nu|\phi_\nu>) = 0, \qquad (1.12)$$

by replacing with the total energy E_0 expression (1.11) one can find the following set of equations:

$$< \delta\phi_\nu|\mathrm{h}|\psi_\nu > + \sum_{\mu\neq\nu}(< \delta\phi_\nu\psi_\mu|\mathrm{V}|\psi_\nu\psi_\mu > - < \delta\phi_\nu\psi_\mu|\mathrm{V}|\psi_\mu\psi_\nu >) - \varepsilon_\nu < \delta\psi_\nu|\psi_\nu >= 0,$$

(1.13)

Since this equation must hold for any given choice of $\delta\psi_\nu$ then one can define an operator F (Fock operator) with the following matrix elements:

$$\mathrm{f}_{\nu\mu} =< \phi_\nu|\mathrm{h}|\psi_\nu > + \sum_\rho^\mathrm{N}(< \phi_\nu\psi_\rho|\mathrm{v}|\psi_\nu\psi_\rho > - < \delta\phi_\nu\psi_\rho|\mathrm{v}|\psi_\rho\psi_\nu >),$$

(1.14)

leading to a set of self-consistent field equations known as the Hartree-Fock equations (HF). In principle, the equations are a set of one-electron equations, nonetheless, the effective potential present in these equations require the knowledge of the wavefunctions [35]. Thus, one starts with a set of trial-functions $|\psi_\nu(0) >$, computes the Fock operator and with the equation $\mathrm{F}|\psi_\nu(0) >= \varepsilon_\nu|\psi_\nu(0) >$ one can get a second set of solutions $|\psi_\nu(1) >$ until self-consistency is achieved [29, 33]. The eigenvalues are obtained from the diagonal form of the Fock matrix. Moreover, the total energy has been changed since at this point is not simply the sum over all the associated eigenvalues of the single particle picture but corrected by the two-electron term as:

$$\mathrm{E}_0 = \sum_\nu^\mathrm{N}\varepsilon_\nu - \sum_{\nu\mu}^\mathrm{N}\frac{1}{2}(< \phi_\nu\psi_\mu|\mathrm{v}|\psi_\nu\psi_\mu > - < \phi_\nu\psi_\mu|\mathrm{v}|\psi_\mu\psi_\nu >),$$

(1.15)

preventing the double counting of interactions [31, 33]. The Fock operator (F) can be further investigated in terms of the effective one-particle potential. Thus, by using the formal definitions of h(i) and v(i,j), one can recast the Fock operator as

$$\left(-\frac{\nabla^2}{2\mathrm{m}} + \mathrm{V}(\vec{r}) + 2\mathrm{e}^2\sum_{\nu\neq\mu}^{\frac{\mathrm{N}}{2}}\int \mathrm{d}^3\mathrm{r}'\frac{|\psi_\nu(\mathrm{r}')|^2}{|\vec{r}-\vec{r}'|}\right)\phi_\nu(\vec{r}\sigma),$$

$$-\mathrm{e}^2\sum_{\nu\neq\mu}^\mathrm{N}\delta_{\sigma_\nu\sigma}\int \mathrm{d}^3\mathrm{r}'\frac{\psi_\nu^*(\mathrm{r}')\psi_\mu(\mathrm{r}')}{|\vec{r}-\vec{r}'|}\phi_\mu(\vec{r}\sigma) = \varepsilon_\nu\phi_\nu(\vec{r}\sigma).$$

(1.16)

where the Kronecker $\delta_{\sigma_\nu\sigma}$ enforces a closed shell configuration of the spins. A closer inspection of the equations lead to a natural partition of the problem. Firstly, the term:

$$\mathrm{V}_\mathrm{C}(\vec{r}) = \mathrm{e}^2\sum_{\nu\neq\mu}\int \mathrm{d}^3\mathrm{r}'\frac{|\psi_\nu(\mathrm{r}')|^2}{|\vec{r}-\vec{r}'|},$$

(1.17)

describes the repulsive interaction (Coulomb potential) between an electron and the effective potential created by the charge distribution of the remaining electrons of the system [31, 33]. Secondly, the remaining part of the equation can recast as:

$$\left(-\frac{\nabla^2}{2m} + V(\vec{r}) + 2e^2 \int d^3r' \frac{\rho(\vec{r'}) - \rho_\nu^{HF}(\vec{r},\vec{r'})}{|\vec{r}-\vec{r'}|}\right)\psi_\nu(\vec{r}) = \varepsilon_\nu\,\psi_\nu(\vec{r}), \qquad (1.18)$$

where the density has been denfined as $\rho(\vec{r'}) = 2\sum_{\nu=1}^{\frac{N}{2}}|\psi_\nu(\vec{r'})|^2$. However, when this representation of electronic density is replaced in the Hamiltonian (1.16), one has to take into account a self-interaction term that can be corrected using the HF density defined as:

$$\rho_{\nu\mu}^{HF}(\vec{r},\vec{r'}) = \sum_\nu^{\frac{N}{2}} \frac{\psi_\nu^*(\vec{r})\psi_\mu(\vec{r})}{|\psi_\nu(r)|^2}\psi_\mu^*(\vec{r'})\psi_\nu(\vec{r'}), \qquad (1.19)$$

As a result of this term, the solution of the SCF equations become a complicated task to obtain a reliable solution [32]. In the case of a finite basis set, one can start for recasting the total wavefunction (1.9) in the second quantization formalism in which the total wavefunction is written as $|\Psi_{SCF}> = \prod_{\nu\sigma}c_{\nu\sigma}^\dagger|0>$, where the term $c_{\nu\sigma}^\dagger$ is the creation operator for an electron with spin σ and $|0>$ is the vacuum state [33]. The corresponding expectation value of the total Hamiltonian ?? is given by:

$$\begin{aligned}
E_0 &= \sum_{ij}^{L}\sum_\sigma t_{ij} < \Psi_{SCF}|a_{i\sigma}^\dagger a_{i\sigma}|\Psi_{SCF}>, \\
&\quad + \frac{1}{2}\sum_{ijkl}\sigma_{\sigma\sigma'}V_{ijkl} < \Psi_{SCF}|a_{i\sigma}^\dagger a_{k\sigma'}^\dagger a_{l\sigma'}a_{j\sigma'}|\Psi_{SCF}> .
\end{aligned} \qquad (1.20)$$

where the operators a and c are related by the equation:

$$c_{\mu\sigma}^\dagger = \sum_{n=1}^{L}d_{\nu n}a_{n\sigma}^\dagger, \qquad (1.21)$$

using the fact that the occupied orbitals of the ground state wavefunction are expanded into the basis set $a_{i\sigma}f_i(\vec{r})$ with $f_i(\vec{r})$ acting as basis functions [33]. In this matter, one can redefine the total density $\rho(r)$ in terms of the operators a as:

$$\begin{aligned}
\rho(\vec{r}) &= 2\sum_{\nu=1}^{\frac{N}{2}}|\psi_\nu(\vec{2})|^2, \\
&= 2\sum_{ij}P_{ij}f_i^*(\vec{r})f_j(\vec{r}).
\end{aligned}$$

where $P_{ij} = \sum_\sigma < a_{i\sigma}^\dagger a_{j\sigma}>$ and can be interpreted as the statistical weight of this specific density when compared with the total density [33]. Subsequently, the

expectation value of the two-body operator $< \Psi | a_{i\sigma}^{\dagger} a_{k\sigma'}^{\dagger} a_{l\sigma'} a_{j\sigma'} | \Psi >$ can be reduced by assuming the mean-field approximation and can be calculated as:

$$
= \begin{cases}
< a_{i\sigma}^{\dagger} a_{j\sigma} >< a_{k\sigma'}^{\dagger} a_{l\sigma'} > & \text{if } \sigma \neq \sigma', \\
< a_{i\sigma}^{\dagger} a_{j\sigma} >< a_{k\sigma'}^{\dagger} a_{l\sigma'} > - < a_{i\sigma}^{\dagger} a_{l\sigma} >< a_{k\sigma'}^{\dagger} a_{j\sigma'} > & \text{if } \sigma \neq \sigma'.
\end{cases}
$$

Thus, one can recast the total energy as:

$$
E_0 = \sum_{ij} t_{ij} P_{ij} + \frac{1}{2} \sum_{ijkl} (V_{ijkl} - \frac{1}{2} V_{ilkj}) P_{ij} P_{kl}, \tag{1.22}
$$

where the total energy varies as a function of the occupation coefficients $d_{\nu n}$ that completely specifies the operator $c_{\nu\sigma}^{\dagger}$ and therefore the total wavefunction Ψ [33]. The SCF equations can be obtained in this formulation by applying the variational principle to Equation (1.22) leading to a set of equations:

$$
\sum_{j=1}^{L} (f_{ij} - \varepsilon_{\nu} S_{ij}) d_{\nu j} = 0, \tag{1.23}
$$

depending on the coefficents $d_{\nu j}$ and the functions f_{ij}, that are defined as:

$$
f_{ij} = t_{ij} + \sum_{kl} (V_{ijkl} - \frac{1}{2} V_{ilkj}) P_{kl}, \tag{1.24}
$$

Finally, the variational condition can be formally satisfied by introducing the Fock operator (in a finite basis set) as:

$$
F = \sum_{ij\sigma} f_{ij} (a_{i\sigma}^{\dagger} a_{j\sigma} - < a_{i\sigma}^{\dagger} a_{j\sigma} >), \tag{1.25}
$$

imposing the fulfilment of the self-consistent relations:

$$
F c_{\nu\sigma} | \Psi > = -\varepsilon_{\mu} c_{\nu\sigma} | \Psi >,
$$
$$
F c_{i\sigma} | \Psi > = -\varepsilon_{i} c_{i\sigma} | \Psi > .
$$

which are the solutions for the occupied (ε_{μ}) or unoccupied (ε_{i}) orbitals and leading to the usual representation for molecules of the canonical molecular orbitals [33].

1.2.3 Beyond Hartree-Fock: Coupled Cluster method

In the Hartree-Fock approximation a single-slater determinant is used in order to obtain the ground-state many-body wavefunction [32]. The main issue is the correlation between electrons, that can be understood as an interaction between electrons that arise from the fact that electrons with anti-parallel spin can be closer in the spatial state that electrons with parallel spins, is neglected [36]. Initially, the correlation effects are given by the difference of the Total electronic Energy and the Hartree-Fock energy:

$$E_{\text{correlation}} = E_{\text{exact}} - E_{\text{HF}}^{\infty}, \tag{1.26}$$

However, this is an impractical definition since the exact energy is not known and, for real systems, the E_{HF}^{∞} tends to be untraceable strongly depending on the size of the basis—set used [32]. In order to include excitations one has to distinguish which excitations are the most important ones that can contribute to complete the single determinant picture. In this way, the Brillouin theorem states that single excitations do not carry correlations therefore making the double excitations the ones used to complete the Slater single determinant picture [32]. The spirit of the Coupled-Cluster method relies on the description of the excitations via the cluster operator, in which all possible excitations can be described [32]. Once the reference wavefunction has been computed (usually is the Hartree-Fock determinant), the ground-state can be recast as:

$$\psi = e^{\hat{T}} \Phi_0, \tag{1.27}$$

where the $e^{\hat{T}}$ is the wave-operator while $\hat{T}$ is the cluster-operator [32]. Likewise, in the Coupled-Cluster method the normalization of the ground-state with the supplied slater-determinant is required providing the following condition $< \psi | \Phi_0 >= 1$. Thus, the strong assumption of this method is that excitations can be written as:

$$\hat{T} = \hat{T}_1 + \hat{T}_2 + \hat{T}_3 + \ldots, \tag{1.28}$$

where

$$T_1 = \sum_{a,r} t_a^r \hat{r}^{\dagger} \hat{a}, \tag{1.29}$$

$$T_2 = \frac{1}{4} \sum_{ab,rs} t_{ab}^{rs} \hat{s}^{\dagger} \hat{r}^{\dagger} \hat{a} \hat{b}. \tag{1.30}$$

are the operators for single-excitations ($\hat{T}_1$) and the double-excitations ($\hat{T}_2$), respectively. In this notation, the letters a, b refers to spin-orbitals which are occupied and r, s the ones unoccupied. The main objective of the method is to seek for the best t coefficients that represent the amplitude of the corresponding ground-state

function based on the excitation series expansion [36]. In order to get the coefficients, the ground state wavefunction ψ solves the Schrödinger equation that can be recast as:

$$e^{-\hat{T}}\hat{H}e^{\hat{T}}\Phi_0 = E\Phi_0, \qquad (1.31)$$

since the operator $e^{-\hat{T}}$ can be expanded in a series of commutators, one can write this equation until second order as:

$$e^{-\hat{T}}\hat{H}e^{\hat{T}}\Phi_0 = \hat{H} + [\hat{H}, \hat{T}] + \frac{1}{2!}[[\hat{H}, \hat{T}], \hat{T}] + \dots, \qquad (1.32)$$

since this expansion is finite, one can replace the operator terms by the commutator expansion in 1.31 and concluding by multiplying from the left with the excited states obtained from the action of the many-body operators coming from the cluster operator one can recast the Schrödinger equation as:

$$\langle {}^{mn}_{ab}|\hat{H} + [\hat{H}, \hat{T}] + \frac{1}{2!}[[\hat{H}, \hat{T}], \hat{T}] + \cdots\}|\Phi_0\rangle = 0, \qquad (1.33)$$

leading to the fundamental equation of the Coupled-Cluster theory [32, 36]. Interestingly, the number of coefficients sought is equal to the number of excited configurations used therefore making the set of equations complete. It is worth noticing, that in this method the variational principle has not been used and therefore one can not ensure that the wavefunction is the real ground-state. The Coupled-Cluster method has been also extended to solve this problem but scalability issues due to the size of the wavefunction are expected and its use only limited to small systems [32].

1.3 ELECTRONIC STRUCTURE : THE DENSITY FUNCTIONAL THEORY (DFT) METHOD

Density functional theory (DFT) is a ground-state theory in which all the relevant properties of a system can be described by the electronic density $\rho(r)$. DFT has been proven as a successful theory in which the mechanical and electronic properties of many different systems ranging from molecules to solids can be studied. The main advantage of this method is its rather computational affordability while describing accurately the main properties of the system. In principle, DFT is an exact theory of many-body systems. The formalism can be applied to any system of interacting particles in an external potential $V_{ext}(r)$ with a special emphasis on the problem of electrons moving under the action of an external potential generated by fixed nuclei. The Hamiltonian of such system can be written as:

$$\hat{H} = -\frac{\hbar^2}{2m_e}\sum_i \nabla_i^2 + \sum_i V_{ext}(r_i) + \sum_{i=1}^{N}\sum_{i\neq j} U(\vec{r}_i, \vec{r}_j), \qquad (1.34)$$

Thus, in principle once this Hamiltonian is solved the electronic structure of the system and their mechanical properties can be obtained. However, the rather complicated N-body Schrdinger equation can be solved by mapping it into a system of single-particle equations, the so-called Kohn-Sham equations, by invoking the Hohenberg-Kohn theorems [29].

1.3.1 The Hohenberg-Kohn Theorems

The DFT method starts assuming the validity of the Born-Oppenheimer approximation in which the total wavefuntion of the system can be separated into non-correlated nuclear and electronic parts [30]. Subsequently, the electronic wavefunction can be obtained at each fixed nuclei position and where one can write the total electronic density of the system as:

$$\rho(r) = N \sum_{\sigma = -\frac{1}{2}, \frac{1}{2}} \int |\Psi(\vec{r}_1, \sigma_1, ..., \vec{r}_n, \sigma_n)|^2 d\vec{r}_1 ... d\vec{r}_n, \qquad (1.35)$$

As starting point, the first Hohenberg-Kohn theorem states that there is only one external potential $V(r)$ that yields a given ground-state charge density $\rho(r)$. The demonstration of this property is rather simple and can be achieved by reduction to absurd (reductio ad absurdum) and can be found in many text books [29]. The main consequence of this theorem is that there are no two different external potentials whose ground state density is the same and therefore allowing to write uniquely the total energy as:

$$E[n(r)] = \langle \psi | T + U + V | \psi \rangle = F[n(r)] + \int n(\vec{r})V(\vec{r})d\vec{r}, \qquad (1.36)$$

where the $F[n(r)]$ is a universal functional of the charge density and independent of $V(r)$. Subsequently, the second theorem states that for any particular $V_{ext}(\vec{r})$ the exact ground-state energy of the system is the global minimum value of this function. Moreover, the associated density that minimizes the functional is the exact ground state density $n_0(\vec{r})$. In order to prove this theorem one has to clarify the meaning of being a functional of the electronic density and the space of such mathematical construction. Basically, a functional is a function from a vector space into its underlying scalar field or a set of functions of the real numbers [30]. In its original formulation, the density space has been restricted to the space of densities which are ground states of the electronic Hamiltonian (1.34) with some external potential $V_{ext}(\vec{r})$. In this special case, all the important quantities such as kinetic energy, internal energies, etc are uniquely defined once the correct $n(\vec{r})$ has been determined [29, 32]. Subsequently, the total energy of the system provided by the electronic Hamiltonian (1.34) can be recast in terms of the electronic density as:

$$E_{HK}[n] = T[n] + E_{int}[n] + \int d\vec{r} \ V_{ext}(\vec{r})n(\vec{r}) + E_{II}, \qquad (1.37)$$

where $T[n] = < \Psi | \hat{T} | \Psi >$ is the kinetic energy, $E_{int}[n] = < \Psi | V_{ee} | Psi >$ is the electron-electron repulsion term and E_{II} refers to the electrostatic repulsive ion-ion interaction energy. Once the equation(1.37) has been written one can re-define it as

$$E_{HK}[n] = F_{HK}[n] + \int d\vec{r}\ V_{ext}(\vec{r})n(\vec{r}) + E_{II}, \qquad (1.38)$$

making the term $F_{HK}[n]$ as the required universal functional since the kinetic and interaction energies are functional dependent on the electron density [29, 30]. As a consequence of this construction, once the functional $F_{HK}[n]$ is determined then by minimizing the total energy defined by equation (1.38) with respect to the variations in the density $\delta n(\vec{r})$ one could find the exact ground-state density and energy [29]. Consequently, all the ground-state properties of the system can be obtained by this minimization procedure. Nonetheless, the previous procedure is not useful enough in order to provide insight into a possible numerical solution. An alternative definition has been suggested by Levy and Lieb [29, 31] in which a two-step minimization procedure is suggested in order to get the density that minimizes the total energy functional. The main advantage of this procedure lies in the fact that clarifies the physical meaning of the functional, provide a way to get the exact functional and lead to the same formulation of the original Hohenberg-Kohn analysis. The procedure starts by writing the general expression of the energy in terms of the many-body wavefunction as:

$$E_{HK}[n] = \langle \Psi | \hat{T} | \Psi \rangle + \langle \Psi | \hat{V}_{int} | \Psi \rangle + \int d\vec{r}\ V_{ext}(\vec{r})n(\vec{r}), \qquad (1.39)$$

and by minimizing the Energy by all the variables which are contained in the total many-body wavefunction. However, this procedure is computational expensive and untraceable for big systems. Instead of doing so, one can consider only the energy for the class of total-wavefunctions Ψ that have the same density n(r). Thus, finding a minimum for this kind of wavefunctions leads to the equation:

$$E_{HK}[n] = \min_{\Psi \to n(\vec{r})} [\langle \Psi | \hat{T} | \Psi \rangle + \langle \Psi | \hat{V}_{int} | \Psi \rangle] + \int d\vec{r}\ V_{ext}(\vec{r})n(\vec{r}) + E_{II}, \qquad (1.40)$$

The formulation stated in (1.40) provides a clear physical insight into the functional stating that is the minimum of the sum of the kinetic and interaction energies of all possible wavefunctions that can describe a given electronic density $n(\vec{r})$. Thus, the Levy-Lieb functional is defined for any density $n(\vec{r})$ derivable from a many-body function Ψ_N [29].

1.4   KOHN-SHAM EQUATIONS AND COMPUTATIONAL APPROACHES

The Kohn-Sham approach offers an alternative view in which a complicated system of many-body particles can be replaced by a different auxiliary system of non-interacting particles that can be solved. Since there is no a unique selection for this system the first assumption is that the ground-state density of the original N-body interacting system is equal to that of some non-interacting system [29, 30]. Hence, this fictitious non-interacting system can be solved as a single particle problem where

the whole many-body interacting terms are included into the exchange-correlation functional of the density [29, 31]. Finally, the solution of this system produces a ground state electronic density that must be equal to the electronic density of the many-body interacting system and ensured by the first theorem of the DFT. Thus, this auxiliary system can be written as:

$$H_R = \sum_{i=1}^{N} \left[-\frac{\hbar}{2m} \nabla^2 + v_R(r_i) \right], \qquad (1.41)$$

where the subindex R states for a N electron reference system. Likewise, the potential v_R is such that the ground-state density of H_R equals the density $\rho(\vec{r})$. Since the reference system has not electron-electron interaction, one can write the total wavefunction as a single Slater determinant :

$$\Phi(r) = \frac{1}{\sqrt{N_s!}} [\varphi_1(r_1) \cdots \varphi_{N_s}(r_{N_s})], \qquad (1.42)$$

and assuming that the system is in a closed shell configuration [37]. Hence, the density can be recast as:

$$\rho(\vec{r}) = 2 \sum_{i=1}^{N_s} |\phi_i(\vec{r})|^2, \qquad (1.43)$$

then, the reference kinetic energy term can be read as:

$$T_R[\rho] = -\frac{\hbar^2}{m} \sum_{i=1}^{N_s} < \varphi_i | \nabla^2 | \varphi_i >, \qquad (1.44)$$

where the single-particle orbitals $\phi(\vec{r})$ are the lowest energy eigenfuntions of the associated one-electron Kohn-Sham Hamiltonian:

$$H_{KS} = -\frac{\hbar^2}{2m} \nabla^2 + v_R(\vec{r}), \qquad (1.45)$$

Thus, by employing this basis-set the universal density functional can be expressed as:

$$F[\rho] = T_R[\rho] + \frac{1}{2} \int \int \frac{\rho(\vec{r})\rho(\vec{r'})}{|\vec{r} - \vec{r'}|} d\vec{r} d\vec{r'} + \tilde{E}_{xc}[\rho], \qquad (1.46)$$

in which the term $\tilde{E}_{xc}$ contains also the corrections of the many-body kinetic energy operator [32]. Finally, replacing the expression (1.46) into the Equation (1.40) of the total energy functional, one can write the following expression:

$$E_{KS}[\rho] = T_R[\rho] + \int \rho(\vec{r})v_{ext}(\vec{r})d\vec{r} + \frac{1}{2}\int\int \frac{\rho(\vec{r})\rho(\vec{r'})}{|\vec{r}-\vec{r'}|}d\vec{r}d\vec{r'} + \tilde{E}_{xc}[\rho], \qquad (1.47)$$

in which the total energy functional is expressed in terms of the N_s one-particle orbitals (the Kohn-Sham orbitals) associated to the electronic density $\rho(\vec{r})$ that minimizes the non-interacting electronic kinetic energy and the v_R potential [32]. In priciple, the exact for of the $v_R(\vec{r})$ potential is unknown but must ensure that the electronic density obtained is the same as the one corresponding to the N-body interacting system [35]. Thus, since the ground state is uniquely defined one can resort in the fact that the minimization of the KS functional (1.47) with respect to the density. The problem also displays a constraint since the number of electrons is fixed (N_s) and therefore the variational equation can be written as:

$$\frac{\delta}{\delta\rho(\vec{r})}\left(E_{KS}[\rho] - \mu \int \rho(r)d\vec{r}\right) = 0, \qquad (1.48)$$

where μ states for the chemical potential [32]. By expapanding the equation into its compoenets, the minimized ground state density can be recast as:

$$\frac{\delta T_R[\rho]}{\delta\rho(\vec{r})} + v_{ext}(\vec{r}) + \int \frac{\rho(r')}{|\vec{r}-\vec{r'}|}d\vec{r}' + \frac{\tilde{E}_{xc}[\rho]}{\delta\rho(\vec{r})} = \mu, \qquad (1.49)$$

Thus, the kinetic term can be obtained from the reference system H_R. Thus, since there is no electron-electron interaction the energy associated with the reference system can be read as:

$$E_{v_R}[\tilde{\rho}] = T_R[\tilde{\rho}] + \int \tilde{\rho}(\vec{r})v_R(\vec{r})d\vec{r}, \qquad (1.50)$$

whose ground state energy is exactly the same as the one obtained from the interacting system [32]. Thus, one can take the derivative with respect to the density (ρ) and one can obtain:

$$\frac{\delta T_R[\rho]}{\delta\rho(\vec{r})} + v_R(\vec{r}) = \mu_R, \qquad (1.51)$$

where μ_R is the chemical potential of the non-interacting reference system [32]. By a direct comparison with the Equation (1.49) one can define the reference potential as:

$$v_R(\vec{r}) = v_{ext}(\vec{r}) + \int \frac{\rho(\vec{r'})}{|\vec{r}-\vec{r'}|}dr' + \mu_{XC}[\rho](\vec{r}), \qquad (1.52)$$

with the chemical potential just defined as the derivative of the exchange-correlation energy term $\mu_{XC}[\rho](\vec{r}) = \frac{\delta\tilde{E}_{XC}[\rho]}{\delta\rho(\vec{r})}$ [29, 32]. The important part of this approxima-tion is related with the fact that the reference potential depends on the solution of the one-particle Kohn-Sham Hamiltonian through the electronic density making necessary a numerical self-consistent solution [32].

1.4.1 Exchange-Correlation Hole

A further approximation done in the Kohn-Sham formalism implies the separation of the kinetic energy and the long-range Hartree terms leading to a local description of the $E_{xc}[n]$. This means that the E_{xc} can be expressed in terms of energy per electron at a given point $\vec{r}$ that depends upon the density $n(\vec{r}, \sigma)$ around the charge neighborhood [29]. This energy density, called in literature as $\varepsilon_{xc}([n], \vec{r})$, is not unique but can be estimated by relating this quantity to the exchange-hole and applying the adiabatic connection to the electron charge present in the density [29, 32]. The only necessary constraint needed to fulfill the conditions of the Hohenberg-Kohn theorems is that the electronic density should remain constant during the adiabatic variation. Hence, the change in energy is given by:

$$E_{xc}[n] = \int_0^{e^2} d\lambda \langle \Psi_\lambda | \frac{dV_{int}}{d\lambda} | \Psi_\lambda \rangle - E_{Hartree}[n], \qquad (1.53)$$

where

$$E_{Hartree}[n] = \frac{1}{2} \int d^3 r d^3 r' \frac{n(\vec{r})n(\vec{r'})}{|\vec{r} - \vec{r'}|}, \qquad (1.54)$$

Finally, one can write the local change of the energy in terms of the coupling-constant averaged hole:

$$E_{xc}[n] = \frac{1}{2} \int d^3 \vec{r} n(\vec{r}) \int d^3 \vec{r'} \frac{\bar{n}_{xc}(\vec{r}, \vec{r'})}{|\vec{r} - \vec{r'}|}, \qquad (1.55)$$

where

$$\bar{n}_{xc} = \int_0^1 d\lambda n_{xc}^\lambda (\vec{r}, r'), \qquad (1.56)$$

The obtained result is important since shows that the exact-correlation energy can be understood in terms of the potential energy due to the exchange-correlation hole averaged over the interaction from $e^2 = 0$ to $e^2 = 1$. Hence, the $E_{xc}[n]$ can be considered as an interpolation from the only exchange to the full correlated energies at the given density $n(\vec{r}, \sigma)$.

1.4.2 Mermin functional and Ensemble Density Functional theory

In the original formulation the system is considered as a closed system in which well defined discrete states are computed. Nonetheless, this is not the case of many interesting systems such as solids in which instead of having a set of discrete states a continuum of states is obtained where the occupation probabilities can be fractional. Therefore, a further extension to the original DFT can be carried out in

which an equilibrium thermal distribution can be included in order to overcome the problem of the fractional occupancy number [29, 30, 31]. Hence, this can be done by constructing the electronic density corresponding to the thermal ensemble [29]. In addition, for every of the theorems stated by Hohenberg and Kohn for the discrete ground-state theory there is a similar argument for a system in thermal equilibrium. In order to achieve this, Mermin [29, 30] constructed a grand-canonical potential functional of the corresponding trial density matrices $\hat{\rho}$ that can be recast as [29]:

$$\Omega[\hat{\rho}] = \mathrm{Tr}[\hat{\rho}(\hat{H} - \mu \hat{N}) + \frac{\ln(\hat{\rho})}{\beta}], \tag{1.57}$$

whose minimum is the equilibrium grand potential

$$\Omega[\hat{\rho}_0] = -\frac{1}{\beta}\ln\, \mathrm{Tr}\, e^{-\beta(\hat{H} - \mu \hat{N})}, \tag{1.58}$$

The formulation developed by Mermin is more powerful than the original formulation of Hohenberg-Kohn since make the thermodynamical quantities such as Entropy or specific heat functionals of the equilibrium density. However, this implementation is not widely since the functionals for Entropy usually should include the most important contributing excited states leading to a much more complicated construction of the total energy [29].

1.4.3 Functionals for exchange correlation

As it has been presented in the previous sections the Kohn-Sham equations are in principle exact and can solve the many-body problem by mapping it to a similar one-particle non-interacting Hamiltonian. However, the only approximation done in order to solve the Kohn-Sham equations is related with the actual mathematical form of the $E_{xc}[n]$ functional [30]. Thus, in this section the implementations of the functionals used in this work will be discussed and its functional form explicitly described.

General-Gradient Approximation GGAs

Based on the ideas of partitioning the long-range and kinetic energy from the rest of the $E_{xc}[n]$ Kohn and Sham suggested a way to create working functionals in a local and semi-local way. The local density approximation (LDA) [38] has been successfully applied to many metals and semiconductors describing correctly quantities such as band structures, lattice constants and cohesion energies among many other measured properties. Thus, a first step to improve this functional is to expand the $E_{xc}[n]$ energy in terms of the gradient of the density $|\bigtriangledown^{\sigma} n|$. The exchange-correlation functional is written as a function of the local density and of the local gradient of the density, usually as an "enhancement factor" F_{xc} multiplying the homogeneous electron results:

$$E_{xc}^{GGA}[n] = \int dr^3\, n(\vec{r})\varepsilon_x^{hom}(n)\, F_{xc}(n, |\nabla n|), \tag{1.59}$$

where the enhancement factor can be written in terms of a dimensionless parameter r_s and a dimensionless reduced density gradient s(r):

$$s(r) = \frac{|\nabla^m n|}{(2k_f)^m n}, \tag{1.60}$$

with $k_f = 3(\frac{(\frac{2}{3}\pi)^{\frac{1}{3}}}{r_s})$. The s_m is proportional to the mth-order derivative and normalized by the average distance between electrons [29]. Many different implementations have been parametrized using the lowest order terms such as B88 [39], PBE [40], BLYP [41].

Hybrid Functionals

Another kind of implementations use the fact that one can combine the coupling constant integration used to obtain the original exchange-correlation hole as a portion of the exact and orbital-dependent Hartree-Fock term while combining an explicit density functional [29, 36]. In terms of chemistry measurements, these functionals are the most accurate in terms of energetics. This formulation exploits the fact that the coupling-constant-averaged hole (Eq. 1.53) can be divided into two regimes, where $\lambda = 0$ is equal to the pure exchange hole while $\lambda = 1$ can be well described by a proper density like LDA or GGA leading to an initial form of:

$$E_{xc} = \frac{1}{2}(E_x^{HF} + E_{xc}^{LDA/GGA}), \tag{1.61}$$

Subsequent to this first approximation more modern functionals have been suggested including the well-known B3LYP that combines three parameter functional that mixes the full GGA B88 functional with the LYP correlation part leading to a function like:

$$E_{xc} = E_{xc}^{LDA} + a_0(E_x^{HF} - E_x^{B88}) + a_x E_x^{Becke} + a_c E_c, \tag{1.62}$$

with coefficients that have been statistically fitted to describe atomic and molecular data [42].

Long-range corrected Functionals

One of the most prominent problems of the DFT formalism is the underestimation of the band gap for insulating and semiconductor systems [29]. In many cases, the structural properties can be usually obtained using GGA implementations whereas electronic characteristics are much better described by Hybrid exchange-correlation functionals [36]. In principle, many of the problems of the Hybrid implementations to describe mechanical properties are related with the GGA part of the exchange and to lesser extent the inclusion of the exact HF operator [43]. Thus, suitable methodologies have been suggested in order to treat this problem like the screened

exchange-hybrid developed by Heyd, Scuseria and Ernzerhof [44]. The main assumption of this functional is to use a screened Coulomb potential for the exact interaction that produces at the same time good quality results and maintain the scalability of the method. However, in order to extend the use of these functionals to a rather broader range of systems the screened exchange-hybrid procedure should be further developed. Thus, in the range of the possible exchange interactions one can have two extreme cases, namely, insulators in which this term decays exponentially as a function of the band gap while for metals the same interaction decays algebraically. Thus, within these two ranges, there are only two possible alternatives, namely, the exchange interaction is artificially truncated or their spatial decay accelerated [43]. The truncation schemes are a good approximation for systems where charge localization occurs and the HF exchange decays rapidly but present convergence problems for systems with small or nonexistent band gap. Moreover, in delocalized systems not only the convergence problem is maintained but also uncertainties in the predicted energy has been reported [43]. The second option to circumvent the previous inconvenients but with the cost that important interaction of the system can be neglected. Thus, in order to enhance the applicability of this family of functionals one has to resort in the following property of the Coulomb operator, namely:

$$
\frac{1}{r} = \left(\frac{\mathrm{erfc}(\omega r)}{r}\right)_{\mathrm{SR}} + \left(\frac{\mathrm{erf}(\omega r)}{r}\right)_{\mathrm{LR}}, \tag{1.63}
$$

in which the full Coulomb operator has been divided into a short-range and long-range part components. The way in which the operator can be split is somehow arbitrary and the functions erfc and erf has been choosen due to convenience since those can be analytically integrated by Gaussian functions [43]. Extreme cases of the operator can be verified by letting $\omega \to 0$ in which the short-range of the operator dominates and becomes the full Coulomb interaction (including a degree of screening). In the other case, when $\omega \to \infty$ the long-range dominates and neglecting the small contributions given by the short-range term. In the specific case of the PBE0 implementation [45, 46], the exchange energy of the functional is divided into short- and long- range components leading to a total truncated scheme that can be written as:

$$
\begin{aligned}
\mathrm{E_x^{PBE0}} = {}& \mathrm{a_{mix}E_X^{HF,SR}}(\omega) + \mathrm{a_{mix}E_X^{HF,LR}} + (1 - \mathrm{a_{mix}})\mathrm{E_X^{PBE,SR}}(\omega) \\
& + \mathrm{E_x^{PBE,LR}}(\omega) - \mathrm{a_{mix}E_x^{PBE,LR}}(\omega),
\end{aligned} \tag{1.64}
$$

where this hybridization-scheme is based on the GGA-PBE implementation. The calculation of the SR term, which includes the four-body term, can be obtained from the SR electron-repulsion integral of the Hartree-Fock energies. As it has been suggested [47], one can use a contracted Gaussian-type basis set in which the integral:

$$
\langle \mu \nu | \lambda \sigma \rangle = \int \int d\vec{r_1} d\vec{r_2} \phi_\mu^*(\vec{r_1}) \phi_\mu^*(\vec{r_2}) \frac{\mathrm{erfc}(\omega \vec{r}_{12})}{\vec{r}_{12}} \phi_\lambda(\vec{r_1}) \phi_\sigma(\vec{r_2}), \tag{1.65}
$$

For this specific implementation the screened part of the Hybrid exchange-correlation can be treated in an accurate way by using the analytical form of the original GGA-PBE implementation leading to a good description of important properties such as single bonds in crystals [48].

1.5 VAN DER WAALS (DISPERSION) INTERACTION

The origin of the so-called van der Waals forces (vdW) is the interaction between two non-bonded chemical entities that are coupled by the electric field generated by instantaneous fluctuations of the electronic density in each chemical fragment [32]. In principle, these are dynamical correlations that cannot be correctly described within the local (LDA) or semi-local (GGA) formalism. Likewise, limiting cases should be fulfilled by this interactions, for instance, at long-distances this force should approach the classical dipole-dipole expression $E_{vdW} = \frac{-C_6}{R^6}$ where R is the inter-molecular distance [32]. In a first approximation, the Leonard-Jones $12-6$ potential can be used to represent these interactions and successful approaches have been developed within the DFT framework in which the dispersion effects have been included [49]. Alternatively, the electron-electron interaction can be separated into short-range and long-range terms whence the long-range part is the responsible for the vdW interaction [32]. The effective potential that represents this force can be written as:

$$U_{ee}^{lr}(\vec{r}, \vec{r'}) = \frac{A(\vec{r}, \vec{r'})}{|\vec{r} - \vec{r'}|^6},\tag{1.66}$$

depends on a selection of an effective density for the exchange-correlation linear response kernel [32]. Once one the available schemes have been selected, the effective XC-vdW part can be written as:

$$E_{XC}^{lr} = -\frac{3}{\pi} \int_0^\infty du \int_{V_1} d\vec{r_1} \int_{V_2} d\vec{r_2} \frac{\chi_1^z(iu)\chi_2^z(iu)}{|\vec{r} - \vec{r'}|^6},\tag{1.67}$$

where $\chi_1^z(iu)$ is the response of a uniform gas of given density ($\rho(\vec{r_i})$) to a perturbation in the direction of the bond [32, 50]. Recently, functionals in which the vdW forces are directly included have been developed leading to a much better description of the mechanical properties of systems in which vdW forces play a fundamental role like 2d crystals, graphite surfaces among others [49, 50].

1.5.1 Basis-set

The expansion of the single-particle operators can be carried out in terms of a generic basis-set described by the orbitals $|\phi_\alpha\rangle$. In the original KS or HF- Hamiltonians the orbitals are represented in real space, i.e, for each orbital the condition $\langle r|\phi_\alpha\rangle = \phi_\alpha(\vec{r})$ must be fulfilled [29]. In any of the methods, the orbitals can be expanded by using this basis and recast as:

$$\varphi_j(\vec{r}) = \sum_{\alpha=i}^M c_{j\alpha}\varphi_\alpha(\vec{r}),\tag{1.68}$$

where j states from the associated molecular orbital (or band in the continuous case), M is the size of the basis-set and $c_{j\alpha}\varphi_\alpha$ are the amplitudes of the wave-function [29, 31]. The one-electron wavefunctions can be represented in an energy-independent basis set becoming a generalized linear eigenvalue problem that can be recast as:

$$\sum_{\beta=1}^{M} (H_{\alpha\beta} - \varepsilon_j S_{\alpha\beta}) c_{j\beta} = 0, \tag{1.69}$$

The Hamiltonian matrix elements and the overlap matrix due to the non-orthogonality of the basis can be written as :

$$H_{\alpha\beta} \quad = \langle \varphi_\alpha | \hat{H} | \varphi_\beta \rangle, \tag{1.70}$$

$$S_{\alpha\beta} \quad = \langle \varphi_\alpha | \varphi_\beta \rangle. \tag{1.71}$$

Hence, the use of basis-set provides a good approximation in order to estimate the allowed energies of the system. However, the selection of a good basis-set strongly depends on the physical conditions imposed to the system, namely, whether symmetry conditions like translational invariance should be fulfilled or rather this requirement is broken requiring more accurate description of the core-electrons like in an all-electron implementation [29, 32].

1.5.2 Plane-waves

In systems where translational invariance should be ensured a natural basis set can be constructed, namely, the plane-wave basis-set (PW) [29]. This set of functions are the most appropriated selection for these systems since not only the Bloch theorem is always fulfilled but also due to the fact that the size of the basis-set can be effectively reduced by employing crystal symmetry considerations [29]. The orbitals can be written as:

$$\varphi_j^{\vec{k}}(\vec{r}) = e^{i\vec{k}\vec{r}} \sum_{\alpha=1}^{M} c_{j\alpha}^k \varphi_\alpha(\vec{r}), \tag{1.72}$$

where $\vec{k}$ is the wave-vector in the Brillouin zone. Generally, the Bloch's theorem determines that the wavefunction should be composed of a phase factor and a periodic part. Furthermore, the Schrödinger equation can be transformed into reciprocal space by employing the Fourier transform and solved explicitly under the assumption that the external potential (ions in the lattice) is constant [32]. However, once the interstitial region is left and the electrons are approaching closer to the regions of the ions (atomic nuclei and core electrons) the external potential is not constant making necessary to employ more PW to describe the modulations of the external potential [32]. The main condition is placed in the relation between the periodic-potential in real-space and in Fourier-space leading to the relation between reciprocal and real lattice vectors as:

$$\vec{b}_i = 2\pi \frac{\vec{a}_j \times \vec{a}_k}{\Omega}, \qquad (1.73)$$

where $\Omega = b_1 \cdot (b_2 \times b_3)$ defining the volume in reciprocal space. The ionic potential can be described in Fourier space as:

$$u_{\vec{k}}(\vec{r}) = \int e^{i\vec{g}\cdot\vec{r}}\tilde{u}_k(\vec{r})d\vec{g}, \qquad (1.74)$$

where $g = n_1\vec{b}_1 + n_2\vec{b}_2 + n_3\vec{b}_3$. Finally, a general expression for the wavefunction is given by:

$$\varphi^k(\vec{r}) = \frac{e^{i\vec{k}\cdot\vec{r}}}{\sqrt{\Omega}} \sum_{G=0}^{\infty} C_{\vec{k}}(\vec{G})e^{i\vec{G}\cdot\vec{r}}, \qquad (1.75)$$

leading to a Fourier series whose coefficients are given by $C_{\vec{k}}(\vec{G})$. However, equation 1.74 only solves a given eigenstate allowing only the description of a unique solution of the Schrödinger while in the case of periodic systems many eigenstates can be found. Therefore, an extension can be done and the wave function can be recast as:

$$\varphi_j^k(\vec{r}) = \frac{e^{i\vec{k}\cdot\vec{r}}}{\sqrt{\Omega}} \sum_{G=0}^{\infty} C_{j\vec{k}}(\vec{G})e^{i\vec{G}\cdot\vec{r}}, \qquad (1.76)$$

where the phase factor always lies in the first Brillouin zone while the reciprocal lattice vectors always lies outside the first Brillouin zone (except in the case when $\vec{G} = 0$) [29]. Thus, for solid state applications, the KS equations are coupled and one has to solve for each $\vec{k}$-point (within the corresponding Brillouin-zone) the following equation:

$$[-\frac{\hbar^2}{2m}\nabla^2 + v_{ext}(\vec{r}) + \int \frac{\rho(\vec{r}')}{|\vec{r} - \vec{r}'|}dr' + v_{xc}(\vec{r})]\varphi_i^k(\vec{r}) = E_i^k\varphi_i^k(\vec{r}), \qquad (1.77)$$

Finally, the coupling of the different KS-differential equations arise through the electronic density which can be expressed as an averaged weighted sum of the Brillouin zone:

$$\rho(\vec{r}) = \sum_{\vec{k}\in BZ} \omega_{\vec{k}} \sum_{i=1}^{N_k} f_i^k |\varphi_i^{\vec{k}}(\vec{r})|^2, \qquad (1.78)$$

where the weighting factors ω counts the ratio in which the specific point within the irreducible Brillouin contributes to the total energy, f_i is the occupation number of the band i at wave vector k and N_k is the number of electronic states occupied at each k-point [29, 32].

1.5.3 Atomic basis set

For molecular systems the plane wave approximation is not a suitable basis set since plenty of the vacuum region is still taken into account increasing considerably the computational effort [32]. Therefore, one alternative way to represent the possible wavefunction of these systems is the localized basis-sets. Thus, it is usual to expand the one-electron wavefunctions in terms of the atomic orbitals (AO) whose linear combination construct the canonical molecular orbitals (MO) [32]. However, these orbitals should be constructed in a way that are accurate enough to describe the most important properties of the system while scaling should be preserved [36]. Thus, many different kind of atomic orbitals have been suggested in order to construct the corresponding canonical molecular orbitals. For instance, the slater-type or the Gaussian-type orbitals [32]. The main idea behind the localized orbitals is to place the electronic wavefunction at the nucleus position R_j making the description as $\chi(r - R_j)$ for each atom belonging to the system [36]. This assumption makes that these orbitals are non-orthogonal a-priori and creating the necessity to construct an orthogonalization procedure suggested by Löwdin that consist to use the overlap matrix to create orthogonal basis set as:

$$\varphi_\alpha(\vec{r}) = \sum_\beta S_{\alpha\beta}^{-\frac{1}{2}} \varphi_\beta(\vec{r}), \qquad (1.79)$$

Another important issue when finite basis-set are used is the problem of Basis set superposition error (BSSE). In this matter, the calculation of interacting molecules is susceptible to this error since the basis set is not big enough to describe both molecules, in the case of a dimer, leading to a compensation of basis-set that artificially lowers the energy. Many different corrections can be employed ranging from using a bigger basis-set to more accurate methods like the counterpoise corrections [32].

1.5.4 Pseudo-potentials

In order to reduce computational cost further approximations can be carried out in the KS-Hamiltonian. Hence, a further step can be accomplished by averaging the atomic core-electron electrostatic potential. This assumption can be justified since the electrons participating in the bonding formation are mainly provided by the frontier orbitals (valence electrons) while the inert core-electrons can be represented by their isolated atomic distribution [32]. Thus, one of most important ideas in order to numerically create accurate pseudo-potentials rely on the fact that one can construct a set of smooth valence wavefunctions $\tilde{\varphi}_v$ that is not orthogonal to the core states φ_c by suggesting a linear combination of the core and true valence wavefunctions as:

$$|\tilde{\varphi}_v\rangle = |\varphi_v\rangle + \sum_c \alpha_{cv}|\varphi_c\rangle, \qquad (1.80)$$

where the coefficients α_{cv} denotes the overlap matrix between the truly core states and the smooth valence function [32]. Thus, this new electronic wavefunction satisfies the modified Schrödinger equation as:

$$\left[\hat{H} + \sum_c (E_v - E_c)|\varphi_c\rangle\langle\varphi_c| \right] |\tilde{\varphi}_v\rangle = E_v|\tilde{\varphi}_v\rangle, \qquad (1.81)$$

where $\hat{H}$ is the sum of kinetic and potential energy terms including the bare nuclear potential $\hat{V} = \frac{Z_c}{r}\hat{I}$ in the diagonal representation [32]. This modified Hamiltonian:

$$\hat{H}_{PS} = \hat{H} + \sum_c (E_v - E_c)|\varphi_c\rangle\langle\varphi_c|, \qquad (1.82)$$

have the same eigenvalues as the original Hamiltonian but a smoother and nodeless wavefunction whose associated potential can be recast as:

$$\hat{V}_{PS} = \frac{Z_c}{r}\hat{I} + \sum_c (E_v - E_c)|\varphi_c\rangle\langle\varphi_c|, \qquad (1.83)$$

leading to an effective and plausible approximation called pseudo-potentials [32]. Clearly, pseudo-potentials act differently over different angular momenta. Hence, a more general expression for pseudo-potentials can be written as:

$$\hat{V}_{PS}(\vec{r}) = \sum_{l=0}^{\infty} \sum_{m=-l}^{m=l} v_{PS}|lm\rangle\langle lm|, \qquad (1.84)$$

defining a projector over the corresponding l-th angular momentum subspace [32]. Many different implementations are available, namely, the norm-conserving pseudo-potential which ensures the conservation of charge within the cut-off region and should be equal to the core electrons or the ultra-soft pseudo-potentials which smooth the core-electron KS wavefunction preventing the use of a big amount of plane-waves. Finally, a popular selection is the projector-augmented-wave (PAW) pseudo-potentials in which the valence electrons are represented by plane-waves (interstitial regions) while the inner-core electrons is described by localized basis set. This is a powerful approach since the method has some flexibility in terms of the description of the electronic properties than the offered by the other methodologies while producing much better results than the crude frozen-core approximation and enhancing transferability of these pseudo-potentials [32].

1.5.5 Projected Augmented Wave (PWA)

Recently, the projector augmented wave (PAW) is a new and efficient methodology in which pseudo-potentials can be constructed that take the original ideas of the previous calculations and reformulate them to make it more computationally affordable [32]. The main development of the method is conserved, namely, the separation between projectors and auxiliary localized functions while defining a functional for the total energy [29]. This method has been widely applied for atoms, molecules and solids leading to a good results and good computational scalability. The main idea behind the method is to take advantage of the projector operator as:

$$\hat{V}_{PS} = \sum_{l=0}^{\infty} V_{PS}^l(\vec{r})\hat{P}_l, \tag{1.85}$$

where $\hat{P}_l = \sum_{m=-l}^{m=l}|lm\rangle\langle lm|$ is the projector operator for different angular momenta within the all-electron wavefunction. Thus, in order to define a new transformation operator for the all-electron wavefunction one can define a unitary operator as:

$$U = 1 + \sum_m (|\varphi_m\rangle - |\tilde{\varphi}_m\rangle)\langle p_m|, \tag{1.86}$$

where $\langle p_m|$ is a set of projection operators. Thus, from this operator one can create a transformation acting on the smooth part of the wavefunctions and whose result can be recast as:

$$\tilde{A} = U^\dagger\hat{A}U = \hat{A} + \sum_{m'm} |\tilde{p}_m\rangle\left(\langle\Psi_m|\hat{A}|\Psi_{m'}\rangle - \langle\tilde{\Psi}_m|\hat{A}|\tilde{\Psi}_{m'}\rangle\right)\langle\tilde{p}_m|, \tag{1.87}$$

which is similar to a pseudo-potential operator. This new methodology has the advantage to be inserted in the KS-formalism in which the density can be written as:

$$n(\vec{r}) = \tilde{n}(\vec{r}) + n^{(1)}(\vec{r}) + \tilde{n}^{(1)}(\vec{r}), \tag{1.88}$$

in which the three contributions can be written in terms of a basis-set like the single-particle KS eigenstates and the atomic (band) occupation number f_i leading to the following expressions:

$$n^{(1)}(\vec{r}) = \sum_i f_i \sum_{mm'} \langle\tilde{\Psi}_i|\tilde{\Psi}_m\rangle\Psi_m^*(\vec{r})\Psi_{m'}(\vec{r})\langle\tilde{\Psi}_{m'}|\tilde{\Psi}_i\rangle,$$
$$\tilde{n}^{(1)}(\vec{r}) = \sum_i f_i \sum_{mm'} \langle\tilde{\Psi}_i|\tilde{\Psi}_m\rangle\tilde{\Psi}_m^*(\vec{r})\tilde{\Psi}_{m'}(\vec{r})\langle\tilde{\Psi}_{m'}|\tilde{\Psi}_i\rangle.$$

The interpretation of $n^{(1)}(\vec{r})$ and $\tilde{n}^1(\vec{r})$ can be done in terms of localized wavefunctions around each atom (or ion) and among the different angular momenta numbers emulating the all-electron wavefunction [29, 32].

1.6 MODERN THEORY OF ELECTRIC POLARIZATION

Electric polarization is one of the most basic properties of matter, which has played a fundamental role in the functionalization of and creation of new devices. However, a proper definition of electron polarization has been a major challenge in physics for several years [51]. Conceptually, even for perfect crystalline systems, the electron

polarization can not be defined simple as the dipole moment of the charge density that is cut into finite pieces in resemblance to the concept of unit-cell [52]. Thus, one of the major theoretical advances in order to understand this property is the use of Berry-phases and Wannier orbitals in which the electric polarization theory can be applied to real materials. In order to construct a general theory of electric polarization one has to take into account that many different effects must explained. Thus, in a presence of an external field a metal will react by moving electric charge within the sample to effectively screen the external perturbation while leaving the bulk properties unaffected [52]. In the opposite side, while an insulator can support an external electric field without substantially changing its properties instantaneous time-dependent currents can appear leading to the appearances of currents. In principle, the main quantity to be studied is the macroscopic polarization $P(\vec{r}, t)$ that can be defined as:

$$\nabla . P(\vec{r}, t) = -\delta\rho(\vec{r}, t), \tag{1.89}$$

where $\rho(\vec{r}, t)$ is the change of the electronic density. In the same manner, the polarization field can be related with the current as:

$$\frac{dP(\vec{r}, t)}{dt} = j(\vec{r}, t), \tag{1.90}$$

that besides a curl of an arbitrary vector-field is an exact expression [51]. The equation (1.90) relates the polarization with a changing property over time. In principle, one can replace time for another quantity that can be adiabatically changed in time and leads to the desired study of the dynamical response of the system. Thus, one is interested to define the static macroscopic polarization $\vec{P}$ taking into account that outside the sample $\vec{P} = 0$ that can be written as:

$$\vec{P} = \frac{1}{V_c} \int_{\text{sample}} \vec{r}\rho(\vec{r})d\vec{r}, \tag{1.91}$$

using this definition, one can conclude that the polarization depends on the change of the charge density and it is independent of the path chosen within the sample [52]. However, in this definition the volume of the sample is used as a normalization constant and any try to define the dipole moment within a unit-cell as:

$$\vec{d} = \int_{V_c} \vec{r}\rho(\vec{r})d\vec{r}, \tag{1.92}$$

fails since the dipole-operator changes its value even by the rigid shift imposed by the Bloch theorem to ensure translational invariance [52]. Therefore, a new approach to treat the Polarization must be constructed in which the total Hamiltonian of the system depends on an external parameter and leading to the appearance of the Berry phases [51]. The geometric phase is an interesting property that appears in systems when they are driven by an "external" force that is included in the total Hamiltonian. Usually, the the quantum system depends parametrically on an external parameter leading to Schrödinger equation of the form:

$$H(\hat{\lambda})|\Psi(\lambda)\rangle = E(\lambda)|\Psi(\lambda)\rangle, \tag{1.93}$$

in order to solve this system, one can assume that all the $|\Psi(\lambda)\rangle$ generated by λ are ground-states and single-valued. Thus, taking to two different solutions at different values of λ, i.e, $|\Psi(\lambda_1)\rangle$ and $|\Psi(\lambda_2)\rangle$ one can define a phase-difference between the two wavefunctions as :

$$e^{-i\Delta\phi_{12}} = \frac{\langle\Psi(\lambda_1)|\Psi(\lambda_2)\rangle}{|\langle\Psi(\lambda_1)|\Psi(\lambda_2)\rangle|}, \tag{1.94}$$

the phase difference plays a little role in the physical interpretation of the dynamics of the system, but, rather is just consequence of the gauge-dependency of the solution of the Hamiltonian (1.93). This quantity is uniquely defined unless the two corresponding states are orthogonal to each other [52]. Now, when the system is dynamically observed there is a continuous Berry phase (or geometric phase) which is a limiting case of the previous analysis. Then, the phase-difference can be written in terms of a discretization scheme, such as:

$$e^{-i\Delta\phi_{12}} = \frac{\langle\Psi(\lambda)|\Psi(\lambda+\triangle\lambda)\rangle}{|\langle\Psi(\lambda)|\Psi(\lambda+\triangle\lambda)\rangle|}, \tag{1.95}$$

if one can find a gauge in which the wavefunction is differentiable with respect to the changing parameter, then one can create a differential equation for the change of the gauge as:

$$-\iota d\phi = \langle\Psi(\lambda)|\nabla_\lambda\Psi(\lambda)\rangle d\lambda, \tag{1.96}$$

The interesting conclusion that leads this differential equation is that Berry-phases are real numbers (after integration of the differential equation) within the contour in the parametric space defined by all $d\phi$ and potential observables of the system that can not be related as the expectation value of any operator [51].

1.6.1 Berry phase theory of electric polarization

In terms of the single-particle states of the KS-Hamiltonian one can write the Schrödinger as:

$$(-\frac{\nabla^2}{2} + V_\lambda(\vec{r}))\Psi_n^\lambda(\vec{r}) = E_n^\lambda\Psi_n^\lambda(\vec{r}), \tag{1.97}$$

whence the total electronic density that depends on this external parameter can be defined as:

$$\rho_e^\lambda(\vec{r}) = e\sum_{n\leq M}|\Psi_n^\lambda(\vec{r})|^2, \tag{1.98}$$

where M is the highest occupied levels and $\Psi_n^\lambda(\vec{r})$ are the single-particle states of the Kohn-Sham Hamiltonian. The external parameter λ can be a multidimensional variable that can be defined as the atomic displacements within the crystal and using it as a derivative parameter one can recast the total Polarization P_e^λ as:

$$\frac{\partial P_e^\lambda}{\partial \lambda} = \frac{e}{V_c} \sum_{n \leq M} (\langle \frac{\partial \Psi_n^\lambda}{\partial \lambda} | \vec{r} | \Psi_n^\lambda \rangle + \langle \Psi_n^\lambda | \vec{r} | \frac{\partial \Psi_n^\lambda}{\partial \lambda} \rangle), \qquad (1.99)$$

Assuming that those changes are small and that the crystal is finite one can employ to calculate this quantity perturbation theory [52]. Thus, one can write the perturbation of the gauge-invariant polarization as:

$$\frac{\partial P_e^\lambda}{\partial \lambda} = \frac{2e}{(2\pi)^3} \Im \sum_{n \leq M} \sum_{m \neq M}^{\infty} \frac{\langle \Psi_{n\vec{k}}^\lambda | \vec{p} | \Psi_{n\vec{k}}^\lambda \rangle \langle \Psi_{n\vec{k}}^\lambda | \frac{\partial \vec{V}^\lambda}{\partial \lambda} | \Psi_{n\vec{k}}^\lambda \rangle}{(E_{n\vec{k}}^\lambda - E_{m\vec{k}}^\lambda)^2}, \qquad (1.100)$$

However, it can be argued that using the Bloch orbitals this expression can be also used to describe the polarization as a bulk property that does not depend on the finite effects of the sample but rather as a sum of matrix elements over occupied and unoccupied states integrated over he Brillouin zone and recast as:

$$\frac{\partial P_e^\lambda}{\partial \lambda} = \frac{2e}{(2\pi)^3} \Im \sum_{n \leq M} \sum_{m > M} \int_{BZ} d\vec{k} \frac{\langle \Psi_{n\vec{k}}^\lambda | \vec{p} | \Psi_{n\vec{k}}^\lambda \rangle \langle \Psi_{n\vec{k}}^\lambda | \frac{\partial \vec{V}^\lambda}{\partial \lambda} | \Psi_{n\vec{k}}^\lambda \rangle}{(E_{n\vec{k}}^\lambda - E_{m\vec{k}}^\lambda)^2}, \qquad (1.101)$$

which clearly indicates a connection between the Berry-phase formalism and the electric properties of a system [52]. Furthermore, a more clear connection between the crystal theory and the polarization function has been found where instead of using the wavefunctions $\Psi_n^\lambda(\vec{r})$ one can use the periodic functions derived from the Bloch's theorem (namely $u_{n\vec{k}}^k$) allowing to rewrite the Polarization equation as:

$$\frac{\partial P_e^\lambda}{\partial \lambda} = \frac{2e}{(2\pi)^3} \Im \sum_{n \leq M} \int_{BZ} d\vec{k} \langle \frac{\partial u_{n\vec{k}}^k}{\partial \vec{k}} | \frac{\partial u_{n\vec{k}}^k}{\partial \lambda} \rangle, \qquad (1.102)$$

where the summation runs over the occupied states of the crystal only and opening the door to be implemented in robust numerical schemes like DFT [52]. Thus, this is a gauge-invariant quantity by noticing that the integrand of Eq. (1.102) is the Berry curvature of the M occupied Bloch bands [51]. However, the physical meaning of polarization is related with the fact of reorganization of charge within a system as a reaction to an external stimulus. Thus, the change of polarization during the evolution of λ can be expressed as:

$$\triangle P_e = \int_0^1 \frac{\partial P_e^\lambda}{\partial \lambda} d\lambda, \qquad (1.103)$$

and further combining this expression with the definition of polarization, one can recast the equation as:

$$\triangle P_e = \frac{2e}{(2\pi)^3} \int_{BZ} d\vec{k} \int_0^1 d\lambda \langle \frac{\partial u_{n\vec{k}}^k}{\partial \vec{k}} | \frac{\partial u_{n\vec{k}}^k}{\partial \lambda} \rangle, \qquad (1.104)$$

finally allowing to relate the concept of polarization as the reorganization of charge within a sample when a reference point has been taken [51]. In order to do so, one can use the identity:

$$\langle \frac{\partial u_{n\vec{k}}^k}{\partial \vec{k}} | \frac{\partial u_{n\vec{k}}^k}{\partial \lambda} \rangle - \langle \frac{\partial u_{n\vec{k}}^k}{\partial \lambda} | \frac{\partial u_{n\vec{k}}^k}{\partial \vec{k}} \rangle = \frac{\partial}{\partial \vec{k}} \langle u_{n\vec{k}}^k | \frac{\partial u_{n\vec{k}}^k}{\partial \lambda} \rangle - \frac{\partial}{\partial \lambda} \langle u_{n\vec{k}}^k | \frac{\partial u_{n\vec{k}}^k}{\partial \vec{k}} \rangle, \qquad (1.105)$$

and using integration by parts the total change of the polarization can be effectively split as:

$$\triangle P_e = \frac{2e}{(2\pi)^3} \int_{BZ} d\vec{k} \left(\langle u_{n\vec{k}}^k | \frac{\partial u_{n\vec{k}}^k}{\partial \lambda} \rangle |_0^1 - \int_0^1 d\lambda \frac{\partial}{\partial \vec{k}} \langle u_{n\vec{k}}^k | \frac{\partial u_{n\vec{k}}^k}{\partial \lambda} \rangle \right), \qquad (1.106)$$

leading to conclude that the change of the total polarization can recast as:

$$\triangle P_e = P_e^{(1)} - P_e^{(0)}, \qquad (1.107)$$

and giving a proper definition of polarization for infinite systems that is gauge-invariant and defined as a bulk property for any periodic system [52]. Finally, the Bloch's functions that have been employed in the definition of polarization are defined in the reciprocal space and cannot be related directly with the molecular orbitals formed within the crystals difficulting the interpretation of the influence of this parameter in the electronic structure of the system. However, an alternative picture of can be constructed using the the maximally localized Wannier functions (MLWFs). The Wannier orbitals are related with the Bloch s function by an inverse Fourier transformation which is unitary leading to a good description of the bonding properties in the crystal in real-space and whose details are given elsewhere [51, 52].

1.7 SIMULATION OF STM IMAGES

Simulation of Experimentally observable quantities is one of the most important features in which the full power of DFT calculations can be employed. Recently, with the development of the Scanning tunneling microscopy (STM), a deep understanding of the electronic structure of complicated systems has become accessible and even rutinary [53]. However, the measured quantities are no directly related

with the regular outputs of the ab-initio calculation and, therefore, making necessary approximations to relate the measurements with the theoretical predictions. Thus, the working principle of the STM relies on the fact that an external voltage is applied to the sample across the tip and a sample (usually a molecule) which is separated by a narrow vacuum region [53]. The measured current is created by electrons that quantum-mechanical tunnel from the tip to the sample or vice-versa and whose tunneling probability depends exponentially on the separation between the tip and the sample [53]. However, STM techniques lack of resolution to estimate either the height of the sample or the atomic charge density of the probed system. Rather, these images provide a full picture in which structural and electronic properties of the total system are intermixed and therefore making its direct interpretation difficult. In this manner, theoretical methods that can simulate this complicated situation are necessary in order to validate many of the experimental measurements carried out. The first step towards an atomistically study has been stated in the so-called Bardeen's approach [54] in which it is assumed that tip and sample are weakly coupled and where the total Hamiltonian can written as:

$$\hat{H} = \hat{H}_0 + V_0, \tag{1.108}$$

where $\hat{H}_0$ is the unperturbed system (sample and tip) and V_0 is the interaction between them (perturbation). In order to solve this problem by employing first-principle calculations Tersoff and Hamann [54] suggested a methodology in which, besides using perturbation theory, they assumed that at some spatial point in between the tip-sample system the potential cancels out simplifying the tunneling current expressions. Likewise, they assumed that the main orbital character of the tip is giving by a s-orbital symmetry. Hence, under this framework, one can write the expression for the transfer matrix elements as:

$$M_{ij} = \frac{\hbar^2}{m_e} (2\pi \Omega_{tip}^{-\frac{1}{2}}) \ R_{s-state} \ e^{\vec{k}.\vec{R}}, \tag{1.109}$$

where k is the decay length of the tunneling electron, Ω is the solid angle and $R_{s-state}$ is the radius of the atomic orbital involved in the measurement of the sample (tip atomic orbital) [54]. Concerning the tunneling current the expression can be recast as:

$$I \propto V N_t(E_f) \sum_s |\Psi_s(\vec{r}_0)|^2 \delta(E_s - E_f), \tag{1.110}$$

where V states for the applied voltage and N_t is the density of occupied states. This model provides a rather simple explanation in which the basic quantity measured is the local-density of states of the sample and emphasizing the connection between topographic and electronic features of the sample [54].

1.8   TIME-DEPENDENT DENSITY FUNCTIONAL THE-ORY (TD-DFT)

The Kohn-Sham approach to replace the many-body interacting system by an auxiliary system of a single-particle Hamiltonian is the cornerstone solution to the static Schrödinger equation. Although a powerful tool, this approach provides only quantities that can be related with the ground-state density. Hence, the formalism has been extended by Runge and Gross in order to solve the time-dependent Schrödinger equation (TDDFT) in a similar manner that is carried out for the static case [31, 34]. In the same spirit as the static DFT, the time dependent Kohn-Sham equations can be introduced mapping the problem of many-body interacting electrons moving in a time-dependent external potential $V_{\text{ext}}(\vec{r}, t)$ onto a system of independent electrons moving in a time-dependent effective potential $V_{\text{eff}}(\vec{r}, t)$. The resulting time-dependent Schrödinger equation can be written as:

$$i\frac{\partial \Psi_n(\vec{r}, t)}{\partial t} = [-\sum_i \frac{\hbar^2}{2m}\nabla_i^2 + V_{\text{eff}}[n](\vec{r}, t)]\Psi_n(\vec{r}, t), \qquad (1.111)$$

where the time-dependent electronic density can be written as:

$$n(\vec{r}, t) = 2\sum_{n=\text{occu}} |\Psi_n(\vec{r}, t)|^2, \qquad (1.112)$$

Similarly to the DFT implementation, one can split the effective potential $V_{\text{ext}}[n](\vec{r}, t)$ into three potentials, namely, the external potential, the Hartree potential and the exchange-correlation potential leading to the equation:

$$V_{\text{eff}}[n](\vec{r}, t) = V_{\text{ext}}(\vec{r}, t) + V_{\text{Hartee}}[n](\vec{r}, t) + V_{\text{xc}}[n](\vec{r}, t), \qquad (1.113)$$

where the V_{Hartree} accounts for the classical electron-electron interaction while the V_{xc} comprises all the non-trivial many-body interactions [34]. On the contrary to the static DFT implementation, the XC cannot be simply written as a derivative of the XC energy due to a problem of causality [31]. However, the problem has been solved using a Keldysh formalism allowing to define a new action functional $\tilde{A}$ in which the following relation can be written:

$$V_{\text{xc}}(\vec{r}, t) = \frac{\delta \tilde{A}_{\text{xc}}}{\delta n(r, \tau)}|_{n(\vec{r}, t)}, \qquad (1.114)$$

where τ states for the Keldish pseudo-time. As in the static formalism, the V_{xc} is not exactly known and, therefore, it is necessary to use approximations in order to describe the excitations of the system. As a first approximation one can state that the time-dependent XC potential can be approximated as:

$$V_{\text{xc}}^{\text{Adiabatic}}(\vec{r}, t) = \tilde{V}_{\text{xc}}[n](r)|_{n=n(t)}, \qquad (1.115)$$

leading to the conclusion that the many different successful implementations developed for the static case can be used by evaluating at each time with density $n(\vec{r}, t)$. However, the locality in time is a dramatic approximation that only is valid in the limit where the system is locally close to equilibrium [34]. In the same manner, all the problems inherited from the static XC implementations are present in the adiabatic TDDFT approximation specially in cases where a strong electric field interacts with the system and pushes the electrons in regions far away the nucleus or even ionization yields [31]. Recently, more advanced approaches have been developed trying to exploit mathematical properties of derived from the Runge-Gross Theorem. Thus, the V_{xc} can be explicitly written in terms of the Kohn-Sham orbitals like the exact-exchange functional (EXX) [31] or some new functionals where memory effects can be taken into account [34]. In practice, photo-absorption spectra (excitations of the electrons) can be calculated either by propagating the time-dependent Kohn-Sham equations or by using linear response theory. In the propagation scheme a small perturbation is used, namely, an electric field $v(\vec{r}, t) = -k_0 x_\nu \delta(t)$ where $x_\nu = x, y, z$. Thus, one can propagate the wavefunction by starting at $t = 0^+$ and leading to the propagation equation as:

$$\varphi(\vec{r}, t = 0^+) = e^{ik_0 x_\nu} \tilde{\varphi}_j(\vec{r}), \qquad (1.116)$$

propagating the Kohn-Sham orbitals during a finite time from where the dynamical polarizability can be calculated as:

$$\alpha_\upsilon(\omega) = -\frac{1}{k} \int d\vec{r} \; x_\upsilon \; \delta n(\vec{r}, \omega), \qquad (1.117)$$

where $\delta n(\vec{r}, \omega)$ is the Fourier transform of $n(\vec{r}, t) - \tilde{n}(r)$ with $\tilde{n}(r)$ as the initial ground-state obtained from a static ground-state DFT calculation. The measured quantity in experiments is the photo-absorption cross section that can be related with the dynamical polarizability as:

$$\sigma(\omega) = \frac{4\pi\omega}{c} \frac{1}{3} \Im \sum_\nu \alpha_\nu(\omega), \qquad (1.118)$$

with c as the speed of light. The method is computationally demanding but accurate enough to reproduce good photo-absorption spectra from many different systems and used successfully in the characterization of many different systems. As a second strategy, the linear-response method has been used taking advantage of the fact that when time-dependent potential is small then perturbation theory can be used. Thus, the linear change of the density can be used to calculate the optical absorption spectrum. Once it is assumed that for $t < t_0$ the time-dependent potential depends only on the nuclear potential then a small perturbation can be added leading to a small change in the external potential that can be written as $V_{ext} = V_0 + V_1$. The main consequence of this perturbation of the system is that the electronic density can be expanded in a perturbative series like:

$$n(\vec{r}, t) = n^0(\vec{r}) + n^1(\vec{r}, t) + \dots, \qquad (1.119)$$

being n^1 the linear term of the response function of the system. Subsequently, the density can be written in frequency space as:

$$n^{(1)}(\vec{r}, t) = \int d\vec{r} \; \chi(\vec{r}, \vec{r'}, \omega) \; v_{KS}^{(1)}(\vec{r'}, \omega), \tag{1.120}$$

making use of the fact that the within the TDDFT the density of many inter-acting electrons can be mapped to a fictitious single-particle system in which the response can be written in terms of the KS orbitals [31]. Finally, combining the fact that $\chi_{KS}(\vec{r}, \vec{r'}, \omega)$ and $V_{KS}^{(1)}(\vec{r}, t)$ can be obtained from this formalism, one can write the exact linear density response of the system as:

$$\chi_{KS}(\vec{r}, \vec{r'}, \omega) = \lim_{\eta \to 0^+} \sum_{jk}^{\infty} (f_j - f_k) \frac{\varphi_j(\vec{r}) \varphi_j^*(\vec{r'}) \varphi_k(\vec{r}) \varphi_k^*(\vec{r'})}{\omega - (E_j - E_k) + \iota \, \eta}, \tag{1.121}$$

where the φ represents the KS-orbitals and f_i is the occupation number of the i orbital in the ground-state. Thus, the external perturbation and its subsequent response function are contained in the perturbation series of the V_{KS} potential that can be expanded until the linear-term [31]. Thus, one can explicitly calculate the linear-change of the Kohn-Sham potential by expanding it as:

$$V_{KS}^{(1)}(\vec{r}, t) = V^{(1)}(\vec{r}, t) + V_{Hartree}^{(1)}(\vec{r}, t) + V_{XC}^{(1)}(\vec{r}, t), \tag{1.122}$$

a closer inspection of each of the terms in the KS-potential reveals that the Hartree-potential and the XC-potential contain implicitly a change in the density that can be recast as:

$$V_{Hartree}^{(1)}(\vec{r}, t) = \int d^3\vec{r'} \; \frac{n^{(1)}(\vec{r'}, t)}{|\vec{r} - \vec{r'}|},$$
$$V_{XC}^{(1)}(\vec{r}, t) = \int dt' \int d^3\vec{r'} \; \frac{\delta V_{xc}(\delta \vec{r}, t')}{\delta n(\vec{r'}, t')} \; n^{(1)}(\vec{r'}, t).$$

providing a plausible way in which the linear-response can be calculated. Concerning to the XC-potential term the time-derivative is an important quantity that establishes a relationship between the change of the potential as a function of the density-change with respect to time and can be recast as:

$$f_{xc}(\vec{r}t, \vec{r'}t') = \frac{\delta V_{xc}(r, t)}{\delta n(\vec{r'}, t')}, \tag{1.123}$$

leading to the so-called Kernel quantity. Finally, by transforming to the frequency space one can write the linear-response function as:

$$\chi(\vec{r}, \vec{r'}, \omega) = \chi_{KS}(\vec{r}, \vec{r'}, \omega) +$$
$$\int d^3\vec{x} \int d^3\vec{x'} \; \chi(\vec{r}, \vec{x}, \omega) \left(\frac{1}{|\vec{x} - \vec{x'}|} + f_{xc}(\vec{x}, \vec{x'}, \omega) \right) \chi(\vec{x'}, \vec{r'}, \omega), \tag{1.124}$$

In principle, the perturbation expansion is exact but for the XC term that must be approximated as in the stationary case. The Eq. (1.124) can be solved self-consistently and the exact many-body response χ can be computed from the KS independent linear response function [31]. Nonetheless, since the exact V_{XC} is unknown the f_{xc} can not be exactly computed leading to the necessity of suggest approximations in which the kernel can be effectively computed. In this matter, the first suggested family of Kernels is the adiabatic local density approximation (ALDA) that can be written as:

$$f_{xc}(rt, r't') = \delta(\vec{r} - \vec{r'})\delta(t - t')f_{xc}^{HEG}(n)|_{n=n(\vec{r},t)}, \tag{1.125}$$

where $f_{xc}^{HEG} = \frac{d}{dn}V_{XC}^{HEG}(n)$ is just the derivative of the Homogeneous electron gas (HEG) making the approximation local both in time and space [34]. Recently, many other extensions to the linear-response regime have been developed leading to other kind of Kernel like the one suggested by Petersilka [31] in which the locality of the space is removed while the time locality is maintained. Finally, it is noteworthy to say that the ALDA is usually a good approximation that gives a qualitatively description of the excited-states of many systems within the high-density limit [31, 34].

1.9 FIRST-PRINCIPLE MOLECULAR DYNAMICS

Molecular dynamics (MD) is one of the most powerful simulation techniques in order to emulate microscopic dynamical behavior of a wide range of systems [37]. Hence, MD enables the study of many dynamical properties in equilibrium by solving the classical equations of motion under different conditions ranging from the ideal micro-canonical ensemble where the total energy is conserved to the canonical ensemble in which the system is allowed to exchange energy with the environment [55]. The total Hamiltonian of a system of N-particles can be written as:

$$H(\vec{R}^N, \vec{P}^N) = \sum_{i=1}^{N} \frac{\vec{P}_i^2}{2M_i} + U(\vec{R}^N), \tag{1.126}$$

Thus, according to the Hamilton-Jacobi equations of motion one can obtain the trajectory of the system as:

$$\dot{\vec{R}}_i = \frac{\vec{P}}{M_i} \quad \dot{\vec{P}}_i = -\frac{\partial \vec{U}}{\partial \vec{R}_i},$$

that allows to use the second law of Newton in which forces and displacements are related by the differential equation:

$$M_i\ddot{\vec{R}}_I = F_I(\vec{R}^N), \tag{1.127}$$

Similarly, the Lagrangian formulation in which the associated Euler-Lagrange equation can be written as:

$$\frac{\mathrm{d}}{\mathrm{dt}}\frac{\partial \mathrm{L}}{\partial \dot{\vec{\mathrm{R}}}_i} = \frac{\partial \mathrm{L}}{\partial \vec{\mathrm{R}}_i},\tag{1.128}$$

is more often used in the ab-initio formalism in order to compute the trajectory of the system [37].

1.9.1 Born-Oppenheimer Molecular Dynamics

In order to calculate the solution of the total electronic Schrödinger equation the adiabatic approximation has been used [37]. Hence, the electronic and ionic Hamiltonian have been split using the ionic mass as an adiabatic parameter that allows the separation in time scales between the two-phenomena [56]. Moreover, by doing so the KS energy within the so called Born-Oppenheimer (BO) approximation can be recast as:

$$\mathrm{L_{BO}}(\vec{\mathrm{R}}^N, \dot{\vec{\mathrm{R}}}^N) = \sum_{i=1}^{N}\frac{1}{2}\mathrm{M}_i\dot{\vec{\mathrm{R}}}^2 - \min_{\{\varphi_i\}}\mathrm{E^{KS}}[\{\varphi_i; \vec{\mathrm{R}}^N\}],\tag{1.129}$$

where the minimization is constrained to the condition that $\frac{\delta \mathrm{E}}{\delta \varphi_i} = 0$ using the KS-single particles orbitals and ensuring that the solution is the ground-state of the system. Furthermore, the equations of motion can be written as:

$$\mathrm{M}_i\ddot{\vec{\mathrm{R}}}_i = -\nabla_i\min_{\{\varphi_i\}}\mathrm{E^{KS}}[\{\varphi_i; \vec{\mathrm{R}}^N\}],\tag{1.130}$$

Thus, the time dependence of the problem has been reduced to solving a time-independent quantum problem at every single time-step where the nuclei is propagated via classical-molecular dynamics and making that the variation in the electronic structure a consequence of the nuclear motion [37, 55]. A plausible extension of the ground-state dynamics can be achieve for excited states if one applies the same methodology to a selected excited state. However, this implies that there is a diagonal-correction term given by:

$$\mathrm{D}_i^{kk}(\mathrm{R}_i(\mathrm{t})) = -\int \mathrm{d}\vec{\mathrm{r}}\,\Psi_k^*\nabla_i^2\Psi_k,\tag{1.131}$$

where Ψ_k corresponds to the chosen excited-state [37]. These terms re-normalize the Hamiltonian leading to the clumped-nuclei propagation of the chosen excited-state creating the corresponding potential energy surface for this state [55]. A particular point that should be addressed is the computation of the forces within the KS-formalism. However, the direct calculation of the force expressed in Eq. (1.130) by means of numerical methods is computationally expensive and therefore

further approximation should be developed []. Therefore, a more plausible approach is try to calculate these terms analytically by expanding the derivative as:

$$\nabla_i \langle \psi_0 | \hat{H}_e | \psi_0 \rangle = \langle \psi_0 | \nabla_i \hat{H}_e | \psi_0 \rangle + \langle \nabla_i \psi_0 | \hat{H}_e | \psi_0 \rangle + \langle \psi_0 | \hat{H}_e | \nabla_i \psi_0 \rangle, \qquad (1.132)$$

and usually assuming that the wavefunction is a constant over time one can get the force term as:

$$F_i^{HFT} = \nabla_i \langle \psi_0 | \hat{H}_e | \psi_0 \rangle = \langle \psi_0 | \nabla_i \hat{H}_e | \psi_0 \rangle, \qquad (1.133)$$

where F_i^{HFT} is the force obtained by the Hellman-Feynman theorem in the case of a complete basis set [37]. However, since this is not strictly fulfilled then one has to calculate some corrections due to the finiteness of the basis-set by explicitly taking into account the inner derivative of the wavefunction as:

$$\nabla_i \psi_i = \sum_n \left((\nabla_i c_{in}) f_n(r; \{R_i\}) + c_{in} \nabla_i f_n(r; \{R_i\}) \right), \qquad (1.134)$$

resulting in the total-corrected force that should be calculated in the ab-initio methods [37]. It is noteworthy to state that two clear contributions can be disentangled from this expansion. Firstly, the incomplete-basis-set correction (IBS) contains the nuclear gradients of the basis functions as:

$$F_i^{IBS} = \sum_{inm} \left(\langle \nabla_i f_n | H_e^{NSC} - E_i | f_m \rangle + \langle f_n | H_e^{NSC} - E_i | \nabla_i f_m \rangle \right), \qquad (1.135)$$

where H_e^{NSC} is the non-self-consistent effective one-particle Hamiltonian [37]. A second correction term must be added which leads to the non-self-consistency correction NSC that can be recast as:

$$F_i^{NSC} = - \int d\vec{r} \, (\nabla_i \hat{n})(V^{SCF} - V^{NSC}), \qquad (1.136)$$

which is the difference between the non-self-consistent potential associated with the H_e^{NSC} and the self-consistent potential where $\hat{n}$ is the charge density obtained from the single-particle KS-orbitals [37]. Thus, the original force can be decompose into three terms like:

$$F_I = F_I^{HFT} + F_I^{IBS} + F_I^{NSC}, \qquad (1.137)$$

that can be computed within the KS-formalism and their numerical schemes [37, 55].

1.10   DENSITY-FUNCTIONAL TIGHT-BINDING

Further approximations can be carried out using the full Kohn-Sham Hamiltonian in order to create new methods which can be more computationally affordable for bigger systems [57]. Thus, the main idea of self-consistent-charge density functional tight-binding method (SCC-DFTB) is to expand the original Kohn-Sham Hamiltonian (1.38) in a Taylor functional-expansion using small perturbations of the density. In order to achieve this, first the idea of Harris can be employed by using a suitable initial density ρ^0 (close to the real $\rho^{\mathrm{ground-state}}$) where the KS-Hamiltonian can be written as:

$$\mathrm{E}[\rho] = \sum_{\mathrm{i}}^{\mathrm{occ}} \mathrm{E}_{\mathrm{i}}^{\mathrm{H}} - \int \frac{\rho^0(\vec{\mathrm{r}})\rho^0(\vec{\mathrm{r}}')}{|\vec{\mathrm{r}} - \vec{\mathrm{r}}'|} \mathrm{drdr}' + \mathrm{E}^{\mathrm{XC}}[\rho^0] - \int v^0(\mathrm{r})\mathrm{dr} + \frac{1}{2}\sum_{\alpha\beta} \frac{Z_\alpha Z_\beta}{\mathrm{R}_{\alpha\beta}}, \quad (1.138)$$

leading to the so-called Harris functional [58]. Thus, one can expand this Hamiltonian in terms of $\delta\rho = \rho - \rho^0$ which can be either solved by not self-consistent or by self-consistent numerical schemes [59]. Furthermore, in the self-consistent implementation, the effective potential of the Harris potential can be written as:

$$v^{\mathrm{eff}}[\rho] = v^{\mathrm{eff}}[\rho^0] + \int \frac{\delta v^{\mathrm{eff}}[\rho]}{\delta\rho}\delta\rho\mathrm{dr}, \quad (1.139)$$

leading to an effective second-order expansion of the full KS-Hamiltonian in terms of the fluctuations of the charge-density $\delta\rho$ around a given reference density usually supplied by Full DFT calculations [57]. The SCC-DFTB can written as:

$$\begin{aligned}
\mathrm{E}[\rho] = \sum_{\mathrm{i}}^{\mathrm{occ}} \mathrm{E}_{\mathrm{i}}^{\mathrm{H}} &- \int\int \left(\frac{1}{|\vec{\mathrm{r}} - \vec{\mathrm{r}}'|} + \frac{\delta^2 \mathrm{E}^{\mathrm{xc}}}{\delta\rho\delta\rho'}|_{\rho_0} \right)\Delta\rho\Delta\rho' \\
&+ \mathrm{E}^{\mathrm{XC}}[\rho^0] - \int \frac{\rho^0(\vec{\mathrm{r}})\rho^0(\vec{\mathrm{r}}')}{|\vec{\mathrm{r}} - \vec{\mathrm{r}}'|}\mathrm{drdr}' - \int \mathrm{V}^{\mathrm{XC}}[\rho^0]\rho^0 + \mathrm{E}^{\mathrm{CC}},
\end{aligned} \quad (1.140)$$

where the first term can be effectively computed by assuming the LCAO ansatz $\Psi_{\mathrm{i}} = \sum_{\mathrm{i}} c_{v\mathrm{i}}\varphi_v$. Interestingly, the four last terms of the SCC-DFTB Hamiltonian represent the repulsive energy contribution. These terms can be itemized into two main contributions of the DFT Hamiltonian, namely, the double-counting and the core-core repulsion term [60]. Hence, and assuming that the the atomic density decomposition of the orbitals holds, then the two terms can be written as:

$$\frac{1}{2}\sum_{\alpha\beta} \frac{Z_\alpha Z_\beta}{\mathrm{R}_{\alpha\beta}} - \int \frac{\rho^0(\vec{\mathrm{r}})\rho^0(\vec{\mathrm{r}}')}{|\vec{\mathrm{r}} - \vec{\mathrm{r}}'|}\mathrm{drdr}', \quad (1.141)$$

Which in the case of the first term decays exponentially with the inter-atomic distance due to the fact that atomic densities decay exponentially [60]. The Coulomb

terms can be re-arranged in sums of two-body interactions which in the case of DFTB leads to pairwise atom-atom potentials [57]. Nonetheless, the main supposition of the SCC-DFTB method is that the repulsive energy is a short-range term, which effectively is not true due to the long-range nature of the core-core interaction [58]. At this point, is where a fitting procedure is needed in order to reproduce many experimental quantities such as geometries, vibrational frequencies, reaction energies, proton affinities among others leading to many different strategies to achieve a representation of $E^{rep}[\rho]$ [57]. Finally, from the original DFTB implementation to the SCC-DFTB scheme one has to consider the second order term E^{2nd} in the charge density fluctuations in the Eq. (1.141). To do so, the first simplification is to treat the charge-density fluctuations in a monopole approximation that can be recast as:

$$\Delta\rho_\alpha \approx \Delta q_\alpha R_\alpha^{00} Y^{00}, \tag{1.142}$$

where R_α^{00} states for the normalized radial function of the density while Y^{00} is the angular part of the spherical harmonics. Once this is assumed and used as ansatz for 1.141, an expression can be obtained for the second-order correction as:

$$E^{2nd} = \frac{1}{2}\sum_{\alpha\beta}\Delta q_\alpha \Delta q_\beta \int\int' \left(\frac{1}{|\vec{r}-\vec{r}'|} + \frac{\delta^2 E^{xc}}{\delta\rho\delta\rho'}|_{n_0}\right) F_\alpha^{00} F_\beta^{00} (Y^{00})^2 dr dr', \tag{1.143}$$

This equation can be further analyzed using the atomic distances as parameter. Thus, in the limit of large distances between cores, one can see that the V^{XC} vanishes and leading only to a Coulomb term of the form:

$$E^{2nd} = \frac{1}{2}\sum_{\alpha\beta}\frac{\Delta q_\alpha \Delta q_\beta}{R_{\alpha\beta}}, \tag{1.144}$$

On the contrary, when atomic distances are approaching to zero, the integral describes the electron-electron interaction repulsion on the corresponding atom. This term can be approximated as:

$$E^{2nd} = \frac{1}{2}\Delta q_\alpha^2 U_\alpha, \tag{1.145}$$

where U_α is the Hubbard term, that indicates the energy needed to remove or add electrons to this specific atom species. This last term can be computed by approximating the radial part of the density as a decaying exponent that leads to the expression $E^{2nd} = \frac{1}{2}\sum_{\alpha\beta}\Delta q_\alpha \Delta q_\beta \gamma_{\alpha\beta}$ where the $\gamma_{\alpha\beta}$ parameters are related with the chemical hardness as $\gamma_{\alpha\beta} = \frac{\partial^2 E_\alpha}{\partial^2 q_\alpha}$. The Hubbard term can be estimated from the Janak's theorem in which the ionization potential and electron affinity can be obtained by the first-derivative of the highest-occupied molecular orbital with respect to the occupation number and finally leading to the expression for the SCC-DFTB as:

$$E^{SCC-DFTB} = \sum_{i\nu\mu} c_{\nu i} c_{\mu i} H^0_{\nu\mu} + E^{2nd} + E^{rep}, \qquad (1.146)$$

This semi-empirical method has been implemented in the DFTB+ code in which many different features and extensions of the approximation can be used. Among other extensions of the method one can find implementations such as vdW forces, molecular dynamics calculations in different ensembles, non-equilibrium Green's function, external electric fields among others [57, 58, 60, 61].

Part II

RESULTS

2 CHARACTERIZING THE BISTABILITY OF MOLECULAR QUANTUM CELLULAR AUTOMATA: A COMBINED AB-INITIO AND MODELING STUDY

The main focus of this chapter is to understand the relationship between the molecular electronic properties of a possible candidate with the required QCA implementation functionalities. Thus, this study is focused in the comprehension of charge localization and the electric-field coupling between the first molecular cell and the read-in mechanism. Firstly, the intra-molecular electron transfer (ET) can be understood as consequence of an interaction between functional-groups (moieties) that are capable of accepting and donating electrons (reduction and oxidization, respectively). These redox centers are usually connected by bridging ligands that determine the degree of localization of the charge-carriers acting as an effective tunnel barriers [62]. In this matter, the electronic structure of the bridge also defines the regime in which the electron transfer occurs, namely, super-exchange or hopping [63]. The choice of the redox centers and bridges is a fundamental piece in the implementation of this technology since those are the knobs for fine chemical tuning of the m-QCA response. One of the most important issues is the intrinsic and complex relationship between quantum mechanical effects (such as ET) and classical forces (electrostatic interactions) which compete to fully determine the equilibrium between charge localization, necessary to store readable states, and charge transfer, necessary for state switching and then, ultimately, for computation [64].
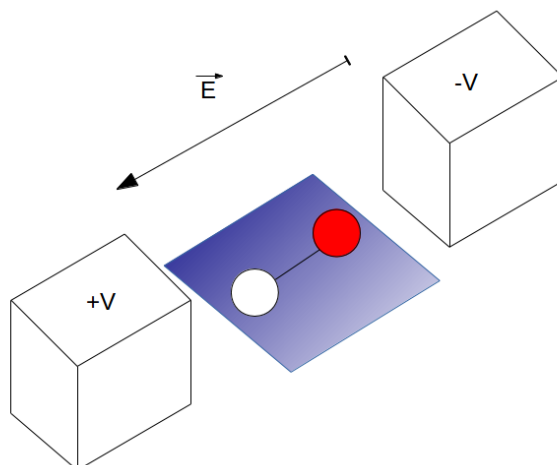
Figure 2.1: Plausible experimental write-in setup device. An electric field is created by a voltage drop across the plates that inscribes the first logical state in the molecule. The switching mechanism is controlled by varying the voltage and inducing an intra-molecular charge transfer in the first m-QCA cell [65].

2.1 THEORETICAL MODEL

2.1.1 Single-molecule QCA

In this study, the simplest m-QCA half cell is represented by two quantum dots (spatial regions in which the electron charge can be localized) which are separated by a tunnel barrier (bridge-ligand). As is presented in Fig. 2.1, the external driver molecule is represented by two point charges whose main function is to start the switching process in the second molecular complex, namely, the target molecule [65], in analogy to the external voltage source needed to set in the switching process in semiconductor and molecular-QCA implementations [9]. Concerning the actual experimental implementation, an assembly of biased, vertically oriented, two-dot cells sandwiched between two electrodes have been constructed in which the working principle relies on the measurement of the capacitance of the parallel plate device as a function of a controllable applied voltage across the plates [66]. In the schematic experimental set-up (Fig. 2.1), one can observe how the molecule is placed in-between the electrodes while an electric field is applied enforcing the first logical state in the molecule. Thus, in the following sections a phenomenological model will be developed in which the main interactions will be considered including the role played by internal and external sources in the switching mechanism.

2.1.2 Diabatic to Adiabatic transformation

In order to model the previous described experimental set-up, a two-state approximation is used [67]. The intra-molecular electron transfer (ET) processes can be modeled taking as a reference point the localized diabatic states representing initial and final stages of the ET process [62]. For a minimal-QCA model containing only two redox centers, the corresponding Hamiltonian matrix can be written as:

$$\begin{bmatrix} H_{aa} & H_{ab} \\ H_{ba} & H_{bb} \end{bmatrix} \begin{bmatrix} c_a \\ c_b \end{bmatrix} = E \begin{bmatrix} c_a \\ c_b \end{bmatrix}, \tag{2.1}$$

where $H_{aa} = \langle \phi_a | H | \phi_a \rangle$, $H_{bb} = \langle \phi_b | H | \phi_b \rangle$ and $H_{ab} = H_{ba}^* = \langle \phi_a | H | \phi_b \rangle$. The corresponding eigenfunctions (diabatic states) for H_{aa} and H_{bb} are denoted by $|\phi_a\rangle$ and $|\phi_b\rangle$ with associated eigenvalues E_a and E_b, respectively. The overlap $\langle \phi_a | \phi_b \rangle$ between the diabatic states is neglected and the coefficients c_a and c_b are normalized $(c_a^2 + c_b^2 = 1)$. The H_{aa} and H_{bb} terms represent the situation where the excess of charge is localized either at the upper or lower part of the target molecule, and can be considered as the initial and final stages of the ET process, respectively. These matrix elements include the influence of the driver (Hg probe in the experimental set-up) and, since the charge is fully localized in those states, H_{aa} and H_{bb} can be computed using classical electrostatics. For the fully symmetrical case, where $d = L$, see the upper left panel of Fig.2.2, the result is simply [67]:

$$\begin{aligned} H_{aa} &= \frac{-e^2}{4\pi\varepsilon_0} \left[\frac{q_1}{L} + \frac{(1-q_1)}{2\sqrt{L}} \right], \\ H_{bb} &= \frac{-e^2}{4\pi\varepsilon_0} \left[\frac{q_1}{\sqrt{2L}} + \frac{(1-q_1)}{L} \right]. \end{aligned} \tag{2.2}$$

The H_{ab} and H_{ba} matrix elements can be then understood as the quantum mechanical mixing between the two electronic diabatic states. Diagonalizing the Hamiltonian is straightforward and the corresponding eigenvalues are given by:

$$2E_{\pm} = H_{aa} + H_{bb} \pm \sqrt{(H_{aa} - H_{bb})^2 + 4H_{ab}^2}, \tag{2.3}$$

Likewise, the associated wavefunctions for the ground state (E_-) and the excited state (E_+) can be written as a linear combination of the diabatic states as:

$$\begin{aligned} \Psi_1 &= c_a\phi_a - c_b\phi_b, \\ \Psi_2 &= c_a\phi_a + c_b\phi_b. \end{aligned} \tag{2.4} \tag{2.5}$$

each one associated with the eigen-energies for the ground-state E_- and excited states E_+, correspondingly. Furthermore, from the adiabatic solutions, one can find the coupling between diabatic states at the degeneracy point $(H_{aa} = H_{bb})$ as:

$$\gamma = H_{ab} = \frac{E_+ - E_-}{2}. \tag{2.6}$$

At this stage, the super-exchange regime for ET is only considered, where the donor-acceptor charge transfer takes place via a tunneling process, with no participating states of the bridge atoms [63]. In the super-exchange regime, one can write γ as an exponential function of the donor-acceptor separation R:

Complex	$\alpha(\mathrm{nm}^{-1})$	$\gamma_0(\mathrm{eV})$	$\gamma(\mathrm{eV})$
1,4-diallyl butane	4.66	6.68	
allyl-$(\mathrm{CH_2})_3$-allyl			0.52
allyl-$(\mathrm{CH_2})_9$-allyl			0.0119
diferrocenylpolyenes	0.84	0.12	
FC-1-FC			0.061
FC-5-FC			0.028

Table 2.1: Typical reference parameters used in Eq. 2.7 for the two studied molecule types [67, 69]

$$\gamma = \gamma_0 \mathrm{e}^{-\alpha \mathrm{R}}, \qquad (2.7)$$

where α is system-dependent [68] and can be obtained from DFT calculations by assuming the Koopman's theorem leading to the expression $\gamma = \frac{\mathrm{E_{LUMO}} - \mathrm{E_{HOMO}}}{2}$. If not stated otherwise, the reference values for the electronic coupling elements are listed in Table (2.1) (see also Ref [67, 69]).

2.1.3 Response function

The efficiency of a candidate molecule for its implementation in a m-QCA cell can quantified via a function that relates the cell response to an external driver [67]. Particularly, a well-defined switching between two states should take place in order to efficiently encode the two classical bits 0 and 1 of information [5]. These two states can be linked to charge reorganization inside the target cell under the action of the driver molecule. Such processes can be used in order to define a polarization function, specified by $\mathrm{P_2} = \mathrm{Tr}(\rho_\mathrm{t}\sigma_3) = |c_\mathrm{a}|^2 - |c_\mathrm{b}|^2 = 2|c_\mathrm{a}|^2 - 1$. Here, ρ_t is the density matrix of the target and $\sigma_3 = \mathrm{diag}(1,-1)$ is a Pauli matrix.

Within the two-state approximation, the $c_\mathrm{a,b}$ are the coefficients of the expansion of the ground state wave function in the diabatic basis. The corresponding polarization for the (classical) driver is then simply $\mathrm{P_1} = q_1 - q_2 = 2q_1 - 1$. Using the adiabatic energy eigenvalues, the expansion coefficient can be written as:

$$|c_\mathrm{a}|^2 = \gamma^2 / (\gamma^2 + (\mathrm{E_+} - \mathrm{H_{aa}})^2), \qquad (2.8)$$

After some simple manipulations [67], the target polarization $\mathrm{P_2}$ can be expressed as a function of the driver polarization $\mathrm{P_1}$ as:

$$\mathrm{P_2} = \frac{2}{1 + \{\beta \mathrm{P_1} + \sqrt{(\beta \mathrm{P_1})^2 + 1}\}^2} - 1, \qquad (2.9)$$
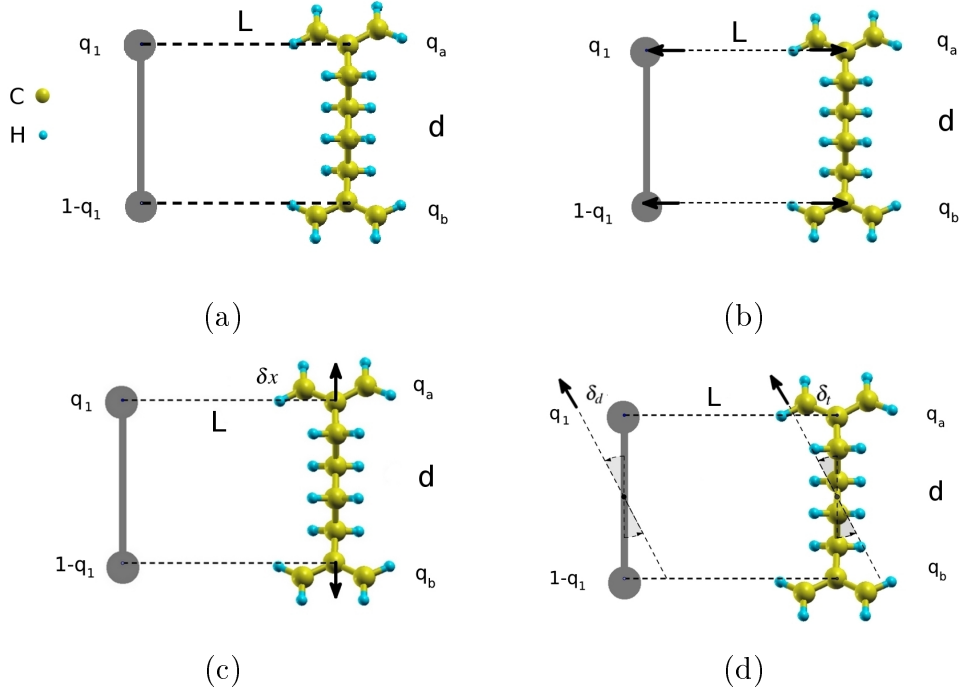
with

Figure 2.2: Schematic representation for the driver-target configurations studied. Only the case of the Aviram molecule (1,4-diallyl butane) is shown. For all other compounds a similar representation holds. The driver molecule is represented by two point-charges q_1, q_2 such that $q_1 + q_2 = 1$, and separated by a distance d. (a) Symmetrical situation where both components are static. (b) The driver molecule is allowed to move along a line perpendicular to the axis of the target. (c) Stretching and compression of the target molecule by δx that only affect the length of the bridge. (d) Coordinated rotations between the driver and the target. In the small angle approximation, the angular distortions can be related to the linear displacements δ_d and δ_t of the driver and target molecules, respectively.

$$\beta = \frac{e^2}{4\pi\varepsilon_0}\left[\frac{2-\sqrt{2}}{2}\right]\frac{1}{\gamma L}. \tag{2.10}$$

2.1.4 Geometrical distortions

Based on the previous results, one can investigate the effect of geometrical distortions that a candidate molecule can undergo in the polarization function. In that respect, it is important to notice that the parameter β relates the electronic properties of the target (γ) and geometrical features of the system (L). This expression was derived in Ref. [67] for a fully symmetric geometry (d = L). Thus, it is interesting to address the problem of how resilient the system will be with respect to static (and dynamic, thermally induced) distortions of this ideal conformation, since such scenarios may be expected in real m-QCA networks and has not been thoroughly studied in the case of the m-QCA implementation [70, 71, 72, 73, 74, 75, 76, 77].

Relative translations between Driver and Target

As a starting point, the first simple modification will be to allow for a change in the linear driver-target distance. Thus, the driver is translated along a line perpendicular to the molecular axis as shown in Fig. 2.2(a), where one can define L as the distance between molecules and d the distance between donor and acceptor centers in the target molecule. Varying the driver-target distance will clearly affect the polarization switching of the target, since it determines the relative position of the diabatic states and whether they will display a crossing point or, in terms of the adiabatic states, an anti-crossing point [78, 79]. The corresponding diabatic states for an arbitrary separation between target and driver $L(\neq d)$ is:

$$
\begin{aligned}
H_{aa} &= \frac{e^2}{4\pi\varepsilon_0}[\frac{q_1}{L} + \frac{(1-q_1)}{\sqrt{L^2+d^2}}], \\
H_{bb} &= \frac{e^2}{4\pi\varepsilon_0}[\frac{q_1}{\sqrt{L^2+d^2}} + \frac{(1-q_1)}{L}].
\end{aligned}
\tag{2.11}
$$

following the similar mathematical procedure as in the previous section, the response function can be recast as:

$$
P_2 = \frac{2}{1+\{\beta^*P_1 + \sqrt{(\beta^*P_1)^2+1}\}^2} - 1,
\tag{2.12}
$$

where now

$$
\beta^* = \frac{e^2}{4\pi\varepsilon_0}\frac{1}{\gamma L}[1 - \frac{1}{\sqrt{1+(\frac{d}{L})^2}}].
\tag{2.13}
$$

At this point and for all cases, one can use the relative separation L/d_{bridge}, since absolute values are clearly very much dependent on the specific molecule type and conformation (see Fig. 2.3). Evidently, for the symmetric case $d = L$ one can recover Eq. (2.10). For $d/L \ll 1$ the β^*-parameter scales as $\beta^* \sim (d^2/L^3)$ and the corresponding polarization as:

$$
P_2 \sim (1/L)(d/L)^2 P_1,
\tag{2.14}
$$

becomes asymptotically insensitive to the driver polarization P_1, as expected. In the opposite case $(d/L \gg 1)$, $\beta^* \sim (1/L) \sim \beta$. The size of the L/d_{bridge} ratio will also strongly depend on its origin like mismatches in the assembly process. In the case of the carbon-only target molecules, Fig. 2.3(a), for short bridges, the non-linear response is rapidly suppressed for larger target-driver separations (~ 1.10 nm), since the contribution from the tunnel coupling $\gamma = 0.52$ eV is too large in this case and hence effectively reducing the parameter β^* ($\beta^* \sim \gamma^{-1}$). Only for rather short driver-target separations the polarization function would recover its non-linear S-shape. For long bridges the non-linear dependence is largely preserved
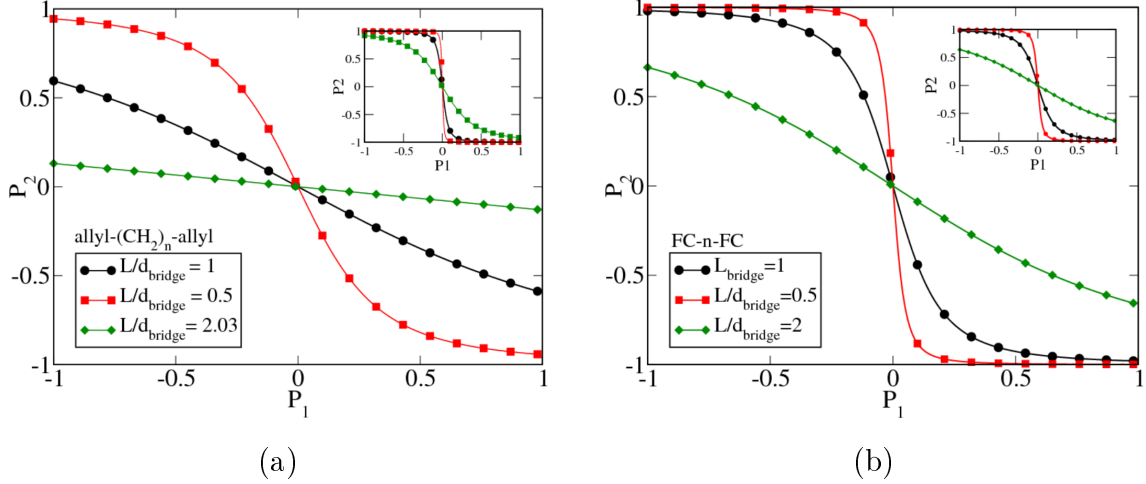
Figure 2.3: Response function of the target molecule for driver–target translations. Results for both, alkyl-diene and diferrocenyl based molecules are shown. In all cases, the insets correspond to longer bridges separating the redox centers (n=9 for alkyl-diene and n=5 for diferrocenyl based molecules), see also Fig. 2.2. For clarity purposes the driver-target separations are given in terms of the ratio L/d_{bridge}.

(see the inset Fig. 2.3(a)), since in this case the tunnel coupling is small enough, $\gamma = 0.012$ eV, to still guarantee charge localization at the donor-acceptor centers. Consider now the diferrocenyl-based molecules, as shown in Fig. 2.3(b). The first point to notice is that for both bridge lengths $n = 1$ and $n = 5$, the tunnel couplings are considerably smaller than for the Carbon-based molecule allyl-$(CH_2)_n$-allyl (see Table 2.1 for actual values). This suggests that the non-linear response of the target may be less sensitive to variations of the driver-target distance. This is clearly seen for the short Fc-1-Fc bridge, where the non-linear response is preserved except for the largest target-driver separation (see Fig. 2.3(b)). The relatively weak change of the tunnel coupling with increasing bridge length also implies that the polarization function does not strongly depend on the bridge length (compare with the inset of the Fig. 2.3(b)).

Elongations in the target molecule

The next possible case scenario is a mismatch between the lengths of the driver and of the molecule [79]. Denoting by δx (positive and negative) the stretching of the target length d (keeping the length of the driver constant and equal d), the diabatic matrix elements can be written as:

$$
\begin{aligned}
H_{aa} &= \frac{e^2}{4\pi\varepsilon_0}\left[\frac{q_1}{\sqrt{L^2 + \delta x^2}} + \frac{(1-q_1)}{\sqrt{L^2 + (d+\delta x)^2}}\right], \\
H_{bb} &= \frac{e^2}{4\pi\varepsilon_0}\left[\frac{q_1}{\sqrt{L^2 + (d+\delta x)^2}} + \frac{(1-q_1)}{\sqrt{L^2 + \delta x^2}}\right],
\end{aligned}
\tag{2.15}
$$

(a)   (b)
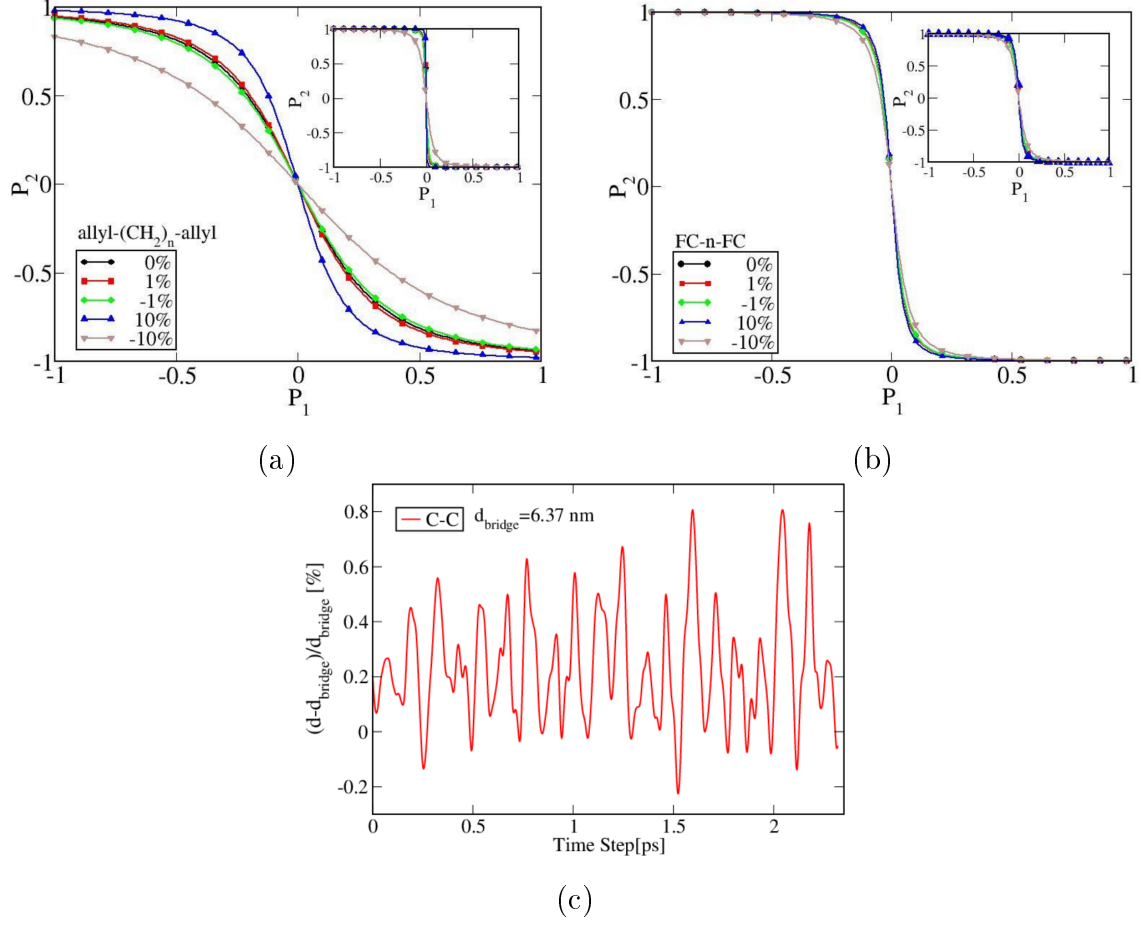

(c)

Figure 2.4: Response function of the target elongations. Results for both, (a) alkyl-diene and (b) diferrocenyl based molecules are shown. In all cases, the insets correspond to longer bridges separating the redox centers (n=9 for alkyl-diene and n=5 for diferrocenyl based molecules), see also Fig 2.2. The elongations of the target are given by d/d_{bridge}. (c) ab-initio molecular dynamics calculations where the distances between the redox centers of the 1,4-diallyl butane has been measured along the computed trajectory.

and the corresponding polarization becomes:

$$P_2 = \frac{2}{1 + \{\beta^{**}P_1 + \sqrt{(\beta^{**}P_1)^2 + 1}\}^2} - 1, \tag{2.16}$$

with the new effective parameter

$$\beta^{**} = \frac{e^2}{4\pi\varepsilon_0} \frac{1}{\gamma L} \left[\frac{1}{\sqrt{1 + (\frac{\delta x}{L})^2}} - \frac{1}{\sqrt{1 + (\frac{d+\delta x}{L})^2}} \right]. \tag{2.17}$$

The possible linear distortions of the target molecule have been simulated by employing the previous developed model in order to investigate the influence of

such distortions in the switching behavior for the m-QCA implementation. The results are shown in Fig. 2.4(a) for the Carbon-only and (b) the Ferrocene based targets. Since now the length of the target molecule is changing, one can compute the corresponding γ-coupling terms according to Eq. 2.7. Due to the assumed small ratio $\delta x/L$, the influence of such distortions turns out to be less dramatic than changes in the target-driver separation. This is clearly the case for longer bridges, where the strong non-linear response is well preserved for distortions of up to ± 10 %. For shorter bridges, the most affected one is, as expected, the allyl-$(CH_2)_3$-allyl due to the rather (on average) large γ. In general terms, elongations of the molecule on the order of $\pm 1\%$ are reasonable and supported by quantum molecular dynamics simulations (see Fig. 2.4(c)), while the other values of $\pm 10\%$ are extreme cases that have been treated for the only purpose of showing how strong a structural distortion may be in order to considerably perturb the non-linearity of the cell response. In this matter, ab-initio molecular dynamics calculations have been carried out in order to investigate in averaged the elongation of the molecule and the results presented in Fig. 2.4. The calculations support the assumption made in the model in terms of the averaged elongation distortions experienced by a complex that in the specific case of the 1,4-diallyl butane elongates around ± 3 % when compared with its original distance [78].

Angular distortions

As a last case of study, one can peruse the static angular distortions which can be grouped into in- and out-of-phase concerted motions of the driver and the target. In Fig. 2.2 one can schematically illustrate this situation, where both, target and driver molecules with length d rotate about their corresponding center-of-mass. The discussion is limited to small angular distortions of size $\theta_{t,d}$ such that $\sin\theta_{t,d} \approx \theta_{t,d} = 2\delta_{t,d}/d$, with t, d denoting the target and driver distortions, respectively [78, 75]. In this limit, θ was expressed in terms of the linear displacements δ_t, δ_d and the diabatic states are found to be:

$$
\begin{aligned}
H_{aa} &= \frac{e^2}{4\pi\varepsilon_0}\Big[\frac{q_1}{(L-\delta_d-\delta_t)} \\
&+ \frac{(1-q_1)}{\sqrt{(L+\delta_d+\delta_t)^2+(d^2-4\delta_t^2)}}\Big], \\
H_{bb} &= \frac{e^2}{4\pi\varepsilon_0}\Big[\frac{q_1}{\sqrt{(L-\delta_d-\delta_t)^2+(d^2-4\delta_d^2)}} \\
&+ \frac{(1-q_1)}{(L+\delta_d-\delta_t)}\Big].
\end{aligned}
$$

$$(2.18)$$

The corresponding polarization function can be cast as:

$$
P_2 = \frac{2}{1+\{(\beta_1 P_1+\beta_2)+\sqrt{(\beta_1 P_1+\beta_2)^2+1}\}^2} - 1. \tag{2.19}
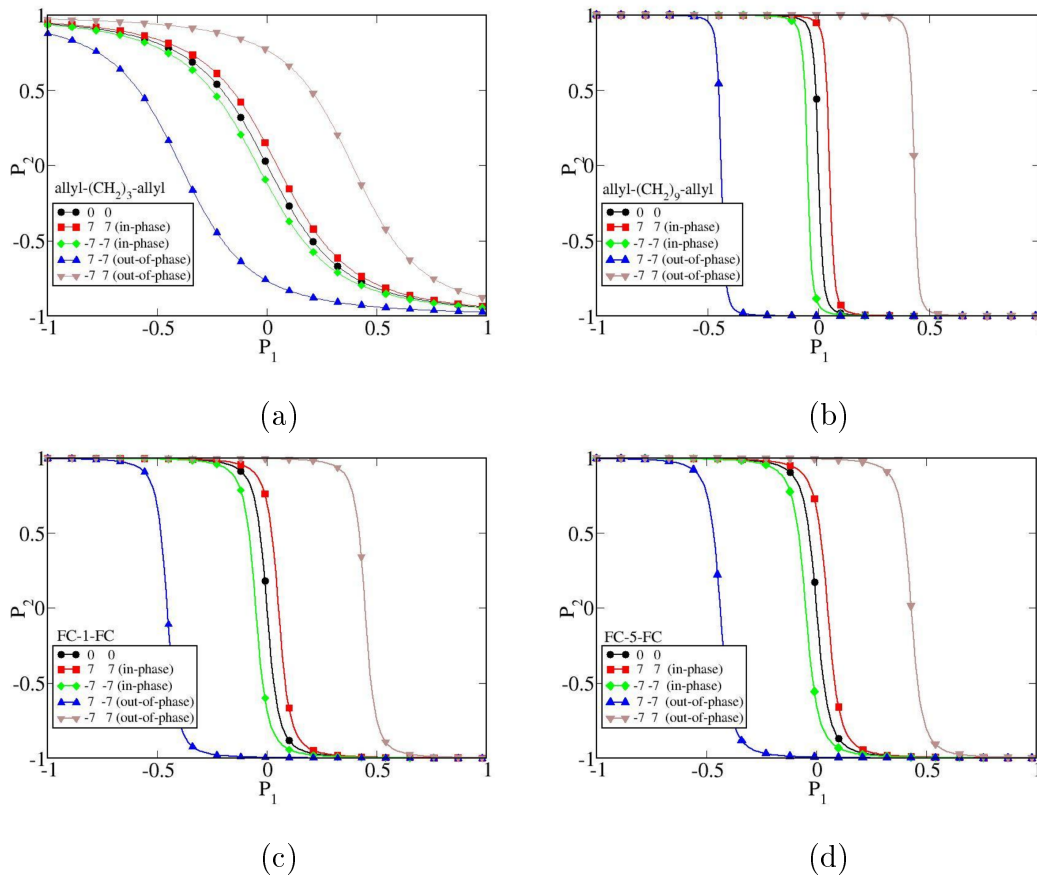$$

(a)

(b)

(c)

(d)

Figure 2.5: Response function of the target molecule as a function of the driver polarization for the case of coupled angular distortions. Results for the alkyl-diene molecules with two different bridge lengths as well as for the diferrocenyl based systems are shown. The general notation θ_d, θ_t indicates the angular distortions (in degrees) of the driver (d) and target (t).

In contrast to linear deformations, small angular distortions lead to an additional term (β_2). The new parameters are given by:

$$
\begin{aligned}
\beta_1 = \frac{e^2}{4\pi\varepsilon_0} \frac{1}{2\gamma} \Big[& \frac{1}{(L - \delta_d + \delta_t)} + \frac{1}{(L + \delta_d - \delta_t)} \\
& - \frac{1}{\sqrt{(L + \delta_d + \delta_t)^2 + (d^2 - 4\delta_t^2)}} \\
& - \frac{1}{\sqrt{(L - \delta_d - \delta_t)^2 + (d^2 - 4\delta_d^2)}} \Big],
\end{aligned}
\tag{2.20}
$$

$$\beta_2 = \frac{e^2}{4\pi\varepsilon_0}\frac{1}{2\gamma}\Big[\frac{1}{(L-\delta_d+\delta_t)} - \frac{1}{(L+\delta_d-\delta_t)}$$

$$+ \frac{1}{\sqrt{(L+\delta_d+\delta_t)^2+(d^2-4\delta_t^2)}}$$

$$- \frac{1}{\sqrt{(L-\delta_d-\delta_t)^2+(d^2-4\delta_d^2)}}\Big]. \tag{2.21}$$

In the previous equations, one can consider in general different distortions for the driver (δ_d) and the target (δ_t). However, to simplify the discussion only symmetric cases are considered where $|\delta_t| = |\delta_d| = \delta$. Notice however, that δ can still take both, positive and negative values. Based on this model, one can define two types of distortions: (i) in-phase displacements, where $\text{sgn}(\delta_t) = \text{sgn}(\delta_d)$, and (ii) out-of-phase displacements with $\text{sgn}(\delta_t) = -\text{sgn}(\delta_d)$. Firstly, in-phase rotations, in which both molecules move in the same direction along the line connecting both molecular axis creating a back and forth movement. Secondly, out-of-phase rotations, where one of the $\delta_{t,d}$ variables is taken negative, while the second one is chosen positive (although with the same absolute value). The results shown in Fig. 2.5 are all obtained for the special case $L = d/2$ where the switching behavior is guaranteed. The main influence of static angular distortions is to shift the target polarization along the P_1-axis in a way that sensitively depends on the type of the considered collective distortions (in- or out-of-phase). This clearly induces a strong perturbation of the QCA response function. The value of P_2 at zero driver polarization is related to the β_2 parameter as $P_2 = 2/(1 + \{\beta_2 + \sqrt{(\beta_2)^2+1}\}^2) - 1$, so that as long as β_2 does not vanish, a non-zero, geometrically-related, residual polarization will exist. the direct impact in the target polarization can be observed in a lag with respect to the driver polarization. Consequently, an additional field may be necessary to reset P_2 to zero in order to preserve the appropriate response of the target molecule in presence of static angular distortions. For angular displacements of the order of $\theta = \pm 7°$, the most notorious modifications of the polarization are found to occur for the out-of-phase distortions inducing a strong shift. In real molecular systems one may expect in general smaller angular distortions. The influence of such distortions should be most likely noticeable for situations where no strong covalent bonding to the substrate takes place or when the active molecular species are attached to the substrate via longer inert linkers increasing the mechanical flexibility of the system. This latter case may be more realistic, since a good electronic decoupling from the substrate may turn out to be important in order to preserve the charge bi-stability of the mQCA cells. The sensitivity on the relative phase of the distortions can be qualitatively understood by looking at the behavior of the β_2 parameter in the limit of $|\delta/(d/2)| \ll 1$. In the case of in-phase motions $(\text{sgn}(\delta_t) = \text{sgn}(\delta_d))$, one gets $\beta_2 \sim -(1/\gamma L)(1+(d/L)^2)^{-3/2}(\delta/L)$, while for the out-of-phase motion $(\text{sgn}(\delta_t) = -\text{sgn}(\delta_d))$, $\beta_2 \sim (1/\gamma L)(\delta/L)$. Therefore, this correction has different signs depending on the type of distortion and it is easy to realize that the shift in P_2 (at $P_1 = 0$) will be stronger for the out-of-phase displacements [78].

2.1.5 Validating the minimal model: First-principle calculations

It is desirable to validate the results obtained using the previously introduced minimal models using some simple molecular system Mainly the influence of static angular distortions needs to be further clarified. Thus, one can perform first-principle
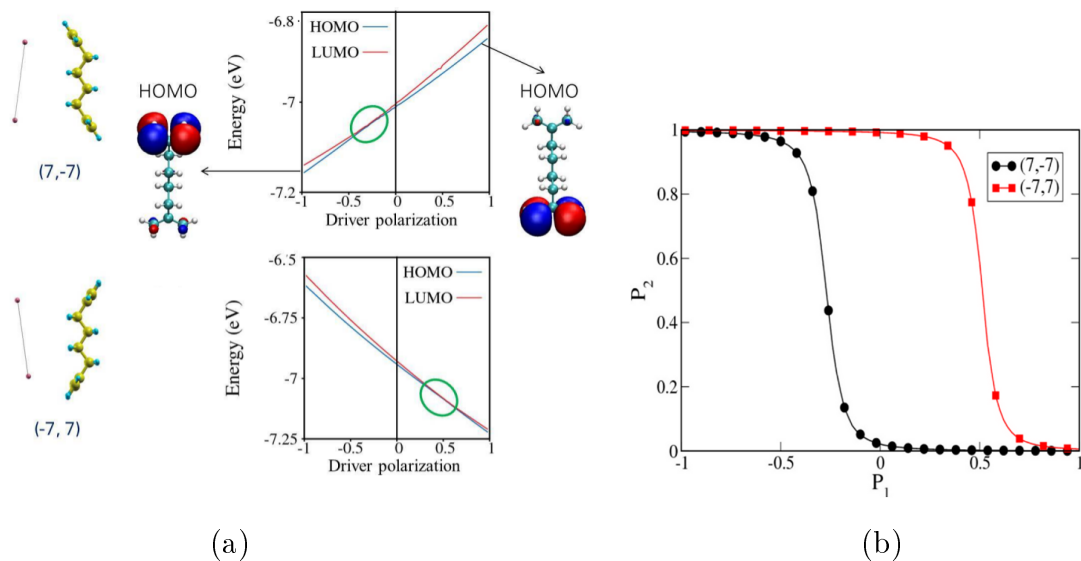
Figure 2.6: (a) Calculated HOMO and LUMO energy levels for the 1,4-diallyl bu-
tane radical cation where (out-of-phase) angular distortions of both target and
driver are taken into account. The angular distortions between driver and target
are (upper panel) (7,-7) and (lower panel) (-7,7). The charge density plots of the
HOMO state for the two limiting driver polarizations $P_1 = -1$ and $P_1 = 1$. (b)
Corresponding cell response function obtained from ab-initio methods.

based calculations of the $1, 4-$diallyl butane radical cation using the density-functional
tight binding code (DFTB+) [57] including self-consistent charge calculations (SCC-
DFTB) as well as dispersion interactions [59, 80, 81]. As starting point, a dipole
driver has been placed parallel to the $1, 4-$diallyl butane radical cation in order to
maintain the same geometrical configurations used in our minimal models. As pre-
viously indicated, the total charge of the driver is 1 and one can plot the variation
of the molecular orbitals of the target while varying the driver polarization P1. To
provide a mobile charge in the system, the molecular cation has been considered,
where an electron has been removed from the lower allyl-group leading to a situation
where the anti-bonding level is singly occupied in the upper group and non-occupied
in the lower allyl group. Charge transfer is expected, since the localized electron at
the lower allyl-group can occupy one of the non-bonding levels that is related with a
molecular orbital from the opposite allyl-end group as can be seen in Fig. 2.6 inset.

In this approach, for a given configuration of the driver polarization P1 ranging
from -1 to 1, the molecule is allowed to relax by using the conjugate gradient algo-
rithm until the root mean square force was less than or equal to 10^{-4} a.u. Since
the point charges on the driver induce an effective force on the molecule, the carbon
atoms located at the center of each of the allyl-end groups are maintained fixed.
In Fig. 2.6, the HOMO and LUMO energy levels for the molecule are plotted as
a function of the driver polarization P1 for the case of out-of-phase rotations by 7
degrees. Notice the shift (encircled in Fig. 2.6) of the anti-crossing point of the
molecular states to the left or right of the zero driver polarization in dependence of
the relative angular distortion of the driver and target. The shifts are not fully sym-
metric, which is only reflecting the fact that the real molecular system is not fully
planar. In general terms, the switching of the target polarization while smoothly
(adiabatically) varying the driver polarization takes place around the anti-crossing
region of the adiabatic states (or at the crossing point of the diabatic states). In a

real molecule, these states can be related to the HOMO and LUMO frontier orbitals. This picture is similar to a Landau−Zener [82, 83] interpretation of charge transfer where the effective (time−dependent) reaction parameter can be associated with the driver−target distance L. In the case of a square geometry with the driver−target distance being similar to the separation between the allyl groups, the anti−crossing point is found at zero driver polarization exactly where the target response function also vanishes (at P1 = 0). However, in the case of angular distortions, a shift in the anti-crossing point is found, whose sign depends on the relative orientation of driver and target (see top and bottom panels in Fig. 2.6(a)). This means, the target polarization is non-vanishing at P1 = 0 and that indeed the target response shows a lag with respect to the driver validating the effect found in the minimal model calculations for static angular distortions (see Fig 2.5 for comparison). It is noteworthy to mention that the found shifts of the target polarization are not fully symmetric around the vertical axis P1 = 0 as is observed in the model calculations. One possible cause for this fact is that the real molecular systems have a full three-dimensional structure, so that there may slight asymmetries in the relative orientation of driver and target [78].

2.2 DYNAMICAL RESPONSE FUNCTION: DRIVING THE CHARGE-TRANSFER VIA A TIME-DEPENDENT ELECTRIC FIELD

One of the crucial points in this technology is the way in which the computation procedure with QCA-cells can be started in a controllable way. In the initial implementations of the QCA paradigm external electric fields have been used to provide a write-in system (forcing an input status) and where non-invasive probe leads have been employed to record the final results of this process [12]. Thus, in a realistic experimental set-up for the m-QCA implementation can be expected that this write-in system also implies the use of external electric fields. Recently, many experimental alternatives have been suggested in which these fields have been used to force an input states (charge configuration within the molecular complex) and drive the intra-molecular charge transfer. From a theoretical viewpoint, this is a new perspective since the QCA-unit is not only exposed to a time-dependent electric field but also interacts with the environment via temperature [28].

2.2.1   Theoretical model

These new experimental setups pose a new theoretical scenario in which the static model previously developed is not accurate enough to represent the physical situation. Therefore, one can extend the model to a time-dependent picture using the corresponding time-dependent Schrödinger equation [5, 84]:

$$i\hbar \frac{\partial |\varphi(\mathrm{t}) >}{\partial \mathrm{t}} = \mathrm{H}|\Psi(\mathrm{t}) >, \tag{2.22}$$

In the specific case of a half-cell m-QCA, one can expand the wave-function $|\varphi(\mathrm{t}) >$ into a complete set of eigenstates $|\alpha >_{\mathrm{t}}$ for the two electrons occupying the

HOMO level. Now, assuming that the cell is exposed to a time-dependent electric external field, the polarization of the driver-cell changes in accordance to a prescribed interaction between the molecular complex and the field. At this point, one has to make a clear distinction between the diabatic and adiabatic basis set by stating that whereas the first one is used to characterize the electron localization at the donor or acceptor of the molecule (initial stages of the ET process) the second provides a description of the ground state of the system with more reliable results at the avoiding crossing region [85, 86, 87]. Thus, one can represent the time-dependent behavior of the wavefuntion by using an expansion like:

$$|\mathbf{\Psi}(t)> = \Sigma_\alpha c_\alpha(t)|\phi>_{a,b}, \qquad (2.23)$$

in which the two-model system can be written as:

$$H_{m,n}(t) = \begin{pmatrix} E_{aa}(t) & \gamma \\ \gamma & E_{bb}(t) \end{pmatrix}, \qquad (2.24)$$

Assuming that the ET (γ) matrix element is constant over time. The suggested model describes the interaction of the discrete HOMO or LUMO level with an external electric field source. In order to establish a link with the previous models, one can re-write the diabatic states (written in Eq. 2.2) as:

$$H_{aa} \quad = \quad \frac{e^2}{4\pi\varepsilon_0}\left(\frac{1}{2}\right)\left[(\frac{1}{L}-\frac{1}{\sqrt{L^2+d^2}})P_1(t)+(\frac{1}{L}+\frac{1}{\sqrt{L^2+d^2}})\right], \qquad (2.25)$$

$$H_{bb} \quad = \quad \frac{e^2}{4\pi\varepsilon_0}\left(\frac{1}{2}\right)\left[(\frac{1}{\sqrt{L^2+d^2}}-\frac{1}{L})P_1(t)+(\frac{1}{L}-\frac{1}{\sqrt{L^2+d^2}})\right]. \qquad (2.26)$$

Allowing to rewrite the total Hamiltonian as:

$$H_{m,n}(t) = \begin{pmatrix} AP_1(t)+B & V_{ab} \\ V_{ab} & CP_1(t)+D \end{pmatrix}, \qquad (2.27)$$

where all the geometrical factors from the molecule and the experimental setup are contained in the coefficients A,B,C and D. In many different scenarios a similar Hamiltonian can be written by employing the term $-E_z d_0 \sigma_z$ which describes the coupling of an electron with an external electric field [77]. Here, the E_z is the z-component (along the Donor-Acceptor axis) of the external electric field and $d_0 \sigma_z$ is the matrix representation of the electric dipole moment operator $\hat{d}_z$ with $d_0 = \frac{ed}{2}$ [88, 87]. By utilizing these definitions one can re-cast the diabatic states as:

$$H_{aa} \quad = \quad \frac{ed}{2}\left(\frac{e}{4\pi}\right)(\frac{1}{d})\left[(\frac{1}{L}-\frac{1}{\sqrt{L^2+d^2}})P_1(t)+(\frac{1}{L}+\frac{1}{\sqrt{L^2+d^2}})\right], \qquad (2.28)$$

$$H_{bb} \quad = \quad \frac{ed}{2}\left(\frac{e}{4\pi}\right)(\frac{1}{d})\left[(\frac{1}{\sqrt{L^2+d^2}}-\frac{1}{L})P_1(t)+(\frac{1}{L}-\frac{1}{\sqrt{L^2+d^2}})\right]. \qquad (2.29)$$
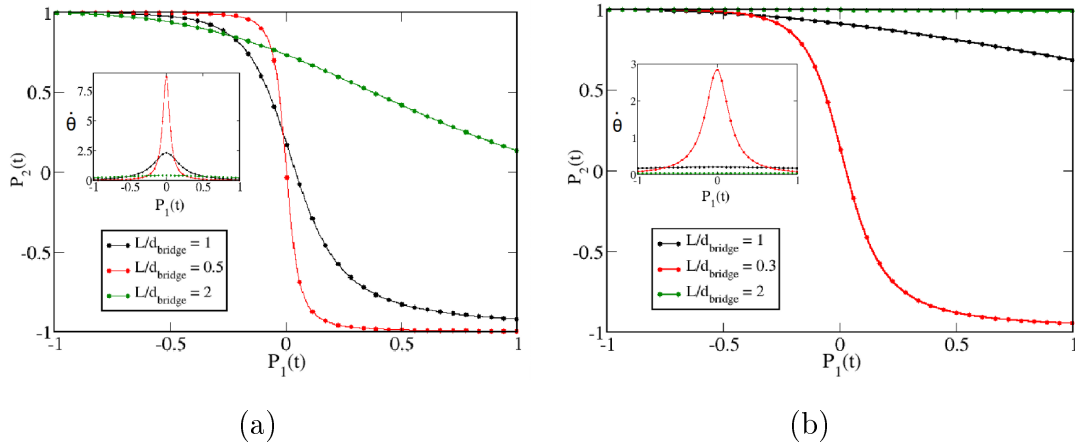
Figure 2.7: Dynamical response function of the target molecule for driver-target translations. Results for both, PNX n=3 and n=5 based molecules are shown. In all cases, the insets correspond to the non-adiabatic corrections $\dot{\theta}$. Driver-target separations are given in terms of the ratio L/d_{bridge}.

and for the symmetric case $(d = L)$, one can write the total Hamiltonian as:

$$H(t) = \gamma\sigma_x - d_0 E_z(t)\sigma_z, \tag{2.30}$$

Hence, it is worth to mention here that the Hamiltonian in Eq. 2.30 is written using the diabatic basis-set. The two adiabatic states, that are defined as the instantaneous eigenstate of the Hamiltonian are given by:

$$
\begin{aligned}
|\Psi_-(t)> &= \phi_1\cos(\theta(t)) - \phi_2\sin(\theta(t)), &\tag{2.31}\\
|\Psi_+(t)> &= \phi_1\sin(\theta(t)) + \phi_2\cos(\theta(t)). &\tag{2.32}
\end{aligned}
$$

Thus, the time evolution of the adiabatic states is derived from the mixing angle $\theta(t)$ making this basis-set time-dependent while the diabatic states are stationary solutions of the Hamiltonian [86]. The probability amplitudes of the diabatic and adiabatic bases are connected via a unitary transformation in 2-d that can be written in terms of the Euler-angles as:

$$\mathbf{U} = \begin{pmatrix} \cos(\theta) & -\sin(\theta) \\ \sin(\theta) & \cos(\theta) \end{pmatrix}, \tag{2.33}$$

in which the amplitudes of diabatic (c) and adiabatic (a(t)) bases can be recast as:

$$c = \mathbf{U}(\theta(t))a(t), \tag{2.34}$$

where $a(t) = [a_-, a_+]^T$ are the probability amplitudes of the adiabatic states $|\Psi_-(t)>$ and $|\Psi_-(t)>$, respectively. Since the initial state is described using the

diabatic basis-set then the truly adiabatic ground-state is obtained by repeatedly employing the unitary transformation at every single time-step of the propagation. Therefore, one has to re-write the TDSE in terms of this unitary transformatio as:

$$i\hbar\frac{\partial U\Psi(t)}{\partial t} = i\hbar(U(t)\frac{\partial\Psi(t)}{\partial t} + \frac{\partial U(t)}{\partial t}\Psi(t)), \qquad (2.35)$$

Assuming that $i\hbar\frac{\partial\Psi(t)}{\partial t} = H(t)U(t)\Psi(t)$, one can re-cast the dynamical Hamiltonian as:

$$i\hbar\frac{\partial\Psi}{\partial t} = D(t)\Psi(t) - i\hbar U^{-1}(t)\frac{\partial U(t)}{\partial t}\Psi(t), \qquad (2.36)$$

where $D(t) = U^{-1}(t)H(t)U(t)$. Interestingly, one can observe that a new term $(U^{-1}(t)\frac{\partial U(t)}{\partial t})$ is calculated and related with the dynamical diagonalization of the Hamiltonian that mixes the diabatic electronic states. The importance of this derivation relies on the fact that now one has a quantity that accounts for the limit in which the static model can be used. At this point, one can use a similar methodology than the Jacobi eigenvalue algorithm [89, 90] and obtain a relationship for the angle $\boldsymbol{\theta}$ of the unitary transformation matrix as:

$$\tan\boldsymbol{\theta} = \frac{2\boldsymbol{\gamma}}{E_a - E_b}, \qquad (2.37)$$

Thus, the static model can be used and propagated once the variation of the diaganolization angle as a function of time is either small compared with the adiabatic eigenvalues or vanishes. Hence, the ratio in which the $\boldsymbol{\theta}$ parameter changes over time is analytically obtained as:

$$\dot{\boldsymbol{\theta}} = -\frac{2\boldsymbol{\gamma}}{(E_+(t) - E_-(t))^2}\frac{dE_z(t)}{dt}, \qquad (2.38)$$

where $\boldsymbol{\gamma}$ is the electronic coupling, $E_\pm$ are the adiabatic energies and $\frac{dE_z(t)}{dt}$ is the rate in which the electric field is changed over time [86]. Finally, the Hamiltonian can be written as a system of coupled differential equations in the adiabatic basis-set of the form:

$$i\hbar\frac{d\Psi_-}{dt} = E_-\Psi_- + \frac{i\hbar\dot{\boldsymbol{\theta}}}{2}\Psi_+, \qquad (2.39)$$

$$i\hbar\frac{d\Psi_+}{dt} = E_+\Psi_+ - \frac{i\hbar\dot{\boldsymbol{\theta}}}{2}\Psi_-. \qquad (2.40)$$

and numerically solved employing a Runge-Kutta 4 numerical scheme. As initial condition, the occupation probability has been selected to depict perfect localization

at the Donor site while the Acceptor contains no population. In this case, the studied γ parameters belong to the PNX (organic implementation) with n=3 and n=5 bridges molecular complexes. These two molecules have been synthesized and both exhibit charge-carrier localization either at the donor and acceptor groups, respectively [91, 92]. The results of the simulations with the minimal model are displayed in Fig. 2.7 where the response-function ($P_2 = 2|c_-|^2 - 1$) and the $\dot{\theta}$ parameter are studied as a function of the linear external electric field. In this new scenario in which the electric field is linearly changing over time ($P_1(t) = t$) and resembling the Landau-Zener model (L-Z) [93, 94]. The computed results indicate that the switching mechanism is preserved once a specific ratio between the target-driver distance and the intramolecular donor-aceptor length has been reached. Thus, this quantity defines the strength of the external electric field at which the resonance process occur. As expected, the stronger non-linear behavior is observed in the PNX n=5 molecular complexes while in the case of PNX a ratio or 0.3 is needed to achieve the S-shape form of the response function. Interestingly, the ET process from this dynamical perspective can be described as a consequence of the non-linear increment in the non-adiabatic correction term (see insets in Fig. 2.7) in the region near where the anticrossing of the adiabatic energy levels happens indicating the important role of non-adiabaticities in the ET intramolecular process. Conceptually, the Landau-Zener model [93, 94] offers a powerful description in which one can understand the behavior of the system in terms of the internal time of the molecular complex ($\tau_{\text{internal}} = \frac{\gamma}{\hbar}$) and the external time ($\tau_{\text{ext}} = \frac{(E_+ - E_-)}{\hbar}$) supplied by the electric field [95]. Thus, since the external electric field is driving the system through an anticrossing regime with a sweep velocity ($\frac{dE}{dt}$) the adiabatic crossing will be obtained only when the condition $\tau_{\text{external}} >> \tau_{\text{internal}}$ is fulfilled leading to the conditions needed to invoke the Quantum-Adiabatic Theorem [86].

Beyond Landau-Zener model: Towards realistic time-dependent electric-field profiles

In order to study a plausible scheme for a controllable Landau-Zener tunneling in a molecule one can propose the use of different electric-field profiles that will provide different sweep velocities and therefore increasing o decreasing the probability to obtain an adiabatic ET process [82, 83]. To achieve this goal, it is worthwhile to study different electric pulses with different shapes but making them also close to experimental pulses [96]. Hence, in this section a set of three non-linear pulses have been selected with the following mathematical description:

- $E_z = E_0 e^{-\frac{t^2}{2\tau^2}}$

- $E_z = E_0 \text{Cos}(\omega t)$

- $E_z = E_0 \text{Tanh}(\omega t)$

where ω is the corresponding frequency of the pulse (trigonometric functions) and τ is the characteristic time of the pulse in the Gaussian pulse. The different profiles are presented in Fig. 2.8(a) including the shape and duration of the pulse. The obtained results indicate that the choice of a pulse strongly affects the non-linear response of the molecular complexes regardless the magnitude of the γ parameter. This is clearly observed in the case of the Exponential pulse, in which the switching behavior is diminished in either of the studied complexes (solid and dashed black
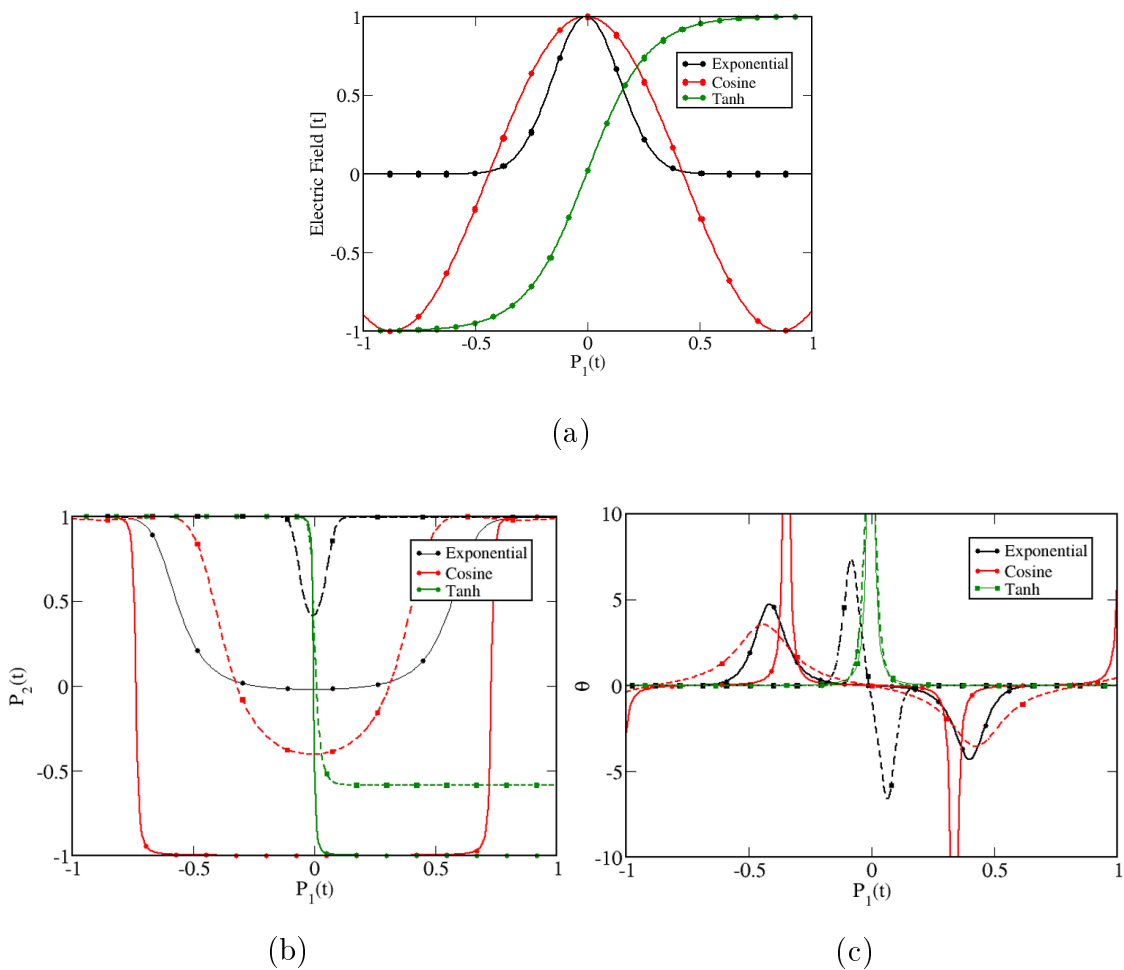
(a)

(b)   (c)

Figure 2.8: Dynamical response function of the target molecule for different electric field profiles. Results for both, PNX n=3 (dashed lines) and PNX n=5 (solid lines) molecules are shown. (a) Three different electric-field profile are used to investigate the switching process. (b) Response function for both molecules and different profiles. (c) Nonadiabatic corrections for both molecules and the different electric field profiles. In both cases, the L/d_{bridge} ratio in which the S-shaped switching behavior is obtained (see Fig. 2.7) has been used for these calculations.

lines in Fig. 2.8(b)). Concerning the Cosine pulse, one can observe that the switching is preserved in the PNX n=5 molecule while in the PNX n=3 an incomplete ET process is reported (solid and dashed red lines in Fig. 2.8(b)). This effect can be also understood in terms of the magnitude of the nonadiabatic term where one can clearly observe a stronger effect in the PNX n=5 molecule (red solid) when compared with the PNX n=3 complex (red dashed) (see Fig. 2.8(c)). Likewise, the pulses (a) and (b) exhibits a leading and trailing edges that pass through the anticrossing points where the adiabatic approximation breaks down and the system undergoes transitions between the ground and excited states via the L-Z mechanism. In connection to this effect, the $\dot{\theta}$ parameter, that accounts for the non-adiabaticity of the system, displays two peaks one upwards and one backwards that are directly related with the process of HOMO-LUMO hybridization and the double switching pattern observed in the response function. This can ascribed to the symmetric shape of the pulse the transition probabilities at the times where the resonant external
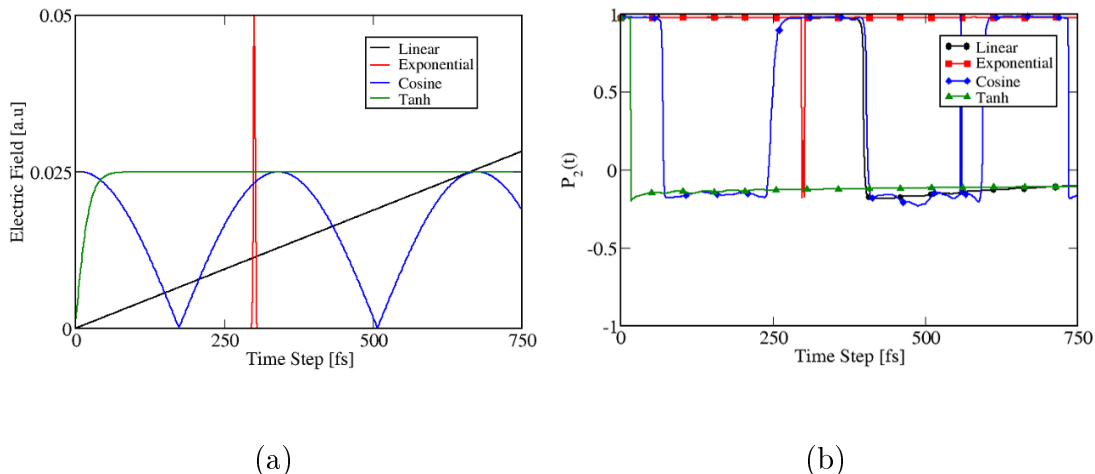
(a)	(b)

Figure 2.9: Electric field profiles (a) and Dynamical response function (b) of the PNX molecule for n = 3 bridge computed with ab-initio molecular dynamics. The insets display the different profiles used for the simulations (Linear, Exponential, Cosine and Tanh) and the response function of the molecule defined as $P_2(t) = 2|C_{Homo}(t)| - 1$ where C_{HOMO} indicates the occupation number of the corresponding molecular orbital.

electric field is achieved as is shown in Fig. 2.8(b) while the nonadiabatic term displays a reverse behavior at the same two times. Finally, the Tanh pulse presents better results to be suggested as a controllable L-Z scheme since in both cases the single switching behavior is preserved (solid and dashed green lines in Fig. 2.8(b)) and the nonadiabatic term is placed at the minimum of the anticrossing of the adiabatic energies in both cases. In conclusion, one can state that the quest for looking to a suitable candidate to implement the m-QCA should not be only focused in the minimization of the ET (γ) parameter but also to consider the shape and sweep rate of the external electric field that forces the first input in the device.

2.2.2   Validating the minimal model: First-principle calculations

In order to validate the results of the model, First-principle calculations have been carried out for the PNX molecular complex in the case of n = 3, 5 bridge-extension. The dynamical nature of the electric-field has been simulated by coupling the time-dependence of the external electric-field with the time-step of the ab-initio molecular dynamics as implemented in the DFTB+ code [57, 80, 81, 59]. Moreover, an in-house extended version of the mentioned code has been created where many different electric field profiles such as the ones used in the L-Z model can be utilized [61, 97]. All simulations have been performed at T = 30 K and the molecules have been previously thermal-equilibrated to this temperature during a period of time of 1 ns. Subsequently, an external electric field has been turned on with different electric field profiles, namely, linear, Gaussian, Tanh and Cosine and allowed to interact with the PNX molecular complex. The results of these calculations are displayed in Fig. 2.9 (n=3) and Fig. 2.10 (n=5). Hence, one can observe that for the short-bridge case one can obtain a partial switching behavior of $P_2(t) \simeq -0.2$ for all different external electric-field profiles. In the specific case of the linear profile, one can observe the corresponding S-shape behavior observed in the L-Z model
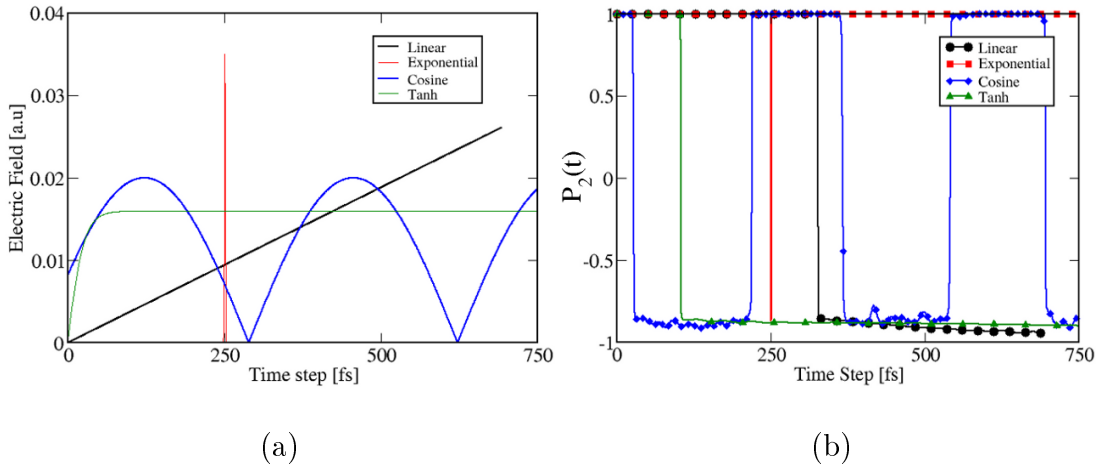
|(a)|(b)|

Figure 2.10: Electric field profiles (a) and Dynamical response function (b) of the PNX molecule for n = 5 bridge computed with ab-initio molecular dynamics. The insets display the different profiles used for the simulations (Linear, Exponential, Cosine and Tanh) and the response function of the molecule defined as $P_2(t) = 2 * |C_{Homo}(t)| - 1$ where C_{HOMO} indicates the occupation number of the corresponding molecular orbital.

around the resonance field. Concerning the exponential and cosine profiles, the charge transfer is achieved for a few femtoseconds (exponential) or for longer period of times (cosine) depending on the duration of the pulse and its periodicity. Finally, the Tanh profile offers an interesting case in which the switching is fast achieved and is constantly maintained along the molecular dynamics trajectory. In all cases the discrepancies between the minimal model and the ab-initio calculations can be ascribed to the fact that for higher external electric fields needed to produce the perfect switching behavior leads to a dissociation of the molecular bonds and therefore destroying the molecular complex. Concerning the long-bridge molecule (n=5), one can observe similar trends as in the previous case but a much more stable behavior of the switching response in all the electric-field cases and therefore leading to a most stable response function. Finally, one can conclude that the profile of the external electric field plays an important-role in the response behavior offering an efficient way to control the intra-molecular charge transfer process necessary to successfully implement this technology.

2.2.3   Vibrionic effects in the charge transfer process

In general terms one has to consider the solution of the full Schrödinger equation for a molecular system in which both electrons and nuclei are present. Usually, in order to simplify this problem one resorts in the Born-Oppenheimer approximation that implies the separation of the total Hamiltonian into electronic and nuclear equations. Thus, once the approximation has been employed this implies that one can solve the electronic Schrödinger equation and obtain the electronic energies $E_i = \langle \Psi(r) | \hat{H}_r | \Psi(r) \rangle_r$ and the associated electronic wave functions $\Psi_i(r)$ disregarding the nuclear wavefunction term. However, one has to recall that the total wavefunction of the system contains both the electronic and the nuclear degrees of freedom and therefore these two quantities depend not only explicitly on the

N-electronic coordinates $\vec{r} = (r_1, r_2...., r_N)$ but also parametrically on the N_I coordinates of the corresponding I nuclei with associated coordinates $\vec{R} = (R_1, R_2, ..., R_I)$ [85, 98]. Hence, the total Hamiltonian including the nuclear terms can be written as:

$$\hat{H}_{total}(\vec{r}, \vec{R}) = H_{BO}(\vec{r}, \vec{R}) + \hat{T}_N(R) + \hat{V}_{N-N}(\vec{R}, \vec{R}'), \qquad (2.41)$$

with

$$H_{BO}(\vec{r}, \vec{R}) = \hat{T}_e(\vec{r}) + \hat{V}_{e-e}(\vec{r}, \vec{r}') + \hat{V}_{e-N}(\vec{r}, \vec{R}), \qquad (2.42)$$

where the potential energy terms are related with the electron-electron repulsion by $\hat{V}_{e-e}(\vec{r}, \vec{r}')$, the electron-nuclear attraction $\hat{V}_{e-N}(\vec{r}, \vec{R})$, the nuclear-nuclear repulsion $\hat{V}_{N-N}(\vec{R}, \vec{R}')$, the $T_N(\vec{R})$ term refers to kinetic energy of the nuclei and $\hat{T}_e(\vec{r})$ is the electron kinetic energy. In the case where there is no external time-dependence in the Hamiltonian, the $H_{BO}(\vec{r}, \vec{R})$ term of the total Hamiltonian 2.41 is the "Adiabatic Born-Oppenheimer" (ABO) set of equations. Therefore, the electronic Hamiltonian depends parametrically on the nuclear coordinate R via the electron-nuclear interaction. The corresponding stationary Schrödinger equation is a solution of the problem at every fixed nuclear configuration $\vec{R}$ and can be recast as:

$$\hat{H}_{BO}(\vec{R})\phi_{\vec{R}}^j(\vec{r}) = \varepsilon_{BO}^j(\vec{R})\phi_{\vec{R}}^j(\vec{r}), \qquad (2.43)$$

which provides with a set of eigenvalues parametrically depend on the nuclear coordinate $\vec{R}$. Hence, assuming that $\Phi_{BO}(r, R, t) \simeq \phi_{\vec{R}}^j(\vec{r})\chi_{j\nu}^{BO}(\vec{R})$ one can write the nuclear ABO Schrödinger equation as:

$$[T_N(\vec{Q}) + \varepsilon_{BO}^j(\vec{Q}) + <\phi_j|T_N|\phi_j> - E_{total}]\chi_{j\nu}(\vec{Q})$$
$$+ \sum_{i \neq j} [<\phi_j|T_N|\phi_i>_r - 2\sum_\kappa \frac{\hbar^2}{2} <\phi_j|\frac{\partial}{\partial Q_\kappa}|\phi_i>_r \frac{\partial}{\partial Q_\kappa}]\chi_{i\nu}(\vec{Q}) = 0, \quad (2.44)$$

where the subindex r indicates integration over the electronic coordinates only. The nuclear coordinates have been transformed to the mass weighted nuclear coordinates given by the expression

$$\vec{R} = \vec{R_0} + M^{-\frac{1}{2}}\vec{A}\vec{Q}, \qquad (2.45)$$

where R and R_0 are $(3N - 6)$-dimensional column vectors of the instantaneous and equilibrium Cartesian coordinates, respectively, associated with the nonzero frequency normal modes. M is the $(3N - 6) \times (3N - 6)$ mass-weighted matrix, A is an orthogonal transformation employed to diagonalize the mass-weighted Hessian (in

Cartesian coordinates) constant matrix, and Q is the dimensionless normal coordinate vector [98]. Once the off-diagonal coupling has been neglected, one can recast the Schrödinger equation as:

$$[T_N(\vec{Q}) + \varepsilon_{BO}^j(\vec{Q}) + <\phi_j|T_N|\phi_j>]\chi_{jv}(\vec{Q}) = E_{jv}\chi_{jv}(\vec{Q}),\qquad(2.46)$$

yielding to a complete and orthonormal set for the electronic states and parametrically depending on the nuclear coordinate Q. Finally, if one neglects the diagonal correction term of the last Hamiltonian (i.e $<\phi_j|T_N|\phi_j>=0$) then one arrives to the known ABO potential energy surfaces that can be obtained with ab-initio methods.

2.2.4   Quasi-static potential energy surfaces

In the previous theoretical studies the motion of one electron as it migrates between the Donor and Acceptor moieties has been perused in order to clarify the role played by different factors such as geometrical distortions or the external electric field profile in the performance of the m-QCA cell. However, the implications in the intramolecular charge transfer process in the vibrational wavefunction ascribed to the two charge localization centers has been disregarded by implicitly assuming the Born-Oppenheimer approximation. Hence, in order to study the impact of this interaction one has to include the vibration of the nuclei and their interactions with the electrons within the molecular complex. The extended model suggested here describe a substantial different situation in which the potential in which the nuclei vibrate is created by the driven electron transfer process and not by the small displacements along the normal coordinate. Therefore, this model is intended to study the nuclei behavior when is subject to this instantaneous electronic potential created by the interaction of the charge-carrier and the external electric field and coupled to the nuclear movement by the electron-vibration interaction. Hence, the Hamiltonian that describes this situation can be written as:

$$\hat{H}_Q^{Total}(\vec{r},t) = \hat{H}_Q^{BO}(\vec{r}) + \hat{V}_{ef}^e(\vec{r},t),\qquad(2.47)$$

where the time dependent term $\hat{V}_{eef}(\vec{r},t)$ refers to the time-dependent external-electric field that and exclusively affecting the electrons. Thus, this Hamiltonian defines a set of eigenenergies which can be written as:

$$\hat{H}_Q^{Total}(\vec{r},t)\Psi_{i,Q}^{QS}(\vec{r},t) = \varepsilon_i^{QS}(Q,t)\Psi_{i,Q}^{QS}(\vec{r},t),\qquad(2.48)$$

and whose eigenvalues $\varepsilon_i^{QS}(Q,t)$ are dynamical and parametrically dependent on the normal mode Q [99]. In order to solve this equation, one can define a time-dependent basis set that provides the instantaneous eigenstates of the instantaneous total Hamiltonian and that can be written as:

$$\Psi_Q^{QS(i)}(\vec{r},t) = \sum_i^N c_i^{QS}(Q,t)\psi_{i,Q_0}^{CA}(\vec{r}),\qquad(2.49)$$
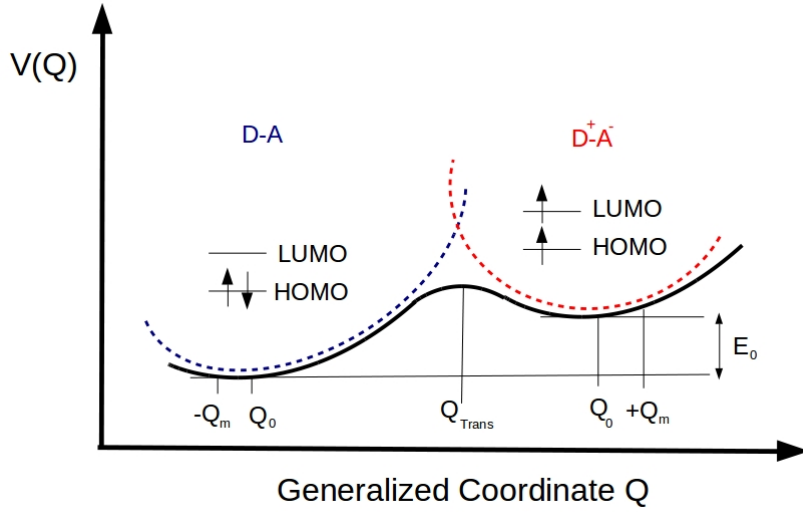
Figure 2.11: Schematic representation of the general two-state charge transfer process. At the starting point of the ET process a diabatic state with a neutral Donor and Acceptor electronic configuration is displayed (blue dashed line). Once the ET process has happened the second diabatic state (red dashed line) displays the new potential energy surface induced by the dynamical change of the electronic levels. The important quantities that are considered in this model are the equilibrium position for each diabatic state (Q_0), the energy difference to active the process E_0 and Q_m is a displacement along the chosen normal mode Q and placing the two diabatic harmonic potentials at different nuclear geometries.

where $\psi_{Q_0}^a(\vec{r})$ represents the spatially localized crude-adiabatic (CA) diabatic states $|\psi_L^{CA}(\vec{r}, Q_0)>$ at a given molecular geometrical configuration so that the eigenvalues and eigenenergies of the eqn (2.47) can be recast as:

$$\begin{pmatrix} < \phi_{1,Q_0}^{CA}|\hat{H}_Q^{Total}(\vec{r},t)|\phi_{1,Q_0}^{CA} > & \cdots & < \phi_{1,Q_0}^{CA}|\hat{H}_Q^{Total}(\vec{r},t)|\phi_{i,Q_0}^{CA} > \\ \vdots & \ddots & \vdots \\ < \phi_{i,Q_0}^{CA}|\hat{H}_Q^{Total}(\vec{r},t)|\phi_{1,Q_0}^{CA} > & \cdots & < \phi_{i,Q_0}^{CA}|\hat{H}_Q^{Total}(\vec{r},t)|\phi_{i,Q_0}^{CA} >) \end{pmatrix} \begin{pmatrix} \vec{c}_1^{QS} \\ \vdots \\ \vec{c}_i^{QS} \end{pmatrix} = \varepsilon_i^{QS} \begin{pmatrix} \vec{c}_1^{QS} \\ \vdots \\ \vec{c}_i^{QS} \end{pmatrix},$$

Thus, this new diabatic basis-set represents not only the localized electron wavefunctions but also a reference static configuration which can represent accurately the initial and final stage of the ET process [100].

2.2.5   Theoretical model

In order to investigate this physical situation, one can extend the suggested two-state Hamiltonian in which one electron is localized either at the Donor or Acceptor sites of the molecule and allowed to instantaneously interact with the corresponding
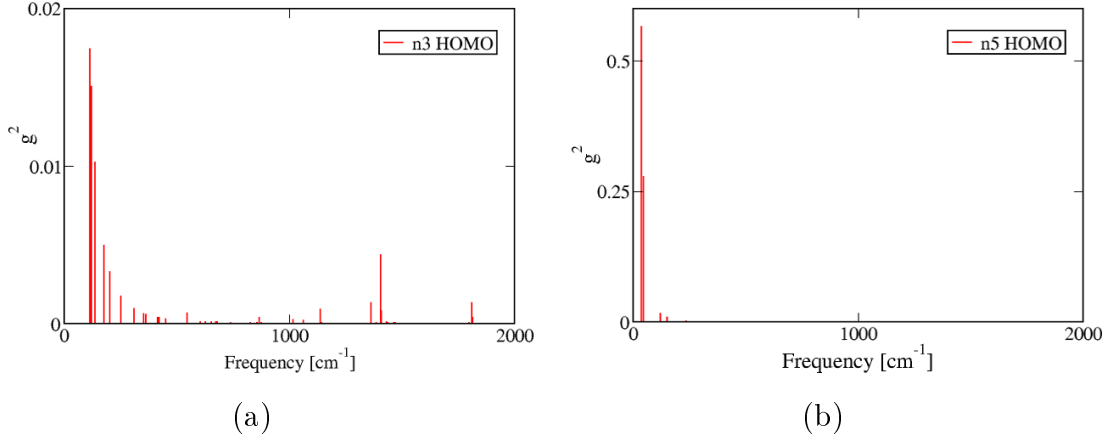
Figure 2.12: Squared electron-vibration coupling constant (HOMO) plotted versus vibration frequency (a) n=3 and (b) n=5 PNX molecular complexes.

vibrational mode. Thus, the corresponding Hamiltonian in matrix form can be written as:

$$
H_{a,b}^{CA}(Q,t) = \begin{pmatrix} H_{aa}^{CA}(Q,t) & H_{ab}^{CA}(Q,t) \\ H_{ab}^{CA}(Q,t) & H_{aa}^{CA}(Q,t) \end{pmatrix}, \tag{2.50}
$$

and whose matrix elements are given by the following expressions in the CA basis set:

$$
H_{aa}^{CA}(Q,t) = \frac{\hbar\boldsymbol{\omega}}{2}(Q+Q_m)^2 - \frac{\hbar\boldsymbol{\omega}}{2}\frac{\partial^2}{\partial Q^2} - d_0 E_z(t), \tag{2.51}
$$

$$
H_{bb}^{CA}(Q,t) = \frac{\hbar\boldsymbol{\omega}}{2}(Q-Q_m)^2 - \frac{\hbar\boldsymbol{\omega}}{2}\frac{\partial^2}{\partial Q^2} + E_0 + d_0 E_z(t), \tag{2.52}
$$

$$
H_{ab}^{CA}(Q,t) = H_{ba}^{CA}(Q) = \boldsymbol{\gamma}. \tag{2.53}
$$

where Q represents the chosen (antisymmetric mode) dimensionless normal mode, Q_m is a displacement that locates the two harmonic potentials at different nuclear geometries, $\boldsymbol{\omega}$ is the vibration frequency of the harmonic diabatic oscillators and E_0 represents the energy change in the ET process an calculated as defined in [101]. The Hamiltonian written in the Crude Adiabatic (CA) basis-set is a good alternative to investigate the coupling between the charge-carrier and the the associated normal mode using the electronic localized basis set (diabatic) [100]. Thus, under these assumptions, one can obtain the one-dimensional vibrational wavefunctions describing the ET process on the adiabatic electronic energy as the corresponding Schrödinger equation:

$$
\left(-\frac{\hbar\boldsymbol{\omega}}{2}\frac{\partial^2}{\partial Q^2} + W_{ii}(r,Q,t) \right)\boldsymbol{\chi}_{nt}(Q) = \boldsymbol{\varepsilon}_Q(r,t)\boldsymbol{\chi}_{nt}(Q), \tag{2.54}
$$

where

$$W_{ii}(r, Q, t) = \frac{E_0}{2} + \frac{\lambda}{4} + \frac{\hbar\omega}{2}Q^2 \pm \sqrt{(-\frac{E_0}{2} + d_0E_z(t) - Q_mQ)^2 + \gamma^2}. \qquad (2.55)$$

and $\lambda = 2\hbar\omega Q_m^2$ is the reorganization energy, γ is the coupling between the electronic diabatic states (CA) and r represents the electronic coordinate. The $W_{ii}(r, Q, t)$ term represents the potential created by the associated Harmonic diabatic oscillator and the external electric field. In order to calculate numerically the reorganization energy, one can resort in the linear approach where a Taylor expansion in the molecular electronic levels is carried out [102]. In this case, the expansion will be formulated in terms of the vibrational coordinates Q_i, where i denotes the mode vector allowing to write the energy as:

$$E = E_0 + \sum_{i=1}^{N} x_i \frac{\partial E(Q)}{\partial X_i} + \cdots , \qquad (2.56)$$

Generally, as a first approximation one can assume that the first order correction is the most important contribution and allowing to write the dimensionless electron-vibration coupling as:

$$g = \frac{\hbar}{\sqrt{2}(\hbar\omega_i)^{\frac{3}{2}}} \frac{\partial E(Q)}{\partial X_i}. \qquad (2.57)$$

The electron-vibration couplings for the two molecules PNX with bridges n=3 and n=5 have been calculated using an in-house developed script based on the DFTB+ code and the results presented in Fig. 2.12. Once the couplings have been obtained the solution of the vibrational Schrödinger equation is carried out by employing the Fourier grid Hamiltonian method with 256 grid points along the mass-weighted normal coordinate Q [86]. The results of these calculations are displayed in Fig. 2.13 and Fig. 2.14 for the molecules n=3 and n=5, respectively.

Thus, for both PNX molecular complexes, one can see that in the case of a $E(t) = -0.05, 0.05$, i.e., before and after the resonance field (Fig 2.13 and Fig 2.14 (a,c)) the vibrational mode is localized at one of the most protruding minima of the adiabatic potential energy surface. This issue can be ascribed to a vibrational trapping effect for the associated wavefunction state that is more visible in the case of the longer bridge (n=5) when compared to the short bridge case (n=3). Concerning the resonance field case, for both complexes, one can observe the appearance of a bistability behavior in the adiabatic potential energy surface and a delocalization effect of the total vibrational wavefunction which is stronger in the n=5 than in the n=3 case. This indicates that once the electric field pulse has achieved the resonance value where the ET process occurs, the associated adiabatic potential energy surface displays a double-well structure that hybridizes the Donor and Acceptor vibrational wavefunctions allowing the electron to be transfered from one vibrational diabatic state to the other. This issue can be understood in terms of the delocalization of total vibrational wavefunction over the complex leading to an effective reduction of the electron trapping effect and therefore opening an instantaneous channel in which the diabatic vibrational modes associated to the Donor and Acceptor sites are degenerated. Finally, one can state that despite the fact that the normal mode that facilitates the electron transfer within the complex was not the strongest coupled at zero electric field, the continuous change of the time-dependent electric-field alters the geometry reference point and creates the conditions to enhance this precise electron-vibration coupling for this given mode and easing the ET process.
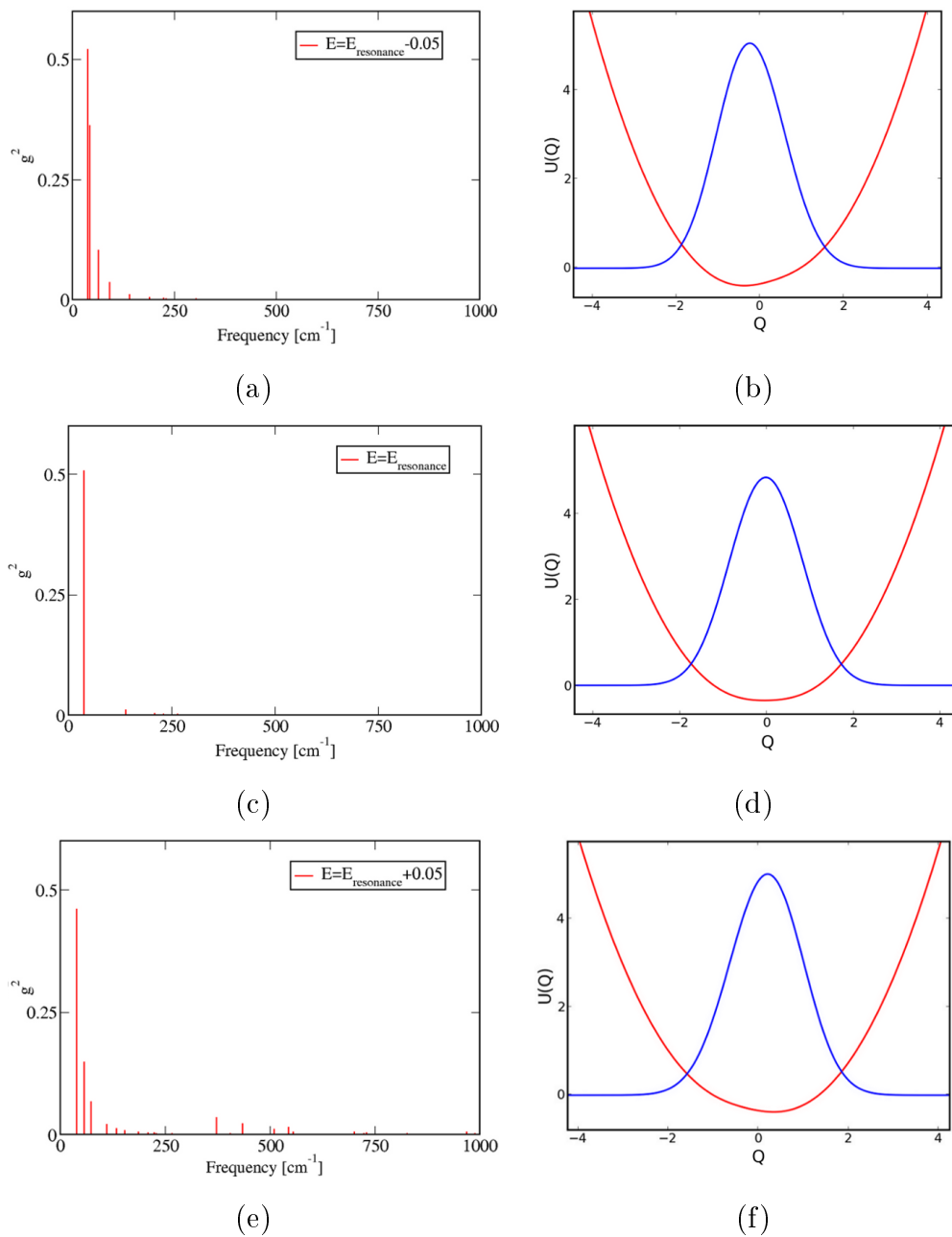
(a)   (b)

(c)   (d)

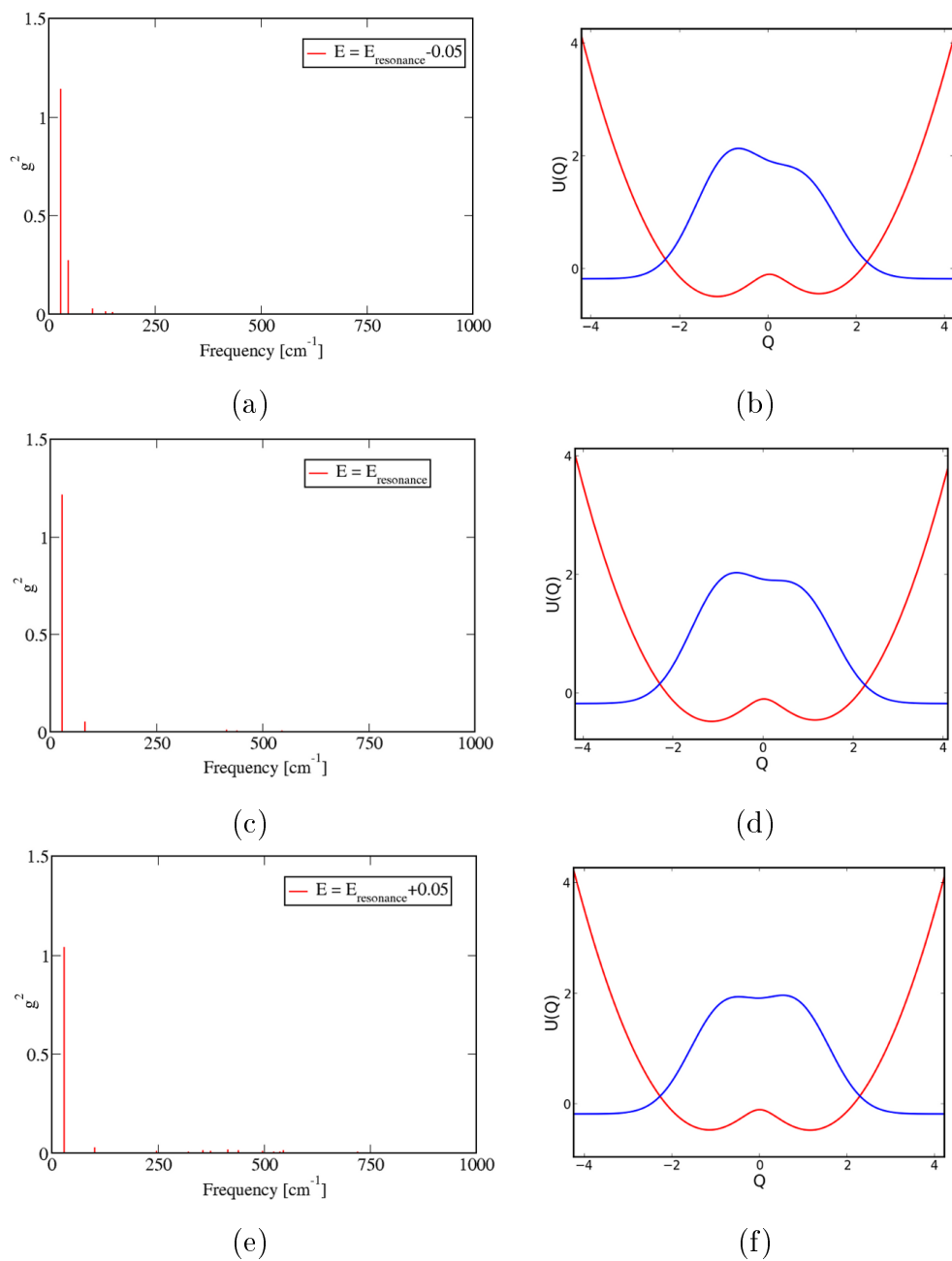(e)   (f)

Figure 2.13: Square electron-vibration coupling (a,c,e) and vibrionic wavefunction with the associated adiabatic potential energy surface (PES) (b,d,f) for the case of PNX n=3 when the electric field values are at (a,b) $E_z(t)=E_{Resonance}-0.05$. (c,d) $E_z(t)=E_{Resonance}$, (e,f) $E_z(t)=E_{Resonance}+0.05$.

Figure 2.14: Square electron-vibration coupling (a,c,e) and vibrionic wavefunction with the associated adiabatic potential energy surface (PES) (b,d,f) for the case of PNX n=5 when the electric-field values are at (a,b) $E_z(t)=E_{Resonance}-0.05$. (c,d) $E_z(t)=E_{Resonance}$, (e,f) $E_z(t)=E_{Resonance}+0.05$.

3 GUANOSINE-BASED QCA: SELF-ORGANIZATION AND LOCALIZATION OF CHARGE

In this chapter a systematic study of a Guanosine-based family of molecular complexes is carried out in order to determine the possibility to implement the m-QCA paradigm. Hence, in section (3.1) the electronic structure properties of the isolated molecules are investigated in order to assess the plausibility to represent information via the allocation of classical binary states to specific localized molecular orbitals. In section (3.2), the electronic properties of the molecules are further investigated by explicitly constructing the two-dimensional Hydrogen-bonding scaffolds. In section (3.3), the interaction amid molecule and surface is perused so as to examine the impact in the total electronic structure of the molecular complexes when those are absorbed on a Highly Ordered Pyrolytic Graphite (HOPG) surface. At this point a comparison with experimental STM images is carried out in order to assess the accuracy of the computed results. Finally, the synthesized complexes have been investigated at room temperature by employing ab-initio molecular dynamics (AIMD) calculations where the trajectories have been analyzed using statistical tools in order to assess the mechanical stability of the supramolecular network formed by the Hydrogen bonding.

3.1 MOLECULAR BUILDING BLOCKS

The implementation of a successful m-QCA unit must fulfill two criteria. Firstly, the electronic charge must be localized on specific sites of the molecule in order to clearly assign the corresponding molecular orbitals to well defined binary states. Secondly, the molecular complex should offer the possibility to obtain electronic bistable states via intra-molecular charge transfer, so as to ensure computation capability of the cell [5]. Nonetheless, a more active role must be played by the candidate molecular complexes in order to achieve the ultimate goal of a fully functional device. In fact, the intercell Coulomb interactions among unit cells should be promoted since the propagation of information is achieved via this force.
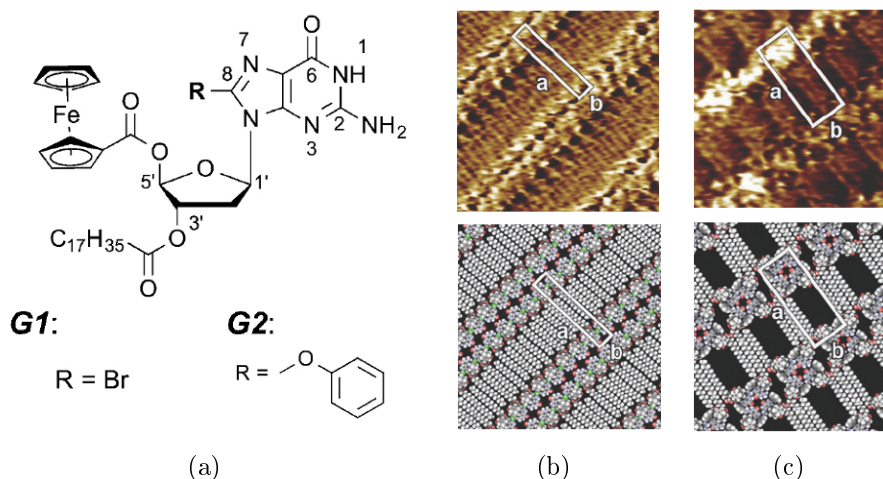
Figure 3.1: Schematic of the guanine synthesized derivatives.(a) Molecular building block including a Ferrocene molecule, sugar moiety an guanine groups.(b) Possible functionalizations, namely, a Bromine atom (G1) or a Phenyl ring (G2) which are attached at the R position of the molecule.

Thus, within this frame, a correct functionalization of the potential molecular candidates plays a fundamental role both to enhance electronic localization and to optimize the inter-cell Coulomb interaction between neighboring cells. The possibility to fulfill these conditions can be achieved by a targeted synthetic design in which the production of conformationally rigid and structurally stable organic building blocks is combined with the appending of charge-container moieties such as the Ferrocene complex [103, 104]. Moreover, to ensure a close interaction between Ferrocene groups the complexes have been functionalized with Guanine moieties to enhance the formation of supramolecular Hydrogen-bond networks [105]. In this manner, the experimental partners associated with the MOLARNET project have successfully synthesized a family of Ferrocene appended Guanine molecular complexes and the two plausible synthesized candidates are displayed in Fig. 3.1 [103]. Hence, it is expected that the presence of the long carbon chains connected to the sugar unit promotes the physisorption on the Highly Ordered Pyrolitec Graphite (HOPG) and therefore avoiding strong interactions with the surface via chemisorption processes that implies possible charge transfer process that possibly will distort the desired electron localization properties [106].

3.1.1 Methodology

To study the electronic, optical properties and perform a vibrational analysis density functional theory (DFT) has been employed as implemented in the Gaussian 09 all-electron code [107]. The B3LYP hybrid exchange-correlation functional has been used in order to optimize the gas-phase molecular structures of the G1 and G2 organometallic complexes [42, 108]. The basis-set employed is a combination of the Lanl2DZ effective core basis set for the iron atom and the $6-311$+G(d,p) basis set for C/H/N/O/Br [109, 110]. Notice that this is an extension from the usual LACVP(d) basis set due to the strong electronegative nature of the Bromine atom. The default cut-offs have been used in the optimization process and the Berry algorithm selected using the redundant internal coordinates for both cases.
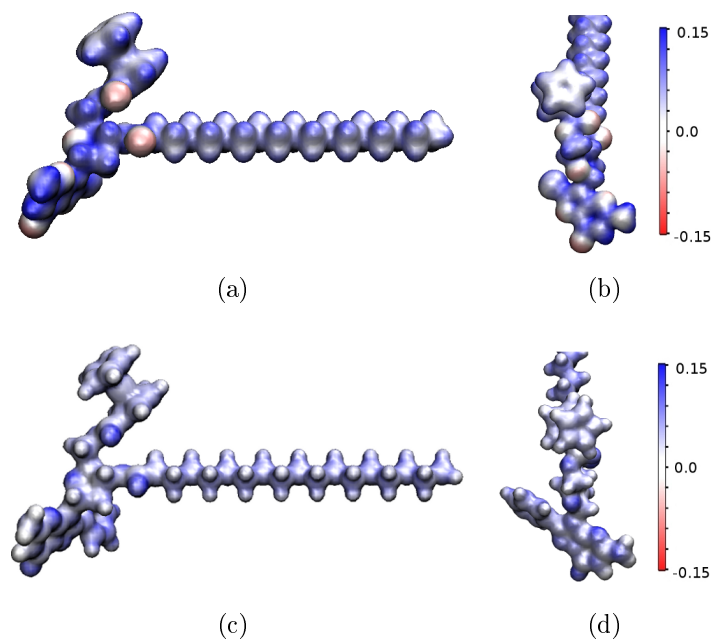
Figure 3.2: Molecular electrostatic potential (MEP) plotted onto the electronic density at the equilibrium geometry for G1 (a,b) and G2 (c,d). The colored contour plot graphic indicates the regions within the molecule where an excess (red) or depletion (blue) of electrons is spotted. All isosurfaces have been plotted at 0.02 e$^-$ Å^{-3}.

For each molecular complex a subsequent vibrational analysis has been performed after the optimization process in order to corroborate whether the energy-minimized structures are in a true local minima in its corresponding potential energy surface. In a second step, the CP2K software has been employed in order to study the experimentally observed motifs and their corresponding unit cells formed by the G1 and G2 molecular complexes [111]. The change in the employed software is necessary due to the large number of atoms needed within each unit cell to represent the measured results. The previous optimized single molecule structures have been used in order to construct the non-covalently linked scaffolds. In all cases, the calculations have been carried out using the BLYP exchange-correlation (XC) functional [41]. The valence electrons are treated by a double-zeta Gaussian basis set, while the core electrons have been averaged by the corresponding norm-conserving pseudopotentials of the Goedecker-Teter-Hutter type [112, 113, 114, 115]. Van-der-Waals interactions have been included through the standard Grimme's D3 approximation [49]. The energy cutoff for the plane wave expansion of the density is set to 500 Ry and the relative cutoff to 50 Ry. The combination of this specific basis set and the XC functional provides a good balance between the amount of correlation needed to describe the electronic structure of the Ferrocene complex while preserving both, structural and electronic features known from the graphite surface (See appendix A for a detailed discussion). In all cases the convergence criteria of 1×10^{-7} Hartree for the SCF energy and 9×10^{-4} Hartree Å^{-1} for the energy gradient are employed.

Molecular Complex	IP (eV)	EA (eV)	χ	μ
G1	5.58	1.06	3.32	4.52
G2	5.34	0.96	3.15	4.38

Table 3.1: Computed values for the ionization potential (IP), electron affinity (EA), chemical potential (χ), and chemical hardness (μ) for the G1 and G2 Guanine derivatives.

3.1.2 Electronic structure, vibrational analysis and optical properties of the G1 and G2 complexes

In the case of the G1 molecular complex, the chemistry of the molecule is much more complex than in the original Guanine configuration due to the replacement of the original Hydrogen atom for a Bromine atom. This functionalization has been suggested not only with the purpose of enhancing supramolecular assembly properties of the complex but also to promote the localization of the electronic charge in the Ferrocene molecule. Concerning the G2 molecular complex, a substitution of the original Hydrogen atom by a Phenyl ring have been carried out. This specific replacement seeks a more relevant role in the network formation promoting the formation of quartets that could lead to a more stable scaffold architecture. In a first step the molecular complexes have undergone a geometrical optimization in the gas-phase. Subsequently, vibrational frequency analysis for both complexes have been carried out and no imaginary frequency have been reported indicating that the structures lie in true local energy minima along their corresponding molecular potential energy surfaces. Since one of the most interesting characteristics of these molecular complexes is the ability to form networks by non-covalent bondings the molecular electrostatic potential (MEP) has been calculated and has proved to be a useful tool in order to investigate the spatial domains at which the molecule can form these links. Hence, in the case of G1 (shown in Fig. 3.2(a)) one can observe a clear agglomeration of charge at the Oxygen atom in the Guanine fragment of the molecule, while in the case of the Nitrogen and Hydrogen positions a depletion of charge is observed. Thus, due to these features one can attribute an active role of those atoms in terms of network formation via Hydrogen bonding interactions. Likewise, the possibility to construct a G-quartet structure by including a Halogen bonding is an open issue that will be further studied in appendix (C). The inhomogeneous distribution of the charge in the G1-molecular complex can be assigned to a strong intra-molecular permanent dipole moment that has been calculated and whose value is 6.10 Debye. For G2 the MEP displays (Fig. 3.2(b)) a more homogeneous distribution than in the previous case due to the lowest electronegativity nature of the functionalized Phenyl group. The places where charge has been concentrated can be assigned to the Oxygen atom placed at the Guanine functional group whereas the Nitrogen-Hydrogen atoms depict a depletion of charge. The former observations lead to conclude that these atoms play an active role in the network formation. The calculated total intra-molecular permanent dipole moment is 1.4 Debye which is substantially smaller than in the previous case. The electronic structure for both complexes has been calculated as well as the energy levels which are displayed in Fig. 3.3 and Fig. 3.4.

Photophysical properties			
Complex	Spin	Energy [eV]	Oscillator Strength
G1	Triplet (LUMO)	1.16	0.000
	Triplet (LUMO+1)	1.19	0.000
	Singlet (LUMO+6)	2.08	0.008
	Triplet (LUMO+9)	2.52	0.006
	Singlet (LUMO+11)	3.36	0.005
G2	Triplet (LUMO)	1.16	0.000
	Triplet (LUMO+1)	1.18	0.000
	Triplet (LUMO+6)	2.07	0.008
	Triplet (LUMO+9)	1.51	0.006
	Singlet (LUMO+11)	3.35	0.004

Table 3.2: Computed electronic excited states by employing TDDFT for (upper) G1 and (lower) G2 molecular complex. First column indicates the spin-symmetry of the state. Second column designates the associated energy of the excitation and third column reports the computed oscillator strength.

Molecular Orbitals

In the case of the G1 molecular complex, the calculated frontier molecular orbitals display a clear localization of the electronic charge density at either the Ferrocene moiety (HOMO, HOMO-1 and HOMO-3) or in the Guanine group (HOMO-2). Similarly, the G2 molecular complex reveal a localization of the electronic charge in the Ferrocene molecule displayed in the HOMO, HOMO-2 and HOMO-3 while a state associated to the Gaunine-functionalized group of the is observed at the HOMO-1 energy level. Interestingly, in both cases the calculated ground state geometry display a configuration in which the Ferrocene-group is in its eclipsed conformation. This feature has been also experimentally observed in different complexes such as vinyl-Ferrocene [116] where the ground states also bears this configuration. The difference between subsequent energy levels is around 80meV which is important in order to protect the electronic structure from thermal fluctuations and from subsequent hybridizations amid molecular levels. Once the ground state configuration is obtained one can examine some interesting chemical quantities such as electron affinity $(EA = E(n+1) - E(n))$, ionization potential $(IP = E(n-1) - E(n))$, chemical potential $(\mu = (IP + EA)/2)$, and chemical hardness $(\chi = IP - EA)$. The results are reported in Table 3.1. The E(n), E(n+1), E(n-1) quantities are electronic total energies corresponding to a total number of electrons n, n+1, n-1. With these results, one can estimate the value of the transport gap (E_t) which is relevant since this is the energy necessary to create a separated electronhole pair that creates electronic current. This is an important issue since the m-QCA technology is based on the idea of a currentless propagation of information in order to reduce the well-known problem of power dissipation energy [5]. Thus, the IP energy values are more related with the extraction of one electron from the Ferrocene moieties while the EA quantities are closer ascribed to the picture of adding one electron in the Guanine associated states of the molecular complexes (see Fig. 3.6 for the corresponding excited-states molecular orbitals).

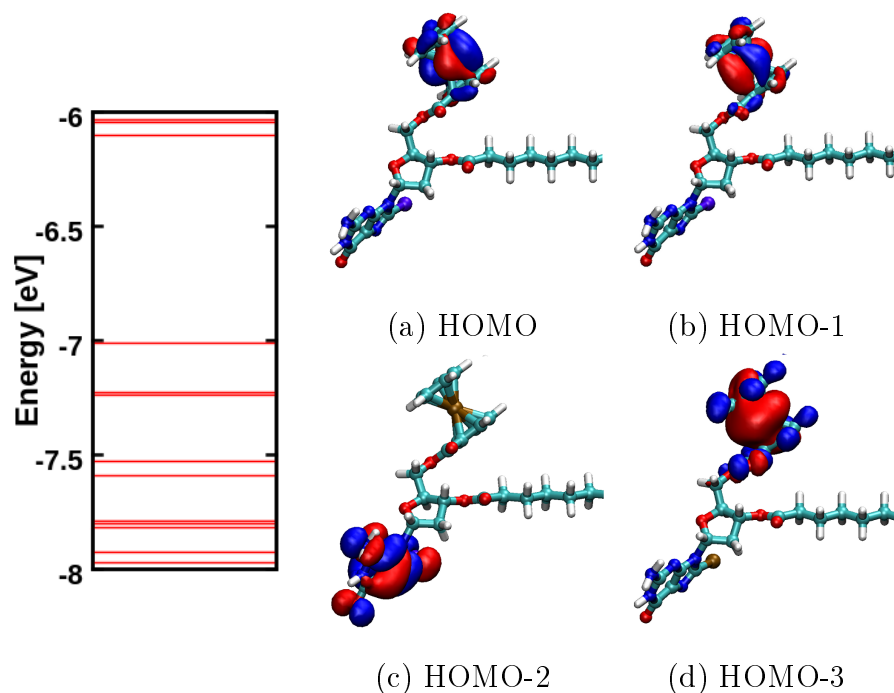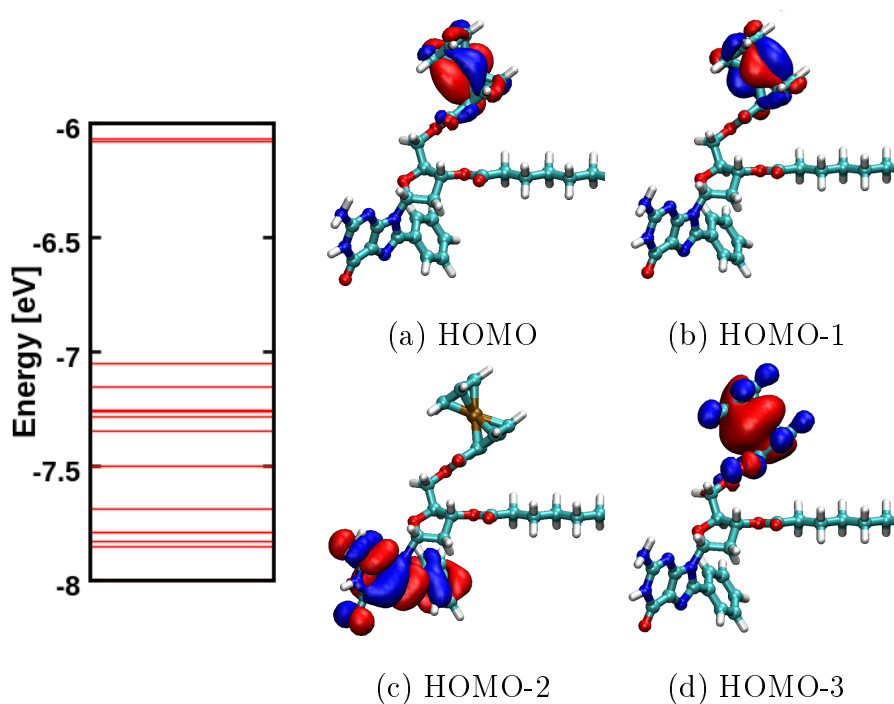(a) HOMO   (b) HOMO-1

(c) HOMO-2   (d) HOMO-3

Figure 3.3: Electronic structure of the G1 molecular complex. Left: Energy diagram for the occupied frontier orbitals. Right: (a-d) Molecular orbitals ranging from HOMO to HOMO-3. All isosurfaces have been plotted at 0.02 e$^-$ Å^{-3}.

(a) HOMO   (b) HOMO-1

(c) HOMO-2   (d) HOMO-3

Figure 3.4: Electronic structure of the G2 molecular complex. Left: Energy diagram for the occupied frontier orbitals. Right: (a-d) Molecular orbitals ranging from HOMO to HOMO-3. All isosurfaces have been plotted at 0.02 e$^-$ Å^{-3}.

Vibrational analysis

The Raman spectra for both molecular complexes have been calculated and displayed in Fig. 3.5(a,b). One of the main advantages of this analysis is the fact that one can determine the specific role of the substitution groups in terms of the activation energy of each mode and its impact in the mechanical stability of the molecule. For G1 the calculated spectrum displays a clear gap of around 1300 cm^{-1} (0.15 eV) where afterwards only higher vibrational modes coming from the Hydrogen atoms located at the long carbon chains are activated. In the lower energy regions of the spectrum one can observe three prominent peaks (1174, 1665 and 1813 cm^{-1}) in which the corresponding intensities are protruding. The associated modes with the corresponding two highest intensities are precisely modes that includes nuclear displacements of the Oxygen, Nitrogen and Hydrogen atoms belonging to the Guanine group of the molecule and responsible of the non-covalent bonding that originates the observed supramolecular architecture. The remaining modes are originated by collective movements of the whole organic-core including the long carbon chain and the sugar moiety. In the case of G2, the Raman spectrum displays a similar profile and a similar band gap (1400 cm^{-1}) as in the G1 case. This resemblance in the spectrum can be attributed to the small structural changes suffered by molecular-building blocks after the substitution process. Correspondingly, the three most prominent emerging peaks (1171, 1660 and 1786 cm^{-1}) can be assigned to collective movements of the Guanine-fragment, sugar-moiety and part of the long carbon chain as in the G1 counterpart. In both cases the remaining peaks of the Raman spectrum of G1 and G2 display either medium or relatively weak intensities and are dispersed through the whole full spectral range. Some of those diffuse modes with relatively medium intensity are found in a range of frequencies between 1000 and 1500 cm^{-1} and are associated with overall nuclear displacements of the organic-core building block with some degree of participation of the Ferrocene molecule.

Photophysics properties

The vertical absorption spectra have been calculated using the TDDFT method for both phases and results presented in Fig. 3.6. The first twelve vertical electronic excitations have been calculated but only the six more relevants have been collected in Table 3.2 with the corresponding spin symmetry, energy excitation and oscillator strength. In both cases the absorption spectra is plotted against the oscillator strength. The strongest oscillator strength has been used as unity in order to renormalize the whole spectra and report the subsequent results in term of relative quantities. As can be found in Fig. 3.6, the electronic excitation spectra of the two molecular-complexes display similar profile and features in terms of excitation energies, oscillator strengths and absorption bands. These three bands are associated with a transition from an occupied metallic state provided by the Ferrocene moiety to an unoccupied metallic state coming from the same functional group (Ferrocene). In the specific case of the strongest band in G1 it is originated from the electron transition from the acetyl-Ferrocene substituent HOMO-1/HOMO to the same acetyl-Ferrocene entity LUMO/LUMO+2/LUMO+6 molecular orbitals. For G2 the mentioned excitation is found to be composed by metallic fragments of the acetyl-Ferrocene HOMO-2/HOMO-1/ to the acetyl-Ferrocene moiety LUMO/LUMO+2/LUMO+8 molecular orbitals. Moreover, the possible metal to ligand charge transfer (MLCT) states amid the metal-like acetyl-Ferrocene molecular orbitals and the low-lying π^* orbitals provided by the Guanosine are observed (excitation 1 and 2 in both cases) but are not optical-active since the reported oscillator strength is 0.
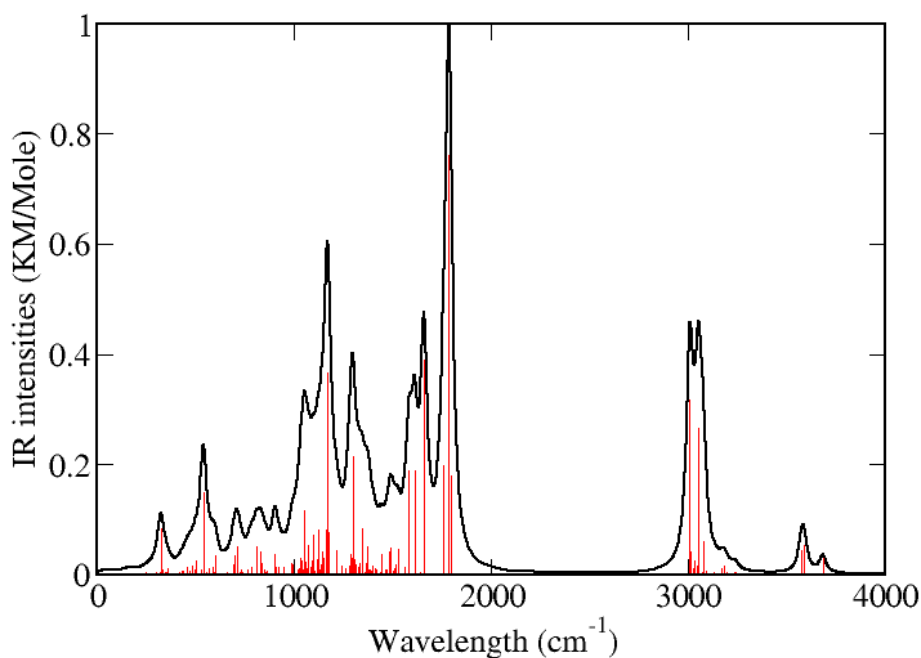
(a)
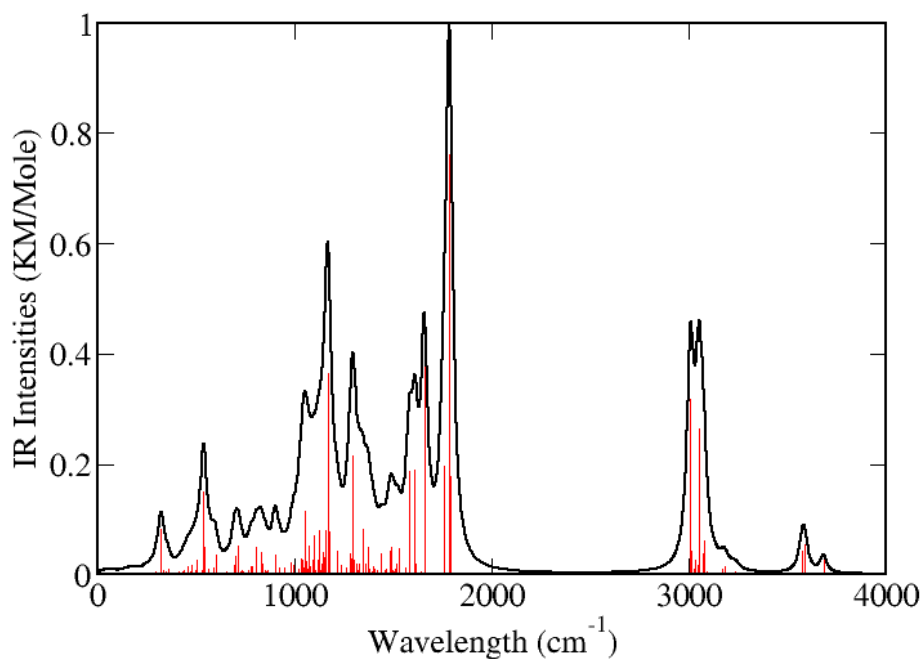
(b)

Figure 3.5: Simulated Raman spectrum for (a) G1 and (b) G2 molecular complexes. Intensities are normalized to the highest intensity found in the system (1813 cm $^{-1}$ for G1 and 1786cm $^{-1}$ for G2) and reported in terms of relative intensities. In both phases the most intense vibrational mode corresponds to a nuclear displacements of the hydrogen, nitrogen and oxygen atoms located at the guanine-group of the molecular-complex and responsible for the self-assembly process linked by non-covalent bonding.
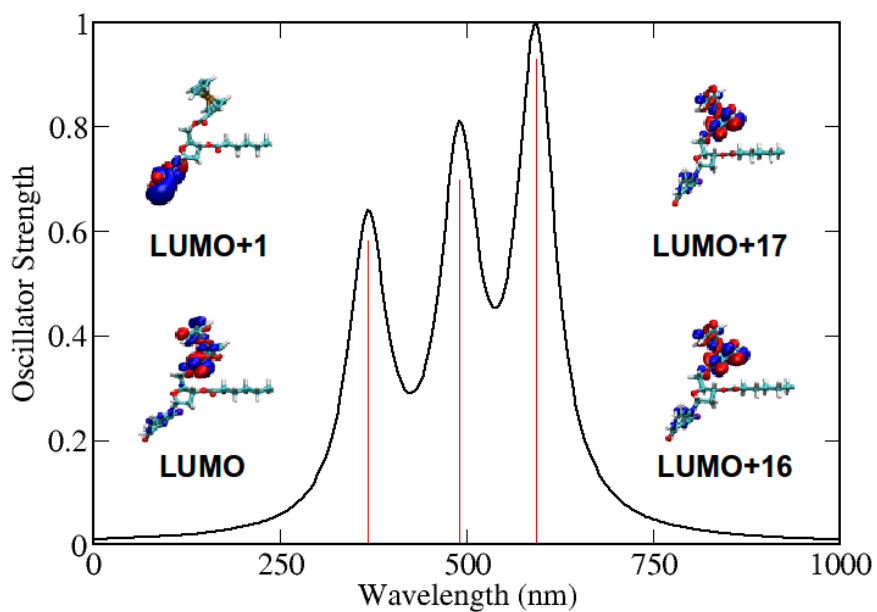
(a)
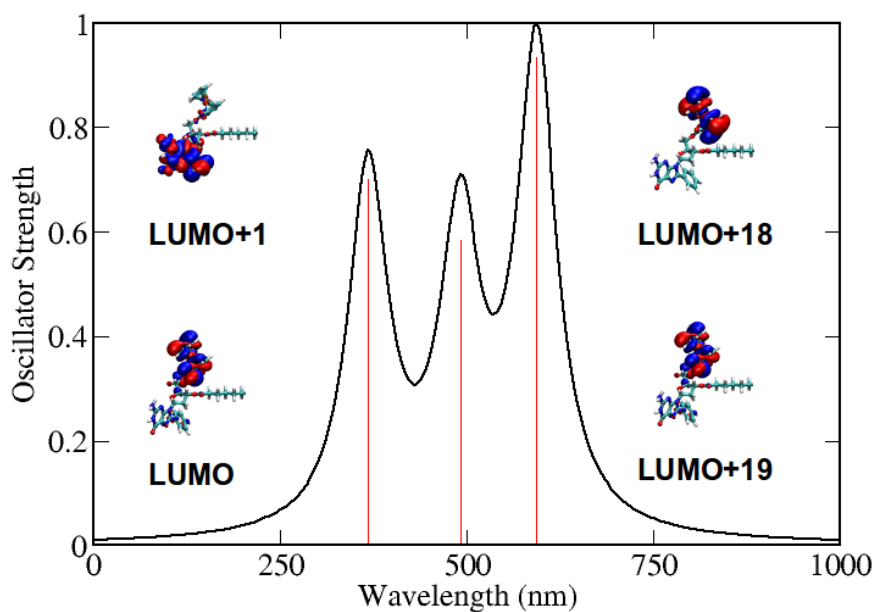
(b)

Figure 3.6: Simulated UV-vis spectra for (a) G1 and (b) G2 molecular complexes. Oscillator strengths are normalized to the computed highest value (0.008 see Table 3.2) and the remaining results reported in relative values. The three bands are associated to d-d transitions from the different d-states symmetries coming from the Ferrocene complex.

3.2 SCAFFOLDING VIA INTRA- AND INTER- MOLEC-
ULAR HYDROGEN BONDING IN THE G1 AND G2
MOLECULAR COMPLEXES

In this section, the interactions driving molecular self-assembly will be described and investigated. Firstly, the main focus of the study will be given to the contribution of each of these interactions, namely, intra- and inter- cell in the global mechanical and energetic stability of the system. Therefore, in order to peruse the many different physical scenarios suitable simulation models will be created and their stabilities will be probed by employing total energy DFT calculations. Afterwards, the optimized unit cells will be used to investigate the electronic structure of the molecules within the two-dimensional networks. This is an important issue since the electronic properties can be changed due to the creation of narrow energy bands raising the question whether electron localization is preserved while the two-dimensional networks are formed.

3.2.1 Network formation in the G1 molecular complex

In the case of the G1 candidate, a network of intermolecular Hydrogen bonds is expected to be formed over the two-dimensional surface. However, the replacement of the Hydrogen atom by the Bromine atom opened the possibility of the formation of Halogen bonds between adjacent molecules in different unit cells [117]. The described scenario can be easily reached just by a slight rotation of the Guanine-functionalized groups leading to a new picture in which the supramolecular architecture is formed via an intercalation of Hydrogen and Halogen bonds. In order to peruse this effect a two-step methodology has been performed. Firstly, a molecular dimer in gas-phase has been relaxed in order to take into account the molecular vdW effects between the long alkyl-chains. Secondly, the relaxed molecular dimer is enclosed in order to create the unit cell using the experimental suggested lattice parameters. This structure is subsequently relaxed for both unit cell and atomic positions and is considered fully relaxed when an accuracy of 1×10^{-7} Hartree for the SCF energy and 9×10^{-4} Hartree Å^{-1} for the force gradient has been reached. The results of the optimization procedure is displayed in Fig. 3.7. The calculated unit cell ($\vec{a} = 42.5$ Å, $\vec{b} = 8.1$ Å) has been compared with the suggested experimental values ($\vec{a} = 41$, $\vec{b} = 9$ Å $\pm$ 1 Å) finding a good agreement between them [103]. In terms of total energy contributions, the unit cell formed by the G1 molecular complex displays a rich variety of both intra- and inter- molecular interactions. Firstly, the intra-cell molecular interactions can be divided into attractive terms coming mainly from the interdigitated arrangement amid adjacent alkyl chains and repulsive terms stemming from the interactions between the Ferrocene moieties due to the electronic charge localization observed in the gas-phase electronic structure. Secondly, the inter-cell molecular interactions are only result from the formation of the Guanine ribbon-like structures but also for the repulsive interaction between the adjacent Ferrocenes from different neighboring cells. Thus, the network formation mechanism is a rather complex interplay between intra and inter-cell interactions whose contribution can be estimated by using total energy first-principle calculations. Hence, different scenarios containing different possible interactions have been calculated (see Fig. 3.8 for the geometries used for the calculations) and the results of the calculations collected and presented in Table (5.3). The results presented for the vdW interactions

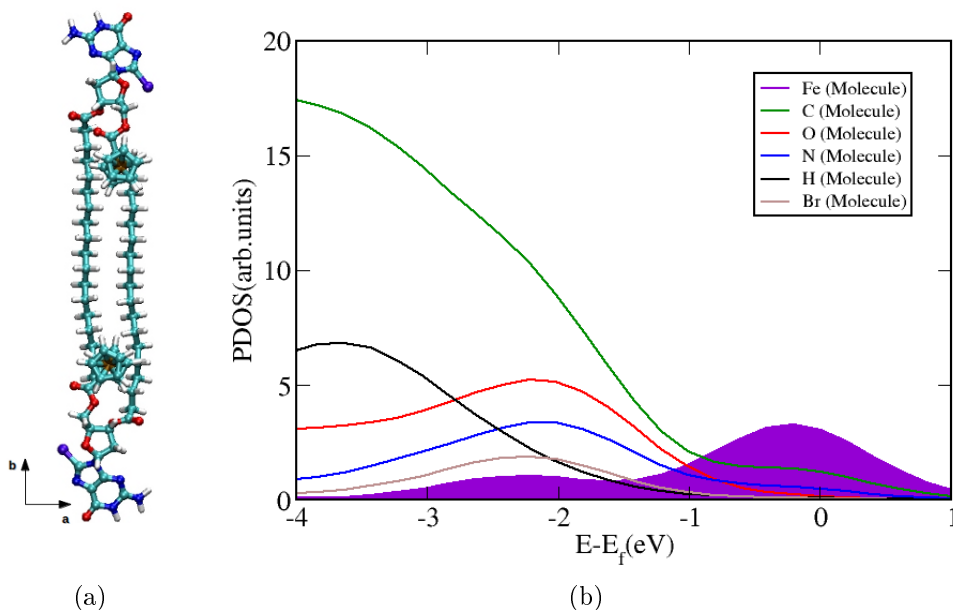(a)   (b)

Figure 3.7: Two-dimensional motif for the G1 molecular complex. (a) Unit cell. (b) Projected Density of States (PDOS). Metallic states provided by the Ferrocene moieties are highlighted with purple color.

and ribbon cohesion energies are in good agreement with previous results reported for close structures [118, 119, 120]

As a result of the optimization procedure of both unit-cell and the atomic positions within it the Halogen bonding scenario has been disregarded since either the distances with the adjacent NH_2 functional groups or the geometrical arrangement within the ribbon do not correspond to the picture where this bonding is playing a relevant role in the formation of the motifs (see appendix C for a more detailed discussion). On the contrary, a dimer with Hydrogen-bonding picture is the most likely scenario to explain the supramolecular architecture observed experimentally. In the same manner, the total energy calculations do not provide a bonding outline for the unit-cell with this molecular arrangement and, hence, strongly suggesting that the adsorption process over the HOPG surface plays a more active role in the formation of the supramolecular architecture. In addition to the previous analysis one can explore the possibility to explain the localization of charge in the molecular orbitals associated to the Ferrocene group by using point group symmetry considerations. Likewise, this analysis can possibly reveal the underlying influence of the ribbon-motif formation in the subsequent space-group symmetry of the unit cell. In the case of the G1 the calculated ribbon point-group symmetry is C4 as it has been also reported in similar structures of the Halogen-substituted base pairs [117]. The experimentally observed unit cell exhibits an orthorhombic nature (a $\neq$ b $\neq$ c) and the molecular dimer within displays a D2 point group symmetry. In terms of symmetry the calculated point-symmetry group [121] exactly matches to one of the point groups of the orthorhombic crystal lattice (sphenoidal). This realization is important since the electronic structure especially the electronic charge localization phenomena can be understood as a result of the spatial restrictions imposed by the specific point-group symmetry that in turn is a consequence of the ribbon-like formation of the supramolecular architecture.

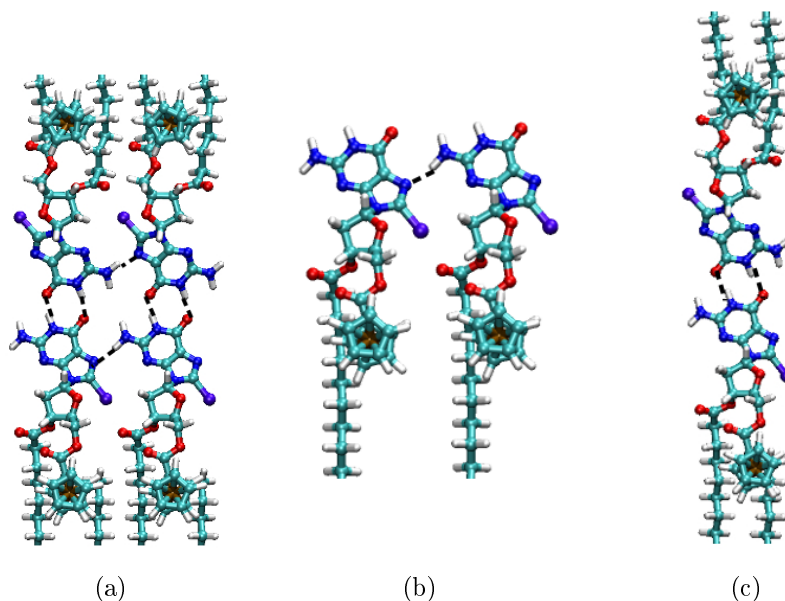<div align="center">(a)   (b)   (c)</div>

Figure 3.8: Schematic of the G1 intra- and inter- molecular interactions indicated with dashed lines. (a) Total ribbon configuration including intra- and inter-cell interactions. (b) Inter-molecular interaction along the $\vec{b}$ lattice vector. (c) Inter-molecular interaction along the $\vec{a}$ lattice vector. These configurations have been used to scrutinize the strength and importance of this non-covalent interaction in the formation energy process of the two-dimensional scaffold.

Furthermore, the possible organization of the molecular orbitals can be scrutinized by employing the calculated point-group symmetry (D2) and by visual inspection of the symmetry of the canonical molecular orbital. Thus, one can observe that the organization (d_{xy}, $d_{x^2-y^2}$ and dz^2) of the molecular orbitals resembles a similar structure as is observed in the Ferrocene moiety in gas phase. Finally, once the unit cell is constructed the molecular orbitals are plotted using a Gaussian broadening of 0.5 eV. The computed projected density of states (PDOS) is presented in Fig. 3.7. In the region near the Fermi energy a more protruding peak is observed stemming from states provided by the Ferrocene moieties. The difference of spectral weights between the states found at -1.0 eV compared with the ones observed at -2.5 eV can be ascribed to the intrinsic degeneracy of the $d_{xy} \cong d_{x^2-y^2}$ provided by the Ferrocene group creating more accessible states in the Fermi energy region. In the same manner, a clear hybridization of states provided by the organic-core and those d-states supplied by the Ferrocene-moieties plays a role in the formation of the self-assembly molecular scaffold.

3.2.2 Network formation in the G2 molecular complex

In the case of G2, the supramolecular architecture is clearly originated from a Hydrogen-bonding interactions amid the Guanine-functionalized groups in the neighboring cells along the $\vec{a}$ lattice vector. In fact, the measured arrangement obeys a classic G-quartet motif that has been reached without the inclusion of any potassium cation. The same two-step methodology as performed in the previous section has been used employing the same convergence criteria.

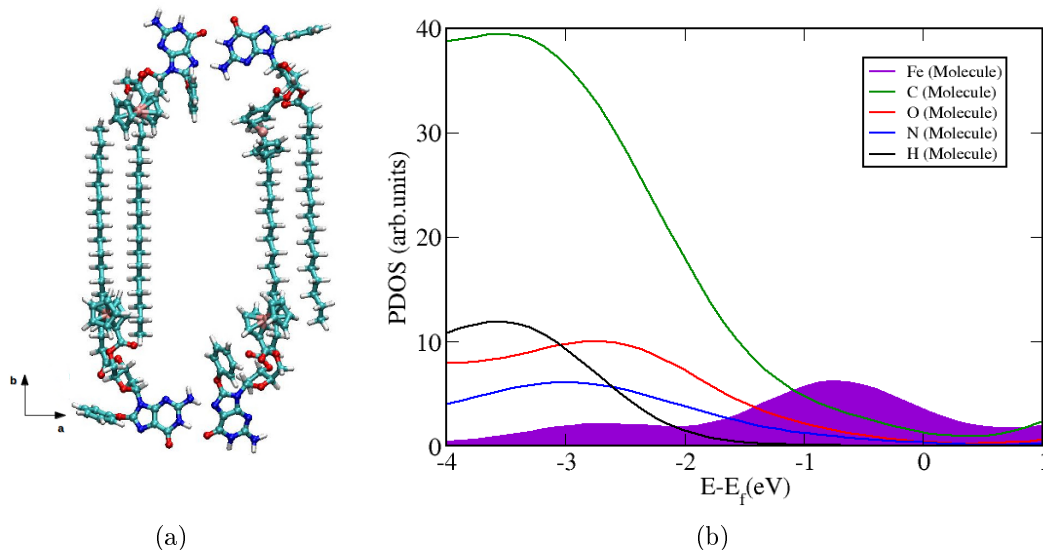(a)   (b)

Figure 3.9: Two-dimensional motif for the G2 molecular complex.(a) Unit cell.(b) Projected Density of States (PDOS). Metallic states provided by the Ferrocene moieties are highlighted with purple color.

The lattice vectors of the optimized unit cell ($\vec{a} = 44.6$ Å $\vec{b} = 20.1$) are in good agreement with the reported experimental values ($\vec{a} = 45$ Å and $\vec{b} = 18 \pm 1$ Å) [103]. In this case, the intra- and inter- molecular interactions can be divided into attractive mainly supplied by the vdW interactions amid the interdigitated long carbon chains along the $\vec{b}$ lattice vector and the ones provided by the G-quartet structure. The results presented for the vdW interactions and ribbon cohesion energies are in good agreement with previous results reported for related structures [118, 119, 120]. The repulsive contributions are primarily originated in the electrostatic interaction between the Ferrocenes groups and the phenyl replacements belonging to different neighboring cells. Thus, the contribution of each of these interactions is considered and the results of the formation energy collected and displayed in Table (5.3). Afterwards the geometry relaxation procedure has been carried out, a possible C_{2v} point group symmetry has been obtained for the specific geometrical arrangement within the unit-cell. Hence, the calculated orthorhombic unit cell (a≠b≠c) can be ascribed as a consequence of the ribbon-like formation displayed at the borders of the neighboring unit cells. Similarly to the former case, the calculated point group of the Quartet molecular complex is in agreement with an associated orthorhombic space-groups within this specific crystal class (pyramidal). These results lead to the conclusion that the ribbon formation process defines in a great measure not only the shape of the unit cell but the electronic structure properties of the self-assembled molecular complex. Thus, using the computed C2V point-group symmetry [121] as basis for the analysis and complemented by a direct inspection of the symmetry of the canonical molecular orbitals suggests that the ordering ($d_{xy} \cong d_{x^2-y^2} > dz^2$) is maintained as in the gas-phase Ferrocene case. Finally, the electronic structure of the two-dimensional network is calculated and the corresponding projected density of states (PDOS) is shown in Fig. 3.9 using a Gaussian broadening of 0.5eV. Thus, one can observe that d-states supplied by the Ferrocene group are located in the region near to the Fermi energy of the molecular self-assembled crystal and are divided into two protruding peaks located at -0.5, and -2.5 eV, respectively.
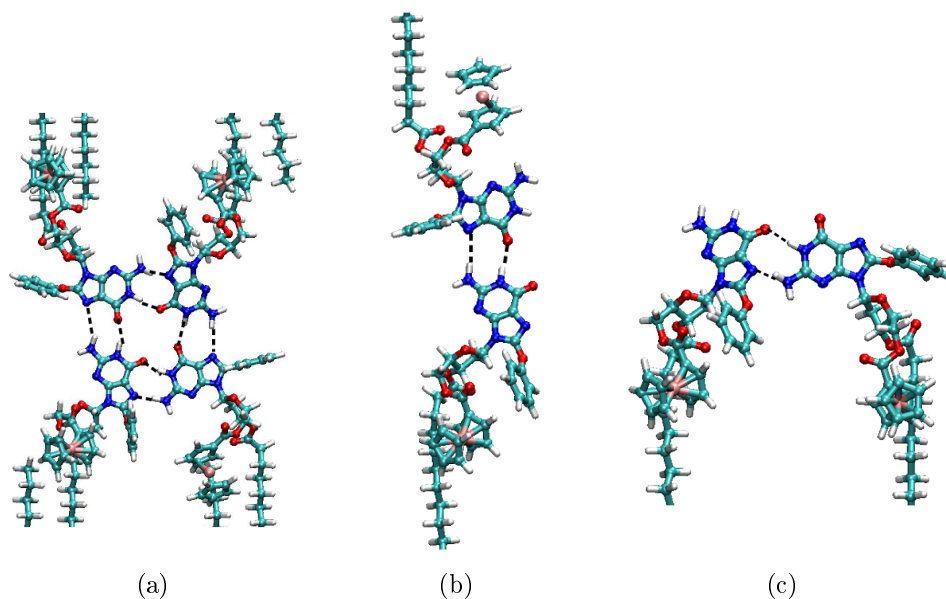
(a)　　　　　　　　　(b)　　　　　　　　　(c)

Figure 3.10: Schematic of the G2 intra- and inter- molecular interactions indicated with dashed lines. (a) Total ribbon configuration including intra- and inter-cell interactions. (b) Inter-molecular interaction along the $\vec{a}$ lattice vector. (c) Intra-molecular interaction along the $\vec{b}$ lattice vector. These configurations have been used to scrutinize the strength and importance of this non-covalent interaction in the formation energy process of the two-dimensional scaffold.

The division of the d-states can be assigned to the breaking of symmetry due to the ribbon formation at the interface of the unit cell motif in which is not totally planar and therefore opening gaps in the states close to the Fermi energy. Finally, the states provided by the Carbon, Oxygen and Nitrogen atoms are recognized in the same energy region but with a lower spectral weight that can be ascribed to the two-dimensional H-bonding scaffold formation and also leading to a possible hybridization with the metallic states provided by the Ferrocene moieties.

3.3　MOLECULE-SURFACE INTERACTION

One of the crucial points in order to implement the m-QCA paradigm is the influence of the adsorption process in the electronic structure of the candidate molecules. Moreover, as it was found in the previous analysis this interaction plays a more fundamental role in terms of energy and mechanical stabilization of the supramolecular architecture. In order to study the effect of the surface on the electronic structure of the G1 and G2 molecules the slab technique has been employed. In the case of HOPG three atomic layers have been included in the previous relaxed unit cells and on top of which 40 Å vacuum space was added to avoid spurious interactions between periodic images. Likewise, since the molecules have been assumed to behave like a two-dimensional lattice the Brillouin zone has been only sampled at the Γ point without loss in accuracy given the fact that large lattice vectors have been used when compared with the original graphite unit cell. To quantify the interaction between the molecules and the substrate, we define an adsorption energy through:

Molecular Complex	vdW (eV)	H − Bonding (eV)	Adsorption (eV)
G1	-0.15	-0.187 (-0.141)	-0.910
G2	-0.19	-0.202	-1.223

Table 3.3: Calculated total energy differences for the different interactions for both complexes. Note that three different interactions have been considered as shown in Fig 3.10 and Fig 3.12.

$$E_{ads} = E_{total} - [E_{G1/G2} + E_{HOPG}] \qquad (3.1)$$

where E_{total} is the total energy of the molecule-surface system, $E_{G1/G2}$ is the total energy of the corresponding molecular complex without surface and finally the E_{HOPG} is the total energy of the surface.

3.3.1 Physisorption of the G1 complex

The mechanical and electronic properties of the G1 molecular complex have been calculated and the optimized structure is shown in Fig 3.11. After the molecules have been deposited onto the HOPG surface a ribbon-like formation is observed suggesting the formation of a supramolecular network under STM environmental conditions [103]. The interaction of the molecule and the surface is mainly driven by the vdW force since the long-alkyl chains and the functionalized Guanine groups of the complex are the moieties directly interacting with the first layer of the Graphite surface. The reported distance after geometry relaxation of the two Ferrocene groups is around 9 Å, strongly suggesting a physisorption of those complexes onto the HOPG surface. The electronic structure of the G1 complex including the surface states has been calculated and the results displayed in Fig. 3.12. Thus, in the projected density of states (PDOS) one can observe an important contribution in terms of the spectral weight of the d-localized states supplied by the Ferrocenes moieties near the Fermi energy. It is also worth to mention that some states provided by the Oxygen, Nitrogen and Carbon atoms have been also found near the Fermi energy and can be assigned to the functionalized Guanine fragment. Moreover, the PDOS results suggest that a possible hybridization between those organic-states provided by the Guanine group and the metallic d-states can take place. This is an important issue since the experimental STM images display protrusions that corresponds with the spatial part where the Ferrocenes and the functionalized Guanines are assumed to be geometrically located. The calculated STM images are presented in Fig. 3.11 and compared with the ones measured in experiments [54]. Hence, one can conclude that at room temperature the localization of the electrons in the d-states of the Ferrocene molecules is distorted due to a combination of factors. Firstly, the molecular discrete energy levels and their associated molecular orbitals are broaden due to the interaction with other molecules (network formation) and the surface (physisorption). Subsequently, the thermal fluctuations make that the differently broadened molecular energy levels get hybridized and therefore not allowing to clearly resolve the Ferrocene moiety localized states.
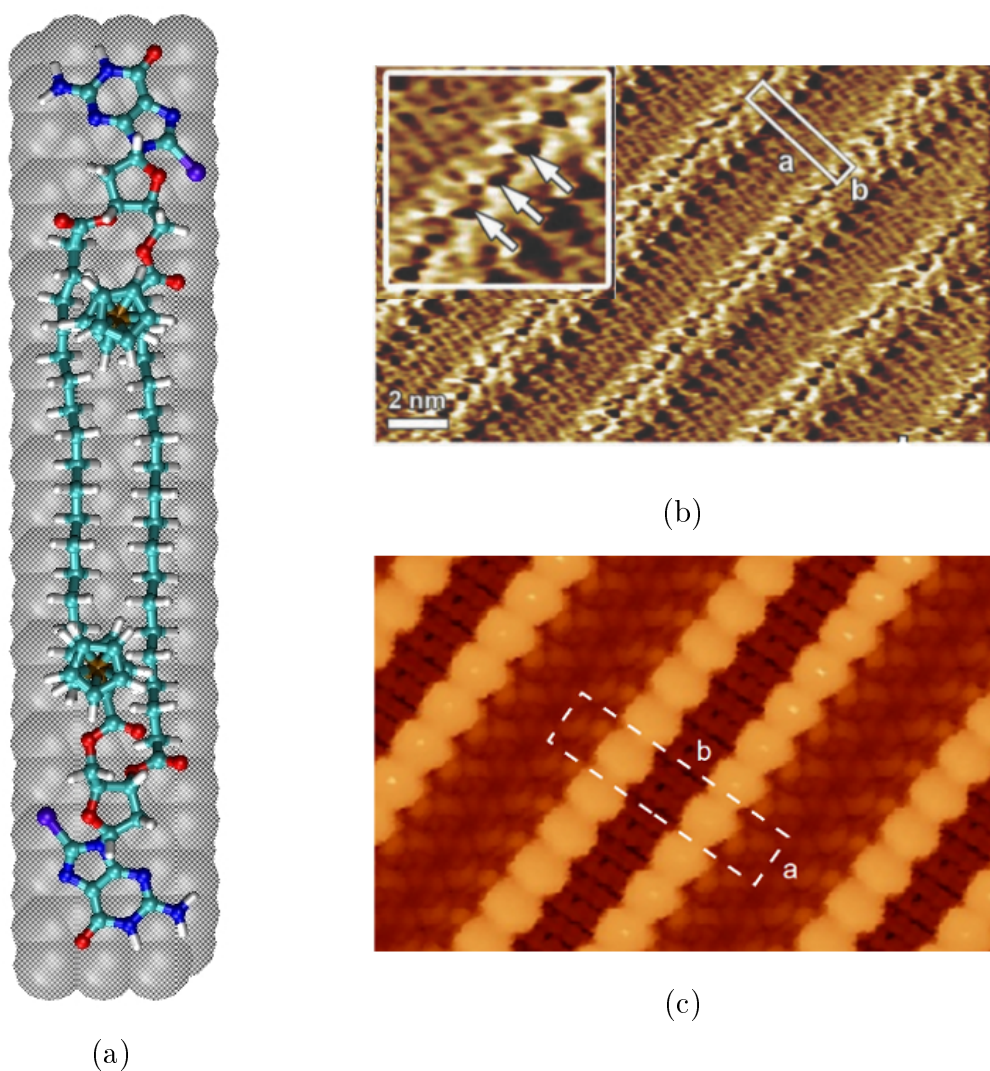
(a)

(b)

(c)

Figure 3.11: The most stable computed molecular conformation for the G1 molecules when is adsorbed on HOGP.(a) Top view. (b) Experimental environmental-STM images. (c) Simulated STM image under experimental conditions (-0.5 V, $|\psi|^2 = 10^{-7}$ Å^{-3} integration of the wavefunction).

3.3.2 Physisorption of the G2 complex

The mechanical and electronic properties of the G2 complex have been investigated and the results of the optimization procedure presented in Fig. 3.13. The experimental STM images display a Quartet ribbon-like structure [103]. In this case, the long alkyl-chains play a more active role since as a result of the self-organization process intra- and inter- vdW interactions amid the molecules are possible. At this point some degree of uncertainty exists in the STM experiments under ambient conditions since the suggested configuration does not clearly show one of the alkyl-chains associated to one of the molecules. Nonetheless, in the calculations the four alkyl-chains have been included. The projected density of states (PDOS) has been calculated and the results presented in Fig. 3.14. Thus, the states located close to the the Fermi energy with a large spectral contribution can be assigned to the localized d-states of the G2 moieties. Similarly, states supplied by the Oxygen, Nitrogen
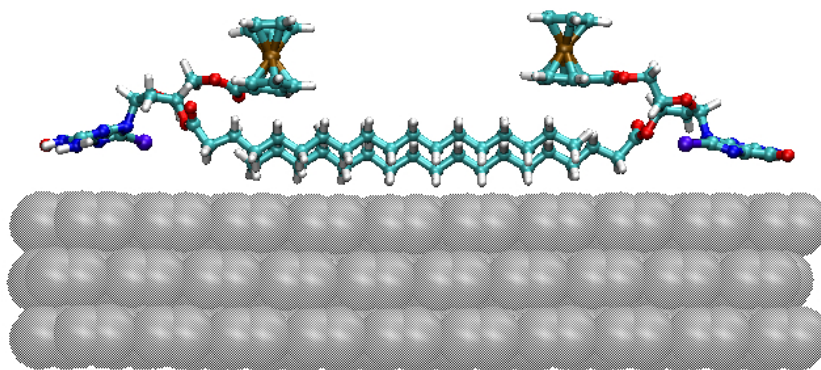
(a)
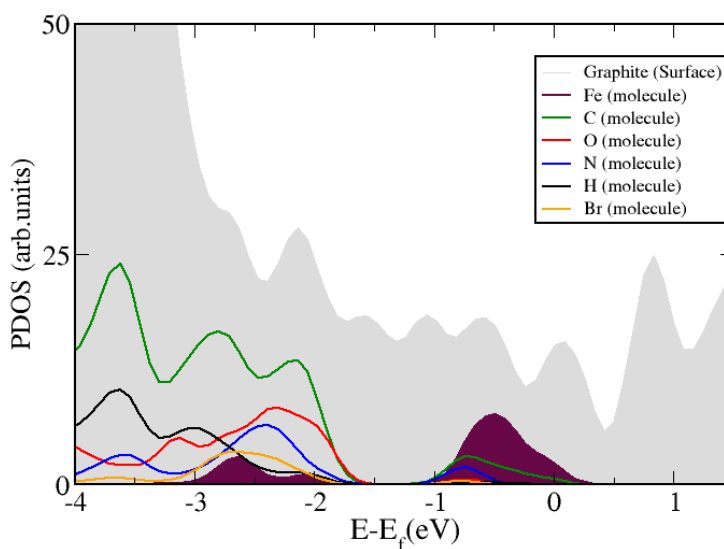
(b)

Figure 3.12: Calculated projected density of states (PDOS) highlighting the contributions from the metallic d-states supplied by the Ferrocene moieties (purple) around the Fermi energy and the surface states in the background (grey).

and Carbon atoms are discerned in this energy region and can be ascribed to the Guanine functionalized fragment of the molecule. The calculated PDOS suggests a probable hybridization among the metallic d-states and the organic π-states associated with the Guanine moiety. The computed STM images are presented in 3.13 and are in good agreement with the experimental results by presenting localization of charge at the Ferrocene moieties [103, 54]. As in the previous case, the interaction of the single G2 molecule with the surface and the formation of a supramolecular network causes a broadening effect in the discrete energy levels promoting the hybridization of the organic and metallic states. This can be observed in the measured STM images where no clear localized electronic states can be resolved.
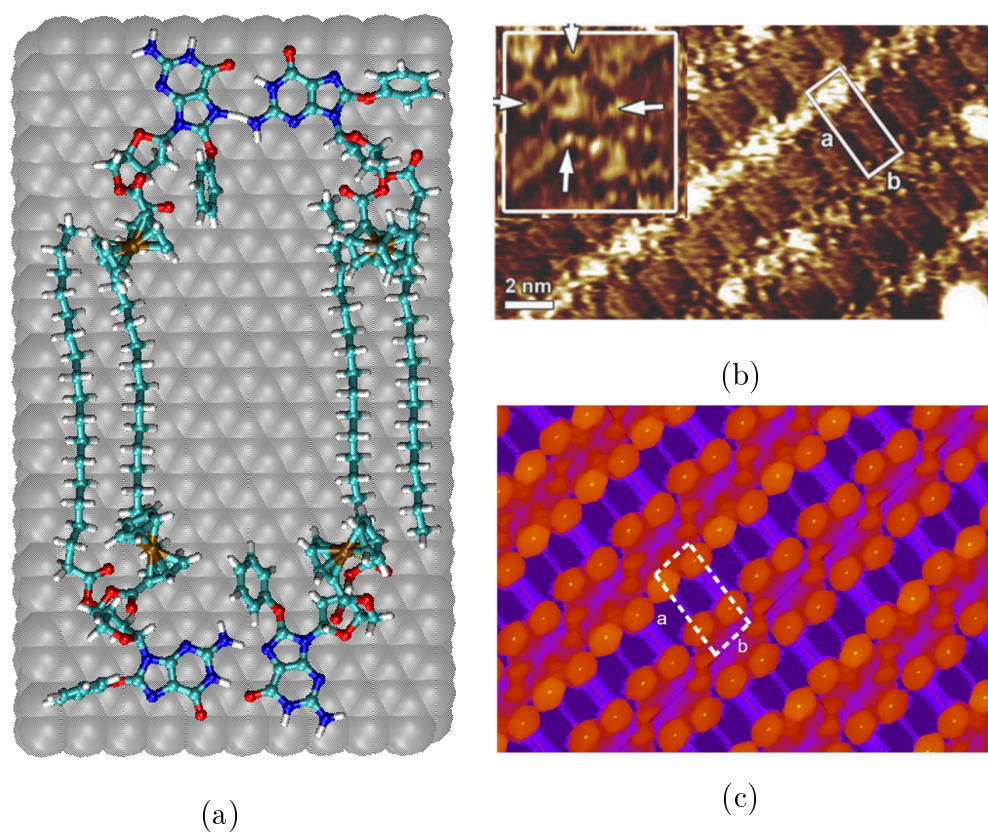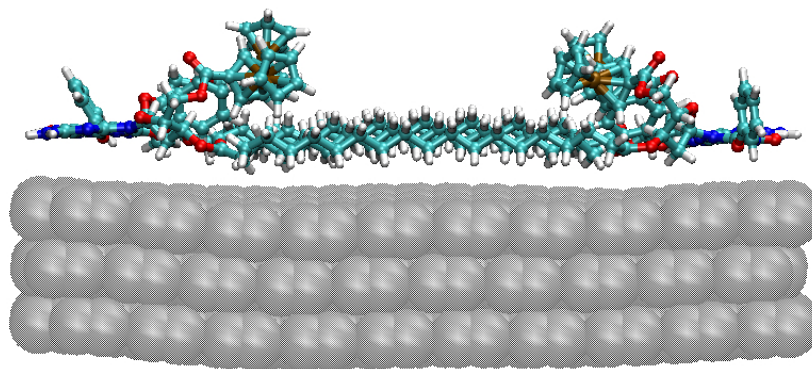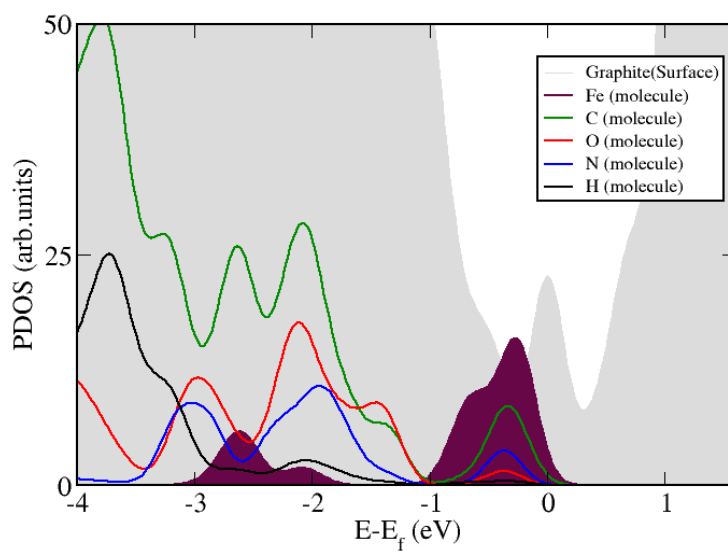
(a)

(b)

(c)

Figure 3.13: The most stable computed molecular conformation for the G2 molecules when is adsorbed on HOGP.(a) Top view. (b)Experimental STM image under environmental conditions.(c) Simulated STM image (-0.5 V, $|\psi|^2 = 10^{-7}$ Å^{-3} integration of the wavefunction).

(a)

(b)

Figure 3.14: (a) Parallel view of the unit cell for the G2 molecules when is absorbed on HOPG.(b) Calculated projected density of states (PDOS) highlighting the contributions from the metallic d-states (purple) around the Fermi energy and the surface states in the background (grey).

3.4 MECHANICAL STABILITY OF THE G1 AND G2 SCAFFOLDS VIA AB-INITIO MOLECULAR DYNAMICS

In order to assess the mechanical stability of the complex ab-initio molecular dynamics simulations (AIMD) have been carried out as implemented in the CP2K software [122]. The fully relaxed structures have been used as starting point of the trajectory. Since the main interest is to recreate the experimental conditions the random velocities for each atom are taken from an ensemble average that corresponds to a temperature of 300 K. Thus, the average temperature along the trajectory is kept close to the aimed temperature by using a Nosé-Hoover thermostat [123, 124]. This specific thermostat allows the system to exchange energy with an external heat reservoir (bath) whereas the statistical correlations are not destroying along the trajectory. Finally, periodic boundary conditions have been employed and where the unit cell dimensions are kept constant as reported in the optimized structure excluding from the simulation effects such as thermal expansion and fluctuations. A simulation of 5 Ps has been carried out in order to investigate the stability of the hydrogen-bond network and the averaged distance between Ferrocene moieties by statistically analyzing the intermolecular distance amid the N-H $\cdots$ O bonds.

3.4.1 Statistical analysis of the molecular dynamics trajectories for the G1 and G2 complex

Ab-initio molecular dynamic simulations (AIMD) produce trajectories of atomic positions as a function of time and provide a representation of the sampling of the accessible conformational states for a given system with quantum mechanical accuracy. Thus, statistical tools are used since they provide the relative likelihood of the random variable (distances amid the intra-cell O $\cdots$ H $-$ N groups) to take a given value. This is an important marker since the strength of the Hydrogen-bond is characterized by its length and the angle formed by constituent groups. It has been already established that bond lengths above 3.5 Å and angles below 90° are not considered to be held by this bond [125]. Thus, one can create a histogram that is used to determine the underlying probability distribution of the corresponding random variable via segmenting the information using a linear bin approach. Thus, whereas for the G1 only three nearest neighbor intercell pairs of N-H $\cdots$ O and N-H $\cdots$ N bonds have been considered (Fig. 3.15 for G2 the four possible combinations including intra- and inter- Hydrogen bonds have been studied (Fig. 3.16). As a result of this analysis, all the studied cases a fitted normal distribution has been added in order to build an unnormalized PDF (Fig. 3.15 with red-dashed line). In order to assess whether the binned histograms obtained from the random variables are coming from a normal distribution a statistical parametric normal test has been performed where the computed p-values range from 0.0001 to 0.000001. This indicates that the null hypothesis must be rejected and that our random variables have not converged in distribution. The statistical correlations have been computed for the only possible combinations between random variables allowed in the G1 complex while for G2 two possible combinations among the random variables have been perused. Hence, in the different cases the value of the Pearson coefficient ranges between 0.15 to 0.20 for each couple of random variables (atomic bonds) in both complexes [126]. These results strongly indicates that the studied pair of random variables are low correlated and therefore not expecting any mutual influence of the different bonds in the dynamics of the motif.
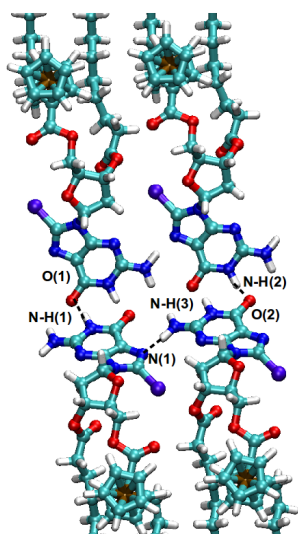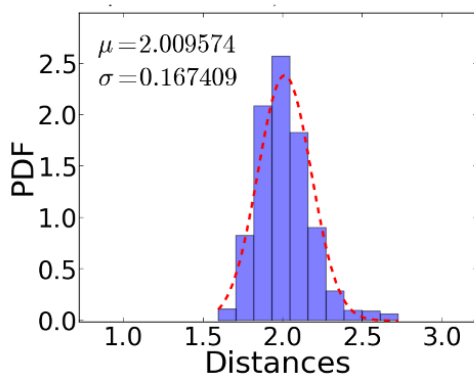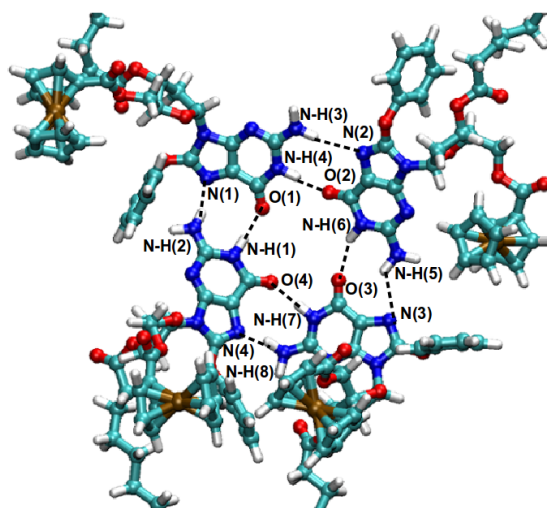
(a)
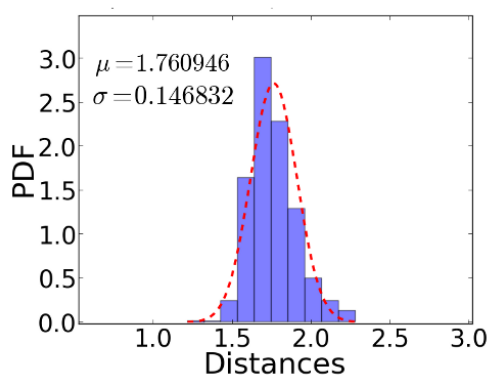
(b)
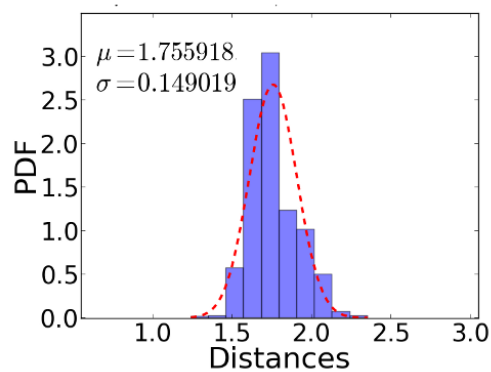
(c)

(d)

Figure 3.15: Statistical analysis including the unnormalized Probability Density Function (PDF) for the different atoms involved in the formation of the dimer ribbon for the G1 molecular complex.(a) G1-dimer snapshot of the AIMD simulation.(b) N(1)-H(1) $\cdots$ O(1).(c) N-H(2) $\cdots$ O(2).(d) N(1)$\cdots$ N-H(3).
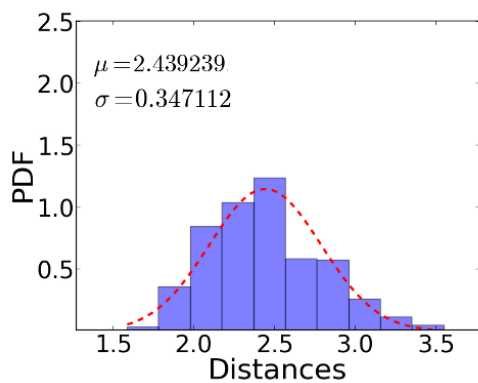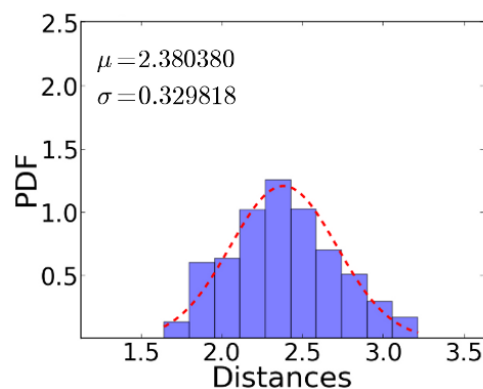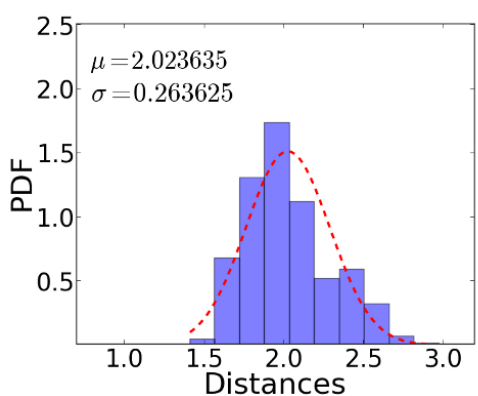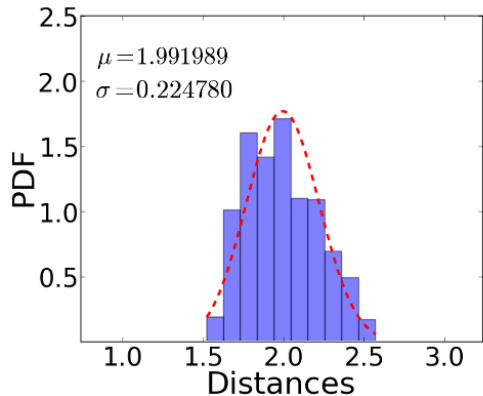
(a)

(b)

(c)

(d)

(e)

Figure 3.16: Statistical analysis including the unnormalized Probability Density Function (PDF) for the different atoms involved in the formation of the G-Quartet ribbon for the G2 molecular complex.(a) G-Quartet snapshot of the AIMD simulation.(b) N(1)···N-H(2). (c) O(1)···N-H(1).(d) N(4)···N-H(8).(e) O(4)···N-H(7).

Although the random variables defined for both complexes can not be assigned to a given PDF, one can conclude that the observed motifs are mechanical stable. The reported distances among the atoms responsible for the Hydrogen bonding are close to the energetically most favorable value with small statistical variations caused by temperature. In conclusion, no statistical correlations have been found among the different combination of random variables for both complexes but mechanical stability has been tested and proved by analyzing the trajectories of selected random variables.

4 TETRAPORPHYRIN-BASED IMPLEMENTATION:

In this chapter a theoretical investigation has been carried out in a possible family of Ferrocene-appended Porphyrin complexes where the the m-QCA paradigm can be implemented. In section (4.1), the main focus is the study of the electronic structure properties of the isolated molecules with the aim of observing possible molecular orbitals that can used to represent the classical binary "0" and "1" sates. The electronic properties of the molecules within their corresponding unit cells have been further examined in section (4.2) by explicitly constructing the two-dimensional scaffolds. The emphasis is given to understand the possible driving forces that allows the network formation, namely, the inter- and intra- cell molecular interactions amid adjacent cells. In section (4.3) the interaction between molecule and surface has been investigated so as to examine the impact in the electronic structure of the molecular complexes when those are absorbed on a Highly Ordered Pyrolytic Graphite (HOPG). Moreover, the mechanical stability of the both molecular complexes with different observed networks has been further investigated by employing ab-initio molecular dynamics calculations (AIMD). The results of these calculations have been statistically analyzed in order to asses the mechanical stability of the experimentally measured motifs at room temperature.

4.1 MOLECULAR BUILDING BLOCKS

The simplest picture of a m-QCA cell relies on a symmetric four-square configuration where at each corner electrons can be spatially confined. Likewise, the paradigm demands an electrostatic coupling between adjacent cells in order to ensure functionality in the ultimate goal of computation. One alternative in order to implement the concept is the use of a combined functionalized complex that includes Ferrocene and Porphyrin molecules. Particularly, these two molecular complexes have attracted attention due to its unique characteristics to display multiple active redox centers necessary for the m-QCA based implementation. Although a large variety of the so-called Ferrocene-appended Porphyrins have been already synthesized [127, 128] its capability to display a self-assembly network formation has been not yet fully achieved and therefore making necessary a further functionalization. Thus, a new family of Ferrocene-appended Porphyrins have been synthesized and the two plausible candidates (called P1 and P2) are displayed in Fig 4.1.
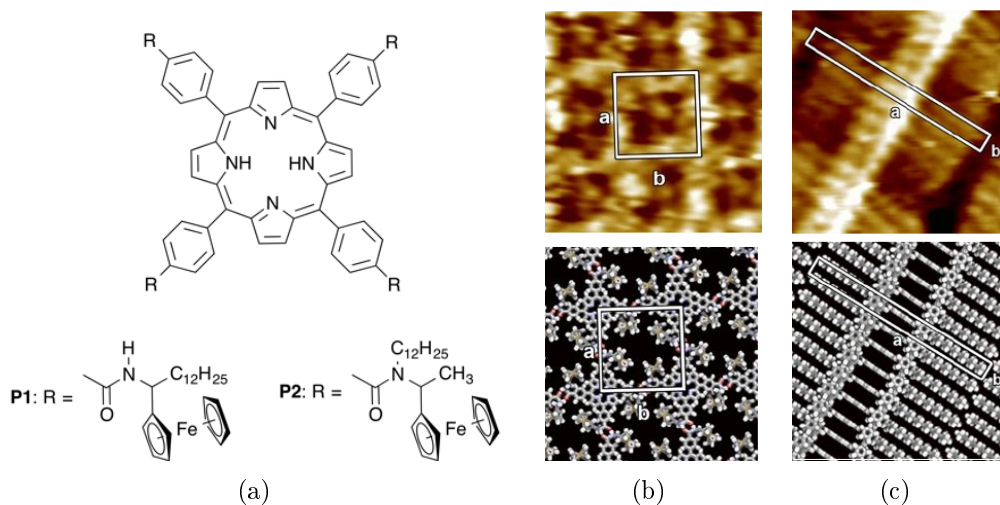
Figure 4.1: The two Ferrocene-appended porphyrins synthesized derivatives.(a) P1 and P2 molecular complex in which the conjugated spacer contains an amide group and to enhance the Hydrogen-bonding amid adjacent molecules. (b) Experimental STM image and suggested motif of the P1 molecular complex absorbed on HOPG.(c) Experimental STM images and suggested motif of the P2 molecular complex absorbed on HOPG.

4.1.1 Methodology

To study the electronic, optical and vibrational properties of the two molecular complexes density functional theory (DFT) have been employed as is implemented in the Gaussian 09 all-electron code [107]. The B3LYP exchange-correlation functionals have been used in order to optimize the isolated gas-phase molecular structures of the P1 and P2 organometallic complexes [42, 108]. The basis-set employed is a combination of the LANL2DZ effective core basis set for the Iron atom and the $6-311G(d,p)$ basis set for C/H/N/O [109, 110]. Notice that this is an extension from the usual LACVP(d) basis set since the normal $6-31++G(d,p)$ basis set does not reproduce exactly the almost degenerated configuration in the TPP framework [129]. The default cut-offs have been used in the optimization process and the Berry algorithm selected using the redundant internal coordinates for both cases . Vibrational analysis have been performed after the optimization process in order to corroborate whether the energy-minimized structures are in a true minima in the potential energy surface. In a second step, the CP2K software has been used [111] in order to study the experimentally spotted motifs and the corresponding unit cells formed by the P1 and P2 complexes. This step is necessary since the number of atoms needed to described the experimental conditions exceeds the computational capabilities of the all-electron codes. The previous optimized single molecule structures have been used in order to construct the experimentally observed non-covalent linked scaffolds. In all cases, the calculations have been performed using the BLYP exchange-correlation (XC) functional [41]. The valence electrons were treated by a double-zeta Gaussian basis set, while the core electrons were treated by norm-conserving pseudopotentials of the Goedecker-Teter-Hutter type [112, 113, 114, 115]. Van-der-Waals interactions have been included through the semi-empirical Grimme's D3 approximation [49]. The energy cutoff for the plane wave expansion of the density was set at 500 Ry and the relative cutoff to 50 Ry. The convergence criteria of 1×10^{-7} Hartree for the SCF energy and 9×10^{-4} Hartree $Å^{-1}$ for the energy gradient have been employed.
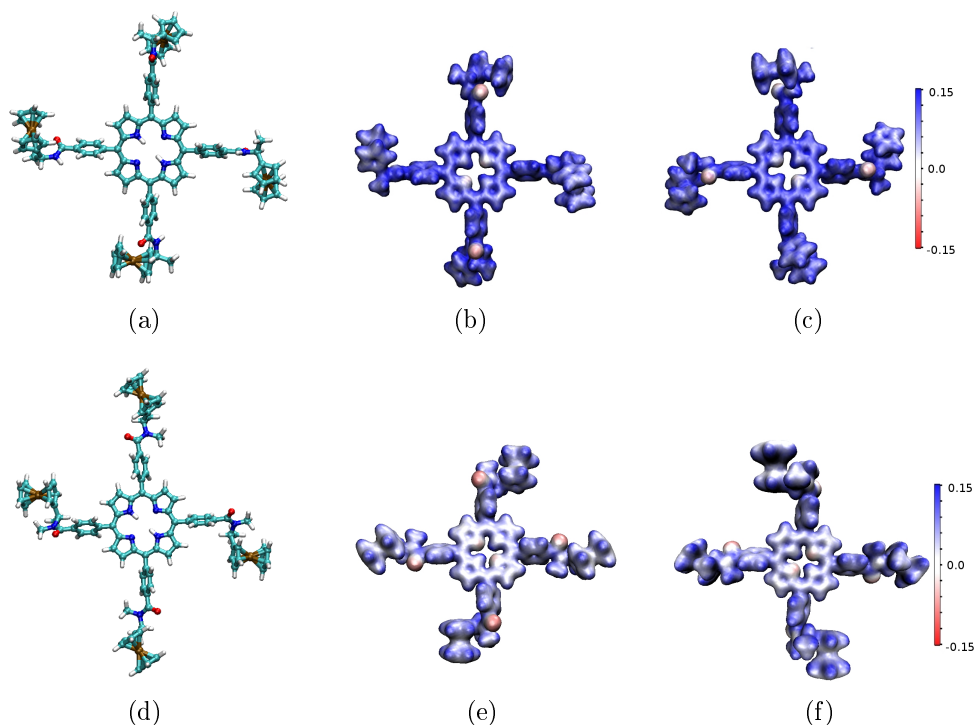
Figure 4.2: Schematic of the P1 and P2 molecular complexes.(a) Equilibrium structure of the P1 isolated molecule. (b,c) Molecular electrostatic potential (MEP) plotted onto the electronic density.(d) Equilibrium structure of the P2 isolated molecule.(e,f) Molecular electrostatic potential (MEP) plotted onto the electronic density. The colored contour plot graphic indicates the regions within the molecule where an excess (red) or lack (blue) of electrons is spotted. All iso-surfaces have been plotted at 0.02 e$^-$ Å^{-3}.

4.1.2 Electronic structure, vibrational analysis and optical properties of the P1 and P2 complexes

As starting point the molecular complexes have been optimized in the gas-phase and the obtained results are displayed in Fig. 4.2. The projection of the molecular electrostatic potential (MEP) onto the electronic density distribution has been calculated for both molecular complexes and used to examine the possible atoms in which the different network formation mechanisms can be ascribed. In the specific case of P1, the amide groups attached to the porphyrin network displays a distinctive H-bond characteristic, namely, an excess and lack of electrons attributed to the Oxygen and Hydrogen atoms located at this functional group, respectively. In the case of P2 the same functional group does not exhibit the same characteristic and therefore the origin of the self-assembly can be attributed to another non-covalent force such as the vdW interaction. Interestingly, the MEP for P1 is more symmetrical distributed within the complex than in the case of P2 where more neutral regions (white) can be observed. Thus, these anomalies of the MEP can be interpreted as regions where accumulation and depletion of charge takes place generating possible intra-molecular dipole moments. In order to investigate further this issue the total magnitude of the dipole moment has been estimated for both complexes. In the case of the P1 a 2.8 Debye dipole moment is reported while for P2 a 6.7 Debye total dipole moment has been obtained leading to the conclusion that the observed

Molecular Complex	IP (eV)	EA (eV)	χ	μ
P1	5.7	1.8	3.7	3.9
P2	5.8	1.5	3.6	4.3

Table 4.1: Computed values for the ionization potential (IP), electron affinity (EA), chemical potential (χ), and chemical hardness (μ) for the P1 and P2 Prophyrin derivatives.

inhomogeneities in the MEP can be related with an enhancement in the total dipole moment.

Molecular Orbitals

Subsequent calculation of the electronic structure properties of the P1 and P2 molecules have been carried out and the results displayed in Fig. 4.3. and Fig. 4.4. In both cases, the frontier orbitals can be related to either the iron d_{xy} or $d_{x^2-y^2}$ states coming from the Ferrocene moieties. The distribution of the energy levels in both complexes also shows that the energy difference between the HOMO and the HOMO-4 energy levels is only about 0.15 eV for P1 and 0.10 eV for P2. The observed close energy distribution of the d-metallic states could be biased due to an effective Coulomb electrostatic interaction (long-range effects [130]) amid the Ferrocenes groups located at the corners of the TPP group. This effect could lead to a reorganization of the electronic density and correspondingly changing the order of the orbital energy diagram since these interactions are not included in the bare B3LYP XC hybrid-parametrization [42]. Thus, in order to assess the impact in the electronic structure of such effects the re-optimized and re-calculated electronic structure using the cam-B3LYP XC has been carried out, where the long-range electrostatic potential is included via tuning the amount of exact exchange (HF) in a Coulomb-interaction truncated scheme [131]. The impact in the distribution of the molecular orbitals and energy levels is minimal (see appendix (A)) leading to the conclusion that the repulsive intra-molecular electrostatic interactions are not playing an essential role in the organization of the energy levels. Subsequently, quantities of interest such as the electron affinity (EA = E(n)E(n-1)), ionization potential (IP=E(n+1)−E(n)), chemical potential (χ = (IP+EA)/2), and chemical hardness (μ = IP EA) have been calculated for both phases and the results reported in Table (5.1). E(n), E(n+1), E(n-1) are electronic total energies corresponding to a total number of electrons n, n+1,n-1. As a result of these calculations one can suggest a physical picture in which the removal of an electron can be related with the direct extraction from one charge carrier of one of the Ferrocene moieties whereas the addition of one electron charge occurs at the molecular organic-core state (Porphyrin group) as it has been also established for similar molecular complexes [130]. This issue has been also observed experimentally via cyclovoltammetry experiments and therefore validating the previous calculated results [128]. Thus, once the localization of the electronic charge has been demonstrated both experimentally and theoretically its physical origin is not yet clearly understood.

Thus, in order to elucidate the possible source of such phenomenon, one can resort in the use of point group symmetry. Hence, by employing the symmetrizer software for the relaxed molecular complexes in the gas-phase ([121] two possible point groups have been obtained, namely, C_2 and C_i. At this point is noteworthy to mention that investigations of the the Porphyrin moiety has been carried in terms

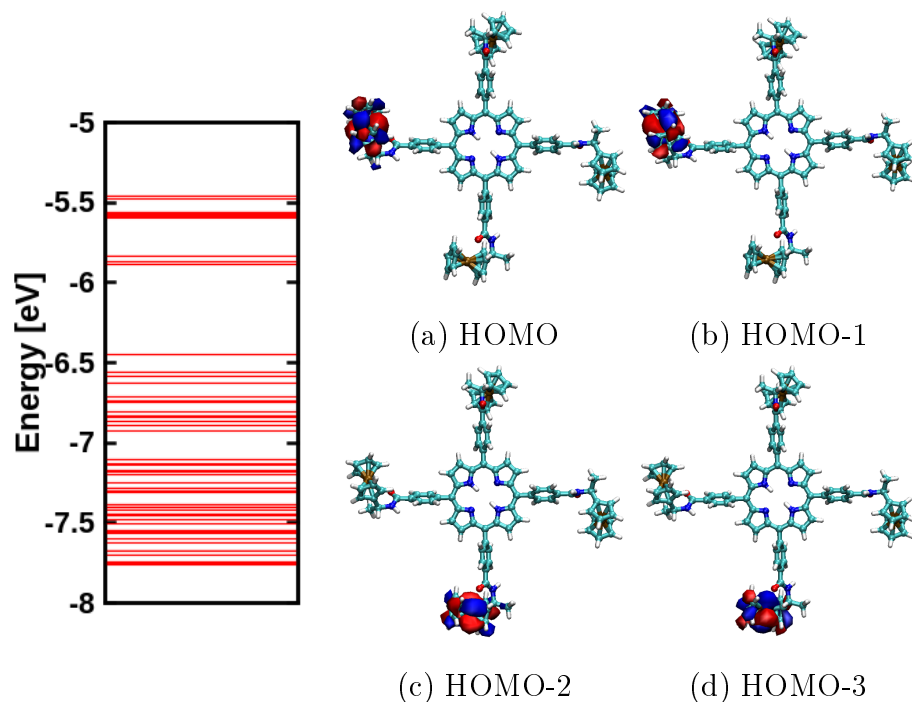(a) HOMO   (b) HOMO-1

(c) HOMO-2   (d) HOMO-3

Figure 4.3: Electronic structure of the P1 molecular complex.(a) The orbital energy diagram. (b-d) Molecular orbitals ranging from HOMO to HOMO-3. All iso-surfaces have been plotted at 0.02 e$^-$ Å^{-3}.

of its point group symmetry leading to establish that the ground state configuration exhibits a C_{2v} symmetry with a closest metastable state with an associated point group symmetry of D_2 [129]. Thus, the calculated point group symmetry for P1 and P2 are in turn subgroups of the TPP-framework preserving until some extension the point group operations inherited from the organic-core ground state symmetry and therefore the playing an important role in the organization of the orbital energies.

Vibrational analysis

In both cases, the vibrational analysis have been carried out using the CP2k code and none imaginary frequencies have been obtained ensuring a ground-state minimal energy configuration [112, 113, 114, 115]. Likewise, the infrared spectra have been simulated for both phases and results presented in Fig 4.5. For P1 the spectrum consists of a major peak located at 1825 cm^{-1} that is a combination of breathing modes of the TPP core and anti-symmetric movements of the Ferrocene moieties. In general terms, the intensity of the modes related with this complex are relatively low and are mainly hybridizations of the modes of the TPP core and the modes of the Ferrocenes functional-groups specially in the energy range of 0 to 1000 cm^{-1}. The highest intensity peaks are observed in the range between 1000 and 2000 cm^{-1} where some high energy modes of the Ferrocenes are mixed with the modes of the TPP leading to combination that are not Raman active. Concerning the P2 molecular candidate, one can observe a similar pattern than in the previous case by an enhanced region of modes that exhibit middle Raman activity ranging from 1000 to 2000 cm^{-1} with the same combinations of high energy Ferrocene moieties modes with middle energy modes from the TPP-core. In this moment one can notice that

(a) HOMO   (b) HOMO-1
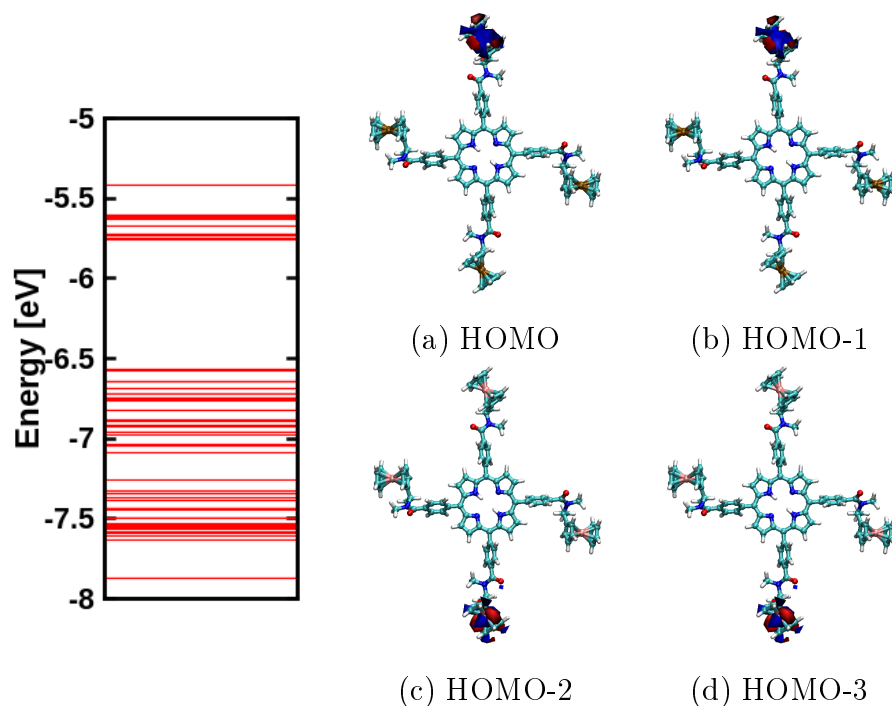
(c) HOMO-2   (d) HOMO-3

Figure 4.4: Electronic structure of the P2 molecular complex. (a) The orbital energy diagram. (b-d) Molecular orbitals ranging from HOMO to HOMO-3. All isosurfaces have been plotted at 0.02 e$^-$ Å^{-3}.

peaks in the P1 complex are more intense than in the P2 case but they are still not active in terms of Raman intensities to be sensitive to external electric fields. Finally, in the region of high-frequency modes (> 3000 cm^{-1}) is where the most notorious difference is found between the two complexes and can be ascribed to the different number of CH$_3$ groups attached to the amide moiety (bigger in P2 than P1). This is a result of the kind of non-covalent bonding intended to be enhanced for each complex, i.e., H-bonding (P1) or vdW (P2).

Photophysical properties

The vertical absorption spectra have been calculated using the TD-DFT method for both phases and results presented in Fig. 4.6. The first eight vertical electronic excitations have been computed and the results collected in Table 4.2 with the corresponding Spin symmetry, Energy excitation and Oscillator strength. In both cases the absorption spectra is plotted against the Oscillator strength. The strongest oscillator strength has been used as unity in order to renormalize the whole spectra and report the subsequent results in term of relative quantities.

As can be found in Fig. 3.6, the electronic excitation spectra of the two molecular-complexes display similar profiles and features in terms of excitation Energies, Oscillator strengths and Absorption bands. However, while for P2 two bands are associated with a transition from an occupied π bonding state provided by the Porphyrin moiety to an unoccupied π^* anti-bonding state provided by the same functional group (Porphyrin) for P1 only one of these bands is reported. In the specific case of the strongest band in P1 its origin can be ascribed to a dipole-allowed spin singlet electronic transition from the TPP moiety (HOMO-7/HOMO-8) to the excited

Photophysical properties			
Complex	Spin	Energy [eV]	Oscillator Strength
P1	Triplet (LUMO)	1.204	0.000
	Triplet (LUMO+1)	1.209	0.000
	Triplet (LUMO+2)	1.390	0.000
	Triplet (LUMO+3)	1.401	0.000
	Singlet (LUMO+4)	2.106	0.000
	Singlet (LUMO+5)	2.108	0.000
	Singlet (LUMO+6)	2.138	0.023
	Singlet (LUMO+6)	2.138	0.023
P2	Triplet (LUMO)	1.392	0.000
	Triplet (LUMO+1)	1.667	0.000
	Triplet (LUMO+2)	1.961	0.000
	Triplet (LUMO+3)	2.009	0.000
	Singlet (LUMO+4)	2.115	0.000
	Singlet (LUMO+5)	2.116	0.001
	Singlet (LUMO+6)	2.138	0.026
	Singlet (LUMO+7)	2.277	0.038

Table 4.2: Computed electronic excited states by employing TDDFT for (upper) P1 and (lower) P2 molecular complex. First column indicates the spin-symmetry of the state. Second column designates the associated energy of the excitation and third column reports the computed oscillator strength.

states associated to the same funtional group (LUMO/LUMO+2/LUMO+6). Interestingly, the other calculated excitations are related with transitions from the ground-state frontier d-states associated with the Ferrocene-moiety (d_{xy} and $d_{x^2-y^2}$ symmetry) to their first excited states (d_{yz} and d_{xz} symmetries). However, once the Oscillator strength is calculated all these metallic transitions are not optical-allowed despite the fact that in the individually functionalized Ferrocene groups one can report strong Oscillator strengths (see A for the UV-vis spectra). This issue can be understood in terms of the symmetry constraints imposed by the TPP-moiety that determines the new optically-allowed transitions. Moreover, transitions that could lead to a possible metal to ligand charge transfer (MLCT) have been obtained (LUMO and LUMO+1) but their oscillator strength is zero making them not optically-allowed. Finally, the energy and symmetry of the first computed excited state agrees with the calculated physical picture of EA where an electron is accommodated in an organic-core state provided by the Porphyrin. Concerning P2, the optically-allowed excitations are found to be composed by π bonding states of the TPP (HOMO-10/HOMO-11) to π^* anti-bonding states of the same moiety (LUMO+6/LUMO+7). Similarly, the possible metal to ligand charge transfer (MLCT) states amid the metal-like functionalized-Ferrocene molecular orbitals and the low-lying π^* orbitals provided by the TPP are obtained (LUMO and LUMO+1) but are not optical-active since the reported oscillator strength is 0. In the end, the computed EA is in good accordance with the calculated first excited-state and confirming the physical picture in which the added electron charge is hosted in an orbital belonging to the organic-core.
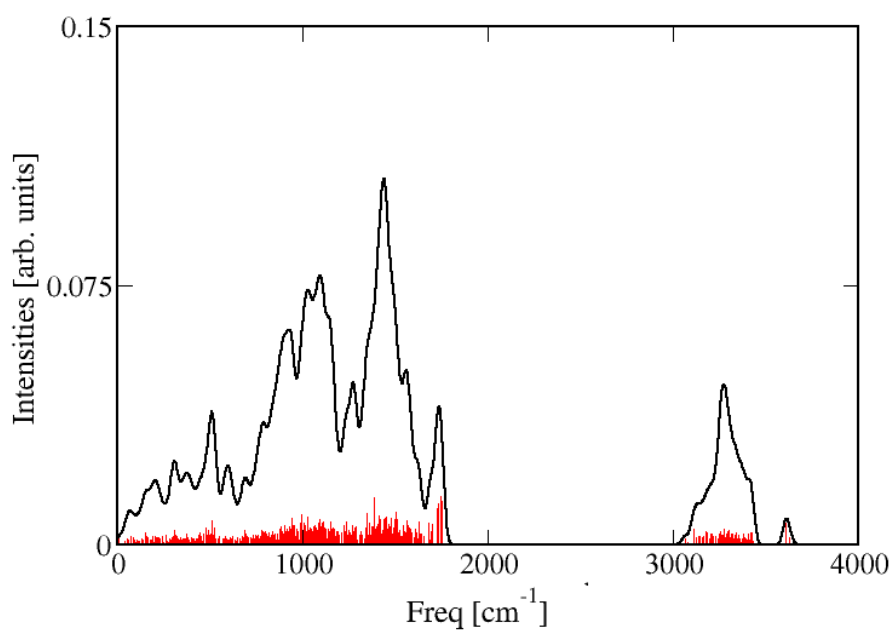
(a)
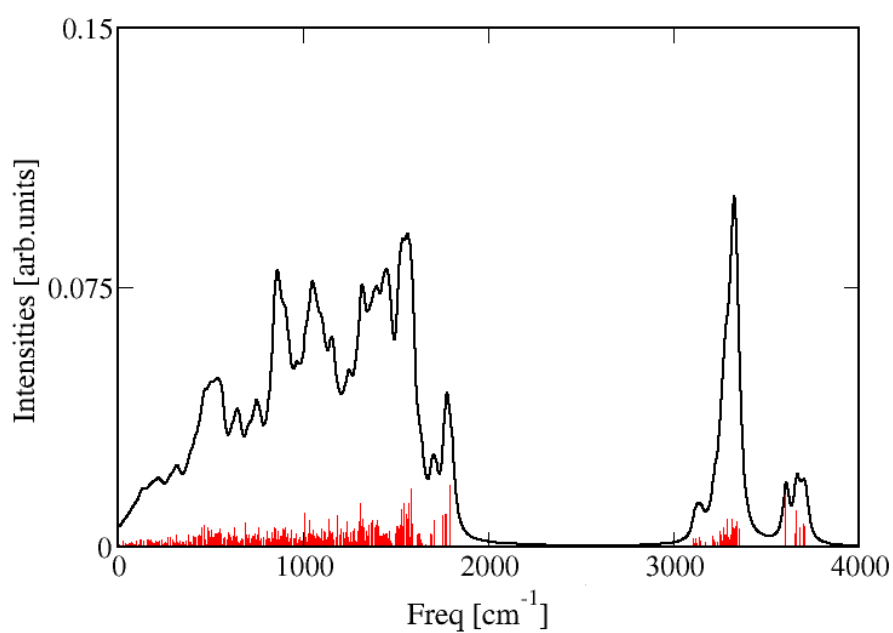
(b)

Figure 4.5: Simulated Raman spectrum for (a) P1 and (b) P2 molecular complexes. In both phases the most intense vibrational mode corresponds to a hybridization of the nuclear displacements of the TPP organic-core moiety and the Ferrocene functional groups. The atoms located at the amide functional group of the P1 and P2 molecules are also involved in these displacements and those are the responsible for the self-assembly process linked by H-bonding bonding and vdW, correspondingly.
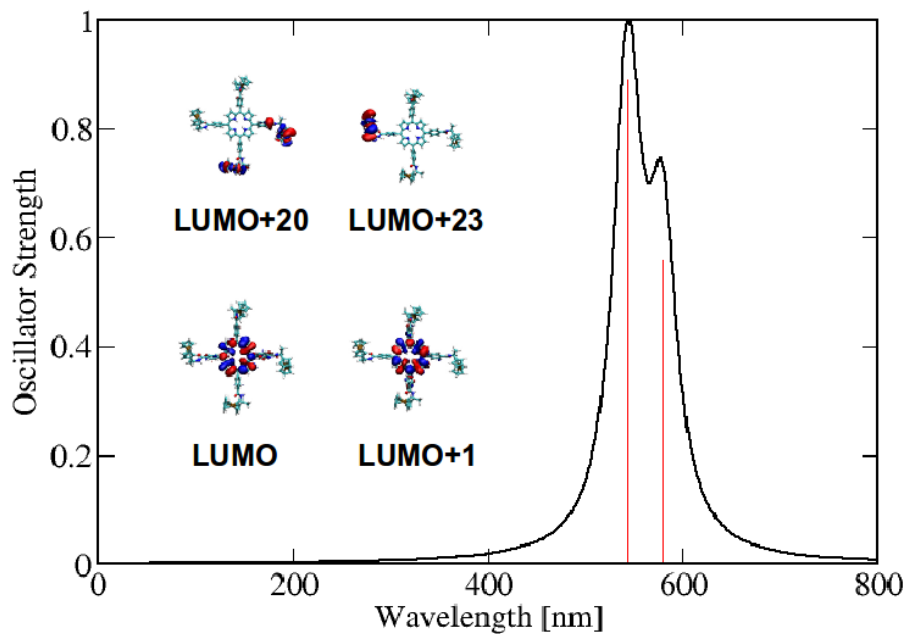
(a)
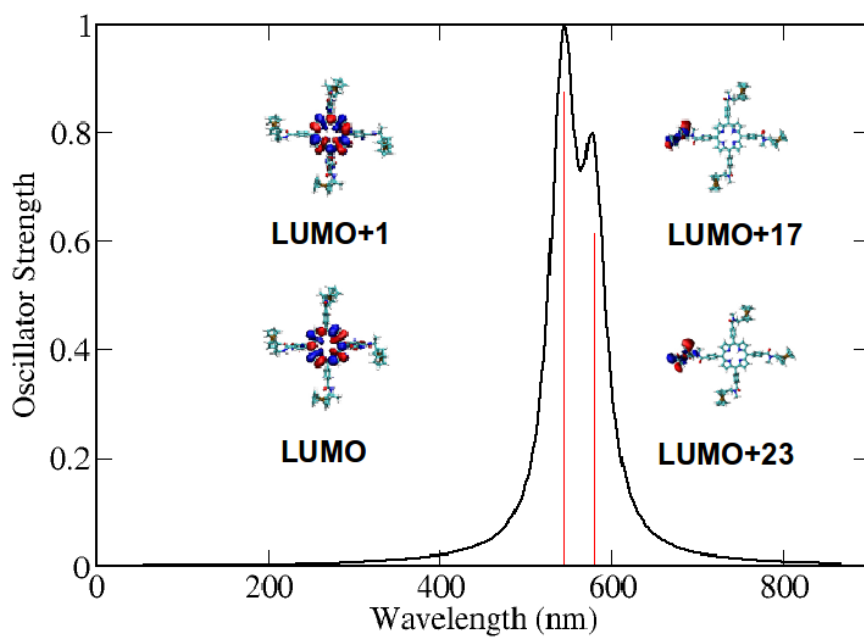
(b)

Figure 4.6: Simulated UV-vis spectra for (a) P1 and (b) P2 molecular complexes. Oscillator strengths are normalized to the highest value and the obtained results reported in relative quantities.

4.2 SCAFFOLDING VIA INTRA-MOLECULAR HYDRO-GEN BONDING IN THE P1 AND VDW FORCES IN THE P2 MOLECULAR COMPLEXES

In this section, the interactions driving the molecular self-assembly process will be described and investigated. Firstly, the main focus of the study will be given to the contribution of each of these interactions, namely, intra- and inter- cell in the global mechanical and energetic stability of the system. Therefore, in order to peruse the many different physical scenarios suitable models are created and their stabilities are tested by employing total energy DFT calculations. Afterwards, the optimized unit cells will be used to investigate the electronic structure of the molecules within the two-dimensional networks. This is an important issue since the electronic properties can be changed due to the creation of narrow energy bands and in consequence raising the question whether electron localization is preserved while the two-dimensional networks have been formed. Thus in order to asses the nature of the network formation one can define the cohesion energy as:

$$E_{cohesion} = E_{Total} - n(E_{Single}) \qquad (4.1)$$

where E_{total} is the total energy of the two possible inter-cell interactions, E_{Single} is the total energy of the isolated P1/P2 complex and n is the number of times the isolated molecule is observed in the interaction.

Network formation in the P1 molecular complex

In order to investigate the experimental observed motifs [128] the previously optimized molecular building block has been used to create the corresponding molecular scaffolds by enclosing the geometrical optimized molecules in gas phase in a unit cell with lattice constant values close to the ones that has been experimentally mesured. Once the unit cell has been created, periodic boundary conditions have been used and both atomic positions and dimensions of the unit cell has been further relaxed and is considered relaxed when an accuracy of $1x10^{-7}$ Hartree for the SCF energy and $9x10^{-4}$ Hartree Å^{-1} for the force gradient has been reached. In the case of the molecular complex P1, the obtained $\vec{a} = 2.1\text{Å}$ and $\vec{b} = 2.2\text{Å}$ lattice constants in our procedure are in good agreement with the ones reported experimentally of $\vec{a} = 2.2\text{Å}$ and $\vec{b} = 2.2\text{Å}$, respectively. For the first Porphyrin derivative (P1), the origin of the self-assembly motif can be ascribed to the targeted functionalization carried out at the meso position of the TPP molecule. Therefore, the amide groups promote the formation of Hydrogen-bond supramolecular structures in a face-on configuration over the HOPG. However, in the formation process of the scaffold structure the Ferrocene moieties belonging to different unit cells are closely packed rising to a possible long-range repulsive electrostatic interaction between the Ferrocene groups that could distort the organization of the energy levels [132]. Thus, in order to peruse the electronic properties of the self-assembled face-on architecture the projected density of states (PDOS) has been calculated and the result displayed in Fig.4.7 where the profiles are obtained by a fixed Lorentzian broadening (fwhm = 0.4 eV).
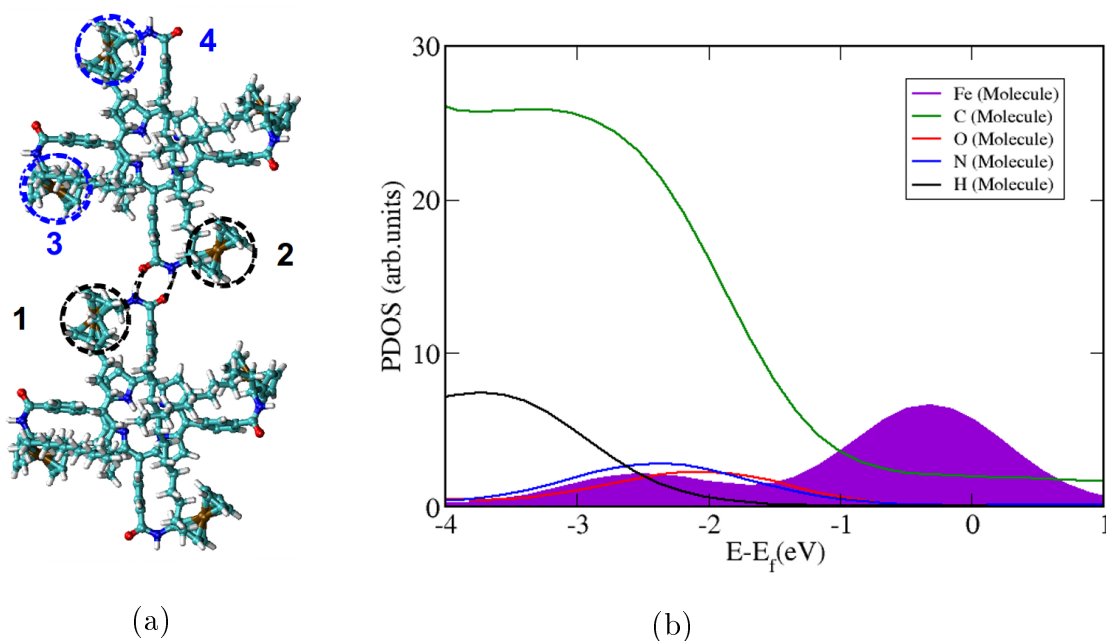
(a)   (b)

Figure 4.7: The inter- and intra- molecular interactions between adjacent cells for the P1 complex.(a) Along the $\vec{a}$ or $\vec{b}$ lattice vector. (b) Projected Density of States (PDOS) close to the Fermi energy. The Ferrocene moieties are encircled with a black (1,2) and blue dashed (3,4) lines indicating inter- and intra- molecular interactions, respectively. The inter H-bond interaction is highlighted with black-dashed lines.

In these diagrams, the energy levels have been rescaled to the HOMO so that the zero energy is relative to this energy level. Thus, the negative and positive energy values are associated, respectively, to occupied and virtual molecular orbitals. Noteworthy, the states provided by the Carbon and Iron atoms depict larger spectral weights when they are compared with other atomic species such as Nitrogen, Oxygen and Hydrogen in the region close to the HOMO-LUMO gap. In terms of spectral weights, one can conclude that the states obtained in energy ranges close to the HOMO are related to the Ferrocene groups. A visual inspection of the associated canonical molecular orbitals corroborates this physical picture since these molecular states display symmetries corresponding to the d_{xy} and $d_{x^2-y^2}$ ideal gas-phase Ferrocene molecular orbitals. Interestingly, the metallic d-states associated with the Ferrocene groups are split into two contributions one of them located at energy ranges of -2.5 eV and displaying a smaller spectral weight contribution than the other associated with the frontier molecular orbitals at the HOMO energy range. This is a consequence of the orbital energy organization of the original isolated Ferrocene moiety in which the HOMO and HOMO-1 energy levels are degenerated while the HOMO-2 is associated with only one d states (with symmetry d_{z^2}). Therefore, once brought together the HOMO states of the four Ferrocenes combine to form the upper part of the electronic structure while the remaining d-states are placed at lower energy ranges and undergoing stronger hybridization with the states associated with the organic-core states. In order to shed light onto the possible mechanisms of network formation a total energy analysis has been carried out where the H-bond mechanism is scrutinized and the model used displayed in Fig. 4.7 and the results of the calculation collected in Table. 5.3. Consequently, the surmised self-assembly mechanism (H-Bond) ascribed to the P1 complex is not
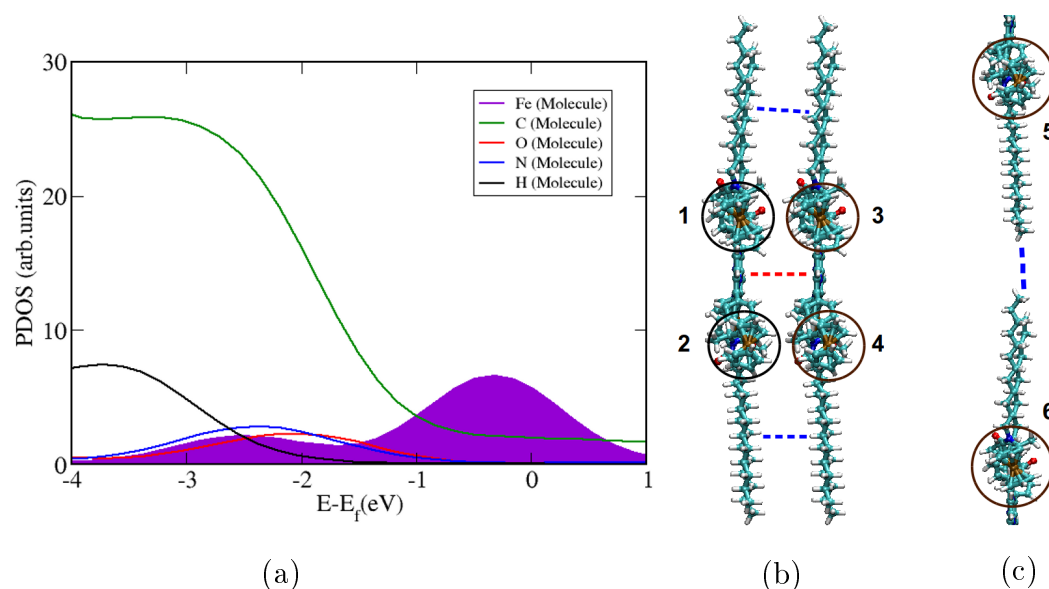
Figure 4.8: The inter- and intra- molecular interactions between adjacent cells for the P2 complex. (a) Along the $\vec{a}$ lattice vector. (b) Along the $\vec{b}$ lattice vector. The Ferrocene molecules are encircled with a dashed line. The possible sources of vdW interactions are highlighted with blue arrows while red arrows indicates the repulsive interaction $\pi - \pi$ interaction of the organic-core.

sufficient to explain the experimentally observed patterns, indicating a stronger influence of the substrate in mediating the energetics and stability of this molecular complex.

Network formation in the P2 molecular complex

Concerning the P2 molecular complex the suggested lay-out is built by a single molecular complex. The formation of these scaffolds are based exclusively on van der Waals interactions by replacing the secondary amides with tertiary ones. Thus, it is expected that the van der Waals interactions between the P2 cores, as well as alkyl side-chains are the driving forces to govern this self-assembly motifs [128]. In consequence, two possible sources of inter-molecular interactions can be inspected and whose models are displayed in Fig. 4.8. In order to peruse the electronic and mechanical properties of the complex this has been geometrically optimized, using periodic boundary conditions, from the gas-phase to the experimentally suggested unit cell. The computed lattice constants ($\vec{a} = 52.1$Å and $\vec{b} = 6.9$Å) are in good agreement with the experimental proposed values ($\vec{a} = 51.0$Å and $\vec{b} = 6.1$Å). A closer inspection to the geometrical arrangement of the molecular complex reveals many possible sources of electrostatic repulsive interactions especially along the $\vec{a}$ lattice vector that can affect the mechanical stability of the network. Firstly, the P2 molecular complex contains four-Ferrocene moieties where localized states have been reported in the gas-phase calculations and leading to a possible repulsive Coulomb interaction between the tightly packed adjacent cells as shown in Fig 4.8(a) [132]. Furthermore, in the same direction the notorious on-edge configuration leads to a possible second source of repulsive interaction due to an effective $\pi - \pi$ arrangement between the organic-cores that has been already experimentally reported for the

Molecular Complex	vdW (eV)	H − Bonding + Repulsion (eV)	Adsorption (eV)
P1	N/A	0.35	-0.45
P2	-0.047	0.11	-0.60

Table 4.3: Calculated total energy differences for the different interactions for both complexes. Note that three different interactions have been considered as shown in Fig.(3.12 (a,b,c)) and Fig.(3.10 (a,b,c)).

TPP complexes [133]. This situation is similar as the one observed in other Carbon structures such as Graphite in which the dispersion and induction effects are important to define the correct distance that balances these two forces. On the contrary, the only pure cohesive interaction observed in the unit cell is between the alkyl chains along the $\vec{b}$ in both cases of intra- and inter- cell interactions. The obtained positive energy results (see Table 5.3) suggests that the experimentally observed motif P2 complex is not mechanical stable if only the vdW interaction is the assumed source of cohesion and suggesting a much more active role played by the surface in the network-process formation.

4.3   MOLECULE-SURFACE INTERACTION:

One of the crucial points in order to implement the m-QCA paradigm is the influence of the adsorption process in the electronic structure of the candidate molecules. Moreover, as it was found in the previous analysis this interaction plays a more fundamental role in terms of energy and mechanical stabilization of the supramolecular architecture. In order to study the effect of the surface on the electronic structure of the P1 and P2 molecules the slab technique has been employed. In the case of HOPG three atomic layers have been included in the previous relaxed unit cells and on top of which 40 Å vacuum space has been added to avoid spurious interactions between periodic images. Likewise, since the molecules have been assumed to behave like a two-dimensional lattice the Brillouin zone has been only sampled at the Γ point without loss in accuracy given the fact that large lattice vectors have been employed to simulate the surface when compared with the original Graphite unit cell. To quantify the interaction between the molecules and the substrate, we define the adsorption energy as:

$$E_{ads} = E_{total} - (E_{P_1/P_2} + E_{HOPG}) \qquad (4.2)$$

where E_{total} is the total energy of the structurally optimized unit cell, E_{P_1/P_2} is the total energy of the geometrically relaxed P1/P2 molecule in vacuum and E_{HOPG} is the total energy of the optimized graphite slab.

Physisorption of the P1 complex

In order to clarify the role played by the surface and the impact of it in the electronic structure of the P1 molecule the Graphite substrate has been included in the previously optimized unit cells through a slab model using three atomic layers
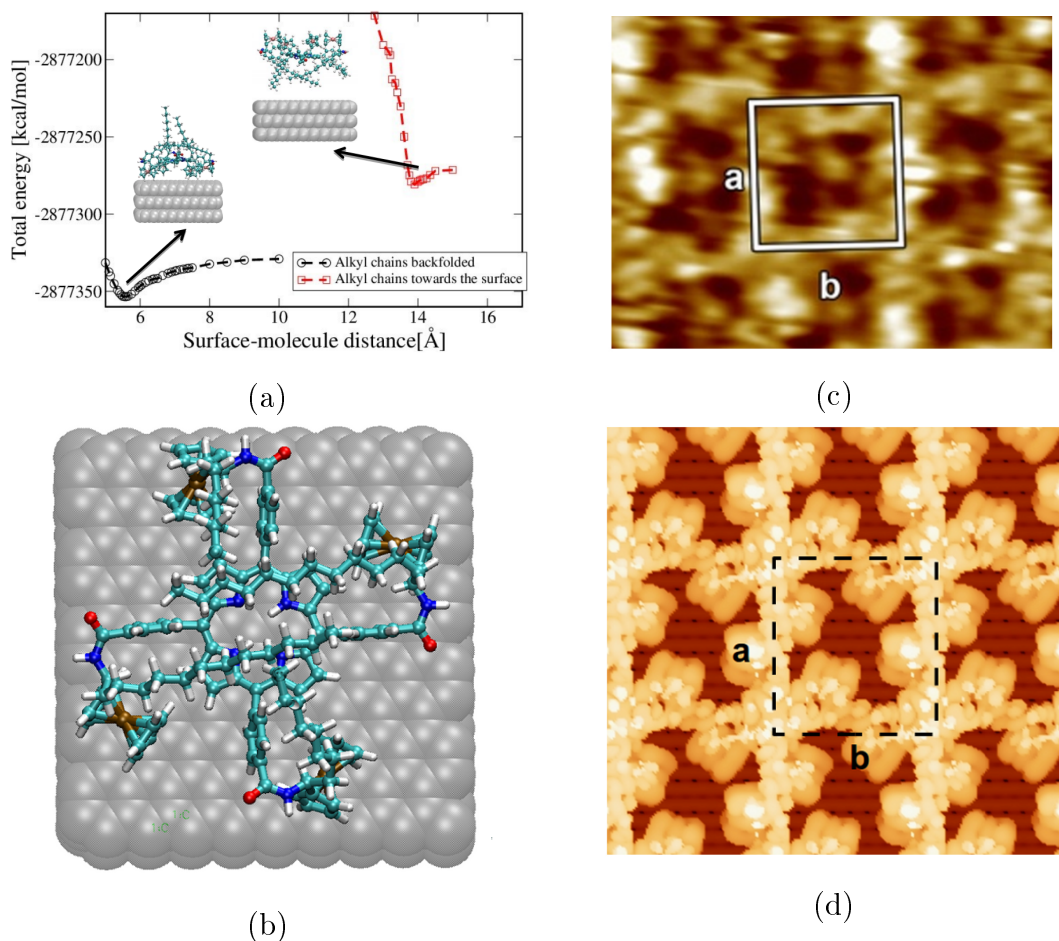
(a)

(c)

(b)

(d)

Figure 4.9: The most stable computed molecular conformation for the P1 molecules when is adsorbed on HOGP.(a) Perpendicular view along the self-organization plane.(c) Experimental environmental-STM image. (d) Simulated STM image under experimental conditions (-500 meV, $|\psi|^2 = 10^{-7}$ Å^{-3} integration of the wavefunction).

on top of which 40 Å of vacuum space has been added to avoid spurious interactions between periodic images. The optimized molecule-surface geometry is shown in Fig(4.9). The projected density of states (PDOS) have been calculated and the results shown in Fig(4.10). Thus, in energy ranges close to the Fermi energy one can observe a large spectral weight coming from the Ferrocene d-states which includes the states provided by the Carbon atoms in the Ferrocene moieties. This feature strongly indicates that the electronic localization is preserved and has been experimentally observed by cyclovoltammetry measurements where the obtained reduction potential is close to the value of the Ferrocene complex. Similarly, the states provided by the Oxygen, Nitrogen and Hydrogen species are also observed in energies ranges of -2 to -1 eV with a rather larger spectral weight; this can be ascribed to the dominance of the Hydrogen bonding in the formation of this network and validating the initial guess of this interaction as the driving mechanism to form the supramolecular architecture. Particular attention has been devoted to peruse the position of the alkyl chains, since it was a puzzling issue to guess the best possible spatial lay-out of the chains within the unit cell. Hence, the potential energy surface has been computed for the case where the chains are back-folded in the supernatant solution, with the conjugated core facing directly the HOPG surface.

The relevant length was chosen to be the distance of the normal vector cantered at the plane created by the four Iron atoms with a Carbon atom of the surface. For each molecule-surface separation, the atomic positions were relaxed leading us to observe a clear minimum at 5.5 Å in the total energy surface (see Fig. 4.9). On the contrary, the minimum distances between the Ferrocene moieties and the Graphite substrate found in the second configuration, with alkyl chains below the porphyrin core and thus closer to the surface, were determined as 10.5 Å. In this case the alkyl chains act a mechanical buffer that decouples the Ferrocene moieties and the conjugated porphyrin cores from the HOPG surface. As a result of this analysis, one can concluded that the long alkyl chains are back-folded, pointing away from the substrate, and that this conformation is the most energetic favorable, in agreement with the experimental results. Moreover, STM images have been simulated for the molecule on the surface and shown in Fig. 4.9(c) and compared with those obtained by environmental STM [54]. Thus, one can observed a good resemblance between the two images supporting the theoretical results where the d-metallic states provided by the Ferrocene molecule are the main states contributing in the range near the Fermi energy. However, from the previous results one can conclude that the mechanical stability cannot be exclusively explained by the non-covalent interaction since the presence of a strong repulsive electrostatic interactions amid adjacent unit cells. Thus, at this point the obtained experimental results can only be explained by a more active role of the surface in mediating the energetic and mechanical stability of the whole network since the important contribution of the associated states of the surface in the calculated PDOS. The obtained adsorption energy (see Table 5.3 for the actual value) is negative and has an absolute value larger than the obtained repulsive energies from the inter-molecular interactions. Hence, one can conclude that the self-assembly process is initiated by a H-bonding process between the amide groups forming the characteristic square two-dimensional assemble but finally mechanical stabilize it by the adsorption energy of the surface. However, from the experimental STM images no clear localized electron states can be resolved and strongly indicating that the paradigm can not be implemented in this system [128].

Physisorbtion of the P2 complex

On the contrary to the P1 molecular complex, the P2 candidate displays a more complex interaction with the HOPG due to a direct adsorption of the Ferrocenes moieties over the first layer. In literature, the adsorption of the gas-phase Ferrocene molecule over many different surfaces has been investigated leading to a range of many possible effects such as charge transfer, magnetization and self-assembly formation [134]. Thus, it is worth mentioning that a experimental investigations of the adsorption of Ferrocene over graphite at low temperatures have been carried out leading to interesting results in which the Ferrocene moiety displays a clear preference to be in a perpendicular configuration rather than in a parallel layout [134, 135]. The calculations have been carried out using the same methodology as in the P1 case where the slab consists of three-layer of 240 Carbon atoms. The obtained optimized structure is shown in Fig. 4.11 (a). In general, both the Ferrocenes complexes and the long alkyl-chains are aligned almost parallel to the stacking axis of the HOPG surface in a similar way as it has been previously suggested in the Graphene case. In order to observe possible magnetization effects a single-point DFT spin-dependent calculation has been carried out. The results of this calculation indicates no magnetization in any of the Ferrocene molecules on the contrary to the obtained in the case of the Ferrocene over the doped-graphene surface [136]. The adsorption distances of the two Ferrocenes moieties are around 5.5 Å. In order to investigate the
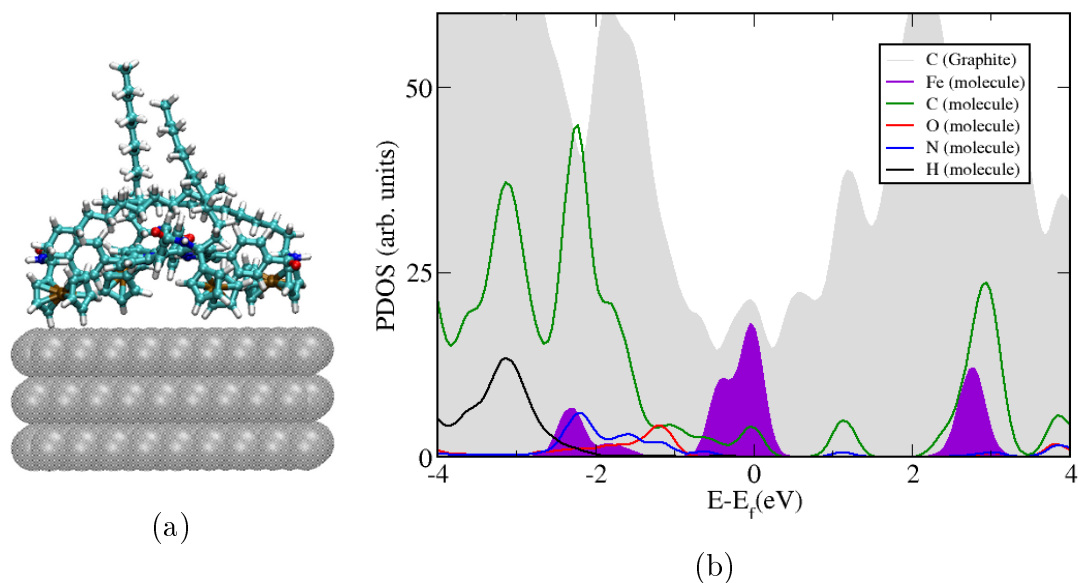
(a)

(b)

Figure 4.10: Electronic structure of the P1 molecular-complex including a HOPG slab.(a) Projected Density of States (PDOS) where all atomic contributions have been added. (b) Associated molecular orbitals to the corresponding four upper molecular levels. Surface was removed to ease the observation of the molecular orbitals.

impact of this interaction on the electronic structure of the molecule the PDOS has been calculated and results displayed in Fig. 4.12. In the region near the Fermi energy the larger spectral weight is assigned to the states provided by the Ferrocene moieties including the Carbon atoms belonging to the complex and strengthen the physical picture of the preservation of the localization of charge. This assumption is experimentally assessed via Cyclovoltammetry measurements where the reduction potential measured for this supramolecular architecture can be closely related with the reduction potential of the Ferrocene in gas-phase providing a corroboration of the localization of the electronic charges at the Ferrocene moieties. Similarly, the states provided by the other atomic species such as Oxygen, Nitrogen and Hydrogen contributes to the PDOS with large spectral weights in energy ranges of -1 to -2 eV. This is a clear indication of the participation of the H-bond in the electronic structure and also the interaction with some localized states provided by the Ferrocene functional groups and due to the splitting between the d_{xz} and $d_{x^2-y^2}$ and the d_{z^2} states. Subsequently, STM images have been simulated for the P2 molecular complex on the surface and shown in Fig. 4.11(c) and compared with those obtained by environmental STM [54]. Thus, one can observed a good resemblance between the two images supporting further the theoretical results where the d-metallic states provided by the Ferrocene molecule are the main states contributing in energy ranges close to the Fermi energy. Nonetheless, the mechanical stability cannot be exclusively explained by the vdW interaction since the presence of a strong repulsive electrostatic interactions amid adjacent unit cells due to this electron localization. Thereby, the adsorption energy of the total system has been computed (see Table 5.3 for the actual value) is negative and its absolute value larger than repulsion energy. In this case, the self-assembly mechanism involves a rather complicated process in which the P2 molecules form a vdW supramolecular motifs in the liquid state and then when they are absorbed onto the HOPG the tendency of the Ferrocene to lie in a parallel configuration over this surface facilitates the formation of the observed packing distribution. Although, from the experimental STM images clear
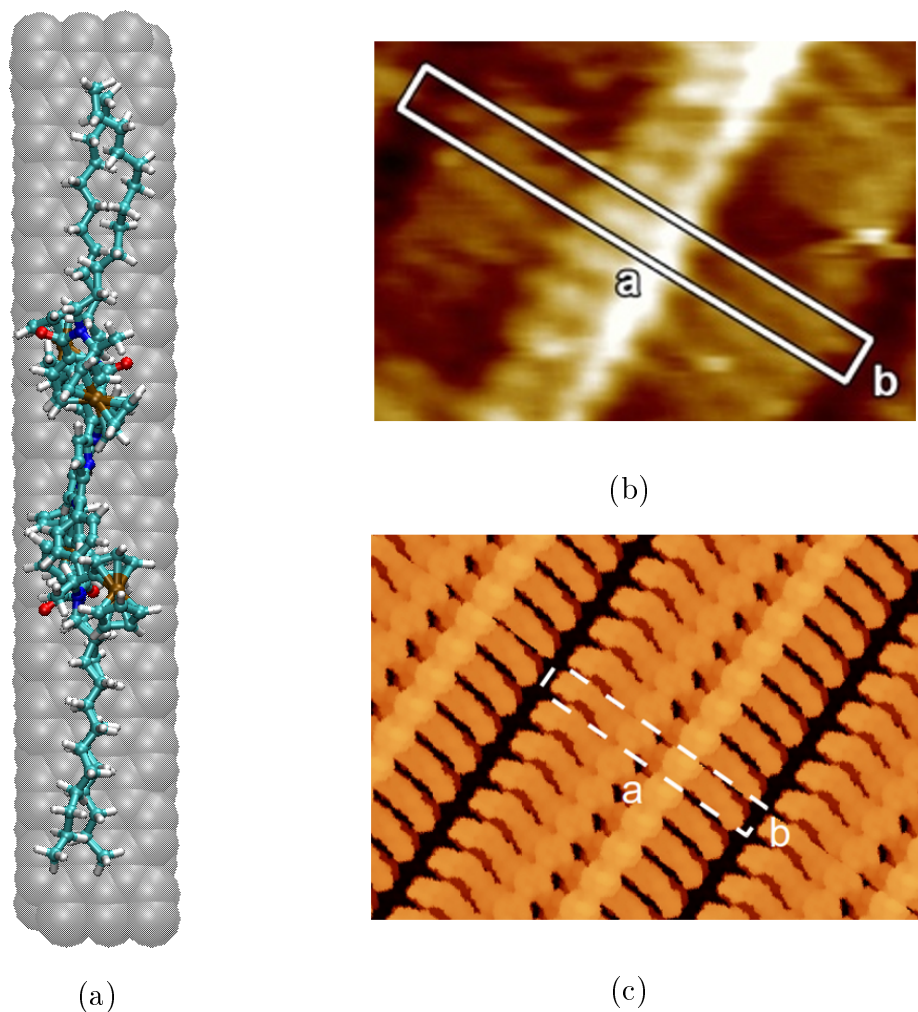
(a)

(b)

(c)

Figure 4.11: The most stable computed molecular conformation for the P2 molecule when is adsorbed on HOGP. (a) Perpendicular view along the self-organization plane. (b) Parallel view along the self-organization plane.(c) Simulated STM image under experimental conditions (-0.5 V, $|\psi|^2=10^{-7}$ Å^{-3} integration of the wavefunction).

indications of localized electron states can be resolved (see Fig. 4.12(b)) not feasible allocation of classical "1" and "0" states can be done and whence one can state that the paradigm can not be implemented in this system.

4.3.1 Statistical analysis of the AIMD trajectory

In order to assess the mechanical stability of the complex ab-initio molecular dynamics simulations (AIMD) have been carried out employing the CP2K sortware [122]. The fully relaxed structures have been used as starting point of the trajectory. Since the main interest is to recreate the experimental conditions the random velocities for each atom are taken from an ensemble average that corresponds to a temperature of 300K. Thus the average temperature along the trajectory is kept close to the aimed temperature by using a Nosé-Hoover thermostat [123, 124]. This specific
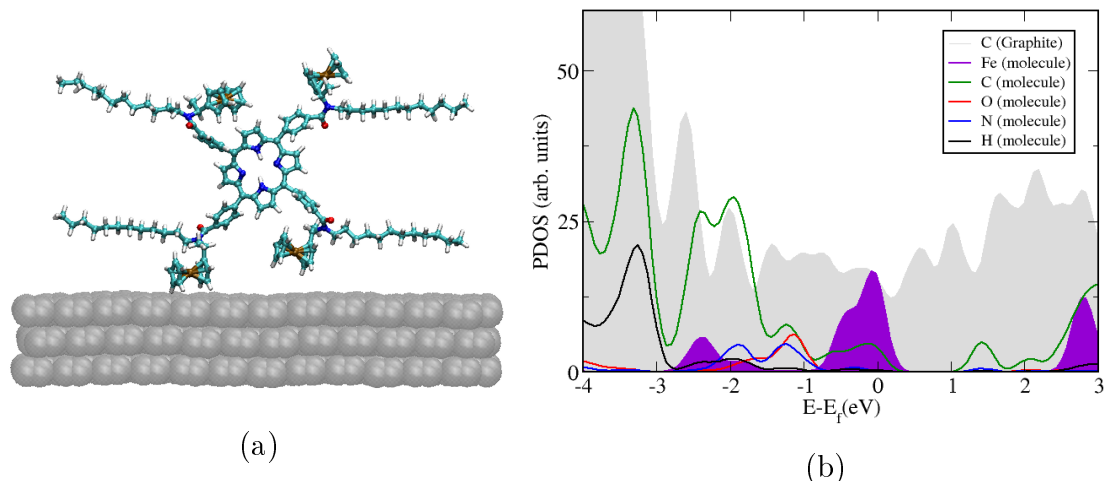
(a)

(b)

Figure 4.12: Electronic structure of the P2 molecular-complex including a HOPG slab.(a) Projected Density of States (PDOS) where all atomic contributions have been added. (b) Associated molecular orbitals to the corresponding four upper molecular levels. Surface was removed to ease the observation of the molecular orbitals.

thermostat allows the system to exchange energy with an external heat reservoir (bath) whereas the statistical correlations are not destroying along the trajectory. Finally, periodic boundary conditions have been employed and where the unit cell dimensions are kept constant as reported in the optimized structure excluding from the simulation effects such as thermal expansion and fluctuations. A trajectory of 1 ns for the P1 complex and 5 ps for the P2 has been computed in order to perform a detailed analysis of the mechanical stability of the molecule at T = 300K.

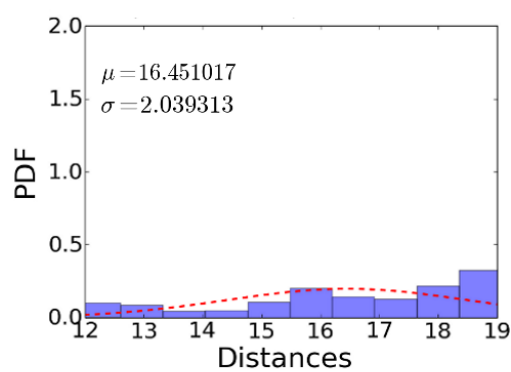## 4.3.2 Statistical analysis of the molecular dynamics trajectories for the P1 and P2 complex

In order to asses the impact of the temperature in the energetic and mechanical stability of the surface and molecule system ab-initio molecular dynamics calculations (AIMD) have been carried out [122]. In order to analyze the stability of the different supramolecular-networks statistical tools have been used in order to peruse for correlation and distributions of the selected random variables. In this case, the selected random variables (see Fig. 4.13) for P1 are the distances amid the atoms that forms the intra-cell Hydrogen-bonding. Likewise, the distances among the Ferrocene moieties both intra- and inter- have been analyzed. Concerning P2, the perused random variables are related with the distance between the long alkane-chains and the organic-cores. Similarly, the distances among the intra- and inter-cell Ferrocene groups have been analyzed (see Fig. 4.14). In the case of P1, in all the studied random variables the computed p-values are lesser than 0.05 where one can conclude that the null-Hypothesis (the random variables come from a normal distribution) must be rejected. For P2, the similar situation occurs where none of the computed p-values for the random-variables is bigger than 0.05. These results indicate that the random variables have not converged in distribution. In order to investigate possible correlation, the Pearson coefficient has been calculated for the
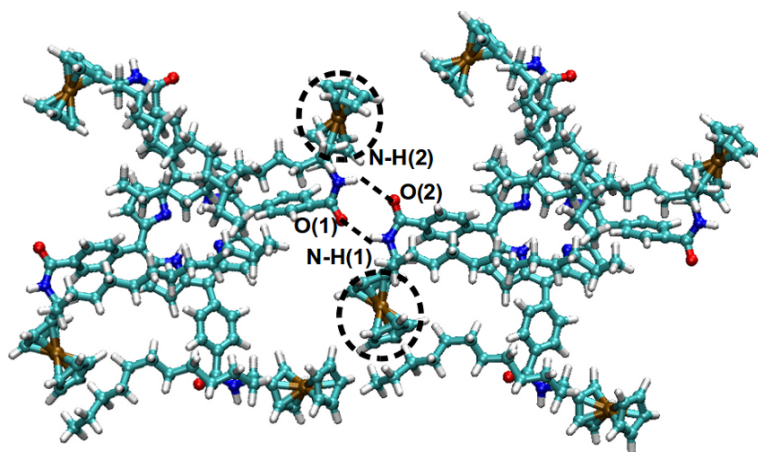
(a)
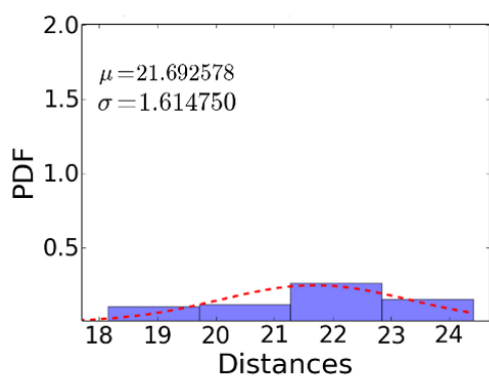
(b)

(c)

(d)

Figure 4.13: Statistical analysis including the unnormalized Probability Density Function (PDF) for the different atoms involved in the formation of the dimer ribbon for the G1 molecular complex.(a) G1-dimer snapshot of the AIMD simulation.(b) N(1)...H(1). (c) O(1)...H(1).(d) N(2)...H(2).
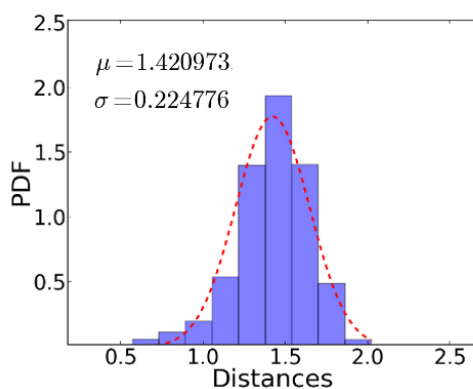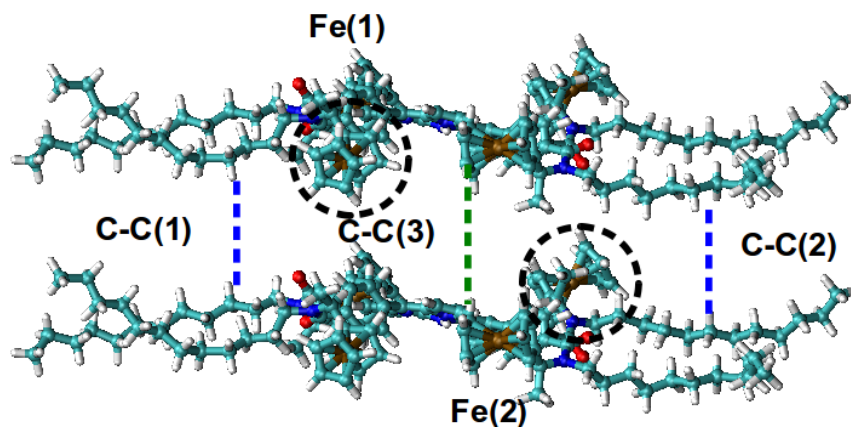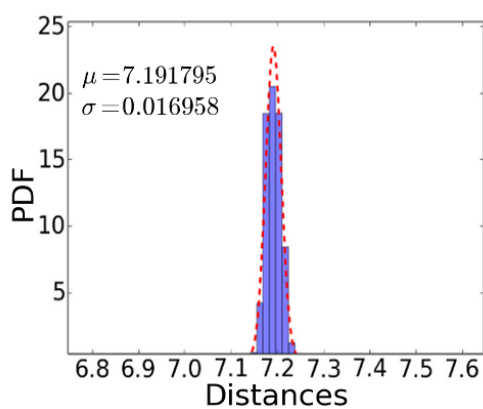
(a)

(b)
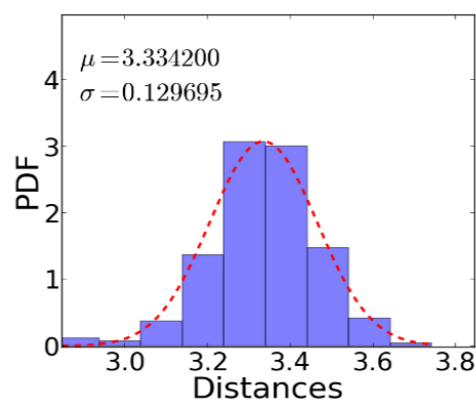
(c)
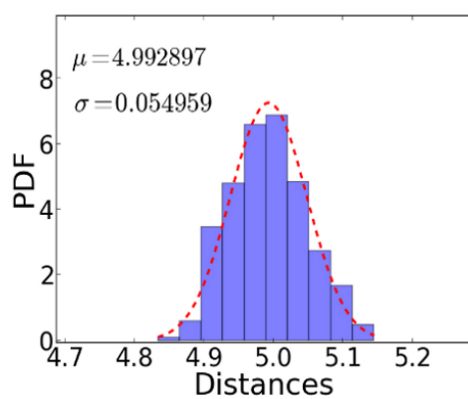
(d)
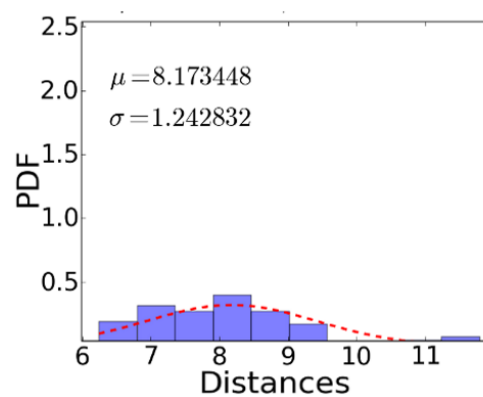
(e)

Figure 4.14: Statistical analysis including the unnormalized Probability Density Function (PDF) for the different atoms involved in the formation of the dimer ribbon for the P2 molecular complex.(a) P2-dimer snapshot of the AIMD simulation.(b) N(1)...H(1). (c) O(1)...H(1).(d) N(2)...H(2).

three-possible combinations of random variables in the P1 complex and four in the case of P2. In both cases, the Pearson coefficients indicates a low linear-correlation that for P1 is positive correlated while for P2 are almost negative correlated [126]. In conclusion, analysis of the trajectories display the mechanical stability of the complexes P1 and P2 in terms of supramolecular motif formation but no statistical correlations between the many different moieties within the molecular complex. Interestingly, the distances of the amide groups in P1 and the long-alkene chains for P2 are stable and displaying small variations which indicates the stability of these bonds against temperature effects.

5 IONIC DOPED FERROCENE-APPENDED TETRAPHENYL IMPLEMENTATION

In this chapter a systematic investigation of a monolayer of Ferrocene-appended porphyrin complexes on a Au(111) metal surface is carried out. Thus, the main objective of this study is to try to understand the metallic-surface interaction and to investigate until what extent this effect can be used as a clocking mechanism in this family of m-QCA candidates. Firstly, either the metallic substrate can modulate (via an induced electric field) the gap between the molecular orbitals of the system or make a more direct impact on the electronic structure via a interface charge transfer (ICT) process [137, 138, 139]. These two strategies can lead to an effective localization of the charge by creating the pair of molecular orbitals needed to represent the classical binary states required in the m-QCA paradigm [5]. Thus, these series of mechanisms can be used to further tune the electronic structure of the molecules and require only the alteration of the local electric field of the molecule while still allowing to carry out computation [5]. Therefore, in section 5.1 the electronic structure of the isolated molecules is investigated in order to understand the role played for the Ferrocene-moieties in the charge localization and the energy-level ordering [140]. In section 5.3, the electronic properties of the molecules within their corresponding unit cells have been further studied by explicitly constructing the two-dimensional scaffolds. The periodic monolayer will be investigated focusing the inquiry in the energy-level organization and the fundamental band-gap as a decisive quantity to understand the energy-level alignment with the surface states [141]. Likewise, the driving forces that allows the network formation, namely, the inter- and intra- cell molecular interactions between adjacent cells are scrutinized to establish its role in the supramolecular architecture. In section 5.5, the interaction between molecule and surface is investigated so as to examine the impact in the electronic structure in the molecular complexes when those are absorbed on a metallic surface Au(111). The results of these calculations are compared with experimental UHV-STM images establishing a good comparison point in order to validate the employed methodology [142].

TPP-P3

M= -H H-

TPP-P4

M = Zn

5 nm

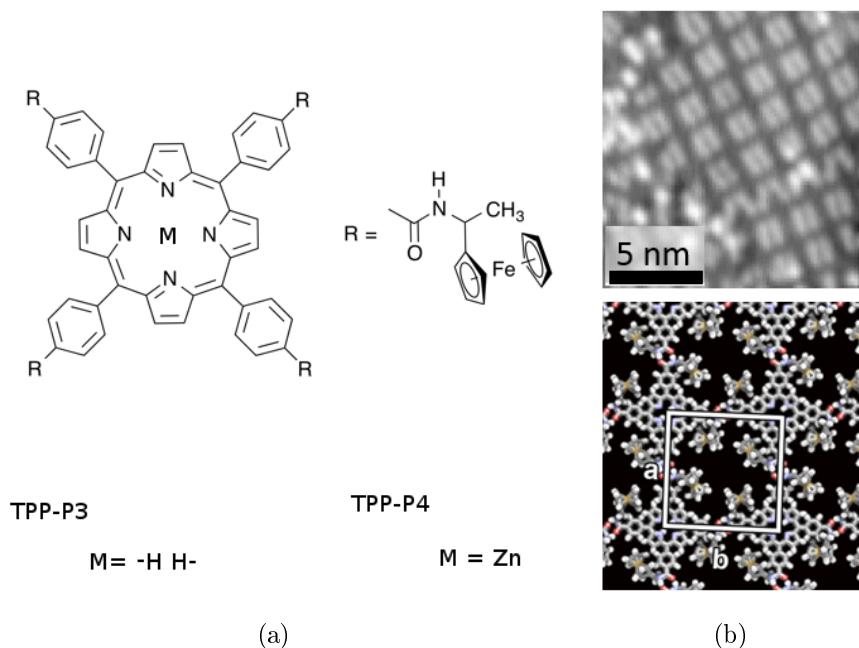(a)   (b)

Figure 5.1: The two synthesized Ferrocene-appended porphyrins derivatives.(a) TPP-P3 and TPP-P4 molecular complexes in which the conjugated spacer contains an amide group to enhance the Hydrogen-bonding between adjacent molecules.(b) Experimental UHV STM image showing occupied states and experimental suggested motif of the TPP-P4 molecular complex absorbed on Au(111).

5.1   MOLECULAR BUILDING BLOCKS

Based on the previous attempts with this family of porphyrins a new-generation of molecular building blocks have been specifically synthesized in order to construct tighter supramolecular architectures while preserving the charge-localization. Hence, a new family of Ferrocene-appended porphyrin moieties, namely, TPP-P3 and TPP-P4 have been assembled and molecular schemes are displayed in Fig. 5.1. The main difference with the previous molecular-complexes is the elimination of the long-alkyl chains (Chapter 5) leading to a formation of a supramolecular architecture only driven by Hydrogen-bonding forces. Likewise, the replacement of the two Hydrogen atoms by a Zn ion in TPP-P4 opens the possibility to provide more d-states in the frontier molecular orbitals and perhaps enhancing the probability to find molecular orbitals with the desired electronic configurations by creating internal electric fields. Finally, the reduction of the size of the long-alkyl chains might shorten the distance between Ferrocene-moieties leading to a strong electrostatic interaction among these groups and providing a mechanism to propagate information along the network while still preserving the long-range spatial coherence provided by the scaffold formation and avoiding growth problems of the Ferrocene moieties when deposited on Au(111) [142, 143].

Figure 5.2: Electronic structure of the TPP-P3. (a) Orbital energy levels diagram. (b) The ten first occupied frontier molecular orbitals.(c) Molecular Electrostatic Potential (MEP) projected over the electronic density where red color indicates a depletion of electrons, white indicates a neutrality and blue excess of electrons. Both molecular orbitals and MEP have been plotted by using an isosurface value of 0.2.

5.2 METHODOLOGY

To study the electronic properties and perform a vibrational analysis density functional theory (DFT) has been employed as implemented in CP2K [111]. The PBE0-LR-TC exchange-correlation functional has been used (for a detailed discussion go to section 5.3) in order to optimize the gas-phase molecular structures of the TPP-P3 and TPP-P4 complexes [144]. This specific functional has been implemented in the CP2K software where the PBE0 hybrid functional has been transformed into a short-range and long-range functional without higher computational cost [45, 48, 46]. Hereby, the GPW formalism has been used in combination with the optimized MOLOPT basis set and completed by an auxiliary plane-wave (PW) expansion used to augment the electronic charge density for the calculation of the Hartree potential [115]. For the auxiliary basis set a cutoff energy of 450 Ry has been used. For the Hartree-Fock term an auxiliary density matrix implementation is used as well as an optimized basis set for an accurate HF calculation similar in
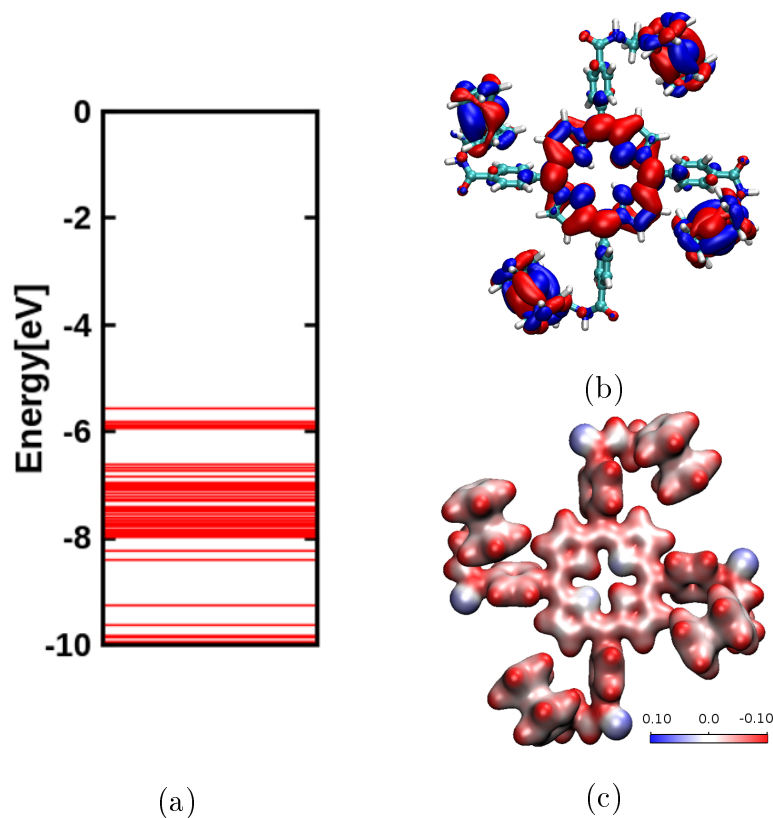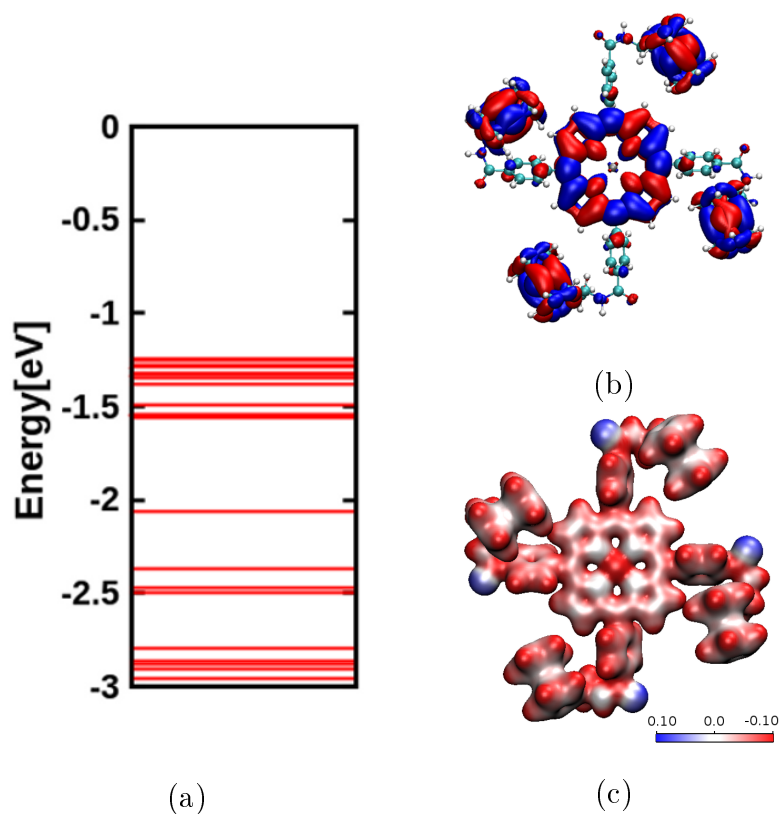
Figure 5.3: Electronic structure of the TPP-P4.(a) Orbital energy level diagram. (b) The ten first occupied frontier molecular orbitals.(c) Molecular Electrostatic Potential (MEP) projected over the electronic density where red color indicates a depletion of electrons, white indicates a neutrality and blue excess of electrons. Both molecular orbitals and MEP have been plotted by using an isodensity value of 0.2.

composition to the polarization consistent (CFIT-3) basis sets derived by Jensen [47, 145, 146]. For the non-covalent interactions the Grimmes D3 parametrization including the C9 parameter has been employed since similar structures have been studied employing this approximation leading to good agreement between theory and experiment [49, 147]. In the case of the TPP-P4 molecular complex a subsequent vibrational analysis has been performed after the optimization process in order to corroborate whether the energy-minimized structure is in a true minima in its corresponding potential energy surface. Concerning the self-assembled monolayer periodic-boundary conditions (PBC) have been used in order to study the electronic structure of both organometallic molecular complexes by employing the corresponding truncated-Coulomb extension for hybrid-functionals [46].

Molecular Complex	IP (eV)	EA (eV)	χ	μ
TPP − **P3**	5.88	2.12	4.0	3.7
TPP − **P4**	5.91	2.01	3.9	3.9

Table 5.1: Computed values for the ionization potential (IP), electron affinity (EA), chemical potential (χ), and chemical hardness (μ) for the TPP-P3 and TPP-P4 Porphyrin derivatives.

5.3 GAS-PHASE PROPERTIES OF THE TPP-P3 AND TPP-P4 MOLECULAR COMPLEXES

In order to investigate the electronic structure of the TPP-P3 and TPP-P4 molecular complexes, the structures have been optimized in the gas-phase. Likewise, basic chemical quantities such as the electron affinity (EA=E[n+1]-E[n]), the ionization potential (IP=E[n]-E[n-1]) and the transport gap (IP−EA) have been perused. All these quantities are calculated and reported in Table 5.1. Here, E[n-1], E[n] and E[n+1] are electronic total energies corresponding to a number of electrons of n-1, n and n+1 with n for neutral molecule. As part of our analysis, the point group symmetry has been computed for the optimized molecules resulting in a C_2/C_i point-group for both complexes [121]. In the gas-phase, the qualitative molecular orbital diagram has been obtained for both molecules and the results are displayed in Fig 5.2 and 5.3. The organization of the molecular orbitals indicates the preservation of the localized d-states from the parent Ferrocene-moiety in the same symmetry ordering. This is a direct consequence of the point-group symmetry of the total complex in which the molecular orbitals with associated d_{xy} and $d_{x^2-y^2}$ are invariant under the action of this group. Likewise, permanent dipole moments with a strength of 1.4 D and 1.8 D in the gas-phase for TPP-P3 and TPP-P4 complexes, respectively. In both phases, the molecular electrostatic potential (MEP) were computed and displaying a rather non-homogeneous distribution of the electronic charge in which the Oxygen-atom belonging to the amide moiety displays an excess of electronic charge while the Hydrogen-atom linked to the same functional group exhibits a depletion of the same charge-carrier. Likewise, in the case of the organic-core one can clearly observe a difference between the TPP-P3 and TPP-P4 molecular complexes (Fig. 5.2 and 5.3 panel (c)) in which a depletion of electronic charge is shown. Interestingly, the Zn-ion reveals a depletion of negative charge stronger than the corresponding H2-TPP organic-core explaining the observed trend in which the dipole moments are stronger in TPP-P4 than in TPP-P3. Inspecting the orbital energy levels diagram, one can notice that the energy separation between successive frontier orbitals is quite small ($\cong$ 150meV in both cases) leading to a possible hybridization between adjacent molecular orbitals specially in the frontier orbitals where a combination of eight Ferrocene related molecular orbitals and 2 organic-core orbitals is found (see Fig. 5.2 and 5.3 panel (b) for the corresponding schemes). In the same manner, the HOMO-LUMO gap is an important quantity that must be accurately calculated in order to correctly estimate the induced dipole moment between the metallic-surface and the organometallic molecular complex. In this matter, it is important to understand that the origin of the underestimation of the HOMO-LUMO gap in the molecular complexes is due to the self-interaction problem [141]. This can be seen in the calculated IP and EA quantities which indicates that the reduction of the molecular-complexes can be associated with the removal of an electron belonging to one of the Ferrocene-moieties, while the oxidation of the molecules can be ascribed to the addition of one charge-carrier to a state provided by the TPP organic-core.

Exchange-Correlation (XC)	E_{Fermi} (eV)	$V(z)$ (eV)	ϕ (eV)
PBESOL	-3.48	1.83	5.31
TPSS	-3.37	1.95	5.32
PBE-TC-LR	-4.05	1.55	5.60

Table 5.2: Calculated theoretical values for the E_{Fermi}, the electrostatic potential at vacuum region $V(z)$ and the corresponding work function ϕ. The values are obtained from a three-layer Au(111) slab for all the used exchange-correlation functionals.

5.4 TWO-DIMENSIONAL NETWORK FORMATION IN THE TPP-P3 AND TPP-P4 MOLECULAR COMPLEXES

In the case of the molecular scaffold formed by the molecular complexes the relaxed lattice cell parameters of the Au(111) gold slab super-cell have been used (a= 22.3Å b= 23.2Å) in order to relax and create the self-assembly monolayer (SAM). Once both the geometry and the unit cell have been relaxed the electronic structure of the periodic monolayers has been investigated focusing in the impact of the formation of supramolecular motifs in the electronic properties of the network which is achieved by the formation of four inter-cell Hydrogen bonds. As seen in Fig 5.4 (b) and (d), in both complexes the PDOS (displayed with a Gaussian broadening of 0.4 eV) exhibits narrow energy bands which are formed by the molecular crystalline structure around the Fermi energy are mainly derived from the d-states coming from the Ferrocene moieties. Likewise, a more active contribution of the organic-core states is found that can be ascribed to the formation of the Hydrogen-bond network. In the periodic scaffold permanent dipole moments of 1.0 D and 1.2 D have been obtained and computed with the modern theory of polarization for the TPP-P3 and TPP-P4 molecular complexes, respectively. The strength of the inter-cell hydrogen bonding has been assessed by employing the formula:

$$E_{H-bond} = E_{dimer} - 2E_{isol} \tag{5.1}$$

where E_{H-bond} corresponds to the magnitude of the H-bonding, E_{dimer} is the total energy of a dimer configuration and E_{isol} is the energy of an isolated reference molecule. The results obtained for both complexes (see Table 5.3) indicate a repulsive inter-cell interaction that can be attributed to electrostatic repulsion between the neighboring Ferrocene complexes. This is due to the charge localization in these spatial regions that leads to possible rotation of these moieties in order to reduce the electrostatic interaction and enhance the vdW interaction among the inter-Ferrocene complexes [132]. Once the 2D network is formed narrow bands will be created by hybridization of the molecular states leading to a possible formation of linear combinations of the different contributing Ferrocene states at different geometrical positions within the molecular complex. Finally, one can observe few remarkable differences between the two PDOSs (Fig 5.4(a,b)) that includes the appearance of the Zn-ion states in the TPP-P4 molecular complex both in the occupied states and the excited states.
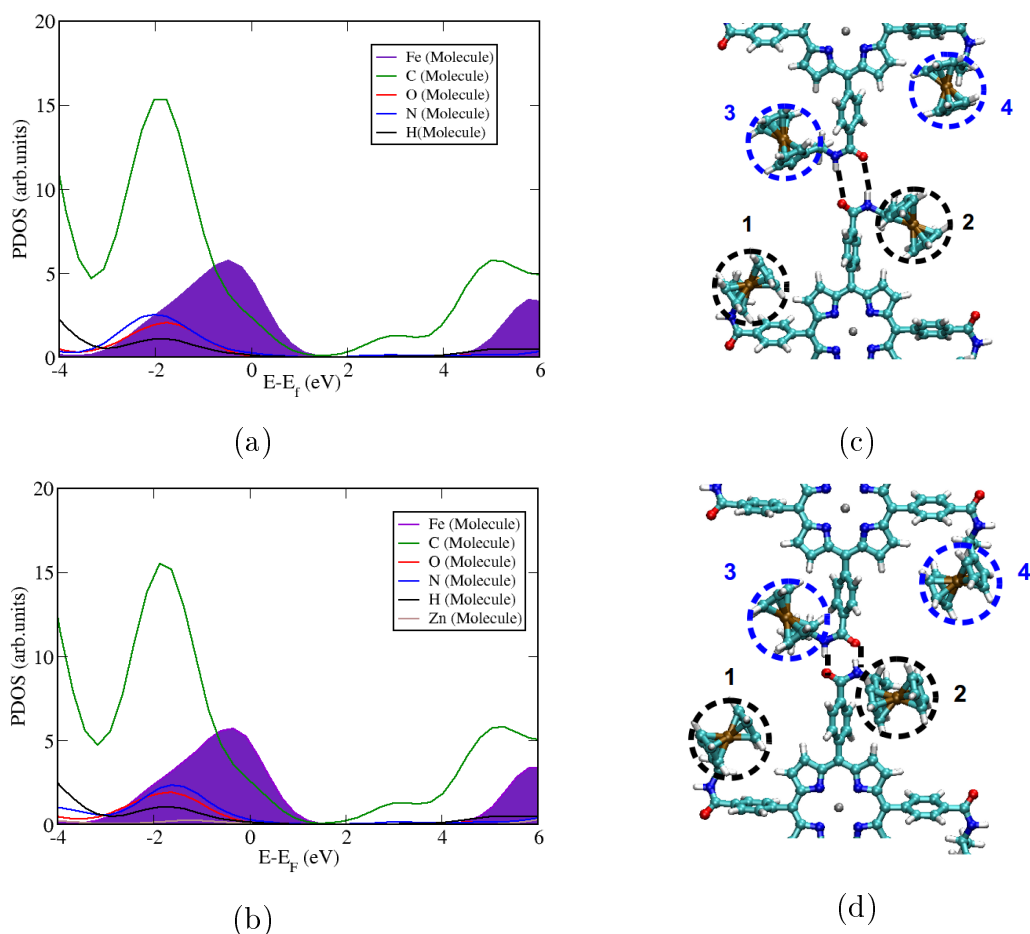
(a)

(c)

(b)

(d)

Figure 5.4: The inter- and intra- molecular interactions between adjacent cells for the TPP-P3 and TPP-P4 molecular complexes. (a) Along the $\vec{a}$ lattice vector.(b) Along the $\vec{b}$ lattice vector. The possible sources of electrostatic for the Ferrocene moieties in terms of intra- and inter-cell along $\vec{a}$ (c) and $\vec{b}$ (d) are indicated and highlighted with blue and black dashed lines, correspondingly.

5.5   MOLECULE-SUBSTRATE INTERACTION FOR THE TPP-P3 AND TPP-P4 MOLECULAR COMPLEXES

The fundamental challenge in the physics of surfaces and interfaces depends on the predictive understanding of physical phenomena such as the electronic structure and the dynamics of excitations and charges at the interfaces [148]. The central issue to solve these kind of problems is how to interpret the electronic structure of the coupled system. Hence, whereas the molecular complexes tend to weakly interact whit each other in SAM scaffold preserving their localized electronic properties the metallic surface is characterized by strongly and itinerant electronic delocalized states [137, 141]. Thus, it is necessary to develop a quantitative understanding of the interfacial electronic structure of the system by taking into account many different interactions. Firstly, the level alignment produced in the interface is the most important quantity in terms of the electronic structure of the total system. Secondly, important electrostatic effects such as depolarization and screening should also be added since they can alter the electronic structure of the molecule by inducing
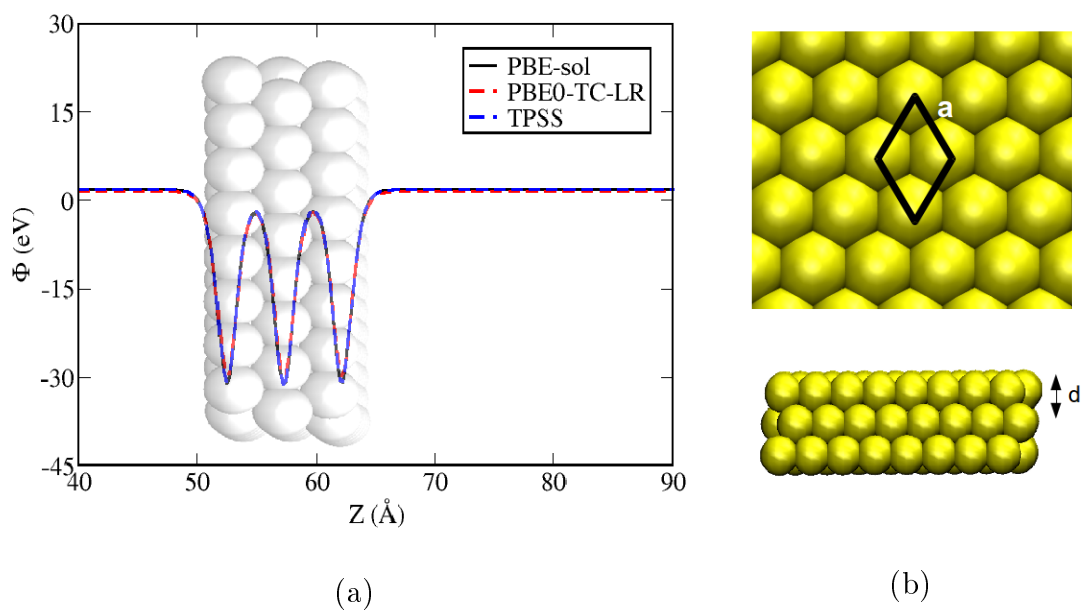
(a)   (b)

Figure 5.5: Comprehensive study of the Au(111) slab unit-cell. (a) Computed plane-averaged electrostatic potential for the Au(111) slab (V(z)) for three different exchange-correlation functionals. (b) Upper panel: top view of the Au(111) slab model where $\vec{a}$ indicates the lattice vector. Lower panel: lateral view of the Au(111) slab-model where d indicates the interlayer distance.

shiftings in the energy-level diagram that in turn might create an interfacial charge-transfer (ICT) dynamics [137]. Hence, in order to rationalize the experimental results first principle methods are employed to study the molecule-surface interface while understanding the role played by the permanent dipole moment on this interaction and its impact on the total electronic structure of the system.

5.5.1   Metallic Slab: Comprehensive study of the PBE0-TC-LR functional

In order to simulate the surface the slab technique has been used. Thus, a three atomic layer of the Au(111) surface has been formed. In the perpendicular direction to the Au(111) surface a vacuum separation of 30 Å has been added so as to avoid spurious interactions between the neighboring slabs. At this stage, both the unit cell and the geometry have been optimized for the initial slab. In this case the rev−PBE exchange-correlation implementation has been used [149]. The structure has been relaxed until the atomic displacements were lower than $9\mathrm{x}10^{-4}$ Bohr and the forces lower than $4.5\mathrm{x}10^{-4}$ Hartree/Bohr. The relaxed in-place lattice vector (2.88Å) and interlayer distance (2.41Å) of the calculated Au(111) slab are in good agreement with the ones theoretically and experimentally obtained and computed (2.82Å for in plane lattice and 2.39Å for successive layers) (see Fig 5.5 panel (b) and (c)) [150, 151, 152]. Conceptually, the work-function can be defined as the minimum energy required to remove an electron from the surface written as [153, 152]:

Molecular Complex	$H - Bonding + Repulsion$ (eV)	Adsorption (eV)
TPP − P3	-0.26	-1.2
TPP − P4	-0.30	-0.9

Table 5.3: Calculated total energy differences for the different interactions for both complexes. Note that three different interactions have been considered as shown in Fig. 3.12 (a,b,c) and Fig 3.10 (a,b,c).

$$\phi = V(\infty) - E_{Fermi} \tag{5.2}$$

where $V(\infty)$ is the electrostatic potential far from the surface and E_F is the Fermi level of the metal. In Table 5.3, the values of the calculated work functions for the different XC implementations [154, 144, 154] have been collected. Interestingly, the PBE0-TC-LR implementation delivers a work function value that is in good agreement with the reported results from both computational and experimental studies (5.2-5.35 eV) [140, 152]. This indicates that the PBE0-TC-LR implementation is a suitable functional that can qualitatively describe both subsystems, namely, the organometallic molecule and the metallic surface providing a qualitatively accurate physical picture of the coupled system.

5.5.2   Molecule-Surface adsorption

In order to investigate the electronic and mechanical properties of the surface-molecule system, the repeated-slab approach has been employed and model the Au(111) surface with a unit cell with lateral and longitudinal lattice vectors of $|\vec{a}| = 22.4$ Å and $|\vec{b}| = 23.4$ Å, correspondingly. The c-axis is taken to be 65 Å ensuring no spurious interactions of the molecule and the periodic image of the slab containing 245 gold atoms. To model the monolayer coverage, each Au(111) unit cell of the gold is made to accommodate exactly one TPP-P3 and TPP-P4 molecule taking into account the intra-cell interactions due to the Hydrogen-bonding. The experimental lattice parameters indicate a slight tilting of the unit cell that has been also observed in the first-principle calculations in which the corresponding computed angles between the different lattice-vectors after relaxation are $\alpha = 89.9°$, $\beta = 87.8°$ and $\gamma = 90.10°$ indicating a possible mismatch between the molecule unit cell parameters and the ones reported for the clean gold surface. The main impact on the system is along the $\vec{b}$-lattice vector direction as a slightly longer H-bonding is obtained than in the $\vec{a}$-lattice vector direction. The total unit cell is made up of 434 atoms in the case of TPP-P3 and 433 for TPP-P4 including four iron metallic ions provided by the four Ferrocene molecules (five in the case of TPP-P4 due to an additional Zn). The adsorption distances and energies have been analyzed by carrying out geometrical optimization at different heights of the molecule-metal system along the stacking-axis and the results displayed in Fig. 5.6 and 5.7. The orientation in which the molecules have been absorbed cannot be experimentally resolved and it poses an open question to theory. Thus, as part of the investigation two plausible models have been suggested (insets in Fig. 5.6 and 5.7) whose main difference is whether the Ferrocene-moieties are facing directly towards the Au(111)-surface (configuration 1) or on the contrary is the TPP-core the directly facing the surface (configuration 2). According to the results the configuration 1 (TPP-core and CH_3 moieties facing directly the surface) is preferred than configuration 2 in both cases. The adsorption distances are z = 6 Å and z = 6.5 Å for the TPP-P3

and TPP-P4 molecules, respectively. Once the correct adsorption geometry is obtained one can further investigate the role played by the surface in the formation of the supramolecular structure and whether the molecular complexes have been chemisorbed or physisorbed. The adsorption energy E_{ads} is calculated accordingly as:

$$E_{ads} = E_{total} - (E_{slab} + E_{molecule}) \qquad (5.3)$$

and the obtained values are -1.1 eV and -0.9 eV for TPP-P3 and TPP-P4, respectively. These values strongly suggest that the metallic surface is playing a fundamental role in the self-assembly behavior of the molecular complexes by providing a favorable electrostatic environment where the supramolecular motifs can be hosted. In order to assess whether our complexes are physisorbed or chemisorbed, the electron localization function (ELF) has been calculated for both complexes [155]. As is observed in Fig 5.6 and Fig 5.7 panel (b) and (c), the ELF takes values between 0.3 and 0.5 at the interface between molecule and metallic surface leading to conclude that both molecular complexes have been physisorbed onto the Au(111) surface and that the main interaction between the Au(111) surface and the molecules is non-covalent in nature. Concerning the intra-bonds of the molecule, the selected volume slice offers a perspective in which one can clearly observe more localized electrons in the Zn region for the TPP-P4 molecular complex (Fig. 5.7 (b,c)) than in the TPP-P3 case (Fig. 5.6 (b,c)). Finally, at the bottom of the potential energy surface the molecular-complexes suffer a distortion in its geometry by varying their almost perfect planar organic-core gas-phase configurations into a non-coplanar arrangement where Ferrocene molecules are tilted and torsionally distorted with respect to the phenyl rings. This new re-arrangement of the molecules due to its interaction with the metallic surface has a direct impact in the electronic structure of the coupled system since the original point-group symmetry is broken, opening energy gaps between degenerated states.

5.5.3   Electronic structure and molecular orbitals

In order to get insight into the nature of the electronic states around the Fermi level the projected density of states (PDOS) has been calculated for both complexes and the results are displayed in Fig 5.8 (a) and (b) for TPP-P3 and TPP-P4, respectively. In both cases, hybridization between the organic-core states mainly provided by the Carbon atoms and the d-states supplied by the Ferrocene-moieties are found in the energy range between the Fermi energy and 1 eV below. Hence, selected frontier molecular orbitals have been plotted (insets in Fig 5.8 (a) and (b)) where a clear charge-carrier localization can be observed in the case where $E_{mol-orb} \cong -1$ eV for both molecules. Furthermore, by direct inspection of the frontier molecular orbitals in the energy range where the three protruding peaks ascribed to the Ferrocene-mioties are found one can find that the associated symmetry corresponds with the sequence d_{xy}, $d_{x^2-y^2}$, and d_{z^2} in clear resemblance to the original gas-phase Ferrocene moiety molecular orbital organization. Nonetheless, when energies around -2 eV are inspected the spectral weight is stronger for states related to the organic-core in the case of the TTP-P3, while for TPP-P4 a contribution of the Zn-metallic ion states is also reported. This feature can be observed in the associated molecular orbital plotted in Fig 5.8 (a) and (b) where a π-organic state provided by the TPP group is clearly observed. In the energy range between -1 eV and -2 eV
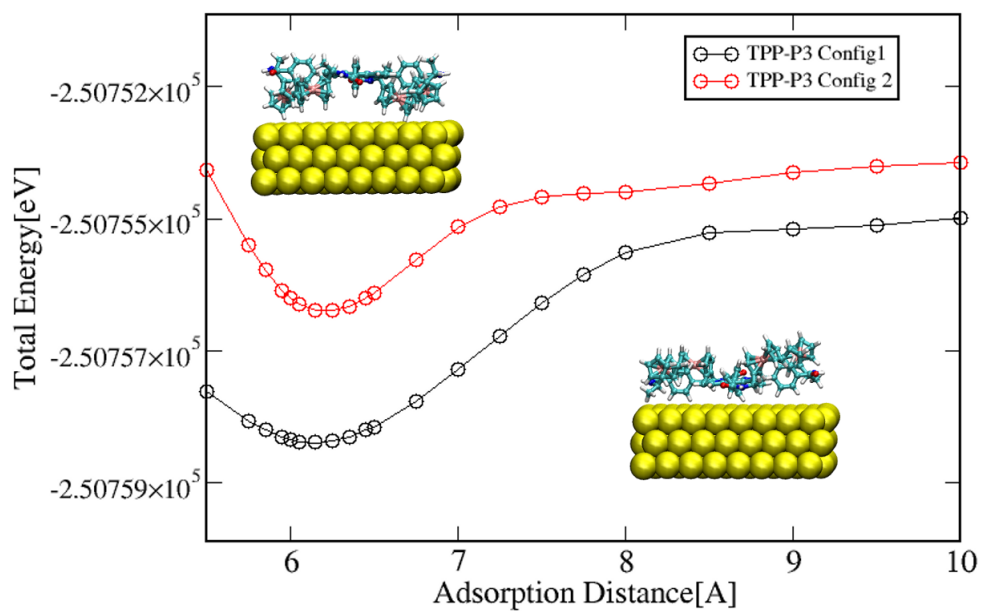
(a)
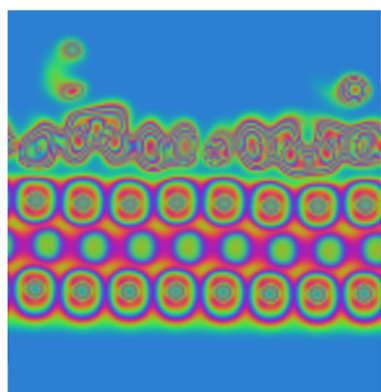
(b)   (c)

Figure 5.6: Total energy of the TPP-P3 / Au(111) interface as a function of a shift of the TPP-P3 along the z-direction. (a) Potential energy surface for configuration up and down (insets). (b) Slice plane of the Electron Localization Function (ELF) along $\vec{a}$ and (c) $\vec{b}$ lattice directions passing through the geometrical center of the molecular complex [155].

one can discern a hybridization between some d-states supplied by the Ferrocene-moieties and some p-states assigned to the organic-core (corresponding molecular orbitals are plotted as insets in Fig 5.8 (a) and (b)) that are not observed in the monolayer-periodic electronic structure and stronger reported in the TPP-P3 than in the TPP-P4 molecular complex. Concerning the excited states for both phases, the LUMO band is centered at 1.8 eV with a tail extending over E_f and can be clearly assigned to the π^* excited-states of the TPP organic-core. In general, a
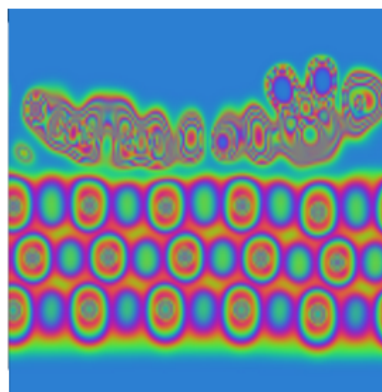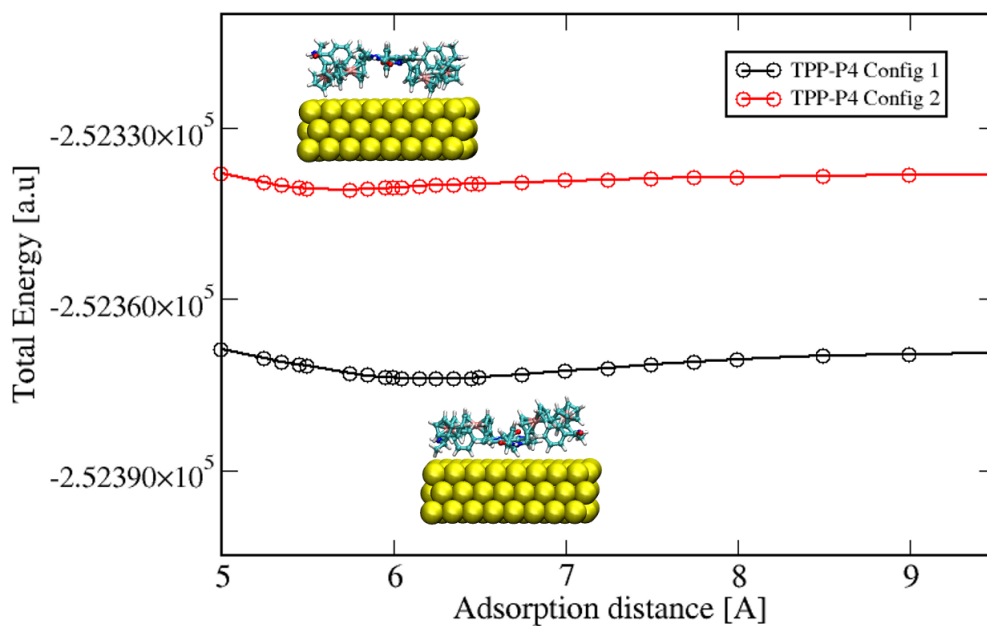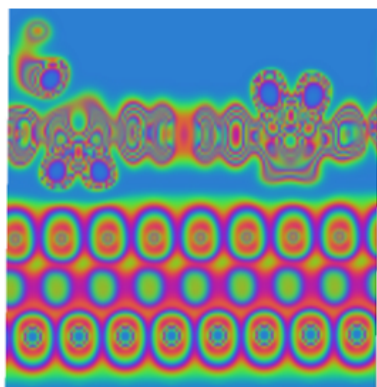
(a)

(b)
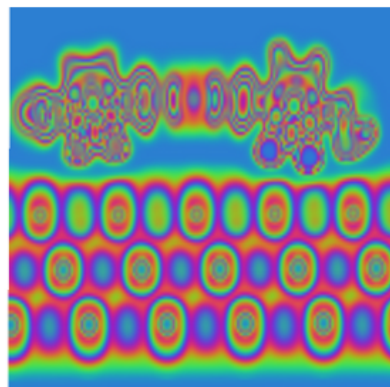
(c)

Figure 5.7: Total energy of the TPP-P4 / Au(111) interface as a function of a shift of the TPP-P4 along the z-direction. (a) Potential energy surface for configuration up and down (insets). (b) Slice plane of the Electron Localization Function (ELF) along $\vec{a}$ and (c) $\vec{b}$ lattice directions passing through the geometrical center of the molecular complex [155].

reduction of the transport gap between the associated HOMO and LUMO states in each molecular complex has been found whose value is around -0.5eV. The decrease of this value can be associated with a lowering in the work-function that is experimentally accessible [142]. Finally, in energy regions around 5.5 eV the excited states can be associated with the excited-states of the Ferrocene mioties and whose value has been also lowered in comparative relation with the ones obtained in Table 5.1.
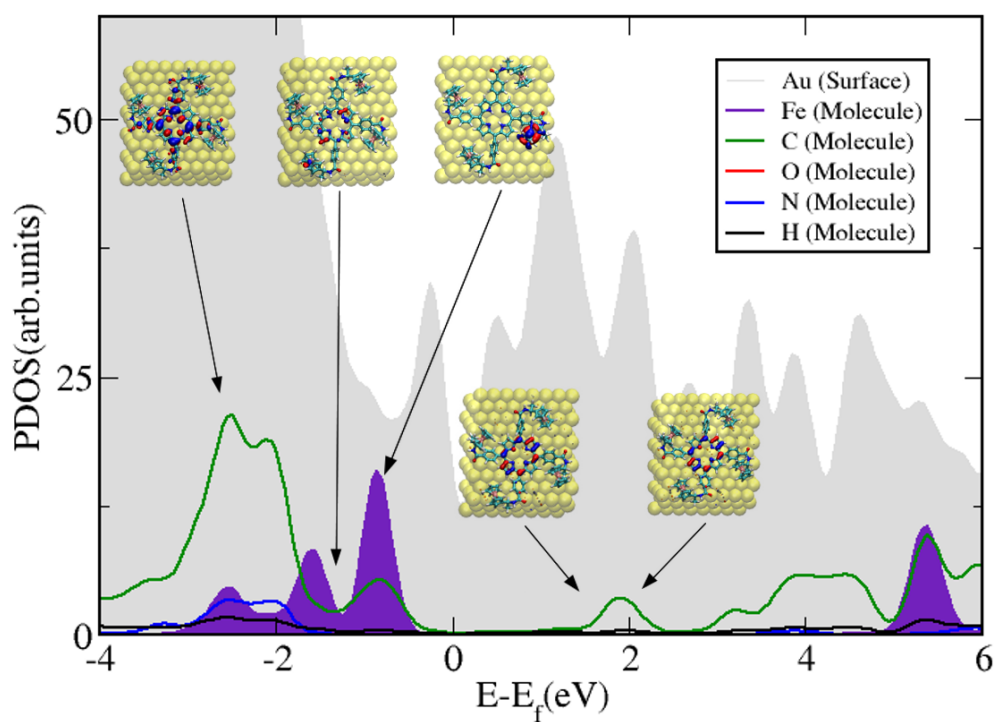
(a)
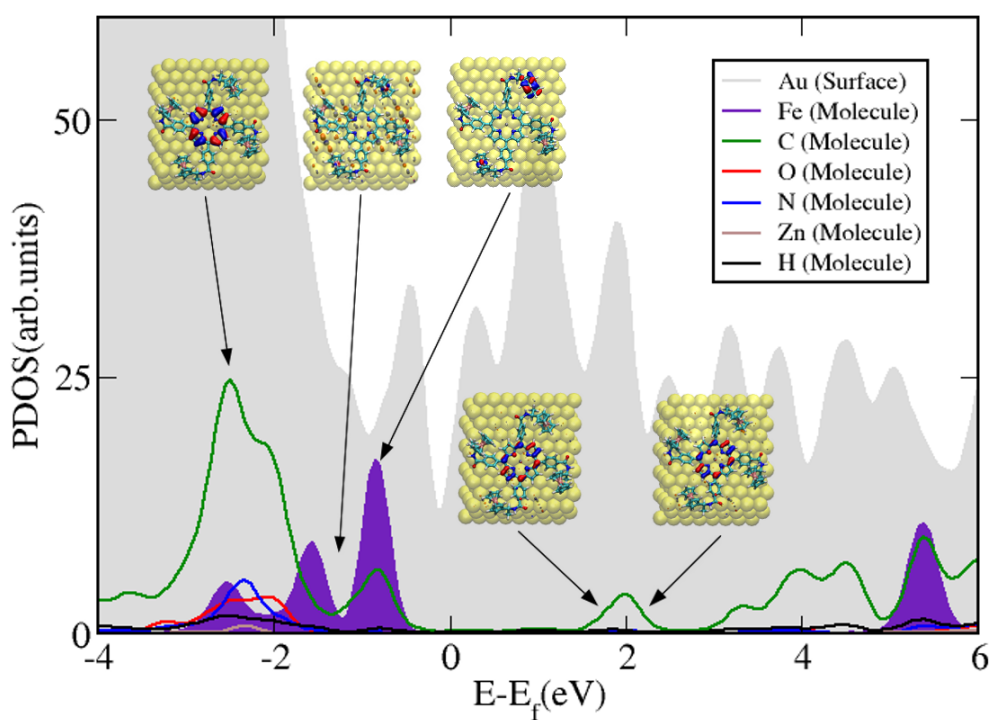
(b)

Figure 5.8: Projected Density of States (PDOS) for TPP-P3 (a) and TPP-P4 (b) molecular complexes. The corresponding molecular diagram as obtained from PBE0-TC-LR exchange-correlation functional is shown [45]. In the case of PDOS the energy is relative to E_f for all atoms.

5.6   AB-INITIO VALIDATION OF THE EXPERIMENTAL RESULTS

In order to accomplish the ultimate goal of implementation of the m-QCA paradigm, experimental efforts have been carried out to peruse the plausibility to achieve charge localization and controllability under real conditions. Hence, new experimental growth techniques have been developed in order to construct a self-assembly supramolecular structure adsorbed onto Au(111) surface [142]. Thus, after successfully achieving the deposition of these molecular complexes over the metallic surface many different experimental measurements such as UH (Ultra-High-Vacuum) ST images, $\frac{dI}{dV}$ and topography images have been obtained. These quantities can be related to theoretical calculations providing a playground in which the newly employed methodology can be further tested. Conceptually, the physical picture states that the electron density at the surface of metal spreads into the vacuum region and creates an interface dipole which has a substantial contribution to the work function of the clean substrate. Once the molecules have been deposited onto the surface the closed shell adsorbate decrease this surface dipole by pushing metal electrons back into the bulk because of Pauli repulsion [137, 148]. This has an overall effect on the total work-function that can be measured and directly compared with the results from $ab-initio$ calculations. The ICT at the molecule-substrate interface can be directly visualized via the calculation of the (surface) averaged electron density difference along the stacking axis defined by [148, 152]:

$$\Delta\rho(\mathrm{z}) = \int \mathrm{dx} \ \mathrm{dy} \ \Delta\rho(\mathrm{x,y,z}) \tag{5.4}$$

where $\Delta\rho(\mathrm{z})$ is the averaged charge-density difference that can be obtained from first-principle calculations once the charge-density difference $\rho(\mathrm{x,y,z})$ is computed as:

$$\Delta\rho(\mathrm{x,y,z}) = \rho(\mathrm{x,y,z})^{\mathrm{Total}} - \rho(\mathrm{x,y,z})^{\mathrm{SLAB}} - \rho(\mathrm{x,y,z})^{\mathrm{SAM}} \tag{5.5}$$

whence $\rho(\mathrm{x,y,z})^{\mathrm{Total}}$ is the total electron density (including ionic contributions) of the system, whereas $\rho(\mathrm{x,y,z})^{\mathrm{SLAB}}$ and $\rho(\mathrm{x,y,z})^{\mathrm{SAM}}$ are the ones related to the surface and the molecule at the optimized adsorption geometry, correspondingly [141, 148]. In Fig 5.9 (c), the creation of a very weak interface dipole is obtained. From a theoretical viewpoint, the weak interaction between the molecular complex and the metallic substrate can be understood in terms of the total wavefunction of the coupled system that can be approximately recast as a product of a wave-function associated with the metallic substrate and a second term associated with the molecular complex. Once the anti-symmetrization procedure of the total wavefunction is carried out, the creation of a repulsive interaction between the electrons of the closed shell molecular complex and the ones from the substrate is obtained in the exchange term of the total Hamiltonian [141, 148, 152]. Thus, the contribution to the work-function shift can be understood at T = 0K as four main contributions. Firstly, the decrease of the metal electron density at the surface due to the Pauli-repulsion effect. Secondly, the intrinsic dipole moment of the molecule. Thirdly, the polarization of the molecule due to an attractive surface potential and finally the possible charge transfer between the interacting subsystems. In the first case, the work-function of the gold surface

(a)

(b)

(c)
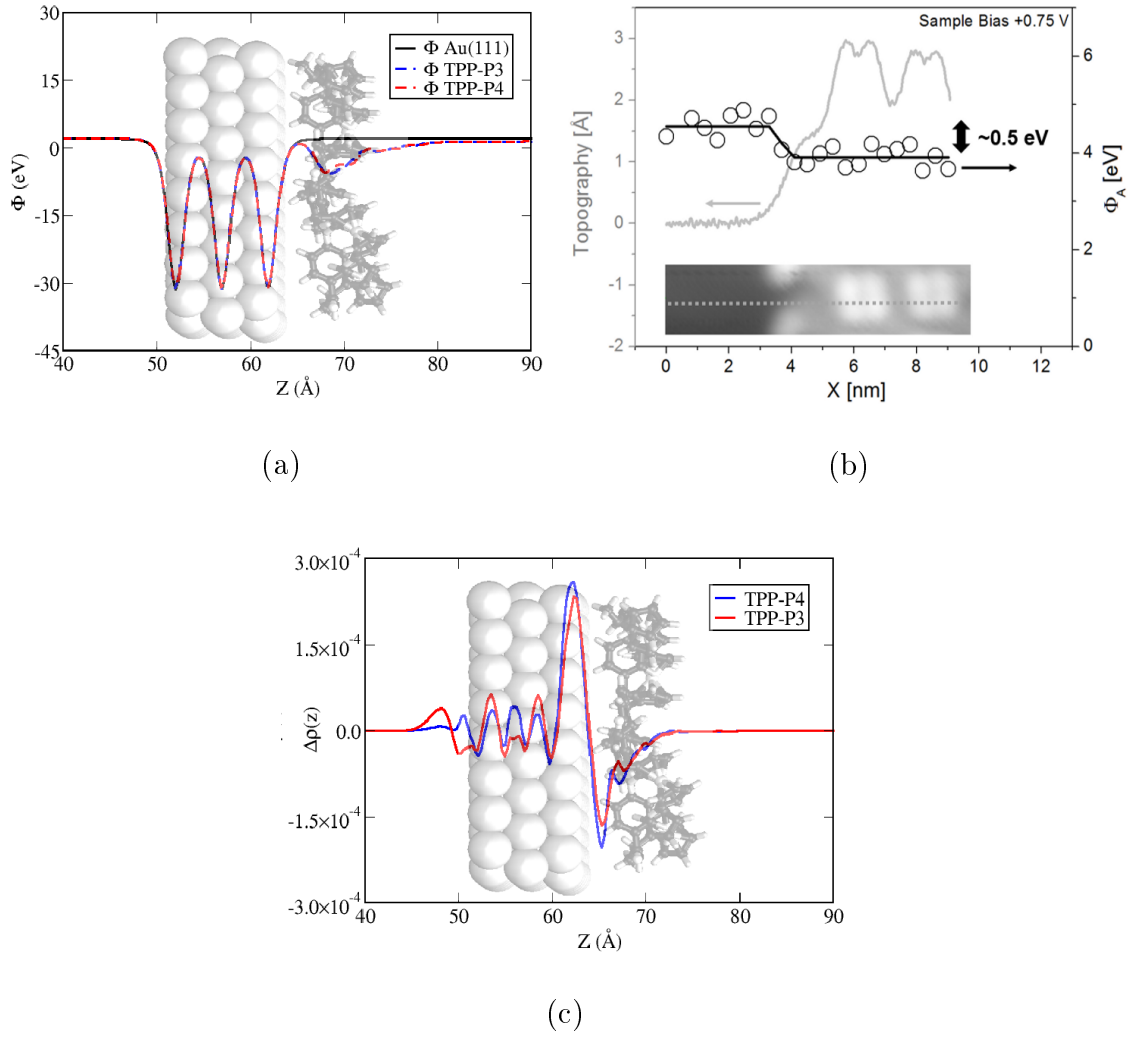
Figure 5.9: Comparative relation of (a) Computed plane-averaged electrostatic potential for the TPP-P3 and TPP-P4 molecular-complexes. (b) Experimental work-function along the associated topography obtained from UHV-STM images. (c) Charge-density difference upon monolayer adsorption. The locations of the Au(111)-slab and TPP-P3/P4 molecule are illustrated in the background of the corresponding plot [142].

modified by the TPP-P3/P4 molecular complexes is calculated and the results are displayed in Fig 5.9 (a). Thus, one can observe that the shift corresponds to a work-function decrease of -0.5 eV with respect to the clean gold surface (black line in Fig 5.9 (a)). This calculated work-function modification is in excellent agreement with the recently reported experimental value (Fig 5.9 (b)). The contribution from the intrinsic dipole of the molecule, $\Delta\Phi_{\rho_{\mathrm{dip}}}$, can be evaluated by using the Helmholtz relationship:

$$\Delta\Phi_{\rho_{\mathrm{dip}}} = \mathrm{e}\Delta\mathrm{V} = \frac{\vec{\mathrm{p}}}{\mathrm{A}\varepsilon_0} \qquad (5.6)$$

(a)   (b)

(c)   (d)
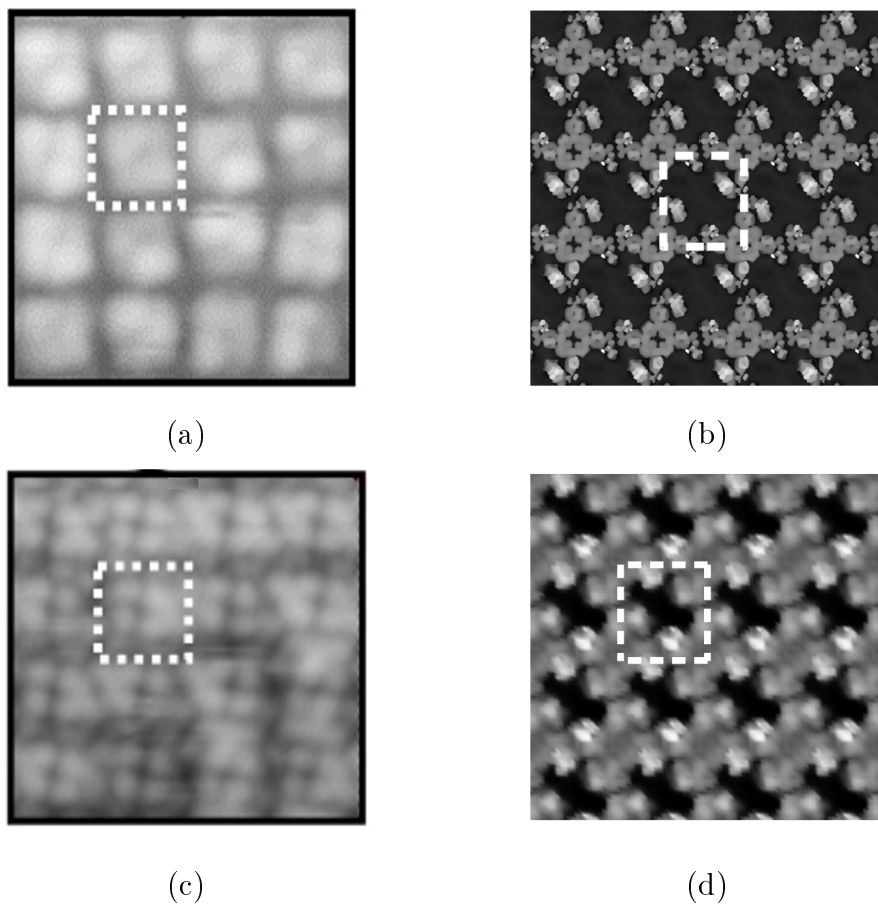
Figure 5.10: Comparison between: (a) the experimental constant-current STM image at bias V_s = -1.0 eV for TPP-P4 molecular complex and (b) the calculated constant-current STM image from E_{Fermi} to E_{Fermi}-1.0 eV (a,b) and E_{Fermi}+2.1 eV (c,d). Similar results have been obtained for TPP-P3 [142].

where $\vec{p}$ is the intrinsic dipole moment of the molecule, A is the surface area per molecule and ε_0 is the dielectric constant [148]. Thus, the contribution of this term to the total work-function shift is negligible since its energy values are around $\cong 0.1$ meV with the computed values for unit-cell and dipole moment of the molecular-complexes. The last two reminder terms in which the work-function can be decomposed also contributes little to the shift of the work-function. Firstly, the induced interface dipole moment is weak as is presented in the computed plane-averaged charge density (Fig 5.9 (c)). In the same manner, one can rule out the charge-transfer term since there is no direct chemical-bond between the surface and the molecule (see Fig 5.6 and Fig 5.7 panels (a,b)).

5.6.1   STM images

Based on the optimized structures of the TPP-P3 and TPP-P4-Au(111) interface, the constant-current STM image has been simulated using a s-orbital tip symmetry with a bias-voltage of -0.8eV and compared with the measured STM images [54]. The results of these calculations are displayed in Fig 5.10 only for the TPP-P4 molecular complex since similar results are obtained for the TPP-P3 molecule.

(a)   (b)

Figure 5.11: Electron density of states (DOS) projections and spatial localization. (a) Theoretical calculated electronic density of states in (Upper panel) gas-phase and the coupled system (Middle panel). (Lower panel) The experimentally obtained local density of states (LDOS) by UHV-STS are plotted with blue for 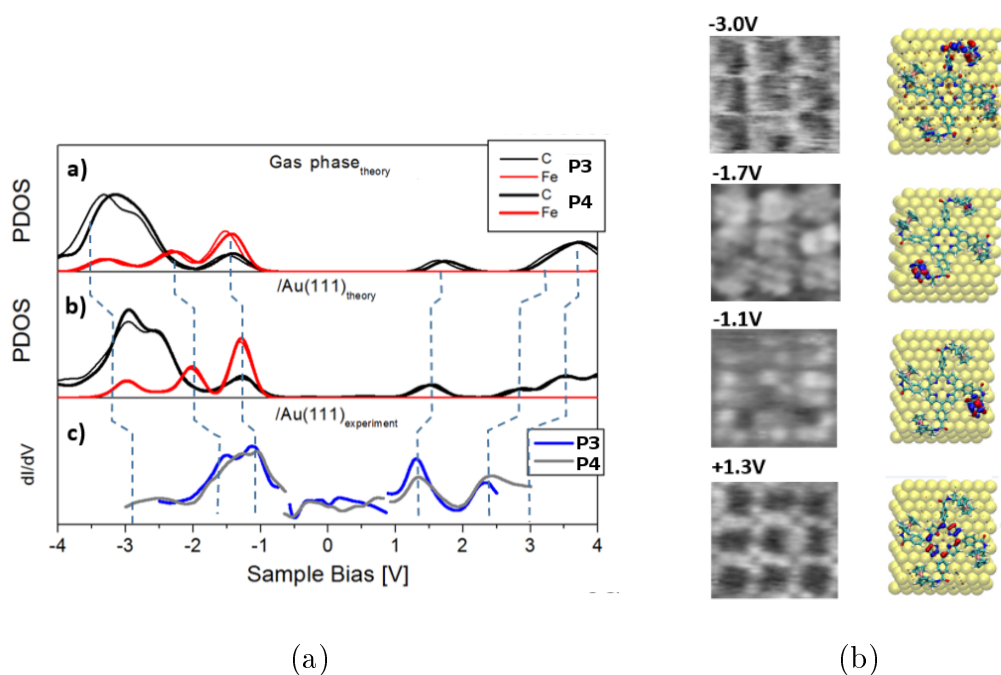the TPP-P3 and grey for the TPP-P4 molecules. The vertical dashed lines follow the evolution of the molecule orbital energy position from gas-phase to experimental results. (b) (Left) The experimental dI/dV images (gray scale) at specific sample biases. (Right) the computed molecular orbitals for these specific energies [142].

In the overall features for both complexes the computed results displayed a good agreement with the experimental images and the simulated ones in which the main issue is the corroboration of the charge localization at the Ferrocene-moieties for molecular orbitals with associated energies below the Fermi energy. In the case of excited states, the measured images displayed an active role played by the $\pi*$ orbitals assigned to the TPP organic-core. This is also predicted by theory along the formation of a stable supramolecular network whose principal driving force is the Hydrogen-bonding promoted by the amide groups appended to the Ferrocene-moieties [142].

5.6.2   Experimental Local Density of States

A direct inspection of the electronic structure of the coupled system, namely, gold-surface and molecular complex can be further perused by employing the $\frac{dI}{dV}$ spectra. This measurement provides straightaway visualization of the occupied and unoccupied molecular orbitals (via the associated LDOS amplitude) at a specific energy. Note that for a more detailed comparison with the full-interface system the molecular orbitals of the isolated system has been considered and the computed PDOSs have been obtained by applying the same Gaussian broadening as the ones calculated for the total system. Noteworthy to mention is that the computed HOMO-LUMO gap

energy is reduced from 3.2 eV to 2.7 eV (5.11 (a) upper and middle panel) which is in a good agreement with the experimental reported value of 2.4 eV [142]. Furthermore, these measurements can be directly compared with the computed frontier canonical molecular-orbitals at different voltages and the results of such procedure are shown in Fig 5.11 (b). When comparing the conductance STS images (left panel) with the corresponding results of the electronic structure calculations one can conclude that the suggested picture of electron localization in the energy region near the Fermi energy level is well captured by the suggested methodology where the Coulomb operator is truncated and the exchange-correlation is divided into long- and short-range regions leading to a good agreement with experimental results [142].

6   CONCLUSIONS AND OUTLOOK

In the present thesis the plausible implementation of the m-QCA paradigm has been investigated by a combination of minimal models and ab-initio calculations. The first part of this thesis focused on the study of the read-in system from a theoretical viewpoint in which the static and dynamical perspectives were approached. As a first step, a static model has been extended and used to analyze the impact of geometrical distortions in the response function. Interestingly, the controllability of the read-in system is strongly affected by static mismatches producing a lag in the response function and therefore in the time-operability of the first unit. The results obtained by this modeling have been contrasted and compared to the findings computed by employing the DFTB+ code [57, 59, 80, 97]. In both cases, the reported trends are similar and strongly suggesting a physical basis of this effect leading to an open question of the geometrical conditions in which the initial set-up system should be built in order to avoid these reported issues.

Subsequently, new ideas have been explored in order to extend the theoretical frame in which the possible initial experimental set-up for the read-in device can be more accurately described. Thus, the dynamical nature of the process has been investigated by including many different time-dependent external electric field profiles both in the minimal models and ab-initio calculations. In the first case, minimal models display an interesting role played by the non-adiabatic correction in the propagation of the occupation number of the molecular orbitals. Hence, the hybridization process can be ascribed to an enhancement of such parameter and producing the non-linear behavior in the response function in the case of a linear external electric field profile. Furthermore, different profiles of external fields resembling more accurate experimental conditions have been added and its impact in the response function has been studied. Hence, despite the preservation of the response function, many different features are observed such as the way in which the time-length of the switching process is extended by some profiles better than in the others. The findings retrieved by the minimal model are contrasted with the ones obtained by an in-house developed version of the DFTB+ code [57, 59, 80, 97] in which the time-dependent external electric field is linked to the MD time step and allowing to create many different profiles as in the modeling case. Both methodologies display similar results leading to the conclusion that the electric field profile is an important external parameter that should be studied closer in order to be optimized. In regard to the issue of which electric field profile delivers the best response function one can address this fact by employing Optimal Control Theory (OCT) that can be also implemented in the first principle code DFTB+ [57, 59, 80, 97].

As a final point, a possible mechanism in order to investigate the role played by the vibrations in the bi-stability process has been developed. In this matter, the corresponding electronic Schrödinger equation has been extended by including the normal modes and the coupling between the corresponding electron associated with a particular energy level and the associated normal modes within the linear regime theory [102]. Hence, the model explored a possible mechanism in which the creation of a bistable potential energy surface can be understood in terms of the mixing of the two normal modes associated with the inital and final states of the electronic diabatic states that is driven by the action of the external electric field. Thus, this result adds an important ingredient in the ET theory since highlights the importance not only of the electronic coupling but also of the electron-vibration term.

In a joint experimental and theoretical work different families of organometallic complexes in which the m-QCA could be hosted have been studied in a systematic way in which the isolated molecular-orbital distribution, self-assembly monolayer electronic structure and the molecule-surface interface Projected density of states (PDOS) were calculated. Hence, in chapter 4 a family of Ferrocene molecules funtionalized with Guanines moieties have been studied in order to assess the plausibility to host the paradigm in these complexes. The experimental findings strongly indicated the formation of H-bonding self-assembly molecular networks triggered by the addition of Guanine groups. The spatial reconstruction of the measured STM images coincides with localization of these Guanine groups at the edges of the corresponding unit and corroborated with the corresponding computed Molecular Electrostatic Potential of the ribbons which showed the plausibility of the formation of this bond. However, a clear localization of electrons within the molecular complexes was not observed since the adjacent molecular orbital gaps have been narrowed by the interactions with the HOPG surface prompting hybridization between them. In both cases, further validation of the atomistic models have been carried out by comparison between accessible experimental STM images and the DFT-based computed images at different bias voltages. The results are in good agreement and strongly indicated that this is the most plausible physical picture in order to understand the self-assembly mechanism for these complexes. Likewise, the mechanical stability of the formed self-assembly networks have been also assessed by carrying out AIMD calculations focusing in the geometrical aspects of the ribbons. Thus, along the calculated trajectory, the distances between the different Guanine groups, which are the responsible of the H-bonding, have been analyzed by employing statistical tools. The results suggested that atomic distances remain within the range of the expected H-bonding distances but the time-length of the computed trajectory is not long enough to conclude a convergence in distribution of these random variables. Nonetheless, the obtained distance distributions for these networks are in the expected distances ranges of the H-bond distances and therefore making them energetically and geometrically stable.

In chapter 5, the building blocks of the QCA cell have been changed by including the TPP moiety instead of the Guanine linkers in order to provide a more rigid organic core. Likewise, by changing the functional end groups of the Ferrocene molecule the formation of single networks has been triggered. Thus, as a result of this substitution the formation of H-bonding and vdW networks were achieved experimentally and studied by means of measuring STM images where models have been suggested to study the formed motifs. Thereby, the electronic structure of the suggested molecules were investigated where electronic charge localization in the Ferrocene moieties was reported in both cases. The formation of the different networks have been understood in terms of the corresponding changes in the Ferrocene linkers and based on the experimental models extracted from the STM images this

physical picture was corroborated. The mechanical stability of both complexes have been assessed by carrying out AIMD calculations and the resulting trajectory analyzed with statistical tools. In both cases, the distances of the involved atoms in the formation of the network were scrutinized leading to the conclusion that AIMD trajectories are not time-wise long enough to statistically conclude that the random variables (interatomic distances) have converged in distribution but showing a clear trend of remaining within distances ranges where these interactions are energetically favorable and reinforcing the experimental and theoretical spatial unit-cell reconstruction. In conclusion, the functionality of organic linkers has a significant impact on the resulting network architecture and implies also different interactions of the organic-core (TPP) and the Ferrocene moieties with the underlying HOPG surface. Likewise, theoretically the charge localization has been reported but can not be experimental resolved due to reduction of the molecular energy level gaps due to the interaction with the surface leading to the conclusion that these set-ups are not suitable to host the QCA cells.

In chapter 6, further functionalization of the Ferrocene appended TPP complexes were carried out where a Zn metallic ion has been added to the TPP organic core while preserving the linkers that can trigger H-bonding formation. Thus, Ultra-High Vacuum (UHV) experimental results and environmental STM images proved independently the formation of such self-assembly scaffolds where they are deposited onto Au(111) and HOPG, correspondingly. In the case of the metallic surface, the adsorption of these molecules onto these kind of surfaces address several fundamental questions regarding to the role played by the electronic metallic states in the localization of electrons at the frontier molecular orbitals of the associated moieties. Therefore, the correct description of the fundamental HOMO-LUMO gap is an important quantity that with normal exchange-correlation implementations is not feasible to achieve. Hence, a new methodology has been developed in which a new kind of exchange-correlation functional (PBE0-TC-LR) has been utilized to study this system and whose main feature is the separation of the Coulomb interactions into short- and long- ranges. As a first step, the isolated and self-assembled molecular complexes displayed localization of electronic charge in the frontier molecular orbitals. Afterwards, the correct adsorption geometry and the nature of the adsorption bond have been investigated leading to conclude that in both cases the moieties are physisorbed on the underlying Au(111) surface. Likewise, the influence of the metallic electronic states in the energy organization of the molecular orbitals were perused leading to the conclusion that no charge transfer took place between the molecule and surface system and that molecular charge localization is possible. These last findings are confirmed by $\frac{dI}{dV}$ images in which the corresponding electronic density associated to an energy range can be observed and directly compared with the results of electronic structure calculations leading to a good agreement between them. Similarly, the change in the metallic work-function due to the Pauli-repulsion as a consequence of the push-back effect has been experimentally measured and theoretically computed leading to an excellent agreement and augmenting the evidence in the reliability of this new developed methodology to describe organometallic complexes deposited on metallic surfaces.

In terms of the actual molecular-candidates, the viability of using molecular complexes in which the charge-carrier can be localized has been demonstrated including the fact that those complexes can be self-organized over different kind of surfaces. Although bi-stability has been also observed in the TPP-P4 molecule candidate, its controllability is still an open issue that can be solved via self-doping mechanism opening a further work line to optimize this plausible candidate. As a possible future working lines the influence of the environment in the ET process must studied in order to observe under which conditions the electron charge transfer process is
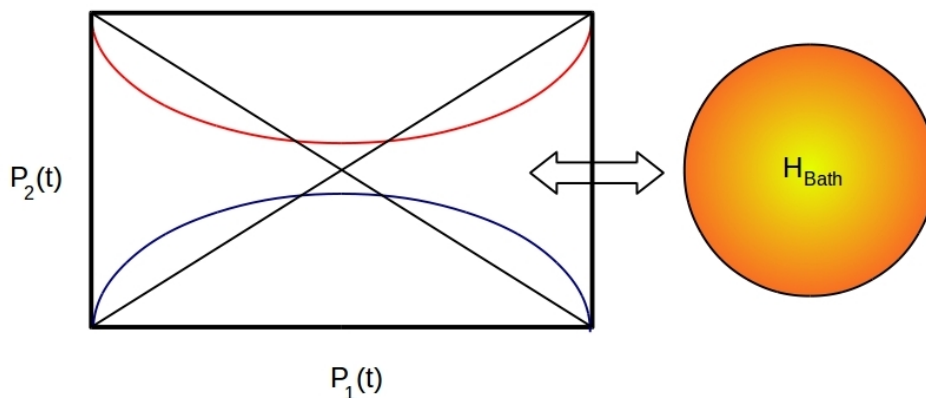
Figure 6.1: Schematic representation of the coupling of the QCA-cell to the environment. In this matter, the bath is composed of the uncoupled vibrations of the molecule and the possible normal modes of the surface in which the molecular is attached.

maintained by identifying the key couplings between the interactions with a possible bath composed by vibrations of the molecule and the vibrations of the surface as is schematically presented in Fig 6.1. Likewise, the cell-to-cell interaction is a fundamental part of the paradigm which has not been fully perused. The crux of this interaction has been also understood as a fully Coulomb interaction between cells that might not be the best physical representation for this mechanism. Instead, one can start to wonder whether the electronic-states in the two adjacent cells are electronically-correlated and that the transfer of energy can be described accordingly with the FRET (Foerster energy resonance transfer) model in the case of complexes that are activated by light or via the electric field switching mechanism by creating an intra-molecular electron-hole pair. Therefore, many interesting ideas have been demonstrated such as the compatibility of self-assembly and electron charge localization within molecular complexes but still many challenges are ahead in order to finally implement a fully functional m-QCA cell at room-temperature.

A BENCHMARKING THE ELECTRONIC STRUCTURE, VIBRATIONAL ANALYSIS AND OPTICAL PROPERTIES OF THE FERROCENE MOLECULE

The discovery of the whole family of Metallocenes, including the well-known Ferrocene molecule, opened the door to the establishment of the contemporary organometallic chemistry. Particularly, the calculation of many physical properties of these complexes such as the electronic structure, vibrational frequencies and absorption spectrum remained as an open question for many years [156, 157, 158, 159, 160, 161]. The basic problem displayed by these complexes is the interaction present between the π-orbital states coming from the ciclopentadienyl ring and the metal d-orbitals provided by the iron ion. As a first step, the calculation of the electronic structure of the Ferrocene conformers (eclipsed and staggered configurations) was carried out at many different levels of theory where many different results were obtained [156]. Later, with the help of group theory, the organization of the energy levels for the valence orbitals was clarified allowing also to have a preliminary idea of the possible arrangement of the electronic states especially near the Highest-Occupied Molecular Orbital (HOMO) [157]. Nowadays, Density-Functional-Theory (DFT) and time-dependent density functional theory (TDDFT) have been employed as tools to investigate ground and excited states properties in the transition metal complexes [116]. Despite its effectiveness and rather simplicity DFT faces many theoretical drawbacks that are special sensitive in the case of the metallocene family (exchange-correlation implementation) but still offers advantages over the highly accurate wavefunction-based methods. Firstly, the computational cost scales more favorably with system size. Secondly the inclusion of static electron correlation within the DFT methodology is a crucial point over other ab-initio and semi-empirical methodologies [108]. In this appendix, the results of an extensive benchmark procedure will be presented in order to investigate the accuracy of well-established families of exchange-corelation functionals such as the B3LYP [42], BLYP [41], PBE0 [144] and compared with the new families of exchange-correlation potential implementations such as long-range corrected functionals like wb97xd [162].

Bond	Exp.(GED/XRD)	CCSD	B3LYP	BLYP	PBE0	wb97xD	TPSSh
Fe-C_5	1.66	1.64	1.68	1.71	1.69	1.644	1.683
Fe-C	2.053/2.059	2.068	2.073	2.045	2.056	2.046	2.039
C-C	1.435/1.431	1.428	1.458	1.438	1.449	1.423	1.446
C-H	1.080	1.07	1.091	1.12	1.094	1.094	1.098

Table A.1: Bond lengths for the eclipsed configuration (D_{5h}) [161].

Likewise, the influence of the basis-set size has been taken into account since a minimum and necessary amount of diffuse d-type of functions are needed to describe correctly the energy difference between the atomic $3d^n 4s^1$ and the $3d^{n-1} 4s^2$ states [160]. Thus, in this study, the best possible combination to achieve good quality results at moderate computational cost will be the main target making a special emphasis on comparison with known experiments and similar theoretical works [116].

A.1 GEOMETRY OPTIMIZATION

Nowadays accurate molecular equilibrium structures can be obtained by using ab-initio methods. In contrast, in the case of molecules that contain transition metals the accuracy can be achieved only by using an appropriate combination of exchange-correlation implementation and basis-set to represent the physical situation. In the case of Ferrocene, the complex exhibits a complicated bonding situations in which the vertical metal-ligand bond plays a fundamental role in the determination of the organization of the d-metallic states. Similarly, two almost iso-energetic mechanic conformations, namely, eclipsed (ground state) and staggered (saddle point) which are displayed in Fig.(A.1) have been reported both experimentally and studied theoretically [161, 116]. Many different levels of theory have been employed leading to the conclusion that coupled-cluster method including singlets and doublets excitations is the most accurate methodology where the calculated geometrical bonds are within the the experimental measurements [161]. Based on these results, many more levels of theory have been employed leading to the conclusion that only certain families of exchange−correlation implementations are suitable to describe relatively good the reported bonds [158]. Furthermore, not only it has been established that the employed exchange-correlation implementation plays a fundamental role but also the size of the basis−set used in order to describe the atoms is an important fact making a special emphasis on the d-states of iron. Thus, a benchmark procedure has been carried in order to assess the accuracy of the basis-set used for the calculations presented in this work. All calculations have been carried out using the Gaussian 09 computational chemistry package [107] where the default values have been imposed in order to achieve a precise level of accuracy both in energy and forces. The basis−set used for the DFT calculations is an extended version of the usual LACVP(d) in which the transition metal ion is described by the LANL2DZ effective−core potential and the organic−core is described by the $6 - 311++G(d,p)$ basis set instead of the usual $6 - 31G(d)$ [109, 110]. The results of the geometry optimization procedure for eclipsed (Table(A.1)) conformations are presented along with experimental values when available. Thus, the equilibrium structure of the Ferrocene molecule in its ground state has been determined and the selected family of exchange-correlations that displays a good agreement with experiment (for the eclipsed phase) and previous theoretical works [160, 161].
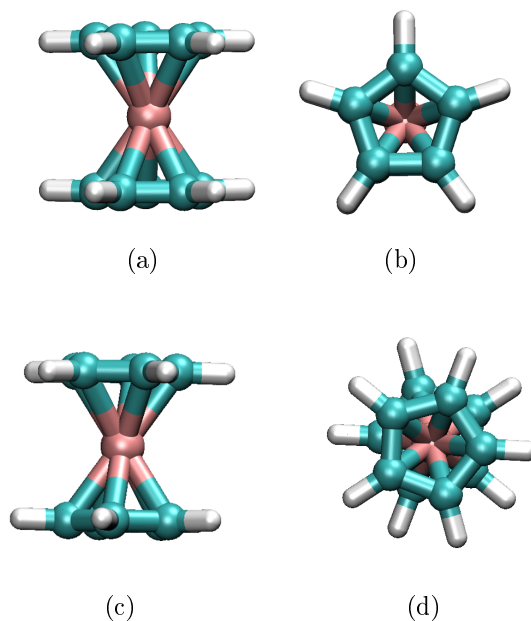
(a)   (b)

(c)   (d)

Figure A.1: Geometry optimized structure

A.2 ELECTRONIC STRUCTURE

The electronic structure of the two Ferrocene conformers is investigated using as starting point the previous geometry optimized models. A qualitative molecular orbital (MO) for the Ferrocene molecule is presented in Fig.(A.2) and provides a more explicit picture of the bonding within the Ferrocene molecule. Thus, the electronic structure is the result of the interactions of the ligand provided by the cyclopentadienyl (CP) ring and the metal orbitals coming from the iron ion. In this matter, the molecular orbital organization can be explained in terms of symmetry properties since molecular orbitals must follow the geometrical constraints imposed by the corresponding point group symmetry. Thus, the highest occupied molecular orbital (HOMO) can be seen as the combination of π anti$-$bonding CP (e_{2g} symmetry) states with the $d_{x^2-y^2}$ and d_{xy} metallic states provided by the iron ion. In the case of the lowest unoccupied molecular orbitals (LUMO) the combination comes from the occupied orbitals of the CP ring (e_{1g} symmetry) and the d_{xz}/d_{yz} iron orbitals [116].

A.3 HARMONIC VIBRATIONAL FREQUENCIES AND IR SPECTROSCOPY

Vibrational spectrum analysis is one of the most useful tools in order to determine many important properties of the studied complexes ranging from discerning whether an obtained geometrically optimized structure is a ground state conformation along its potential energy surface to simulated Infrared (IR) and Raman spectroscopy. Indeed, in the case of the Ferrocene complex the IR vapor spectra have been both experimentally and theoretically obtained [163, 164]. The outcome of the calculations carried out with the five exchange$-$correlation potentials are in
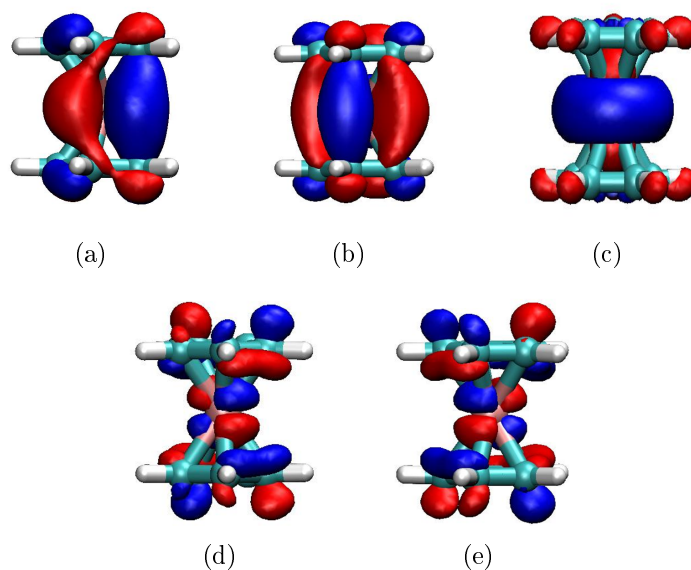
Figure A.2: Electronic structure of the Ferrocene molecule. (a) First four occupied frontier molecular orbitals with the corresponding energy values. The structure displays a point-group symmetry of D5$_h$ [116].

qualitatively good agreement with established results. The most important obtained picture is to show clearly the six dominant peaks in the spectra which are related to allowed dipole−transitions generated by distortions of the structure that creates inner non−permanent dipole moments [163, 164]. These transitions are observed in the energy ranges between the 300 cm^{-1} and 1500 cm^{-1} with a protruding peak at 840 cm^{-1} whose intensity is around 130 $\frac{KM}{Mol}$. The obtained results (Fig.B.6) with the basis set LANL2DZ $+ 6-311++$G(d,p) and all different exchange-correlation implementations are in good agreement with similar calculations and experimentally reported frequencies (see values in Table (A.2) and (A.3)). Likewise, in all cases, an imaginary frequency in the case of the staggered configuration (D5$_h$) is reported and, therefore, corroborating the picture of an eclipsed conformation as ground state in the vapor phase. Therefore, one can conclude that all used exchange-correlation implementations describe the most important physical features observed in experiments. However, a general tendency is that hybrid implementations of the exchange-correlation potential (B3LYP [42], TPSSh [165], PBE0 [144] and wb97xD [162]) give more accurate results in terms of frequencies assignments than the GGA implementation (BLYP) [41] counterpart and therefore making them more suitable to study gas-phase experimental results.

Bond	CCSD	B3LYP	BLYP	PBE0	wb97xD	TPPSh
Fe-C$_5$	1.658	1.678	1.691	1.681	1.649	1.665
Fe-C	2.060	2.075	2.101	2.067	2.068	2.054
C-C	1.429	1.435	1.413	1.439	1.442	1.442
C-H	1.075	1.090	1.101	1.082	1.093	1.090

Table A.4: Bond lengths for the Ferrocene-staggered configuration (D$_{5h}$) [161].

Exp. Technique	Expt Freq (1) (cm^{-1})	Expt. Freq. (2) (cm^{-1})
IR (1) / INS (2)	478	485
	492	504
	820	820-860
	1005	–
	1110	–
	3077	–
Exchange-correlation	Theoretical Frequencies (cm^{-1})	Theoretical Intensities ($\frac{KM}{Mol}$)
B3LYP	456.08	10.20
	465.6	19.50
	821.6	102.58
	1023.1	23.6
	1130.3	23.41
	3236.73	17.08
BLYP	452.28	6.31
	464.6	18.6
	827.03	116.7
	1029.40	24.44
	1136.23	21.32
	3250.14	16.52
PBE0	489.48	21.23
	502.40	23.65
	829.85	92.72
	1032.33	23.60
	1150.11	23.19
	3260.72	12.33
TPSS	491.65	30.50
	491.65	30.49
	828.88	67.26
	1024.07	19.52
	1125.90	26.75
	3233.60	26.80
wb97xd	495.59	19.44
	508.72	23.57
	836.50	106.24
	1025.21	23.83
	1151.43	21.60
	3260.78	14.48

Table A.2: Experimental and Theoretical reported Harmonic frequencies and intensities for the Ferrocene-eclipsed (D5$_d$) configuration [163, 164].
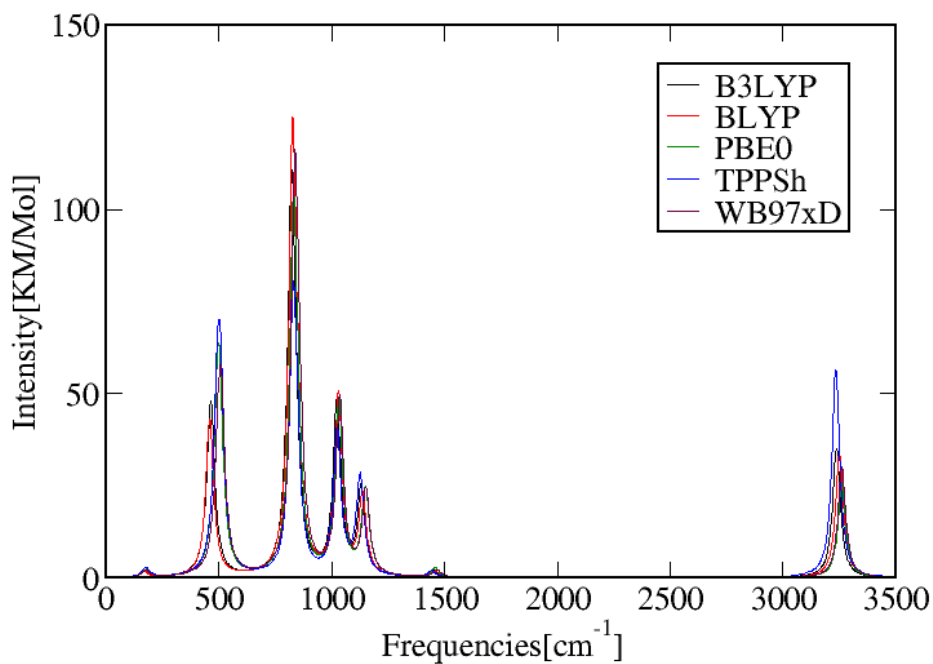
(a)
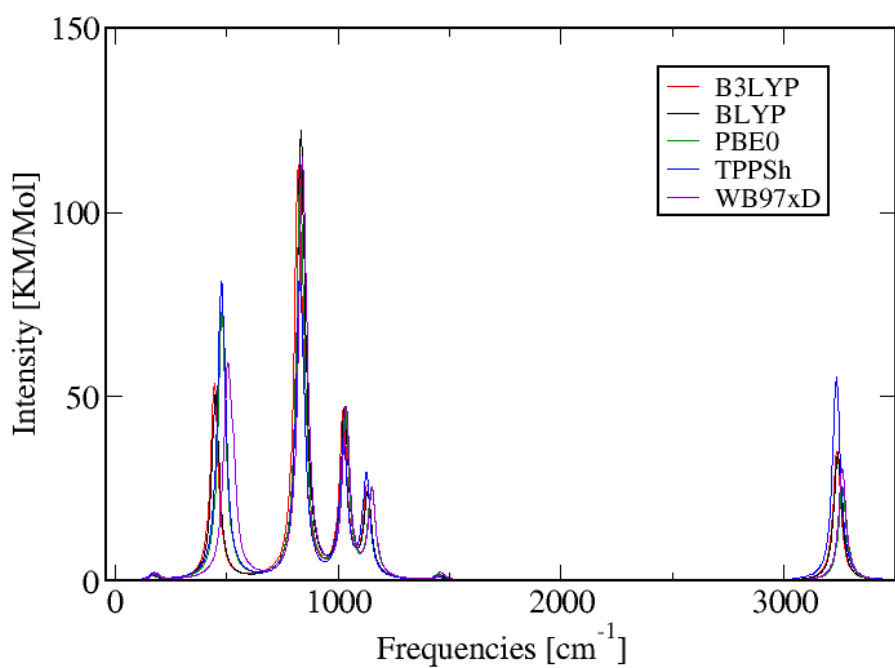
(b)

Figure A.3: Theoretical IR-spectra of the Ferrocene (a) eclipsed (D5$_\mathrm{d}$) and (b) staggered (D5$_\mathrm{h}$) configurations [163, 164].

| Exchange-correlation	Theoretical Frequencies (cm^{-1})	Theoretical Intensities ($\frac{KM}{Mol}$)
B3LYP	444.26	22.19
	450.68	10.5
	820.16	103.53
	1023.16	22.40
	1130.69	23.98
	3236.46	17.15
BLYP	449.30	21.47
	457.48	8.10
	832.61	112.53
	1029.74	22.51
	1133.35	22.48
	3239.59	17.03
PBE0	477.38	26.83
	477.60	28.83
	828.10	93.80
	1032.55	22.14
	1150.63	23.90
	3260.20	12.38
TPSS	473.67	28.23
	473.92	28.24
	826.26	66.05
	1023.83	18.52
	1126.50	27.71
	3233.45	26.65
wb97xd	500.96	25.24
	506.65	26.49
	838.92	103.59
	1035.95	22.63
	1152.43	23.30
	3259.81	14.96

Table A.3: Theoretical reported Harmonic frequencies and intensities for the Ferrocene-staggered ($D5_h$) configuration [163, 164].

A.4 OPTICAL PROPERTIES

The optical properties of Ferrocene have been well studied with a special focus on the ultraviolet−visible (UV−vis) spectrum. Thus, both diverse experimental techniques and different levels of theory have been employed in order to examine and understand the measured results [116]. In the vapor−phase case a first excitation with low oscillator strength at 5.59 eV and the strongest dipole−allowed transition is experimentally observed around 6.31 eV and subsequently theoretically confirmed by TDDFT. The relaxed eclipsed and staggered configurations have been used as starting point and the results from the absorption spectra are presented in Fig(A.4,A.5). Accordingly, no dipole−allowed transition are found in the visible range for both conformers in any of the different XC implementations used in this study and in agreement with previously reported studies [166]. In the case of the B3LYP [42] implementation the first excited state occurs at 5.49 eV while the second strongest dipole−allowed transition is obtained at 6.49 eV which are in reasonable agreement with previous studies where values of 5.26 eV and 6.49 eV have been reported. Similarly, for the BLYP [41] XC implementation the corresponding peaks are located at 5.75 eV and 6.68 eV which are slightly higher than the reference but still leading to a qualitatively good description of the spectra for the two conformers. The reported excitation energies for the PBE0 [144] and wb97xD [162] functionals are correspondingly higher in energy and increased by 0.3 eV 0.7 eV for the first excited state. For the second excited state the overestimation is around 0.4 eV in the case of PBE0 [144] but for the range-separated hybrid is around 0.8 eV. This tendency is observed for the two conformers and is in agreement with previous calculations [166]. Finally, the TPSSh [165] XC implementation predicts a splitting of the peaks both for the first excited state and the dipole−allowed transition excited state. In conclusion, the absorption spectra properties of the two Ferrocene conformers are well described by the B3LYP [42] XC functional with the LANL2DZ + 6−311++G(d,p) basis set. Similarly, the PBE0 [144] and BLYP [41] XC functionals described quantitatively well the energy gaps and the oscillator strengths for the first and dipole− allowed first excited state. Finally, neither the TPSS [154] nor the wb97xD [162] range-separated XC functionals are able to predict even qualitatively the excited states of the Ferrocene complexes for both conformers.

A.4.1 Conclusions

A systematic study of the two Ferrocene conformers, namely eclipsed and staggered, have been carried out. In terms of describing the ground state structure the hybrid exchange implementations (B3LYP [42], PBE0 [144], TPSS [154]) describe in a good agreement the length of the many selected bonds and the correct ground state once the corresponding vibrational analysis has been carried out. Likewise, the electronic structure, namely, the organization of the energy levels is correctly depicted. However, in the description of the excited states the B3LYP [42] a good quantitative and qualitative description of the absorptions bands while the TPSSh [165] implementation fails to describe correctly the absorption spectra and PBE0 [144] overestimates the excitation energies in a range of 0.3 eV. In the case of the BLYP [41] the GGA implementation describes qualitatively well the bond lengths and the truly ground state conformer but fails in describing correctly the order of molecular levels by underestimating the energy level associated with the d_{z^2} molecular orbital. In terms of UV−vis spectrum, this functional reports qualitatively good results in terms of energy gaps and oscillator strengths. Finally, the range-separated wb97xD [162] functional describes correct the geometry of the two conformers and
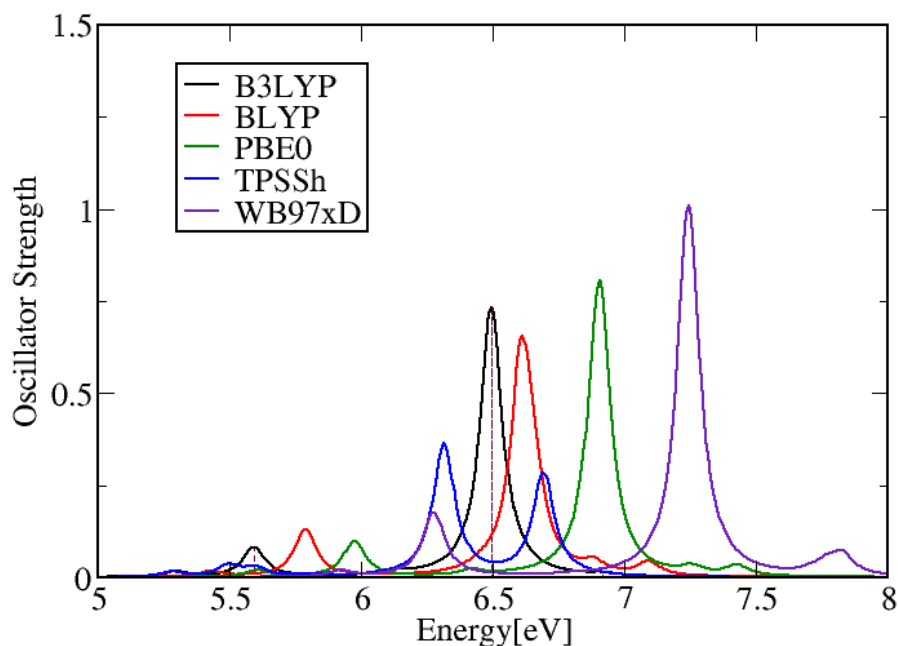
(a)

Figure A.4: Simulated UV-vis spectra for the Ferrocene eclipsed (($D5_d$)) configuration.

the corresponding bond lengths. Likewise, the functional is able to predict the correct ground state and the IR frequencies obtained are in good accordance with the experimental values. However, the UV−vis spectrum is not correctly represented by this functional leading to an overestimation of 0.8 eV in the dipole−allowed transition energy. Therefore, as a results of this systematic study one can conclude that gas−phase properties are best depicted by using the B3LYP [42] XC functional. However, the BLYP [41] functional offers the flexibility to describe physical properties of surfaces such as graphite with a good degree of accuracy and therefore this is a useful implementation that can be used in order to study of adsorption process of these molecules over Highly Oriented Pyrolytic Graphite (HOPG). In the same manner, PBE0 [144] can be used as alternative when the molecules are deposited onto metallic surfaces since this functional can be range-separated in order to describe long−range interactions as a GGA functional whilst short−range interactions can be described by the hybrid generated for PBE0 [46].
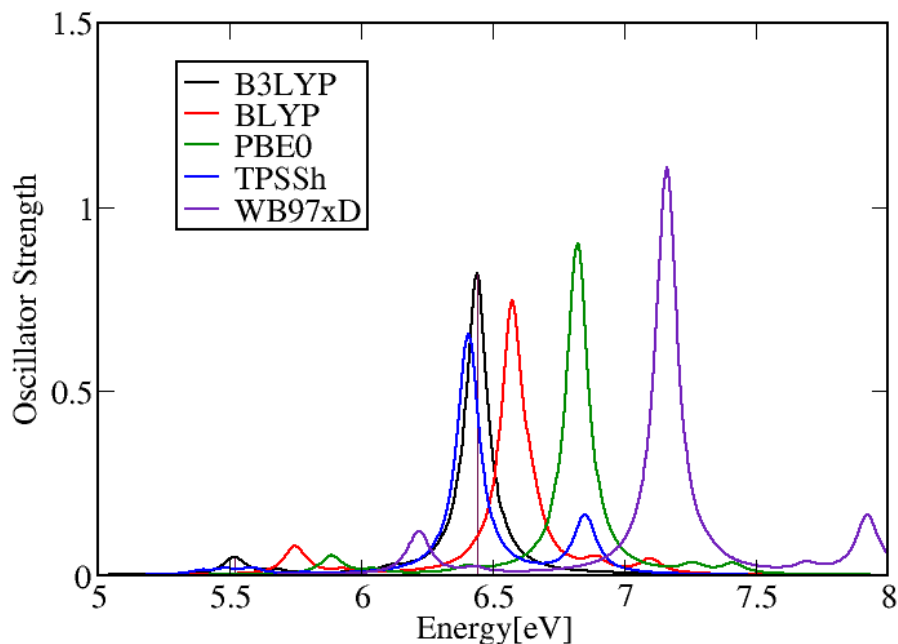
(a)

Figure A.5: Simulated UV-vis spectra for the Ferrocene-staggered configuration (D_{5h}).

A.5 CP2K BENCHMARK PROCEDURE

In this section the results of a benchmark procedure are presented in order to assess the correct combination of parameters for the Cutoff and Relative cutoff energies. This is a necessary procedure since in this implementation of DFT a grid is used in order to represent the electronic density making the accuracy of the results crucially dependent on these values. Thus, as a reference point for the electronic structure the former calculations carried out with the all electron code Gaussian 09 [107] will be used. At this point the main objective is to describe correctly the valence part of the electronic structure and the possible organization of the energy levels. Another important aspect is to assess the accuracy of the norm conserving, separable and dual space GTH-PP in order to describe the electronic structure of metalorganic complexes since in this approximation the chemically inert core electrons are averaged by a local and non-local effective potential fitted to a total all-electron wavefunction obtained of a fully relativistic density functional calculation of the atomic species [111, 112, 113, 114]. Thus, one can observe that a minimum of 300 Ry and 50 Ry for the Cutoff and Relative Cutoff, correspondingly, is needed in order to obtain negligible changes in the total energy for the Ferrocene molecule.
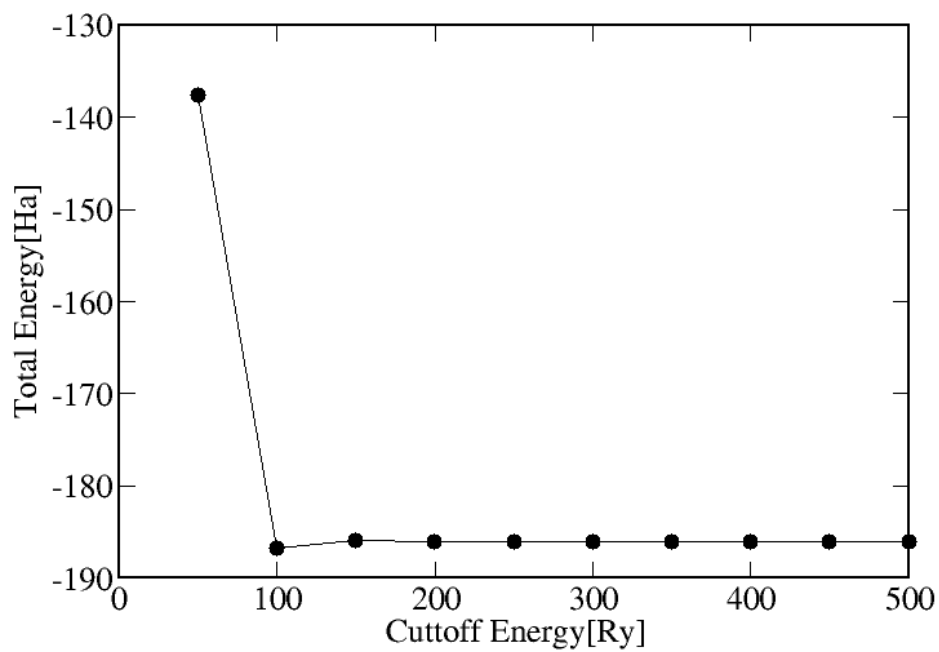
(a)
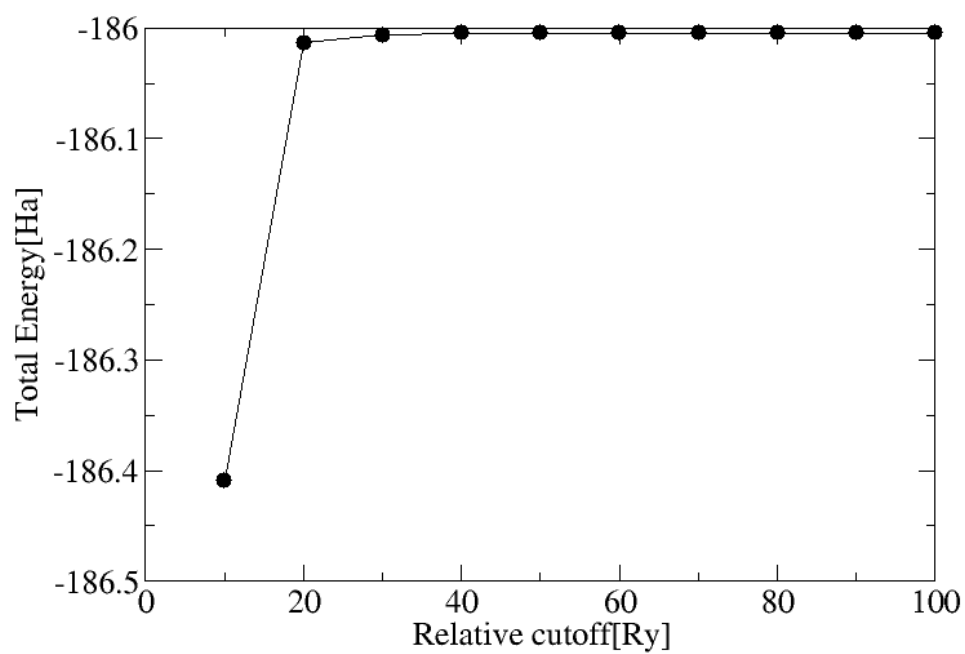
(b)

Figure A.6: Benchmark procedure in order to determine the CUTOFF and REL CUTOFF parameters in the CP2K software for the ferrocene molecule.

B BENCHMARKING THE ELECTRONIC STRUCTURE, VIBRATIONAL ANALYSIS AND OPTICAL PROPERTIES OF THE TETRAPHORPHYRIN

Porphyrin and its many different relate compounds have attracted much attention due to their intrinsically interesting electron features such as magnetism and the facility to carry out electrochemical processes such as reduction or oxidation [167]. In fact, tetraphenylprophyrins (TPP) are well known to be easily functionalized by metallic ions placed in the middle of the highly-symmetric molecular skeleton. However, there is still some discrepancies in the literature regarding to the truly ground state of many of these complexes since many different configurations have been examined and suggested as plausible ground states. In the case of the meso-TPP two possible configurations have been addressed as possible ground states, namely, a D4$_h$ and a C2$_v$ symmetries. Hence, it is important to assess which one of these structures is a plausible ground state since three plausible complexes using as organic-core the meso-TPP have been functionalized by adding amide groups at the edges of the phenyl rings allowing a possible self-assembly mechanism.

B.1 GEOMETRY OPTIMIZATION

The two possible meso-TPP complexes (Fig. B.1) have been relaxed using the Gaussian 09 software and by employing the B3LYP exchange-correlation functional in the case of TPP while for Zn-TPP-Zn the PBE0 has been used for computations [107, 42, 144]. Based on previous works carried out in the porphines complexes the 6−311++G(d,p) basis set has been used for the organic-moiety while for the metallic ion (Zn) the effective-core potential LANL2DZ has been employed [109, 110]. In the case of the meso-TPP with the original two hydrogen atoms, the results shows that the C2$_v$

(a)   (b)
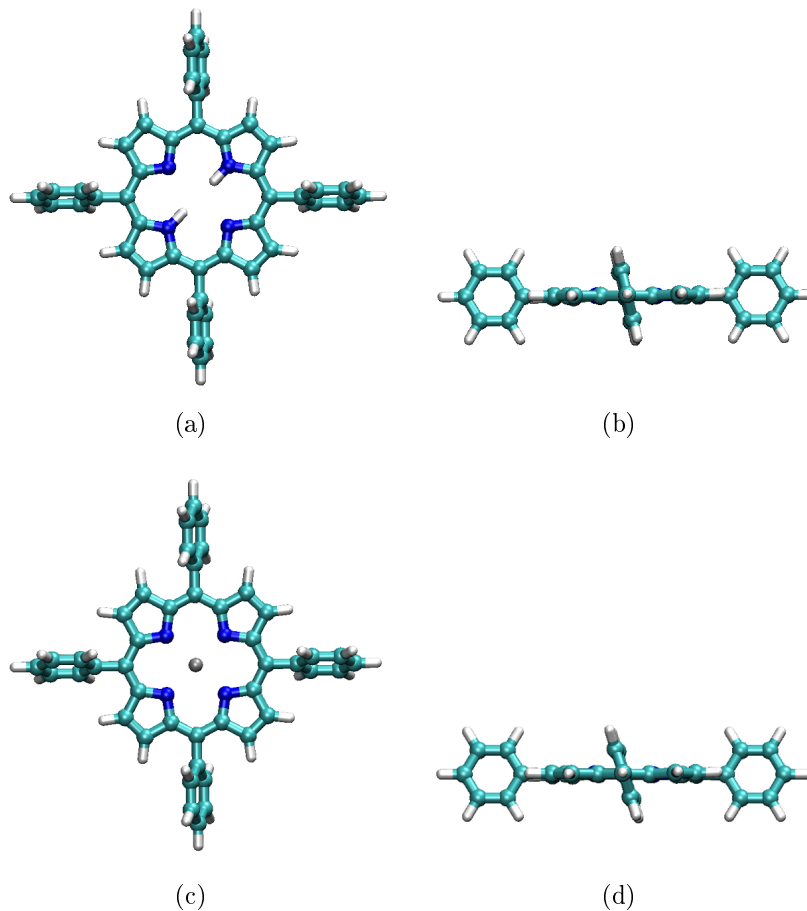
(c)   (d)

Figure B.1: Geometry optimized structure of the (a) meso-TPP and (b) meso-TPP-Zn molecular complexes. The ground state is found to be a $C2_v$ configuration where the phenyl rings are arranged .

configuration is energetically more favorable than the D_2 with an energy difference between the two of 150 meV. This is in agreement with recent experimental and theoretical work where this configuration has been observed by means of STM images in ultrahigh-vacuum (UHV) and environmental conditions [128]. In the case of the doped Zn meso-TPP the relaxed structure preserved the same point group symmetry ($C2_v$). The main difference between the two configurations is the torsional angle created amid the phenyl rings and the organic-porphyrin core. Likewise, the computed TPP molecular complex exhibits a near-planar porphyrin cores as it has been theoretical and experimentally established [168, 133]. Principally, the bonds formed in the meso-TPP are double- and single- bonds between the Carbon, Hydrogen and Nitrogen atomic species define the distances within the moieties. Thus, as highlighted in Fig. B.1 (a,b) the distances corresponds to either a single-Carbon bond ($\cong 1.45$ Å), double-Carbon bond ($\cong 1.40$ Å), double Nitrogen-Carbon bond ($\cong 1.36$ Å) and single- Hydrogen-Nitrogen bond ($\cong 1.01$ Å) [168]. In the case of the Zn-meso-TPP, the distances have changed since the inclusion of a metallic-ion distorts the atomic environment by electrostatic repulsion of the different atomic species. Thus, the computed Zn-N bond distance is $\cong 2.05$ Å in good agreement with reported distances from experimental measurements ($\cong 2.042$ Å) [169, 170]. Moreover, one can observed that besides the stretching of some lengths of the imidazole ring ($\cong 0.02$ Å in comparison with the meso-TPP) one can see no changes

in the structure of the parent meso-TPP bond-structure [169].. Finally, in the case of the meso-TPP also the torsional-angle of the phenyl-rings with respect to the porphyrin core can be further perused since its magnitude defines the point group symmetry in which the molecular-complex can be characterized. Thus, the obtained angles are 66.01° for all the phenyl-rings leading to a highly-symmetric molecule that displays a highly-symmetric point-group [169, 170].

B.2   ELECTRONIC STRUCTURE

The electronic structure of both TPP and Zn-TPP-Zn have been further investigated in order to understand the influence of the point group symmetry in the organization of the frontier orbitals. Thus, the HOMO-1, HOMO, LUMO and LUMO+1 electronic states of the different substituted meso-TPP complexes and the corresponding energy level diagram have been computed and the results displayed in Fig. B.2 and Fig. B.3. In both cases, the HOMO and HOMO-1 (Fig. B.2 (c,d) and Fig. B.3 (c,d)) are nearly degenerated supporting while the LUMO and LUMO+1 (Fig. B.2 (a,b) and Fig. B.3 (a,b)) should be strictly degenerated by symmetry reasons but due to the single-particle representation used in DFT one has a really small splitting in energy ($\cong 10$ meV).

(a) LUMO   (b) LUMO+1
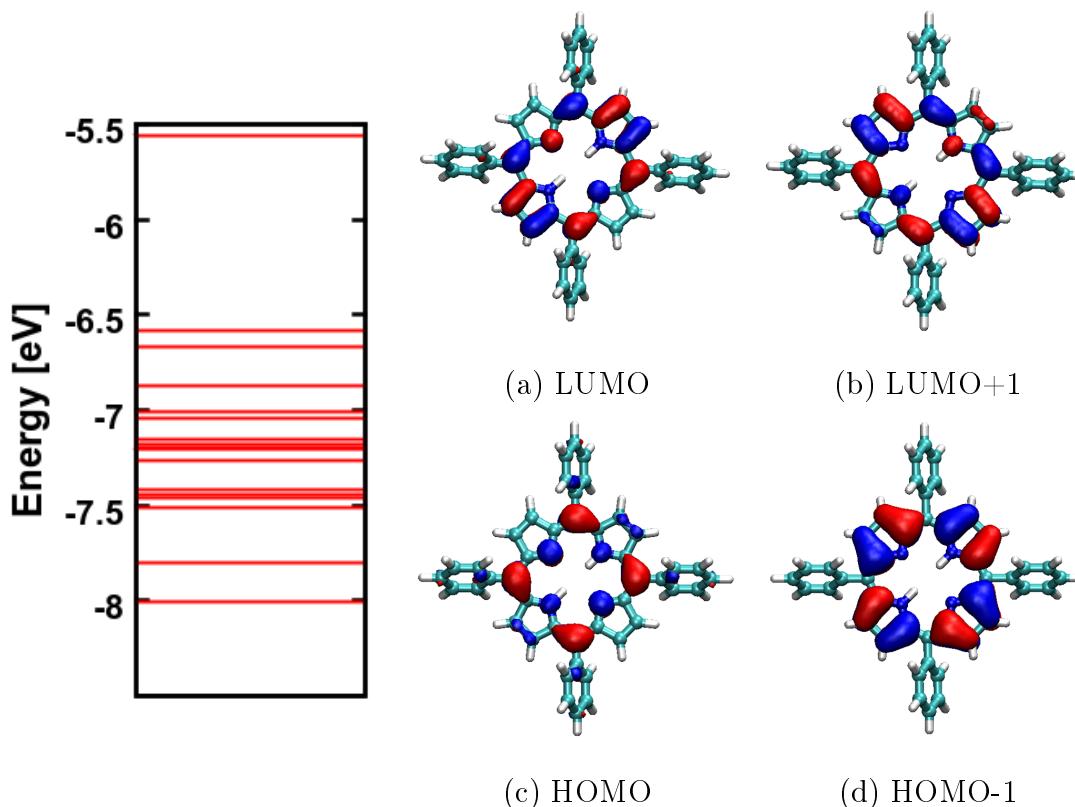
(c) HOMO   (d) HOMO-1

Figure B.2: Electronic structure of the TPP complex. (a,b) First two unoccupied and (c,d) two occupied frontier molecular orbitals with the corresponding energy values. The structure displays a point-group symmetry of S_4 and small splitting amid consecutive energy levels.

These results are in good agreement with the four model orbital suggested by Gouterman in order to explain the electronic structure of the meso-TPP moiety [168]. In the case of the meso-Zn-TPP moiety, the expected contribution of the 3d states is not observed in the frontier molecular orbitals. The HOMO and HOMO-1 states are mainly constructed by porphyrin σ bonds and not a d_π bond has been reported in the frontier orbitals leading to the conclusion that d-states of the Zn ion do not participate actively in the formation of bonds and those states can be found in deeper regions of the energy level diagram [169]. The FMO in both cases are delocalized mainly on the porphyrin macrocycle but also with an important contribution of the phenyl-ring groups that is stronger noticed in the TPP compound than in the Zn-TPP moiety [168, 169].

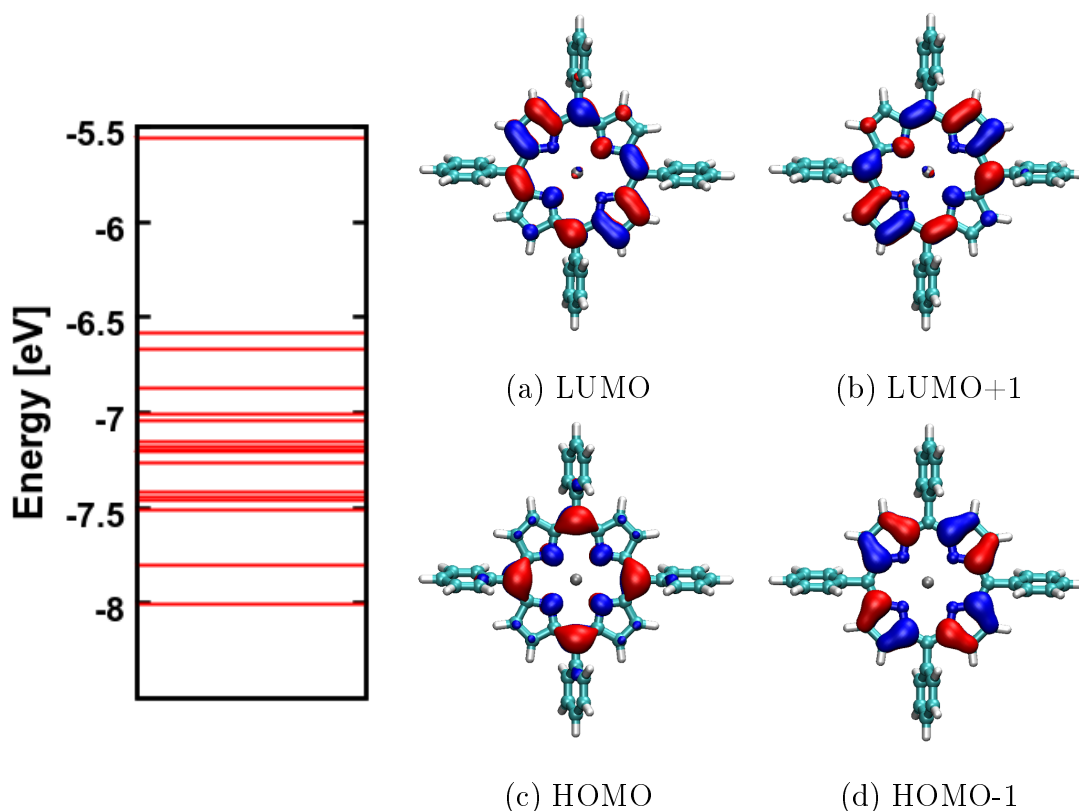(a) LUMO   (b) LUMO+1

(c) HOMO   (d) HOMO-1

Figure B.3: Electronic structure of the Zn-TPP complex. (a,b) First two unoccupied (c,d) First two occupied frontier molecular orbitals with the corresponding energy values. The structure displays a point-group symmetry of C_4 and small splitting amid consecutive energy levels.

B.3 PHOTOPHYSICAL PROPERTIES

The vertical excitations of the meso-TPP has been calculated using a TDDFT formalism and the results displayed in Fig. B.4. In this case, a benchmark procedure has been carried out in order to establish the accuracy of five different exchange-correlation functionals ranging from GGA approximations to long-range implementations. In general terms, the five different XC-functionals used to explore the optical allowed excited states described the main features of the absorption spectra with small shifts in the wavelengths of the strongest allowed states [167, 168].
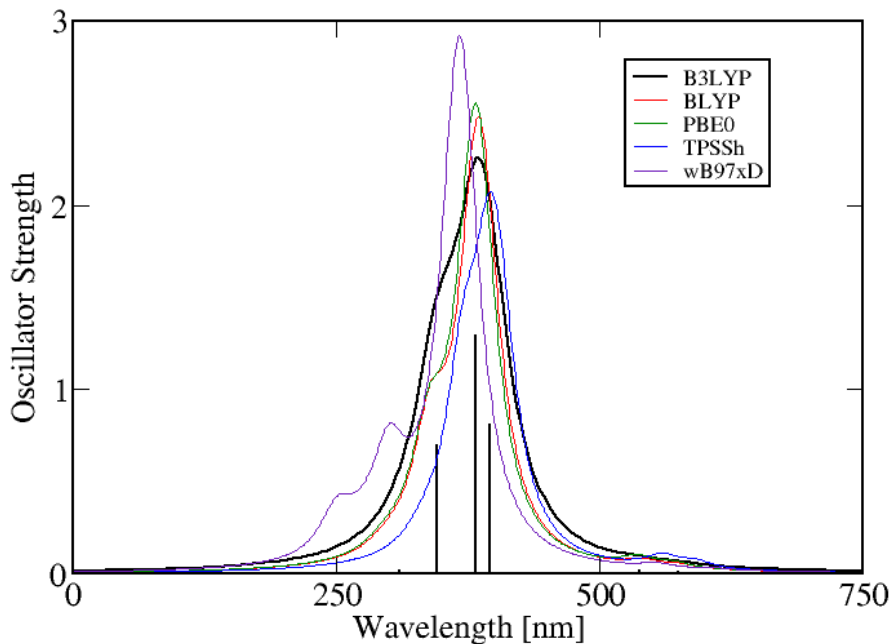
(a)

Figure B.4: UV-vis absorption spectra of the TPP molecular complex.

In the case of the long-correct implementation (wB97xD [162]) one can observe that some optical allowed states are reported in a range between 250 and 300 nm which are not experimentally observed leading to the conclusion that this functional is not describing qualitatively correct the physical picture [167, 168, 169]. The Soret or the B band could be adsorbed around 400 nm, which is intense due to the existence of highly conjugated ring system in porphyrins. On the low energy region, weaker intensities between 500 nm and 800 nm have been computed, which are generally assigned as Q band [167, 168, 169]. Their spectral transitions can be interpreted by means of the four orbital Goutermans model in which the most intense peaks can be assigned to an interplay between the HOMO-1, HOMO, LUMO and LUMO+1. Concerning the Zn-TPP molecular complex the vertical excitations have been also calculated by employed only the PBE0-XC functional [144]. In this case, the first optically allowed excited states are singlets and almost degenerated in energy ($\cong$ 2.296 and $\cong$ 2.298, respectively) and are formed by a linear combination of HOMO, LUMO and LUMO+1. The strongest bands are related also with the Q bands with reported oscillator strengths of 1.315 and 1.317, respectively. The participating molecular orbitals are related with transitions of the HOMO and HOMO-1 to LUMO and LUMO+1 with a small participation of a metallic state provided by the state HOMO-14 that goes to LUMO+1. The same arrangement between Soret and Q bands is observed as in the parent meso-TPP in which strong absorption peaks are reported around 380 nm (SORET) while weak optically allowed dipole-moment transitions are obtained in the region nearby 500 nm to 800 nm [167, 168, 169].
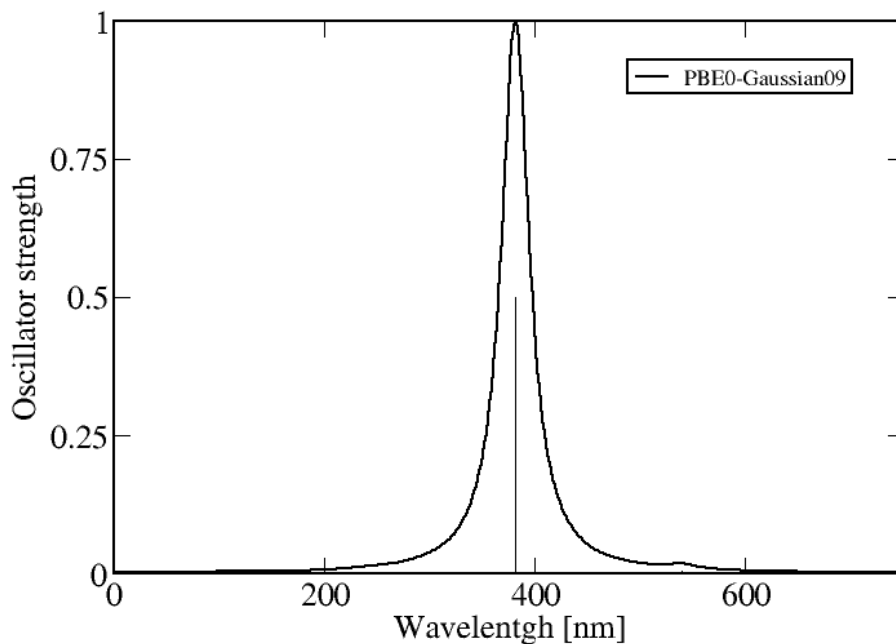
(a)

Figure B.5: UV-vis absorption spectra of the Zn-TPP molecular complex.

B.4   VIBRATIONAL ANALYSIS

The resonance Raman spectrum of the meso-TPP and Zn-TPP has been computed and further analyzed in order to clarify the impact played in the normal modes the substitution carried out with the Zn-ion [129, 170]. Likewise, since experimental values are available in literature, this calculation permits us to test the accuracy of the CP2k in order to describe the Raman properties of a molecular complex [111, 112, 113, 114]. Thus, in the case of meso-TPP the benchmark procedure has been carried out in order to observe how the different XC-functionals describe the Raman spectrum of this moiety. In general terms all XC-functional tested describes the same physical picture except in the frequency region between 1100 cm^{-1} and 1800 cm^{-1} some discrepancies are found in PBE0 and TPPS with B3LYP [144, 154, 42]. In both cases, the spectrum shows a high-frequency bands which are related with in-plane movements of the central porphyrin core [129]. At this point, for the Zn-TPP moiety one has to notice that there is a marked disparity is found between CP2k and Gaussian-09 calculations [111, 107]. These disagreements can be due to the fact that PAW pseudo-potentials have been employed in CP2k and those are not employed in the all-electron calculations like Gaussian 09. In the middle- and lower- frequency bands one can find many Raman features with medium and relatively weak intensities while strong modes with high intensity are found more concentrated in the 500 cm^{-1} to 1100 cm^{-1} frequency band region [129]. In the meso-TPP moiety, one can observe a high-intensity peak at 969 cm^{-1} which is a combination of a rocking displacements of the phenyl-rings and stretching shifting of the Nitrogen atoms in the porphyrin-core [129].

Finally, a peak with frequency of 1504 cm^{-1} and high-intensity is a combination of rocking-displacement phenyl-rings and scissoring movements of the four imidazole moiety [129]. In the case of the Zn-meso-TPP molecular complex one can observe a broad variety of Raman features including high-frequency bands throughout the whole spectrum [170]. In this matter a medium intensity peak can be found at 418 cm^{-1} which is a twisting displacement of the carbon atoms within the four-phenyl rings. Likewise, a peak located around 788 cm^{-1} is related with wagging collective movements also of the four-phenyl rings. The most protruding peak in the spectrum at 1029 cm^{-1} can be assigned to a stretching movement of the Carbon atoms within the phenyl-rings moiety coordinated in the four-phenyl rings and stretching movements of the Nitrogen atoms located at the porphyrin-core [170] . In conclusion, the Raman spectra of meso-TPP and Zn-meso-TPPS molecular complexes display similar features in terms of combination of movements of the different molecular-groups within the molecular complexes. Likewise, the comparison carried out between Gaussian-09 (all-electron code) and the PAW pseudo-potential implementation (CP2K) show a remarkable good agreement describing the main Raman features of the Zn-meso-TPP molecular complex and validating the use of this tool in the study of more complicated molecules like the ones carried out in this work [111, 107].
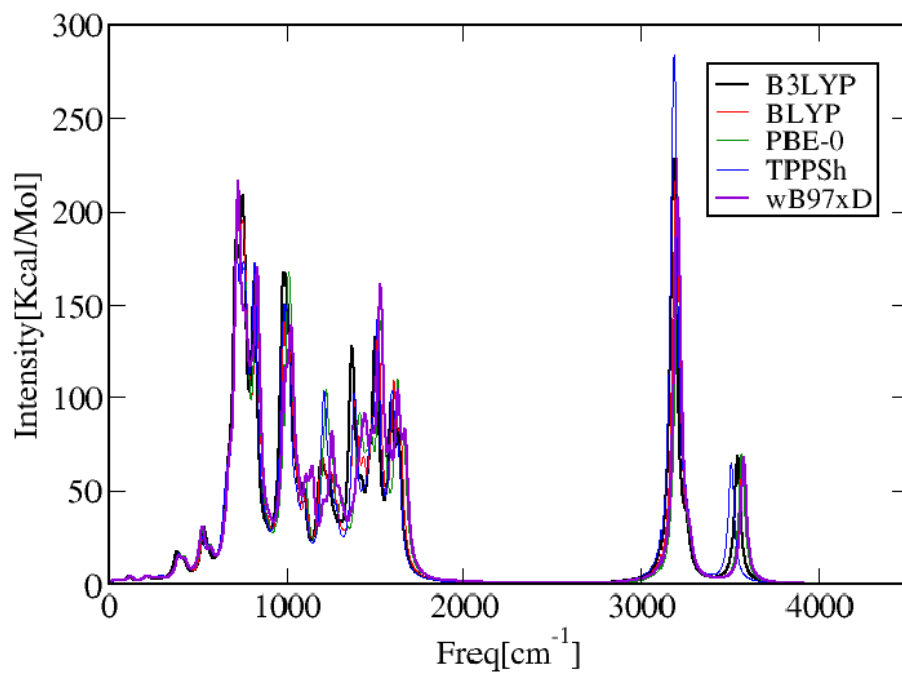
(a)
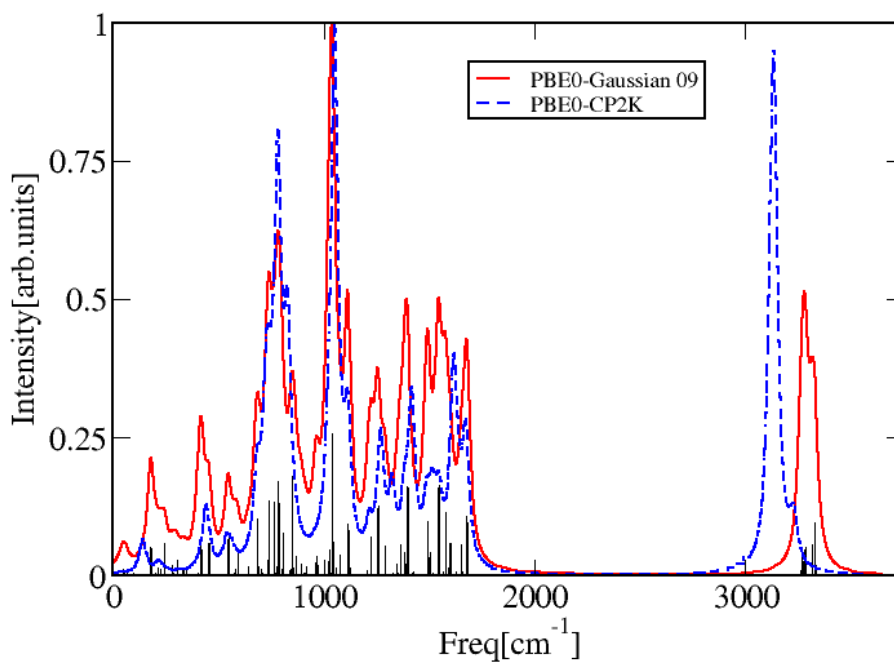
(b)

Figure B.6: Theoretical IR-spectra of the (a) TPP (a) and (b) TPP-ZN configurations.

C BENCHMARKING THE ELECTRONIC STRUCTURE AND VIBRATIONAL STATES OF THE GUANINE-QUARTETS

Base pairs linked by hydrogen bonds constitute one of the most important structural motif in order to achieve self-assembly. Thus, many theoretical work has been carried with the aim to obtain correct geometrical structures and assess the interaction energies of these bonds. Guanine quartets have attracted much interest since these structures are known to be formed in parts of the human genome or as a result of electrostatic interactions within Guanosine-gels. In terms of the m-QCA architecture, those characteristics are desired since self-assembly can be used as driving force to design electronic circuitry and therefore the original base pair has been further functionalized in order to enhanced such properties [171].

C.1 GEOMETRY OPTIMIZATION

In this appendix a benchmark procedure is presented in order to supplement the results obtained in chapter . Calculations have been performed by using the Gaussian 09 software [107] using the B3LYP exchange-correlation since previous theoretical results have shown a good agreement in terms of structure and the energy description between this function when is compared both with experimental data and MP2 calculations [119, 42]. A $6-311+G(d,p)$ basis-set has been used throughout the calculations with the exception of the Bromine atom where the LANL2DZ basis set has been used [109, 110]. In order to determine the structures and interactions energies of the individual molecules and as part of the quartet-configurations the initial configuration has been relaxed using the very tight option of the program in the optimization procedure for both cases and results displayed in Fig.C.1. It has been already shown that G-quartets are intrinsically non-planar presenting deviations from the total planar C_{4h} structure. For the further functionalized structures this feature is preserved and is more strongly observed in G2 than in G1. A point
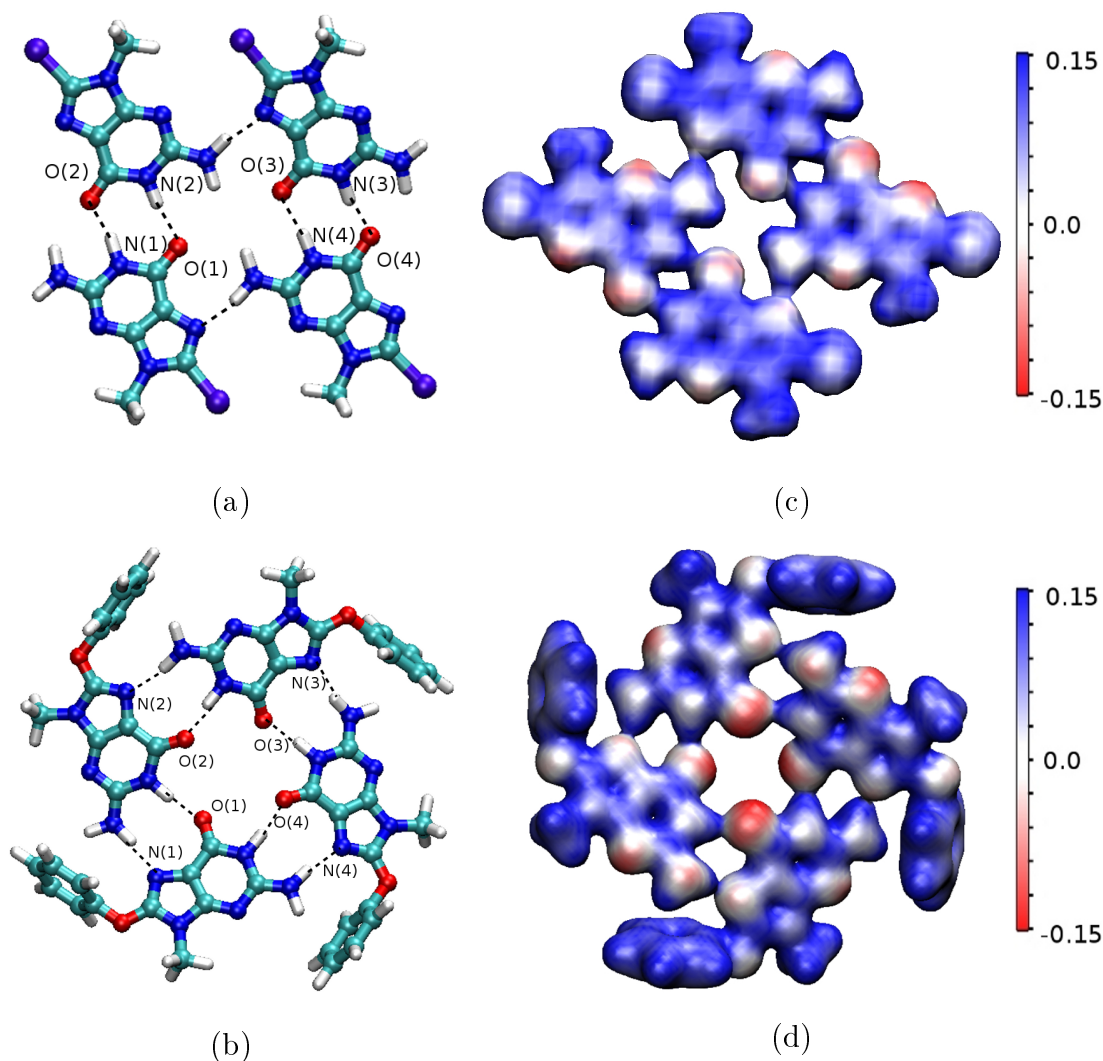
(a)

(c)

(b)

(d)

Figure C.1: Geometry optimized structure for G1 and G2 motifs, respectively. (a,b) Relaxed structure perpendicular to the ribbon formation plane. (c,d) Molecular electrostatic potential (MEP).

group analysis of both structures have been carried out and where two possible point groups, namely, S_4 and C_4 have been obtained in the case of G2 whereas in G1 only the C_2 has been obtained as a possible point group symmetry [121]. In the relaxed structure one can clearly observed that the ribbon structure is formed by the pairs $O \cdots H-N$ for ribbons which are in facing each other and parallel to the $\vec{a}$ fo the unit cell. The possible bromine halogen bonding can take place along the $\vec{b}$ lattice vector and is formed via a possible $Br \cdots H-N$ bond. In literature, similar cases have been reported and already established that the typical distances of these bonds can range from 2.5 Å in the case of $Br \cdots N-H$ to 3.39 Å in the case of a very weak intermolecular interaction of $C{=}N \cdots Br$ kind for crystalline measured phases [119, 172]. Thus, the obtained distance amid the Bromine and the Hydrogen atom is of the order of 3.2 Å which corresponds to a picture of a very weak halogen bonding. Likewise, the molecular electrostatic potential displays a picture in which the ribbon formation is favored more by a dimer picture supported by the $O \cdots H-N$ bonds rather than a truly quartet generated for a much more symmetrical arrangement of

the Br atoms within the ribbon. In the case of G2, the G-quartet is optimized for a Hoogsteen-type geometry with a classical hydrogen picture where the network is formed by the O$\cdots$ H-N pairs [119, 172]. Interestingly is that the intrinsically non-planarity observed in the original G-quartet is still noticed in the G2 structure and subsequent corroborated by a point group symmetry analysis where a S4 is obtained and in good agreement with previous works for the G-quartet. In both cases the interaction energies have been calculated according to $\Delta E = E(B_4) - 4E(B)$ where $E(B_4)$ is the total energy of the ribbon including the BSSE correction scheme and E_B is the total energy of a single base. Results are collected in Table (C.1) in which one can observe that both ribbons are predicted to be mechanical stable

Ribbon	Total Energy (a.u)	Monomers	ΔE	BSSE
G1 (Bromine)	-12612.216525	-12612.101661	-0.114915	0.012011203171
G2 (G-quartet)	-3552.849860	-3552.739242	-0.110612	0.007883615194

C.2 VIBRATIONAL ANALYSIS

For both cases vibrational analysis has been carried out leading to conclude that both geometrically minimized structures are in a minimum at the potential energy surface since no imaginary frequencies have been reported in the IR simulated spectra (Fig. C.2). The simulation of the spectra have been carried our and complemented by using a Lorentzian band shape with band width on half-height 10 cm^1.In fact, the IR spectra provides a clear view of how atoms are bonded and therefore clarifying the role played by the Bromine replacement in the G1 molecular complex. Thus, the most protruding modes have been selected for both the G1 functionalized Bromine and the G2 quartet structure in order to observe the kind of bonds created in these motifs. As a result of the calculations, in both cases the spectrum displays interesting features since modes with large spectral weights are located in the frequencies ranging from 1000 cm^{-1} to 2000 cm^{-1}. In the case of the G1 complex, the calculated vibrational mode with a computed intensity of 3750 $\frac{Kcal}{mol}$ and frequency of 1714 cm^{-1} is mainly associated to a collective movement of the O(1), O(2), N(1) and N(2) atoms which are actively participates in the Hydrogen bonding scaffold in the dimerized ribbon structures (see Fig. C.1 for enumeration). Furthermore, once the other vibrational modes which have a significative weight contribution in the spectra have been visually inspected and all of them are related with combinations of movements associated with atoms O(1), O(2), N(1) and N(2) (including the Hydrogen atoms) and the aromatic rings supplied by the Guanine scaffold. Finally, vibrational modes associated with the Bromine atom are spotted in the lower region of the IR-spectra (1-100 cm^{-1}) where weak contributions are observed. Thus, one can conclude that the Halogen bonding is not playing a significative role in the formation of the motif and rather one can ascribed the supramolecular network as a formation of single and doble Hydrogen bonds between the Bromine functionalized Guanines. Similarly, the IR-spectrum for the G2 complex has been calculated and analyzed with a special emphasis in the mode with associated frequency of 1787 cm^{-1} and an intensity of 980 $\frac{Kcal}{mol}$. This particular vibrational mode involves the participation in collective movements of the O(1),O(2), O(3) and O(4) with the corresponding N(1), N(2), N(3) and N(4) (including the Hydrogens) atoms in a series of collective rocking and scissoring movements. Precisely, these atoms are the ones responsible for the formation of the G-quartet ribbon structure and therefore reinforcing the physical picture of a Hydrogen bonding G-quartet supramolecular scaffold.
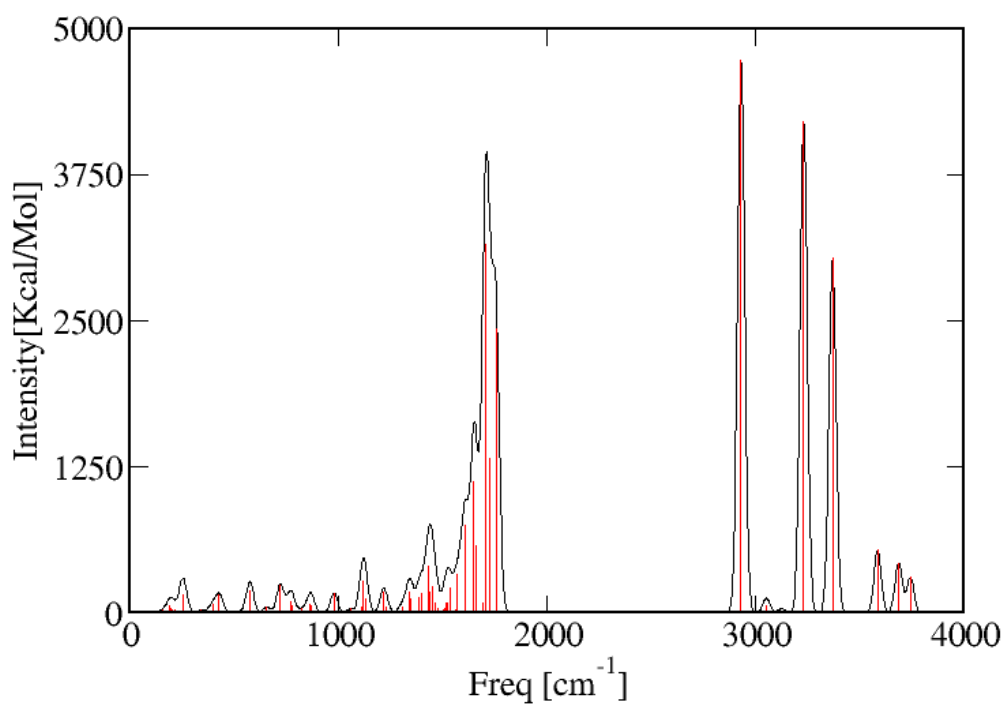
(a)
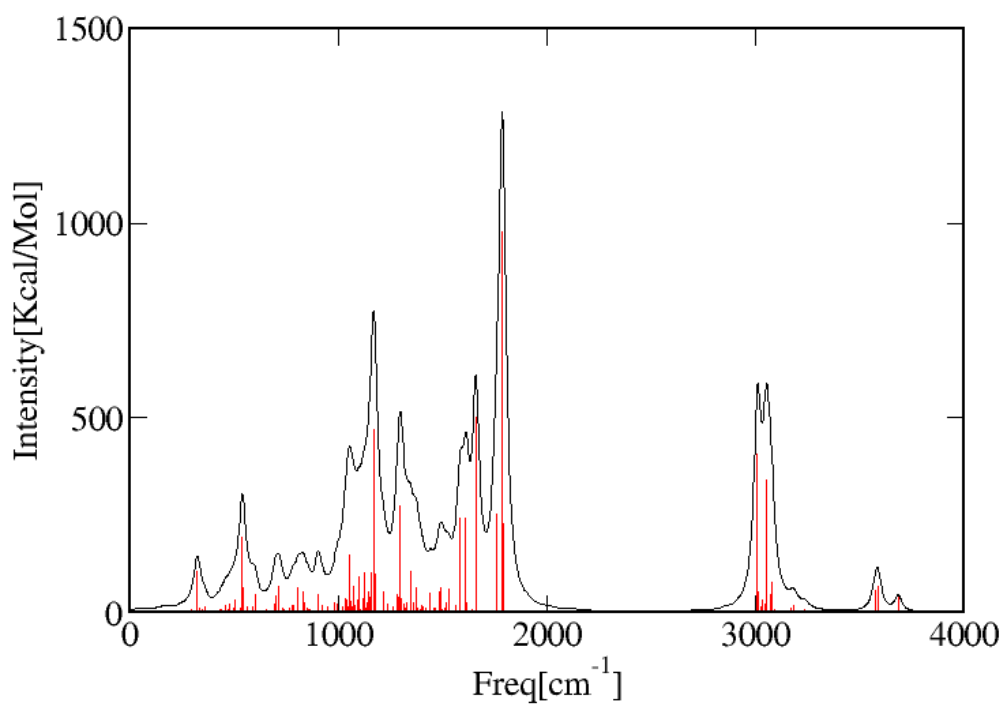
(b)

Figure C.2: Simulated vibrational spectra for (a) G1 and (b) G2 molecular complexes.

C.3   ELECTRONIC STRUCTURE

The electronic structure of both structures has been studied and discussed in terms of the molecular orbital distribution and energy levels (Fig. C.3 and C.4). In the case of G1 the frontier orbitals are geometrically localized at each of the base pairs forming the quartet and the difference between associated energy levels is small (around meV amid consecutive energy levels). This issue can be understood in terms of symmetry since the G1 ribbon displays a planar configuration closer to the highly-symmetric C_4h point group symmetry and therefore leading to degeneracies in the electronic structure. On the contrary, for the G2 functionalized complex we observed a much better separated energy levels and more delocalized compared with the previous case. This is a consequence of a lower point-group symmetry that imposes fewer restrictions to the electronic density and therefore allowing a more delocalized picture of the molecular orbitals. Finally, The HOMO-LUMO gap has been calculated using TDDFT and obtained as 1.3 eV and 1.5 eV for G1 and G2, correspondingly.

(a) HOMO   (b) HOMO-1

(c) HOMO-2   (d) HOMO-3

Figure C.3: Electronic structure of the G1 complex. (a) First four occupied frontier molecular orbitals with the corresponding energy values. The structure displays a point-group symmetry of S_4 and small splitting amid consecutive energy levels.
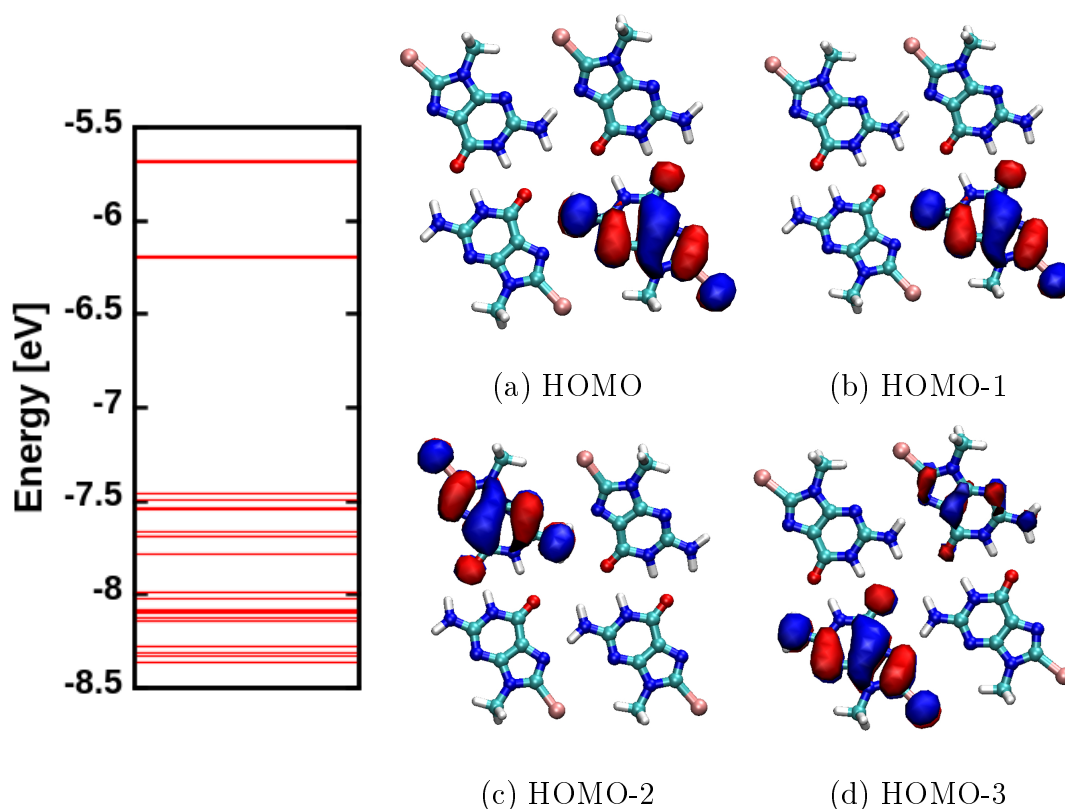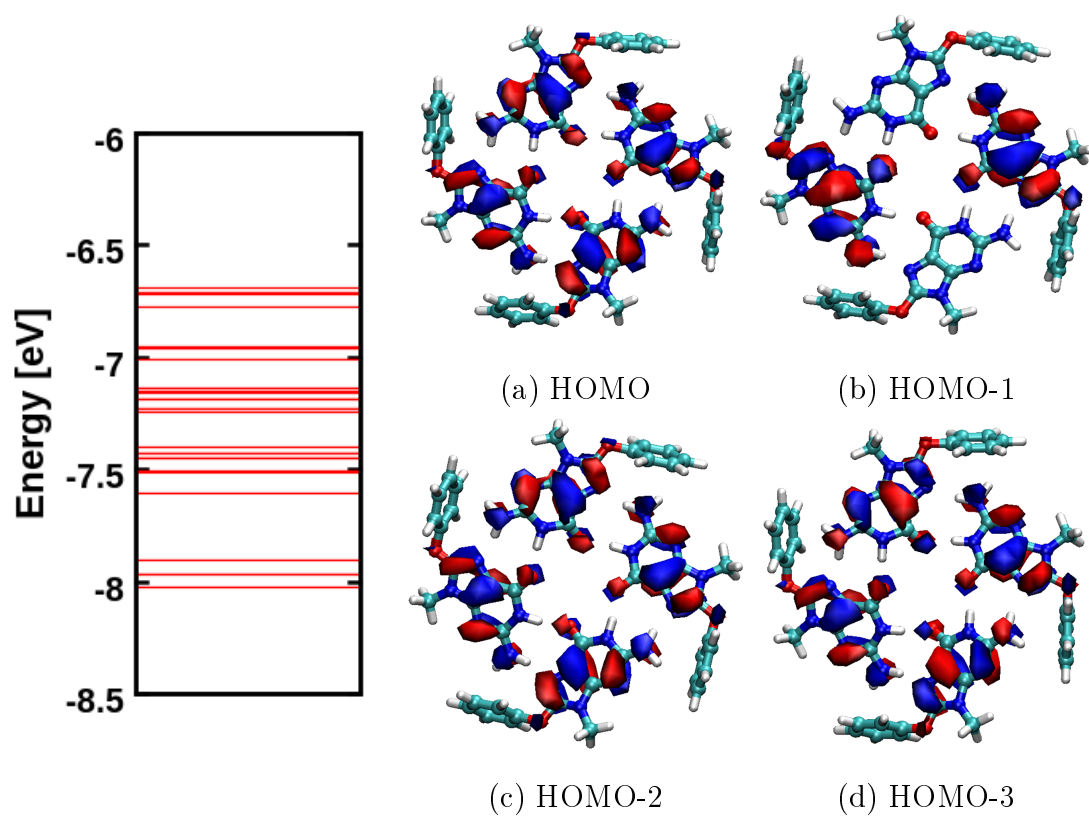
(a) HOMO

(b) HOMO-1

(c) HOMO-2

(d) HOMO-3

Figure C.4: Electronic structure of the G2 complex. (a) First four occupied frontier molecular orbitals with the corresponding energy values. The structure displays a point-group symmetry of S$_4$ and small splitting amid consecutive energy levels.

D ACKNOWLEDGMENTS

At this point, my personal gratitude with plenty of people that made my life more interesting in Dresden and also known as the members of the "Gang", namely, Carlito, Sara Vanessa, Nacho, Bruno, Nga, Manuela, Thomas and Mitra. With those "Partners in crime" it would not be possible to have such a nice afternoons of guitar hero and fun that we had.

En este espacio también quisiera agradecer muy especialmente el apoyo de mi Familia, con la cual no hubiera podido ni siquiera empezar este viaje. Muchas gracias! A todos y cada uno de ellos que han sido una fuente de inspiración y fortaleza en este proceso en el cual, y que con mucha fortuna, he concluído. A mi Mamá Marta, mi Abuela Alba, mi Tía Claudia, mi Hermano Andres y mi Padre Pedro, porque ellos siempre estuvieron allí alentándome en las no pocas amargas y sombrías horas en las que este proyecto se desenvolvió. Quisiera agradecer a los "inmortales" a mis amigos más leales con los he contado siempre, a Nelson, a Goyes, a José Luis, a Alberto y a Diego porque con sus chistes, comentarios y anécdotas siempre me recordaron que apesar de las circunstancias siempre encontramos la manera de salir victoriosos, a ellos, que siempre me dijeron "h tan h epi ta" quiero dedicarles este trabajo. También, una mención a aquellos que ya partieron pero no por eso han dejado de ser importantes, hablo de mis abuelos Antonio y Daniel, que

a través de su ejemplo y sus aún resonantes palabras han sido fundamentales para recordarme de donde vengo, hacia donde voy y de qué material estoy hecho, este que ha sido, en una especie de gran lotería cósmica, la esencia de la que estoy compuesto. Finalmente, no puedo dejar de mencionar a la mujer que, con su compañía, siempre ha hecho mi vida un lugar y un tiempo especial, y por eso es también para ella este trabajo, nuestro trabajo, para Marzena.

E PUBLICATIONS, PRESENTATIONS AND CV

E.1 THESIS BASED ON

1. Bonilla, A. S., Gutierrez, R., Sandonas, L. M., Nozaki, D., Bramanti, A. P., Cuniberti, G. (2014). Structural distortions in molecular-based quantum cellular automata: a minimal model based study. Physical Chemistry Chemical Physics, 16(33), 17777-17785.

2. Bonilla, A. S., Sandonas, L. M., Nozaki, D., Gutierrez, R., Cuniberti, G. (2014). Time-dependent study of the electron-transfer effect: a minimal model based study. Submitted.

3. El Garah, M., Perone, R. C., Bonilla, A. S., Haar, S., Campitiello, M., Gutierrez, R., Gianaurelio Cuniberti, Stefano Masiero, Artur Ciesielski, Samorì, P. (2015). Guanosine-based hydrogen-bonded 2D scaffolds: metal-free formation of G-quartet and G-ribbon architectures at the solid/liquid interface. Chemical Communications, 51(58), 11677-11680.

4. El Garah, M., Bonilla, A. S., Ciesielski, A., Gualandi, A., Mengozzi, L., Fiorani, A., Calvaresi, M. F. Zerbetto, G. Cuniberti, P. G. Cozzi, F. Paolucci and P. Samorì (2016). Molecular design driving tetraporphyrin self-assembly on graphite: a joint STM, electrochemical and computational study. Nanoscale, 8(28), 13678-13686.

5. Naydenov, B. Torsney, S. Santana-Bonilla, A. El Garah, M. Ciesielski, A. Gualandi, A. and Mengozzi, L. Cozzi, P. G. Gutierrez, R. Samori, P. Cuniberti, G. Boland, J. J (2016). From ultra-high vacuum to ambient conditions: STM/STS characterization of modelled 2D molecular networks. Submitted.

E.2 OTHER PUBLICATIONS

1. El Garah, M., Sinn, S., Dianat, A., Santana-Bonilla, A., Gutierrez, R., De Cola, L., Gianaurelio Cuniberti, Artur Ciesielski, Samorì, P. (2016). Discrete

polygonal supramolecular architectures of isocytosine-based Pt (ii) complexes at the solution/graphite interface. Chemical Communications, 52(74), 11163-11166.

2. Nozaki, D., Lokamani, Santana-Bonilla, A., Dianat, A., Gutierrez, R., Cuniberti, G. (2015). Switchable Negative Differential Resistance Induced by Quantum Interference Effects in Porphyrin-based Molecular Junctions. The journal of physical chemistry letters, 6(19), 3950-3955.

3. Bramanti, A. P., Santana-Bonilla, A., Rinaldi, R. (2015). Quantum-dot Cellular Automata: Computation with Real-world Molecules. International Journal of Unconventional Computing, 11(1).

E.3   CV

1. Education:

    (a) 2012-2016 Technische Universität Dresden (TUD, Dresden University of Technology) Dresden, Germany. PhD Candidate/Dr.rer.nat in Physics Advisor: Pr. G. Cuniberti

    (b) 2007-2009 Universität Stuttgart (University of Stuttgart) Stuttgart, Germany MSc in Physics. Advisor: Pr. Dr Hans-Rainer Trebin

    (c) 2001-2006 Universidad de los Andes Bogotá, Colombia BCs in Physics Advisor Prof Ángela Camacho.

2. Methods and computational skills:

    (a) Ab-initio codes: VASP, CP2K, Gaussian, Octopus, DFTB+, Classical Molecular Dynamics (IMD code)

3. Programming languages:

    (a) Mathematica / Matlab / c++ / Fortran / Python (including cython)

4. Schools:

    (a) Photoinitiated Molecular processes, Organized by the International Max Planck Research School and University of Chemistry and Technology, Prague, SS 2015.

    (b) 2014 TRUCE Summer School on Unconventional Computation, Universidad de Málaga, España, SS 2014.

    (c) 44th IFF Spring School on Quantum Information, Jüllich Forschungszentrum, WS 2013.

    (d) GPU Computing - Methods and Applications in the Natural Sciences, Organized by the International Max Planck Research School and Institute for Low Temprature and Structure Research of the Polish Academy of Sciences, Wroclaw, WS 2012.

5. Conferences:

(a) Influence of structural distortions on the polarization function in molecular-based quantum cellular automata: a minimal model approach-Oral Alejandro Santana, Rafael Gutierrez, Gianaurelio Cuniberti DPG 2014, Dresden, Germany.

(b) Charged transfer in a dynamical Landau-Zener Model: Application in QCA-Oral Alejandro Santana, Rafael Gutierrez, Gianaurelio Cuniberti DPG 2015, Berlin, Germany.

(c) Molecular Quantum Cellular Automata (m-QCA): a new paradigm of information processing-Oral (selected) Alejandro Santana, Rafael Gutierrez, Gianaurelio Cuniberti Theory meets experiment: molecular nanoscience and applications 2015, London, UK.

BIBLIOGRAPHY

[1] R. P. Feynman. Simulating physics with computers. International Journal of Theoretical Physics, 21(6):467–488, 1982.

[2] Charles F. Hawkins Jaume Segura. CMOS electronics: How it works, how it fails. John Wiley and Sons, 2004.

[3] H.G Parks D.M. Brown J Pimbley, M. Ghezzo. Advanced CMOS Process Techonology, volume 19. Academic Press, 1989.

[4] B. De Lacy Costello S. Stepney C. Teuscher Andrew Adamatzky, L Bull, editor. Unconventional Computing. Luniver Press, 2007.

[5] Massimo Macucci, editor. Quantum Cellular Automata: Theory, Experimentation and Prospects. Imperial College Press, 2006.

[6] C. S. Lent, P. D. Tougaw, G. Porod, and G. H. Bernstein. Quantum cellular automata. Nanotechnology, 4(1):49, 1993.

[7] I. Amlani, A. O. Orlov, G. L. Snider, C. S. Lent, and G. H. Bernstein. Demonstration of a functional quantum−dot cellular automata cell. Journal of Vacuum Science and Technology B, 16(6):3795–3799, 1998.

[8] M. Mitic, M. C. Cassidy, K. D. Petersson, R. P. Starrett, E. Gauja, R. Brenner, R. G. Clark, A. S. Dzurak, C. Yang, and D. N. Jamieson. Demonstration of a silicon−based quantum cellular automata cell. Applied Physics Letters, 89(1), 2006.

[9] S. Gardelis, C. G. Smith, J. Cooper, D. A. Ritchie, E. H. Linfield, and Y. Jin. Evidence for transfer of polarization in a quantum dot cellular automata cell consisting of semiconductor quantum dots. Phys. Rev. B, 67:033302, Jan 2003.

[10] M. Macucci, M. Gattobigio, L. Bonci, G. Iannaccone, Prins. G. E., C. Single, G. Wetekam, and D. P. Kern.

[11] G. H. Bernstein, A. Imre, V. Metlushko, A. O. Orlov, L. Zhou, L. Ji, G. Csaba, and W. Porod. Magnetic qca systems. Microelectronics Journal, 36(7):619 – 624, 2005.

[12] H. Qi, S. Sharma, Z. Li, G. L. Snider, A. O Orlov, C. S. Lent, and T. P. Fehlner. Molecular quantum cellular automata cells. electric field driven switching of a silicon surface bound array of vertically oriented two-dot molecular quantum cellular automata. Journal of the American Chemical Society, 125(49):15250–15259, 2003.

[13] Z. Li and T. P. Fehlner. Molecular qca cells. 2. characterization of an unsymmetrical dinuclear mixed−valence complex bound to a au surface by an organic linker. Inorganic Chemistry, 42(18):5715–5721, 2003.

[14] Z. Li, A. M. Beatty, and T. P. Fehlner. Molecular qca cells. 1. structure and functionalization of an unsymmetrical dinuclear mixed-valence complex for surface binding. Inorganic Chemistry, 42(18):5707–5714, 2003.

[15] S. B. Braun-Sand and O. Wiest. Theoretical studies of mixed-valence transition metal complexes for molecular computing. The Journal of Physical Chemistry A, 107(2):285–291, 2003.

[16] V. Arima, M. Iurlo, L. Zoli, S. Kumar, M. Piacenza, F. Della Sala, F. Matino, G. Maruccio, R. Rinaldi, F. Paolucci, M. Marcaccio, P. G. Cozzi, and A. P. Bramanti. Toward quantum−dot cellular automata units: thiolated−carbazole linked bisferrocenes. Nanoscale, 4:813–823, 2012.

[17] W. Hu, K. Sarveswaran, M. Lieberman, and G. H. Bernstein. High−resolution electron beam lithography and dna nano−patterning for molecular qca. IEEE Transactions on Nanotechnology, 4(3):312–316, May 2005.

[18] A. O. Orlov, R. K. Kummamuru, R. Ramasubramaniam, G. Toth, C. S. Lent, G. H. Bernstein, and G. L. Snider. Experimental demonstration of a latch in clocked quantum−dot cellular automata. Applied Physics Letters, 78(11):1625–1627, 2001.

[19] R. P. Cowburn and M. E. Welland. Room temperature magnetic quantum cellular automata. Science, 287(5457):1466–1468, 2000.

[20] A. Pulimeno, M. Graziano, C. Abrardi, D. Demarchi, and G. Piccinini. Molecular qca: A write−in system based on electric fields. In Nanoelectronics Conference (INEC), 2011 IEEE 4th International, pages 1–2, June 2011.

[21] I. Amlani, A. O. Orlov, G. Toth, G. H. Bernstein, C. S. Lent, and G. L. Snider. Digital logic gate using quantum−dot cellular automata. 284(5412):289–291, 1999.

[22] A. O. Orlov, I. Amlani, G. Toth, C. S. Lent, G. H. Bernstein, and G. L. Snider. Experimental demonstration of a binary wire for quantum−dot cellular automata. Applied Physics Letters, 74(19):2875–2877, 1999.

[23] G. L Snider, A. O. Orlov, I. Amlani, G. H. Bernstein, C. S. Lent, J. L. Merz, and W. Porod. Quantum−dot cellular automata: Line and majority logic gate. Japanese Journal of Applied Physics, 38(12S):7227, 1999.

[24] C. S. Lent and B. Isaksen. Clocked molecular quantum−dot cellular automata. IEEE Transactions on Electron Devices, 50(9):1890–1896, Sept 2003.

[25] H Qi, A. Gupta, B.C Noll, G. L. Snider, Y. Lu, C. S. Lent, and T. P. Fehlner. Dependence of field switched ordered arrays of dinuclear mixed−valence complexes on the distance between the redox centers and the size of the counterions. Journal of the American Chemical Society, 127(43):15218–15227, 2005.

[26] J. Jiao, G. J. Long, L. Rebbouh, F. Grandjean, A. M. Beatty, and T. P. Fehlner. Properties of a mixed−valence (feii)2(feiii)2 square cell for utilization in the quantum cellular automata paradigm for molecular electronics. Journal of the American Chemical Society, 127(50):17819–17831, 2005.

[27] Y. Lu, R. Quardokus, C.S. Lent, F. Justaud, C. Lapinte, and S. A. Kandel. Charge localization in isolated mixed−valence complexes: An stm and theoretical study. Journal of the American Chemical Society, 132(38):13519–13524, 2010.

[28] W. Zhongqing, S. Guo, and S. A Kandel. Observation of single dinuclear metal−complex molecules using scanning tunneling microscopy. The Journal of Physical Chemistry B, 110(43):21846–21849, 2006.

[29] By Richard M. Martin. Electronic Structure: Basic Theory and Practical Methods. Cambridge University Press, 2004.

[30] Yang Weitao Robert G. Parr. Density-Functional Theory of Atoms and Molecules. Oxford University Press, 1989.

[31] Reiner M. Dreizler Eberhard Engel. Density Functional Theory: An Advanced Course. Springer.

[32] Jorge Kohanoff. Electronic Structure Calculations for Solids and Molecules: Theory and Computational Methods. Cambridge University Press, 2006.

[33] Peter Fulde. Electron Correlations in Molecules and Solids. Springer.

[34] Miguel Marques, editor. Time-Dependent Density Functional Theory. Springer.

[35] Jorge M. Seminario Perla Balbuena, editor. Molecular Dynamics: From Classical to Quantum Methods. Elsevier, 1999.

[36] Lucjan Piela. Ideas of Quantum Chemistry. ElSevier, 2014.

[37] Juerg Hutter Dominik Marx. Ab Initio Molecular Dynamics: Basic Theory and Advanced Methods. Cambridge University Press, 2012.

[38] U. von Barth and L. Hedin. A local exchange-correlation potential for the spin polarized case. i. Journal of Physics C: Solid State Physics, 5(13):1629, 1972.

[39] Axel D Becke. Density-functional exchange-energy approximation with correct asymptotic behavior. Physical review A, 38(6):3098, 1988.

[40] J. P. Perdew, K. Burke, and M. Ernzerhof. Generalized gradient approximation made simple. Physical review letters, 77(18):3865, 1996.

[41] A. D. Becke. Density−functional exchange−energy approximation with correct asymptotic behavior. Phys. Rev. A, 38:3098–3100, Sep 1988.

[42] A. D. Becke. Densityfunctional thermochemistry. iii. the role of exact exchange. The Journal of Chemical Physics, 98(7), 1993.

[43] Jadran Vrabec Barbara Kirchner. Multiscale Molecular Methods in Applied Chemistry. Springer Science and Business Media, 2012.

[44] Joechen Heyd, Gustavo E. Scuseria, and Matthias Ernzerhof. Erratum: Hybrid functionals based on a screened coulomb potential [j. chem. phys.118, 8207 (2003)]. The Journal of Chemical Physics, 124(21), 2006.

[45] M. Guidon, F. Schiffmann, J. Hutter, and J. VandeVondele. Ab initio molecular dynamics using hybrid density functionals. The Journal of Chemical Physics, 128(21), 2008.

[46] J. Spencer and A. Alavi. Efficient calculation of the exact exchange energy in periodic systems using a truncated coulomb potential. Phys. Rev. B, 77:193110, May 2008.

[47] Guidon M., Hutter J., and VandeVondele J. Auxiliary density matrix methods for hartree−fock exchange calculations. Journal of Chemical Theory and Computation, 6(8):2348–2364, 2010.

[48] Guidon M., Hutter J., and VandeVondele J. Robust periodic hartree−fock exchange for large−scale simulations using gaussian basis sets. Journal of Chemical Theory and Computation, 5(11):3010–3021, 2009.

[49] S. Grimme, J. Antony, S. Ehrlich, and H. Krieg. A consistent and accurate ab initio parametrization of density functional dispersion correction (dft−d) for the 94 elements h−pu. The Journal of Chemical Physics, 132(15), 2010.

[50] D Michael P Mingos Mihai V. Putz, editor. Applications of Density Functional Theory to Biological and Bioinorganic Chemistry. Springer.

[51] Nicola A. Spaldin. A beginner's guide to the modern theory of polarization. Journal of Solid State Chemistry, 195:2 – 10, 2012.

[52] Raffaele Resta and David Vanderbilt. Theory of Polarization: A Modern Approach, pages 31–68. Springer Berlin Heidelberg, Berlin, Heidelberg, 2007.

[53] William J. Kaiser Joseph A. Stroscio, editor. Scanning Tunneling Microscopy. Academic Press, 2013.

[54] J. Tersoff and D. R. Hamann. Theory of the scanning tunneling microscope. Phys. Rev. B, 31:805–813, Jan 1985.

[55] Gerhard Zumbusch Michael Griebel, Stephan Knapek. Numerical Simulation in Molecular Dynamics: Numerics, Algorithms, Parallelization, Applications. Springer Science and Business Media, 2007.

[56] Andrew R. Leach. Molecular Modelling: Principles and Applications. Pearson, 2001.

[57] G. Seifert and J.O. Joswig. Density−functional tight binding: an approximate density−functional theory method. Wiley Interdisciplinary Reviews: Computational Molecular Science, 2(3), 2012.

[58] G. Seifert. Tight−binding density functional theory:âĂĽ an approximate kohn−sham dft scheme. The Journal of Physical Chemistry A, 111(26):5609–5613, 2007.

[59] M. Elstner, D. Porezag, G. Jungnickel, J. Elsner, M. Haugk, Th. Frauenheim, S. Suhai, and G. Seifert. Self−consistent−charge density−functional tight−binding method for simulations of complex materials properties. Phys. Rev. B, 58:7260–7268, Sep 1998.

[60] Jeffrey R. Reimers, editor. Computational Methods for Large Systems: Electronic Structure Approaches for Biotechnology and Nanotechnology. John Wiley and Sons, 2011.

[61] H. A. Witek, K. Morokuma, and A. Stradomska. Modeling vibrational spectra using the self−consistent charge density−functional tight−binding method. i. raman spectra. The Journal of Chemical Physics, 121(11):5171–5178, 2004.

[62] T. Van Voorhis, T. Kowalczyk, B. Kaduk, L.P Wang, C.L Cheng, and Q. Wu. The diabatic picture of electron transfer, reaction barriers, and molecular dynamics. Annual Review of Physical Chemistry, 61(1):149–170, 2010.

[63] J.P Launay. Electron transfer in molecular binuclear complexes and relation with electron transport through nanojunctions. Coordination Chemistry Reviews, 257(9âĂŞ10):1544 − 1554, 2013.

[64] Craig S. Lent. Bypassing the transistor paradigm. Science, 288(5471):1597–1599, 2000.

[65] Pulimeno A., M. Graziano, D. Demarchi, and G. Piccinini. Towards a molecular qca wire: simulation of write-in and read-out systems. Solid-State Electronics, 77:101 − 107, 2012. Special Issue of {IEEE} {INEC} 2011(IEEE International Nano Electronics Conference).

[66] H Qi, S. Sharma, Z. Li, G.L. Snider, A.O. Orlov, C.S Lent, and Fehlner T.P. Molecular quantum cellular automata cells. electric field driven switching of a silicon surface bound array of vertically oriented two-dot molecular quantum cellular automata. Journal of the American Chemical Society, 125(49):15250–15259, 2003.

[67] Y. Lu and Lent C.S. A metric for characterizing the bistability of molecular quantum-dot cellular automata. Nanotechnology, 19(15):155703, 2008.

[68] A. Onipko. An extension of the mcconnell superexchange formula to the case of real conjugated oligomers. Chemical Physics Letters, 292(3):267 − 272, 1998.

[69] A.C Ribou, J.P Launay, M.L. Sachtleben, H. Li, and C.W Spangler. Intervalence electron transfer in mixed valence diferrocenylpolyenes. decay law of the metal−metal coupling with distance. Inorganic Chemistry, 35(13):3735–3740, 1996.

[70] E. Rahimi and S. M. Nejad. Quasi−classical modeling of molecular quantum−dot cellular automata multidriver gates. Nanoscale Research Letters, 7(1):1–12, 2012.

[71] F. Rojas, E. Cota, and S. E. Ulloa. Quantum dynamics, dissipation, and asymmetry effects in quantum dot arrays. Phys. Rev. B, 66:235305, Dec 2002.

[72] N.A Wasio, R.C Quardokus, Forrest R.P, Corcelli S.A., Y. Lu, C.S Lent, F. Justaud, C. Lapinte, and Kandel S. A. Stm imaging of three−metal−center molecules: Comparison of experiment and theory for two mixed−valence oxidation states. The Journal of Physical Chemistry C, 116(48):25486–25492, 2012.

[73] M. Crocker, X. S. Hu, and M. Niemier. Defects and faults in qca-based plas. J. Emerg. Technol. Comput. Syst., 5(2):8:1–8:27, July 2009.

[74] M. Crocker, M. Niemier, X. S. Hu, and M. Lieberman. Molecular qca design with chemically reasonable constraints. J. Emerg. Technol. Comput. Syst., 4(2):9:1–9:21, April 2008.

[75] Dysart T. J. Modeling of electrostatic qca wires. IEEE Transactions on Nanotechnology, 12(4):553–560, July 2013.

[76] A. Pulimeno, M. Graziano, A. Sanginario, V. Cauda, D. Demarchi, and Piccinini G. Bis−ferrocene molecular qca wire: Ab initio simulations of fabrication driven fault tolerance. IEEE Transactions on Nanotechnology, 12(4):498–507, July 2013.

[77] A. Pulimeno, M. M. Graziano, A. Sanginario, V. Cauda, D. Demarchi, and G. Piccinini. Bis−ferrocene molecular qca wire: Ab initio simulations of fabrication driven fault tolerance. IEEE Transactions on Nanotechnology, 12(4):498–507, July 2013.

[78] A. Santana−Bonilla, R. Gutierrez, L. Medrano−Sandonas, D. Nozaki, A. P. Bramanti, and G. Cuniberti. Structural distortions in molecular-based quantum cellular automata: a minimal model based study. Phys. Chem. Chem. Phys., 16:17777–17785, 2014.

[79] C.S. Lent, B. Isaksen, and M. Lieberman. Molecular quantum−dot cellular automata. Journal of the American Chemical Society, 125(4):1056–1063, 2003.

[80] M. Elstner, D. Porezag, G. Jungnickel, J. Elsner, M. Haugk, Th. Frauenheim, S. Suhai, and G. Seifert. Self−consistent−charge density−functional tight−binding method for simulations of complex materials properties. Phys. Rev. B, 58:7260–7268, Sep 1998.

[81] M. Elstner, P. Hobza, T. Frauenheim, S. Suhai, and E. Kaxiras. Hydrogen bonding and stacking interactions of nucleic acid base pairs: A density−functional−theory based treatment. The Journal of Chemical Physics, 114(12):5149–5155, 2001.

[82] G. S. Vasilev and N. V. Vitanov. Coherent excitation of a two−state system by a gaussian field. Phys. Rev. A, 70:053407, Nov 2004.

[83] N. V. Vitanov and Knight P. L. Coherent excitation by asymmetric pulses. Journal of Physics B: Atomic, Molecular and Optical Physics, 28(9):1905, 1995.

[84] K. Tokunaga. Metal dependence of signal transmission through molecularquantum-dot cellular automata (qca): A theoretical studyon fe, ru, and os mixed−valence complexes. Materials, 3(8):4277, 2010.

[85] A. Nitzan. Chemical dynamics in Condensed Phases: Relaxation, Transfer, and Reactions in Condensed Molecular systems. Oxford University Press, 2006.

[86] D. Tannor. Introduction to Quantum mechanics: A time−dependent perspective. University Science Books, 2006.

[87] A. Palii, B. Tsukerblat, Modesto J., J. Clemente, and E. Coronado. Coherent manipulation of polarization in mixed−valence compounds by electric pulse via landau−zener transitions. The Journal of Physical Chemistry C, 116(8):4999–5008, 2012.

[88] A. Farazdel, M. Dupuis, E. Clementi, and Aviram A. Electric−field induced intramolecular electron transfer in spiro .pi.−electron systems and their suitability as molecular electronic devices. a theoretical study. Journal of the American Chemical Society, 112(11):4206–4214, 1990.

[89] Wikipedia. Jacobi eigenvalue algorithm. [Online; accessed 22-July-2014].

[90] W.H. Press, S.A. Teukolsky, W.T. Vetterling, and B.P. Flannery. Numerical Recipes: The Art of Scientific Computing. Cambridge University Press.

[91] T. Mikayama, M. Ara, K. Uehara, A. Sugimoto, K. Mizuno, and N. Inoue. Nanometre−scale photoelectric characteristics of a molecular device monolayer. Phys. Chem. Chem. Phys., 3:3459–3462, 2001.

[92] H. Mizuseki, Niimura K., C. Majumder, R.V. Belosludov, Farajian A.A., Y. Kawazoe, and C. Majumder. Theoretical study of donor−spacer−acceptor structure molecule for stable molecular rectifier. Molecular Crystals and Liquid Crystals, 406(1):11–17, 2003.

[93] Landau L. Phys. Z. Sowjetunion, 2:46, 1932.

[94] Zener C. Proc. R. Soc. London, Ser. A, 137:696, 1932.

[95] N. V. Vitanov and B. M. Garraway. Landau−zener model: Effects of finite coupling duration. Phys. Rev. A, 53:4288–4304, Jun 1996.

[96] C. W. S. Conover. Effects of pulse shape on strongly driven two−level systems. Phys. Rev. A, 84:063416, Dec 2011.

[97] H. A. Witek, S. Irle, and K. Morokuma. Analytical second−order geometrical derivatives of energy for the self−consistent−charge density−functional tight−binding method. Journal of Chemical Physics, 121(11):5163 − 5170, 2004.

[98] Hans J. Kupka, editor. Transitions in Molecular Systems. WILEY-VCH, 2010.

[99] Y. Suzuki, A. Abedi, N. T. Maitra, and EKU Gross. Laser-induced electron localization in h 2+: mixed quantum-classical dynamics based on the exact time-dependent potential energy surface. Physical Chemistry Chemical Physics, 17(43):29271–29280, 2015.

[100] Jeffrey R Reimers, Laura K McKemmish, Ross H McKenzie, and Noel S Hush. Non-adiabatic effects in thermochemistry, spectroscopy and kinetics: the general importance of all three born−oppenheimer breakdown corrections. Physical Chemistry Chemical Physics, 17(38):24641–24665, 2015.

[101] Abbas Farazdel, Michel Dupuis, Enrico Clementi, and Ari Aviram. Electric-field induced intramolecular electron transfer in spiro. pi.-electron systems and their suitability as molecular electronic devices. a theoretical study. Journal of the American Chemical Society, 112(11):4206–4214, 1990.

[102] Materials meets Concepts in Molecule-based Electronics. Ortmann, f. and radke, k s. and guenther, a. and kasemann, d. and leo, k. and cuniberti, g. Advanced Functional Materials, 25:1933–1954, 2015.

[103] M. E. Garah, R. C. Perone, Alejandro Santana-Bonilla, S. Haar, M. Campitiello, R. Gutierrez, G. Cuniberti, S. Masiero, A. Ciesielski, and P. Samori. Guanosine−based hydrogen−bonded 2d scaffolds: metal−free formation of g−quartet and g−ribbon architectures at the solid/liquid interface. Chem. Commun., 51:11677–11680, 2015.

[104] G. P. Spada, S. Lena, S. Masiero, S. Pieraccini, M. Surin, and P. Samori. Guanosine−based hydrogen−bonded scaffolds: Controlling the assembly of oligothiophenes. Advanced Materials, 20(12):2433–2438, 2008.

[105] G. Gottarelli, S. Masiero, E. Mezzina, S. Pieraccini, J. P. Rabe, P. Samori, and G. Spada. The self−assembly of lipophilic guanosine derivatives in solution and on solid surfaces. Chemistry - A European Journal, 6(17):3242–3248, 2000.

[106] A. Ciesielski, S. Lena, S. Masiero, G. Spada, and P. Samori. Dynamers at the solid−liquid interface: Controlling the reversible assembly/reassembly process between two highly ordered supramolecular guanine motifs. Angewandte Chemie International Edition, 49(11):1963–1966, 2010.

[107] M. J. Frisch, G. W. Trucks, H. B. Schlegel, G. E. Scuseria, M. A. Robb, J. R. Cheeseman, G. Scalmani, V. Barone, B. Mennucci, G. A. Petersson, H. Nakatsuji, M. Caricato, X. Li, H. P. Hratchian, A. F. Izmaylov, J. Bloino, G. Zheng, J. L. Sonnenberg, M. Hada, M. Ehara, K. Toyota, R. Fukuda, J. Hasegawa, M. Ishida, T. Nakajima, Y. Honda, O. Kitao, H. Nakai, T. Vreven, J. A. Montgomery, Jr., J. E. Peralta, F. Ogliaro, M. Bearpark, J. J. Heyd, E. Brothers, K. N. Kudin, V. N. Staroverov, R. Kobayashi, J. Normand, K. Raghavachari, A. Rendell, J. C. Burant, S. S. Iyengar, J. Tomasi, M. Cossi, N. Rega, J. M. Millam, M. Klene, J. E. Knox, J. B. Cross, V. Bakken, C. Adamo, J. Jaramillo, R. Gomperts, R. E. Stratmann, O. Yazyev, A. J. Austin, R. Cammi, C. Pomelli, J. W. Ochterski, R. L. Martin, K. Morokuma, V. G. Zakrzewski, G. A. Voth, P. Salvador, J. J. Dannenberg, S. Dapprich, A. D. Daniels, ÃŰ. Farkas, J. B. Foresman, J. V. Ortiz, J. Cioslowski, and D. J. Fox. GaussianâĹij09 Revision E.01. Gaussian Inc. Wallingford CT 2009.

[108] C. J. Cramer and D. G. Truhlar. Density functional theory for transition metals and transition metal chemistry. Phys. Chem. Chem. Phys., 11:10757–10816, 2009.

[109] P. J. Hay and W. R. Wadt. Ab initio effective core potentials for molecular calculations. potentials for the transition metal atoms sc to hg. The Journal of Chemical Physics, 82(1):270–283, 1985.

[110] G. A. Petersson, A. Bennett, T. G. Tensfeldt, M. A. Al-Laham, W. A. Shirley, and J. Mantzaris. A complete basis set model chemistry. i. the total energies of closedshell atoms and hydrides of the firstrow elements. The Journal of Chemical Physics, 89(4):2193–2218, 1988.

[111] G. Lippert, J. Hutter, and M. Parrinello. A hybrid gaussian and plane wave density functional scheme. Molecular Physics, 92(3):477–488, 1997.

[112] S. Goedecker, M. Teter, and J. Hutter. Separable dual−space gaussian pseudopotentials. Phys. Rev. B, 54:1703–1710, Jul 1996.

[113] C. Hartwigsen, S. Goedecker, and J. Hutter. Relativistic separable dual−space gaussian pseudopotentials from h to rn. Phys. Rev. B, 58:3641–3662, Aug 1998.

[114] M. Krack. Pseudopotentials for h to kr optimized for gradient−corrected exchange−correlation functionals. Theoretical Chemistry Accounts, 114(1-3):145–152, 2005.

[115] J. Hutter, M. Iannuzzi, F. Schiffmann, and J. VandeVondele. cp2k: atomistic simulations of condensed matter systems. Wiley Interdisciplinary Reviews: Computational Molecular Science, 4(1):15–25, 2014.

[116] A. J. Atkins, M. Bauer, and C. R. Jacob. The chemical sensitivity of x−ray spectroscopy: high energy resolution xanes versus x−ray emission spectroscopy of substituted ferrocenes. Phys. Chem. Chem. Phys., 15:8095–8105, 2013.

[117] L. P. Wolters, N. W. G. Smits, and C. Fonseca-Guerra. Covalency in resonance−assisted halogen bonds demonstrated with cooperativity in n−halo−guanine quartets. Phys. Chem. Chem. Phys., 17:1585–1592, 2015.

[118] Zou B., K. Dreger, C. Mueck-Lichtenfeld, Grimme S., Schaefer H.J., Fuchs H., and Chi L. Simple and complex lattices of n−alkyl fatty acid amides on a highly oriented pyrolytic graphite surface. Langmuir, 21(4):1364–1370, 2005.

[119] M. Meyer, T. Steinke, M. Brandl, and J. Suehnel. Density functional study of guanine and uracil quartets and of guanine quartet/metal ion complexes. Journal of Computational Chemistry, 22(1):109–124, 2001.

[120] Goursot A., Mineva T., Kevorkyants R., and Talbi D. Interaction between n−alkane chains:âĂL' applicability of the empirically corrected density functional theory for van der waals complexes. Journal of Chemical Theory and Computation, 3(3):755–763, 2007.

[121] R. J. Largent, W. F. Polik, and J. R. Schmidt. Symmetrizer: Algorithmic determination of point groups in nearly symmetric molecules. Journal of Computational Chemistry, 33(19):1637–1642, 2012.

[122] G. Lippert, J. Hutter, and M. Parrinello. Theoretical Chemistry Accounts, 103(2):124–140, 1999.

[123] S. Nosé. A unified formulation of the constant temperature molecular dynamics methods. The Journal of Chemical Physics, 81(1):511–519, 1984.

[124] S. Nosé. A molecular dynamics method for simulations in the canonical ensemble. Molecular Physics, 52(2):255–268, 1984.

[125] V. Setnička, J. Nový, S. Boehm, N. Sreenivasachary, M. Urbanová, and K. Volka. Molecular structure of guanine−quartet supramolecular assemblies in a gel−state based on a dft calculation of infrared and vibrational circular dichroism spectra. Langmuir, 24(14):7520–7527, 2008.

[126] Neil Burdess. Statistics: A Short, Clear Guide. SAGE, 2010.

[127] Bucher C., Devillers C.H., Moutet J.C., Royal G., and Saint-Aman E. Ferrocene−appended porphyrins: Syntheses and properties. Coordination Chemistry Reviews, 253(1âĂŞ2):21 − 36, 2009.

[128] M. El Garah, A. Santana Bonilla, A. Ciesielski, A. Gualandi, L. Mengozzi, A. Fiorani, M. Iurlo, M. Marcaccio, R. Gutierrez, S. Rapino, M. Calvaresi, F. Zerbetto, G. Cuniberti, P. G. Cozzi, F. Paolucci, and P. Samori. Molecular design driving tetraporphyrin self−assembly on graphite: a joint stm, electrochemical and computational study. Nanoscale, 8:13678–13686, 2016.

[129] Aydin M. Dft and raman spectroscopy of porphyrin derivatives: Tetraphenyl-porphine (tpp). Vibrational Spectroscopy, 68:141 – 152, 2013.

[130] Zhang L., Qi D., Zhang Y., Bian Y., and Jiang J. Density functional theory studies on the structures and electronic communication of meso−ferrocenylporphyrins: Long range orbital coupling via porphyrin core. Journal of Molecular Graphics and Modelling, 29(5):717 – 725, 2011.

[131] Takeshi Yanai, David P Tew, and Nicholas C Handy. A new hybrid exchange−correlation functional using the coulomb−attenuating method (cam−b3lyp). Chemical Physics Letters, 393(1âĂŞ3):51 – 57, 2004.

[132] A. Vargas-Caamal, S. Pan, F. Ortiz-Chi, J.L. Cabellos, R. A. Boto, J. Contreras-Garcia, A. Restrepo, P. K. Chattaraj, and G. Merino. How strong are the metallocene−metallocene interactions? cases of ferrocene, ruthenocene, and osmocene. Phys. Chem. Chem. Phys., 18:550–556, 2016.

[133] A. K. Perepogu and P. R. Bangal. Preparation and characterization of free-standing pure porphyrin nanoparticles. Journal of chemical sciences, 120(5):485–491, 2008.

[134] Ormaza M., Abufager P., Bachellier N., Robles R., Verot M., Bahers T.L., Bocquet M.L., Lorente N., and Laurent Limot L. Assembly of ferrocene molecules on metal surfaces revisited. The Journal of Physical Chemistry Letters, 6(3):395–400, 2015.

[135] K. Svensson, T.R. Bedson, and Palmer R.E. Dissociation and desorption of ferrocene on graphite by low energy electron impact. Surface Science, 451(1-3):250 – 254, 2000.

[136] H. S. Kang and A. Pramanik. The effect of doping on the energetics and quantum conductance in graphene nanoribbons with a metallocene adsorbate. The Journal of Chemical Physics, 135(12), 2011.

[137] Monti O. L. A. Understanding interfacial electronic structure and charge transfer: An electrostatic perspective. The Journal of Physical Chemistry Letters, 3(17):2342–2351, 2012.

[138] Fernández-Torrente I., Kreikemeyer-Lorenzo D., Stró żecka A., Franke K. J., and J. I. Pascual. Gating the charge state of single molecules by local electric fields. Phys. Rev. Lett., 108:036801, Jan 2012.

[139] Guo W., Du S.X., Zhang Y.Y., Hofer W.A., Seidel C., Chi L.F., Fuchs H., and Gao H.-J. Electrostatic field effect on molecular structures at metal surfaces. Surface Science, 603(17):2815 – 2819, 2009.

[140] Track A.M., Rissner F., Heimel G., Romaner L., Kaefer D., Bashir A., Rangger G.M., Oliver Hofmann O.T., BuÄḊko T., Witte G., and Zojer E. Simultaneously understanding the geometric and electronic structure of anthracene-selenolate on au(111): A combined theoretical and experimental study. The Journal of Physical Chemistry C, 114(6):2677–2684, 2010.

[141] Andrew Thye Shen Wee Norbert Koch, Nobuo Ueno, editor. The Molecule−Metal Interface. John Wiley and Sons, 2013.

[142] B. Naydenov, S. Torsney, A. Santana-Bonilla, M. El Garah, A. Ciesielski, A. Gualandi, L. Mengozzi, P. G. Cozzi, R. Gutierrez, P. Samori, G. Cuniberti, and J. J Boland. From ultra-high vacuum to ambient conditions: Stm/sts characterization of modelled 2d molecular networks. Submitted.

[143] K.-F. Braun, V. Iancu, N. Pertaya, K.-H. Rieder, and S.-W. Hla. Decompositional incommensurate growth of ferrocene molecules on a au(111) surface. Phys. Rev. Lett., 96:246102, Jun 2006.

[144] C. Adamo and V. Barone. Toward reliable density functional methods without adjustable parameters: The pbe0 model. The Journal of Chemical Physics, 110(13), 1999.

[145] F. Jensen. Polarization consistent basis sets: Principles. The Journal of Chemical Physics, 115(20), 2001.

[146] F. Jensen and T. Helgaker. Polarization consistent basis sets. v. the elements si−cl. The Journal of Chemical Physics, 121(8):3463–3470, 2004.

[147] Lüder J., Sanyal B., Olle E., Puglia C., and Brena B. Comparison of van der waals corrected and sparse−matter density functionals for the metal−free phthalocyanine/gold interface. Phys. Rev. B, 89:045416, Jan 2014.

[148] Terentjevs A., Steele M.P., Blumenfeld M.L., Ilyas N., Kelly L.L., Fabiano E., Monti O.L.A., and Della Sala F. Interfacial electronic structure of the dipolar vanadyl naphthalocyanine on au(111): "push−back" vs dipolar effects. The Journal of Physical Chemistry C, 115(43):21128–21138, 2011.

[149] Y. Zhang and W. Yang. Comment on "generalized gradient approximation made simple". Phys. Rev. Lett., 80:890–890, Jan 1998.

[150] Rusu P.C and Brocks G. Surface dipoles and work functions of alkylthiolates and fluorinated alkylthiolates on au(111). The Journal of Physical Chemistry B, 110(45):22628–22634, 2006.

[151] Sławi ńska J., P. Dabrowski, and I. Zasada. Doping of graphene by a au(111) substrate: Calculation strategy within the local density approximation and a semiempirical van der waals approach. Phys. Rev. B, 83:245429, Jun 2011.

[152] H. Li, Y. Duan, V. Coropceanu, and J.L. Bredas. Electronic structure of the pentacene−gold interface: A density-functional theory study. Organic Electronics, 10(8):1571–1578, 2009.

[153] Fall C.J., Binggeli N., and Baldereschi A. Deriving accurate work functions from thin−slab calculations. Journal of Physics: Condensed Matter, 11(13):2689, 1999.

[154] J. Tao, J. P. Perdew, V. N. Staroverov, and G. E. Scuseria. Climbing the density functional ladder: Nonempirical meta−generalized gradient approximation designed for molecules and solids. Phys. Rev. Lett., 91:146401, Sep 2003.

[155] A. Savin, R. Nesper, S. Wengert, and T. F. Faessler. Elf: The electron localization function. Angewandte Chemie International Edition in English, 36(17):1808–1832, 1997.

[156] H. H. Jaffé. The electronic structure of ferrocene. The Journal of Chemical Physics, 21(1):156–157, 1953.

[157] M.J Mayor-López and J. Weber. Dft calculations of the binding energy of metallocenes. Chemical Physics Letters, 281(1âĂŞ3):226 – 232, 1997.

[158] M. Swart. Metalligand bonding in metallocenes: Differentiation between spin state, electrostatic and covalent bonding. Inorganica Chimica Acta, 360(1):179 – 189, 2007. Inorganic Chemistry - The Next Generation.

[159] J. Frunzke, M. Lein, and G. Frenking. Structures, metal−ligand bond strength, and bonding analysis of ferrocene derivatives with group−15 het-eroligands fe(eta5−e5)2 and fecp(eta5−e5) (e = n, p, as, sb). a theoretical study. Organometallics, 21(16):3351–3359, 2002.

[160] Y. Zhao and D. G. Truhlar. Comparative assessment of density functional methods for 3d transition−metal chemistry. The Journal of Chemical Physics, 124(22), 2006.

[161] S. Coriani, A. Haaland, T. Helgaker, and P. Joergensen. The equilibrium structure of ferrocene. ChemPhysChem, 7(1):245–249, 2006.

[162] J.D Chai and M. Head-Gordon. Long−range corrected hybrid density functionals with damped atom−atom dispersion corrections. Phys. Chem. Chem. Phys., 10:6615–6620, 2008.

[163] W.K. Winter, B. Curnutte, and S. E. Whitcomb. The infrared spectrum and structure of crystalline ferrocene. Spectrochimica Acta, 15:1085 – 1102, 1959.

[164] N. Mohammadi, A. Ganesan, C. T. Chantler, and F. Wang. Differentiation of ferrocene {D5d} and {D5h} conformers using {IR} spectroscopy. Journal of Organometallic Chemistry, 713:51 – 59, 2012.

[165] V. N. Staroverov, G. E Scuseria, J. Tao, and J. P. Perdew. Comparative assessment of a new nonempirical density functional: Molecules and hydrogen-bonded complexes. The Journal of chemical physics, 119(23):12129–12137, 2003.

[166] Ulrike Salzner. Quantitatively correct uv-vis spectrum of ferrocene with tdb3lyp. Journal of Chemical Theory and Computation, 9(9):4064–4073, 2013.

[167] L Edwards, DH Dolphin, M. Gouterman, and A. D Adler. Porphyrins xvii. vapor absorption spectra and redox reactions: tetraphenylporphins and porphin. Journal of Molecular Spectroscopy, 38(1):16–32, 1971.

[168] N. S. Venkataramanan, A. Suvitha, H. Nejo, H. Mizuseki, and Y. Kawazoe. Electronic structures and spectra of symmetric meso-substituted porphyrin: Dft and tddft-pcm investigations. International Journal of Quantum Chemistry, 111(10):2340–2351, 2011.

[169] Kiet A Nguyen and Ruth Pachter. Ground state electronic structures and spectra of zinc complexes of porphyrin, tetraazaporphyrin, tetrabenzoporphyrin, and phthalocyanine: A density functional theory study. The Journal of Chemical Physics, 114(24):10757–10767, 2001.

[170] Zhang Y.H., Zhao W., Jiang P., Zhang L.J., Zhang T., and Wang J. Structural parameters and vibrational spectra of a series of zinc meso-phenylporphyrins: A dft and experimental study. Spectrochimica Acta Part A: Molecular and Biomolecular Spectroscopy, 75(2):880 – 890, 2010.

[171] James R Williamson. G-quartet structures in telomeric dna. Annual review of biophysics and biomolecular structure, 23(1):703–730, 1994.

[172] T. van Mourik and A. J. Dingley. Characterization of the monovalent ion position and hydrogen-bond network in guanine quartets by dft calculations of nmr parameters. Chemistry − A European Journal, 11(20):6064–6079, 2005.